Title	Ultra-low and wide bandwidth vibrational energy harvesting using a statically balanced compliant mechanism
Authors	Liang, Haitong
Publication date	2022-04-21
Original Citation	Liang, H. 2022. Ultra-low and wide bandwidth vibrational energy harvesting using a statically balanced compliant mechanism. PhD Thesis, University College Cork.
Type of publication	Doctoral thesis
Rights	© 2022, Haitong Liang. - https://creativecommons.org/licenses/by/4.0/
Download date	2025-08-05 09:27:22
Item downloaded from	https://hdl.handle.net/10468/13198

University College Cork, Ireland

Coláiste na hOllscoile Corcaigh

ULTRA-LOW AND WIDE BANDWIDTH VIBRATIONAL ENERGY HARVESTING USING A STATICALLY BALANCED COMPLIANT MECHANISM

A thesis submitted in accordance with the requirements for the degree of

Doctor of Philosophy

By

Haitong Liang

Supervisors: Dr. Guangbo Hao;

Dr. Zbigniew Olszewski

School of Engineering and Architecture

Tyndall National Institute

April 2022

"Life will fill the universe."

—— Kevin Kelly

Declaration

This is to certify that the work I am submitting is my own and has not been submitted for another degree, either at University College Cork or elsewhere. All external references and sources are clearly acknowledged and identified within the contents. I have read and understood the regulations of University College Cork concerning plagiarism.

Haitong Liang: *Haitong Liang*

Date: April 2022

List of Publications

Journal papers:

[1] **Liang, H.**, Hao, G.*, Olszewski, O.Z., and Pakrash, V., Ultra-low wide bandwidth vibrational energy harvesting using a statically balanced compliant mechanism. *International Journal of Mechanical Sciences*, 2022: p. 107130. (**This journal paper arises from Chapters 3, 4 and 5 of this thesis**)

[2] **Liang, H.**, Hao, G.* and Olszewski, O.Z.*, A review on vibration-based piezoelectric energy harvesting from the aspect of compliant mechanisms. *Sensors and Actuators A: Physical*, 2021: p. 112743. (**This journal paper arises from Chapter 2 of this thesis**)

[3] **Liang, H.**, Hao, G.*, Olszewski, O.Z. Jiang, Z. and Zhang, K., Design of a twisting origami robot mechanism inspired by Resch Triangular Tessellation, *Mechanism and Machine Theory.* (Submitted and under review) (**This journal paper arises from the report for Module ME6012: Advanced Robotics during the PhD study**)

Conference papers:

[1] **Liang, H.**, Carandell Widmer, M., Olszewski, O.Z. and Hao, G.*, A new nonlinear compliant mechanism for harvesting energy from ocean waves. *IEEE Oceans 2022*, February 21-24, 2022, Chennai, India. (**This conference paper arises from Chapter 6 of this thesis**)

[2] **Liang, H.**, Hao, G.*, Olszewski, O.Z. and Pentek, A., Design of a twisting origami robot inspired by Resch Triangular Tessellation, *5th IEEE/IF ToMM International conference on Reconfigurable Mechanisms and Robots 2021*, August 12-14, 2021, Toronto, Canada. (**This conference paper arises from the report for Module ME6012: Advanced Robotics during the PhD study**)

Oral presentations:

[1] **Liang, H.**, Hao, G., and Olszewski, O.Z., A review on vibration-based piezoelectric energy harvesting from the aspect of compliant mechanisms. *3ʳᵈ International Conference on Vibration and Energy Harvesting Applications,* July 9-12, 2021, Xi'an, Shaanxi, China. (**This oral presentation arises from Chapter 2 of this thesis**)

[2] **Liang, H.**, Hao, G., Olszewski, O.Z. and Pentek, A., Design of a twisting origami robot inspired by Resch Triangular Tessellation, *5th IEEE/IF ToMM International conference on Reconfigurable Mechanisms and Robots 2021*, August 12-14, 2021, Toronto, Canada. (**This oral presentation arises from the report for Module ME6012: Advanced Robotics during the PhD study**)

Posters:

[1] **Liang, H.**, Carandell Widmer, M., Olszewski, O.Z. and Hao, G., A new nonlinear compliant mechanism for harvesting energy from ocean waves. *IEEE Oceans 2022*, February 21-24, 2022, Chennai, India. (**This poster arises from Chapter 6 of this thesis**)

[2] **Liang, H.**, Olszewski, O.Z. and Hao, G., A review on piezoelectric energy harvesters from the aspect of mechanical structures. *NiPS Summer School 2019*, September 3-6, Perugia, Italy. (**This poster arises from Chapter 2 of this thesis**)

Acknowledgement

Abstract

The development of Internet of Things (IoT) in recent times has met with the challenges of powering numerous sensors in a wireless sensor network with traditional batteries, owing to their limited lifetime, environmental pollution, high maintenance cost, etc. Vibrational energy harvesting is an ideal and green powering solution due to the ubiquitous environmental vibrations and their sufficient power density ($\sim$0.3 μW/mm^3). A systematic review on state-of-the-art structural methodologies of vibrational energy harvesters from the aspect of compliant mechanisms (CMs) is first carried out, focusing on the energy conversion mechanism by piezoelectric effect in particular. The frequency gap between the majority of energy harvesting devices (with narrow bandwidth in the high frequency range) and the accessible vibrational sources (at 1-10 Hz levels) is observed and is still to be filled.

In this thesis, a structural solution of vibrational energy harvesters using a statically balanced compliant mechanism (SBCM) is proposed, theoretically characterised, and experimentally demonstrated to address this need. This SBCM is designed based on the concept of stiffness compensation between a linear positive-stiffness component (two double parallelograms in parallel) and a nonlinear negative-stiffness component (two sets of post-buckled fixed-guided compliant beams in parallel). A design guideline of the SBCM starting from using a rapid-design stiffness compensation equation is provided for a reasonable approximation of results. The whole-range nonlinear force-displacement relationship of the SBCM is obtained through nonlinear finite element analysis (FEA) simulations and a 5th order polynomial fit is chosen taking only odd terms into account. Subsequently, a dynamic analytical model of the displacement response of the SBCM to harmonic base excitations has been derived based on the averaging method. The accuracy of this analytical model is confirmed by numerical analysis and FEA simulations. Next, an SBCM prototype was fabricated and its applicability to piezoelectric vibrational energy harvesters (PVEHs) was demonstrated by integrating piezoelectric transducers, made of PVDF films, with compliant beams of the SBCM to generate electric outputs in response to bending of the beams. Static balancing was successfully tuned in the static experiments. Displacement responses and electric outputs were obtained from the preliminary SBCM-based PVEH in the ultra-low and wide frequency range with weak accelerations in the dynamic experiments. Two application cases of the SBCM in macro and

micro scales in vibrational energy harvesting were investigated using FEA simulations. The integration of the SBCM into an oceanic drifter for harvesting vibrational energy from ocean waves was first explored. The SBCM is then miniaturized in the MEMS scale and its dynamic displacement under harmonic base excitation was then demonstrated.

In conclusion, a novel SBCM structure is designed based on the stiffness compensation principle. It is verified analytically, numerically and experimentally that this SBCM structure responds to regular and irregular vibrations over ultra-low wide bandwidth frequencies (theoretically starting above 0 Hz) and low accelerations regardless of the dimensions and scales. It provides an effective structural solution to the ultra-low wide bandwidth vibrational energy harvesters. Future work of this research includes optimization of the SBCM structure and electric circuits, application of the SBCM-based PVEHs in real vibrational conditions, miniaturization of the SBCM in the MEMS scale, and integration of the SBCM with other nonlinear oscillators.

Table of Contents

List of Figures

XIII

List of Tables

List of Acronyms

IoT   Internet of Things

PVEH   Piezoelectric Vibrational Energy Harvester

CM   Compliant Mechanism

SBCM   Statically Balanced Compliant Mechanism

BCM   Beam Constraint Modelling

TBCM   Timashenko-beam-theory-based Beam Constraint Modelling

PRBM   Pseudo-rigid-body Model

PVDF   Polyvinylidene Fluoride

FEA   Finite Element Analysis

FACT   Freedom And Constraint Topology

NPD   Normalized Power Density

RMS   Root Mean Square

FFT   Fast Fourier Transform

MEMS   Microelectromechanical Systems

DoF   Degree of Freedom

Chapter 1 Background and Motivations

In many ways, man-made devices are similar to natural creatures which consume energy and achieve desired functions. Just like the evolution in nature in the past billions of years, man-made devices are now in their own evaluation process which is significantly prompted by the technologies such as advanced materials, large-scale integrated circuits, quantum computing, artificial intelligence, space exploration etc. Kevin Kelly anticipated in his book, *Out of Control*, that "*life will fill the universe*" [3]. It is an exciting prediction that the universe is full of floating artificial creatures with intelligence. However, this evolution is still in its infancy stage. The reachable range and working life time of current devices are significantly limited due to the restrictions imposed by the traditional power sources, e.g. electric wires and batteries. Just like that all the natural creatures capture energy from the environment, from the photosynthesis of plants to hunting behaviors of mammals, artificial creatures are expected to scavenge energy from the ambient environment and self-power automatically. This research targets on the enhancement of vibrational energy harvesting with a novel statically balanced compliant mechanism, which can be tiny but a solid step in the revolutionary process towards a universe full of vigor and intelligence.

1.1 Introduction

A smarter human world is foreseeable in the short future with the rapid development of Internet of Things (IoT) [4, 5]. As a fundamental portion of this global IoT engineering, trillions of low-power-cost sensors and circuits will be distributed all over the world for data collection, environment monitoring, wirelessly information exchange, etc. in the following decade [6]. However, the traditional powering methods bring problems such as limited distribution range and high maintenance costs for replacing or recharging the batteries. Harvesting energy from the ambient environment is an ideal and eco-friendly solution to power the numerous electronics. It is not only because less carbon emission from the traditional energy sources and

less pollution from the batteries, but also this technology expands the distribution range of the sensors to extreme environment, such as deep wells, nuclear factories, and even inside human bodies, where changing or recharging batteries are challenging, risky or impossible. Thanks to the improvement of technologies, e.g. large scale integration, low-energy-cost electronics, etc., over the past decades, the development and application of energy harvesting have been highly promoted [7, 8].

In the ambient environment, energy generally exists in various forms, such as light, heat, electromagnetic fields, mechanical vibrations, etc. Harvesting energy from mechanical vibrations is more attractive. This is because mechanical vibrations, e.g. motions of human and animals, rolling ocean waves, running rivers, blowing winds, seismic activities happening in every minute [9], are ubiquitous and independent of the seasons, weather and locations. In addition, vibrational energy harvesters with appropriate energy-conversion components and electrical circuits have relatively high energy density (about 0.3 μW/mm^3) [10, 11] and the availability of low-power circuits and sensors (μW-mW range) [8] makes vibrational energy harvesting a suitable and practical energy source for various application scenarios.

In principle, the vibrational energy harvester is analogous to an electronic "pump" which forces the electrons to flow in electronic circuits and the pump is driven by the environmental vibrations. To realize the electromechanical coupling between the mechanical and electric domains in vibrational energy harvesters, there are four main mechanisms available: piezoelectric [10, 12, 13], electromagnetic [14-17], electrostatic [18-20] and triboelectric [21-23]. Despite the difference among these principles adopted to convert mechanical vibrations into electrical energy, mechanical structures are equally and fundamentally important to the vibrational energy harvesters. It is because mechanical structures of vibrational energy harvesters act as interfaces between the environmental vibrations and energy-conversion components [24, 25]. Their sensitivity to frequencies and accelerations determines how much mechanical energy can be captured which influences the energy generation capability of the energy harvesters. Therefore, this research attempts to enhance the dynamic performance of the vibrational energy harvesters with novel structural designs which can be combined with different energy-conversion principles. For a clear illustration on the dynamic performance of the advanced structures in the application of vibrational energy harvesting, a specific energy-conversion principle has to be selected as an example and it is not necessary to explore all existing energy-conversion principles in one research project. Piezoelectric effect is utilized in

this research for the assessment and demonstration of the structural design in vibrational energy harvesting and thus piezoelectric vibrational energy harvesters (PVEHs) are focused throughout the thesis.

1.2 Piezoelectric vibrational energy harvesters

In the literature, various structural methodologies have been reported for PVEHs. Piezoelectric cantilevers are the simplest PVEHs [26, 27]. These linear PVEHs have large energy output at fundamental resonant frequencies but their effective frequency bandwidth is narrow and a slight shift from the resonant frequencies will lead to a dramatic drop of the power output [28, 29]. This dynamic displacement-frequency response curve is shown schematically in Fig. 1.1(a). To widen the frequency bandwidth, different kinds of structural solutions have been proposed for PVEHs in the past decades [30]. A comprehensive review is carried out on these structures and it is presented in detail in Chapter 2 to highlight the contributions of the review work without breaking the logic structure of the thesis. According to this review, existing structures of PVEHs can be categorized in to five groups, namely mono-stable structures, multi-stable structures, multi-degree-of-freedom structures, frequency-up-conversion structures and stress optimization structures. It is concluded based on the review that, although operational frequency ranges of PVEHs have been widened with these approaches, the majority of them still lay in the high frequency level.
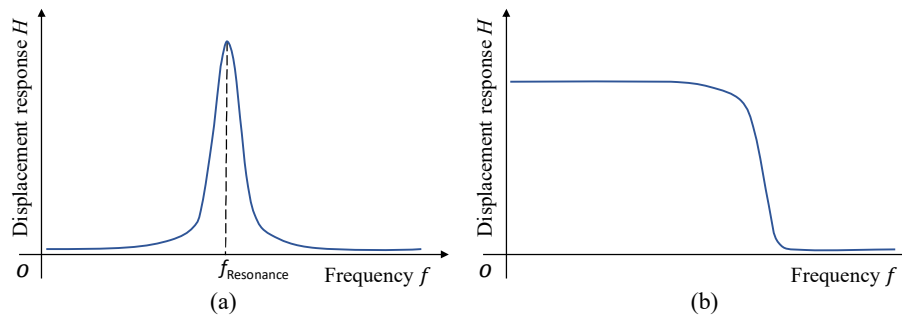
Fig. 1.1. Dynamic displacement-frequency response of (a) linear oscillators and (b) ideal oscillators for PVEHs.

In the ambient environment, vibrational sources are normally in the low frequency range with weak accelerations. The frequency spectrums and accelerations of several typical vibrational sources for PVEHs are compared and illustrated schematically in Fig. 1.2 [7, 8, 31, 32] and the corresponding data are presented in Table 1.1. For example, human activity frequency is

between 0 and 15 Hz [33, 34] and the general acceleration is between 0 to 1.2 g [35]. Bridges vibrate at frequencies from 0.4 to 30 Hz [36, 37] with the maximum acceleration of 0.4 g [38]. The vibrational frequency of Ocean waves is in the range of 0 to 10 Hz [39] with the acceleration up to 0.6 g [40]. Vibrations with high frequencies in the hundreds Hz level, such as industrial vibrations [41], are also favorable energy sources for PVEHs. However, they only exist in certain conditions and are not available in most general cases. Considering that the frequencies of the reachable vibrational sources in our daily life spread in a low and wide frequency range with weak accelerations, existing PVEHs in the literature with narrow response bandwidth or widened bandwidth in the high-frequency level are less effective in real applications. This problem also applies to vibrational energy harvesters with other energy-conversion principles [42-44].

Table 1.1. Frequencies and accelerations of the typical available vibrational sources for PVEHs.

Vibrations	Frequency [Hz]	Acceleration [g]	Vibrations	Frequency [Hz]	Acceleration [g]
Human activities [33-35]	0-15	1.2	Washing machines [31]	10-100	0-0.238
Ocean waves [39]	0-10	0-0.6	Clothes dryers [31]	59	0.43
Bridge vibrations[36, 37]	0-30	0-0.4	Vacuum cleaners [31]	100	0.158
Vehicle engines [7]	12-200	0.1-1.2	Industrial vibrations [41]	>200	0-4.43
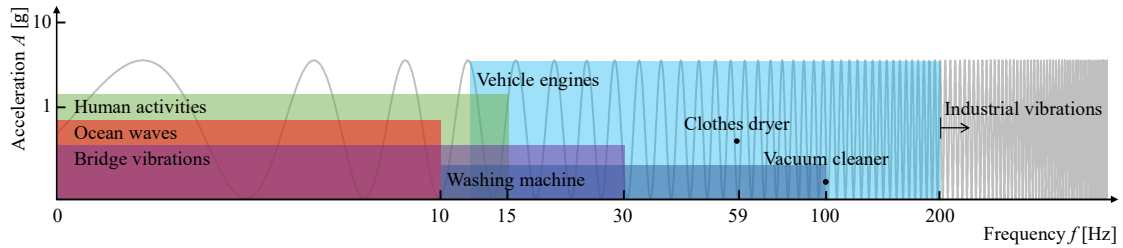
Fig. 1.2. Frequency distributions of typical available vibrational sources for PVEHs [7, 8, 31, 32].

For practical applications, ideal vibrational energy harvesters are expected to have a wide response bandwidth in the ultra-low frequency range, as illustrated in Fig. 1.1(b). Targeting on this ideal dynamic performance, a novel structure of statically balanced compliant mechanism (SBCM) is proposed in this doctoral research as the structural solution for the existing technical issues of vibrational energy harvesters. The SBCM achieves static balancing (zero force/stiffness) in the limited displacement range around the original position while it shows stiffness nonlinearity in the wider displacement range. Due to this unique force-displacement character, the SBCM will be sensitive to ultra-low excitation frequencies in a wide frequency

range with weak accelerations. The SBCM proposed is applicable for vibrational energy harvesters based on all energy-conversion principles not limited to piezoelectric effect only. SBCMs belong to a sub-branch of compliant mechanisms (CMs). A good understanding of the CMs is necessary for the successful development of SBCMs. Therefore, CMs and their design methods are introduced in the next section.

1.3 Compliant mechanisms

The word of "Compliant Mechanisms" might sound unfamiliar to most people, however, CMs widely exist in nature and they are also common in our daily life. Several examples of these CMs are shown in Fig. 1.3. Some Animals, insects and plants have developed special living skills based on compliant structures in the long revolution process. Elephants grasp food with their dexterous trunks (Fig. 1.3(a)). The wing of an earwig can fold and unfold exquisitely in a manner similar with origami which is a sub-branch of CMs [1] (Fig. 1.3(b)). Tree branches bend in wind as a way to unload the external forces and avoid breaking (Fig. 1.3(c)). In our daily life, a U-shaped bar tong (as shown in Fig. 1.3(d)) with deformable central part is used to

(a)   (b)   (c)

(d)   (e)   (f)
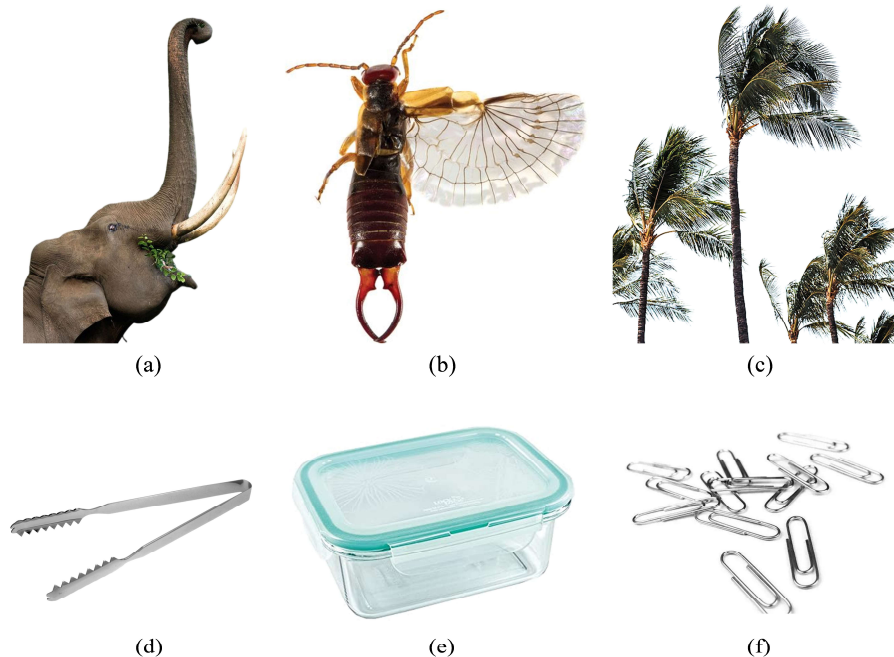
Fig. 1.3. Examples of CMs in nature: (a) the elephant trunk, (b) the earwig wing [1], (c) trees; and in human daily life: (d) a U-shaped bar tong, (e) The plastic lid of a food container with compliant locking ears, (f) Paper clips. (All images, except the one in (b), are from the internet.)

grasp cakes and salad. The plastic lid of a food container (Fig. 1.3(e)) can be easily locked and unlocked through compliant locking ears. Paper clips (Fig. 1.3(f)) are commonly used in the office to hold sheets of paper together by the elastic force of the metal wires when they are bended apart. These simple examples provided would help the researchers out of this field to form an easy understanding on the definition of CMs.

In traditional rigid-body mechanical structures, rigid parts are connected with each other through all types of joints and desired functions are achieved with the relative motions of the rigid parts. An example of the rigid-body mechanism which contains two rods connected by a rotational joint is schematically shown in Fig. 1.4(a). Tip point of the rod 2 reaches position b from position a through the relative rotational motion about the rotational joint R. Different from the traditional mechanisms, CMs transfer motion, load and energy through the deformation of flexible components [45, 46]. The same motion task shown in Fig. 1.4(a) can be alternatively achieved with the bending motion of a single flexible beam (which is a simplest CM) as indicated in Fig. 1.4(b). This flexible character brings CMs valuable advantages [45, 46]. Firstly, less time and cost are spent in the manufacturing and assembling process of CMs, because the total component number is dramatically reduced. In addition, the reduced number of joints reduces or eliminates the fraction and wear in CMs. This also leads to higher operational precisions due to the reduced or eliminated backlash. With less parts and less (or no) joints, CMs can be fabricated in a monolithic form. This gives CMs not only lighter weight but also good scalability into different sizes and good compatibility with microelectromechanical systems (MEMS) technologies. What's more, CMs store strain energy in deflected compliant components where stress/strain is generated, which benefits PVEHs based on the piezoelectric effect in particular.
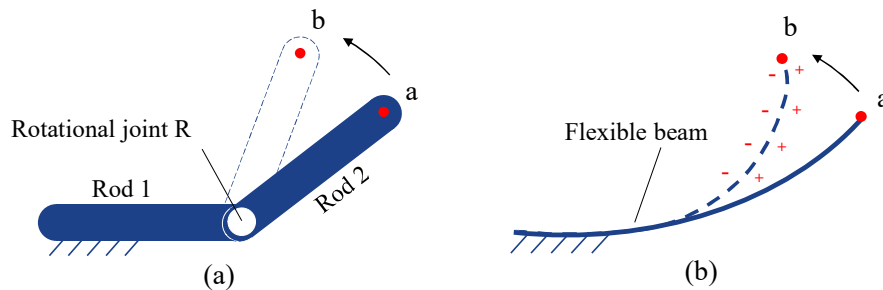
Fig. 1.4. (a) A traditional rigid-body mechanism with two rods connected with a rotational joint; (b) A compliant mechanism with the same motion function ("−" here indicates the compressive stress and "+" indicates the tensile stress).

Because of these unique advantages, CMs have been adopted in various fields for practical applications. Hao G. et al. developed a large-range XY compliant parallel manipulator for high-precision operation [47, 48] (as shown in Fig. 1.5(a)). This parallel manipulator had controllable and well-decoupled motions in XY plane while it also has enhanced out-of-plane stiffness. Tolou N. et al. replaced the traditional sprung balance and escapement in a mechanical watch with monolithic CMs [49] (as shown in Fig. 1.5(b)). The number of the parts in the mechanical watch was reduced by 30 and the precision was highly increased. Merriam E. et al. designed a fully compliant two-degree-of-freedom pointing mechanism [50] (as shown in Fig. 1.5(c)) for space applications, such as antenna, spacecraft thruster etc. Due to the elimination of the friction, lubrication is no longer needed and this benefits operations in vacuum in particular. Origami is the art of folding a sheet of paper into various forms and it can be seen as a sub-branch of CMs [51]. Howell L. and his team proposed a deployable solar panel for space applications based on the Origami principle [52] (as shown in Fig. 1.5(d)). This origami-based design enabled a much larger surface area of the solar panel in the space while it had compact size when it was folded to be launched. These examples are several typical cases among many application reports of CMs. In this study, SBCMs are proposed as structural solutions to enhance the dynamic performance of PVEHs. Before the development of the SBCM, it is necessary to go through the commonly used modelling and synthesis principles of CMs.

In the design procedure of CMs, analytical models must be created for the determination of geometric parameters and confirmation of the desired performance. Different modeling approaches are selected based on the relative deflection amount of the compliant structures [53]. When the beam deflection is much smaller than 10% of the beam length, the traditional deflection analysis method with small-angle assumptions can be used [53]. It should be noted that, with such small deflection, the targeted configuration would be better regarded as a structure instead of a mechanism.

Beam constraint modeling (BCM) method is commonly used in the condition with intermediate deflection in the range of around 10 % of the beam length. This BCM method is proposed by Awtar S. et al. [54, 55] based on the Euler-Bernoulli beam theory that "*plane cross-sections that are perpendicular to the beam centroidal axis prior to deformation remain plane and perpendicular to the neutral axis after deformation*". Advantages of BCM include that it is simple, parametric, closed-form and it captures all the relevant geometric nonlinearities over

this intermediate deflection range [53, 54, 56]. However, the shear deflections caused by the presence of shear loads are neglected due to the Euler-Bernoulli beam theory. BCM method is thus less accurate for stubby beams since the deflection components caused by shear is non-negligible in this case. Chen G. et al. improved the BCM based on the Timashenko beam theory to introduce the shear influence into the model, i.e. TBCM [57]. It was verified that the TBCM showed better prediction accuracy than BCM in the problems where shearing loads appeared.
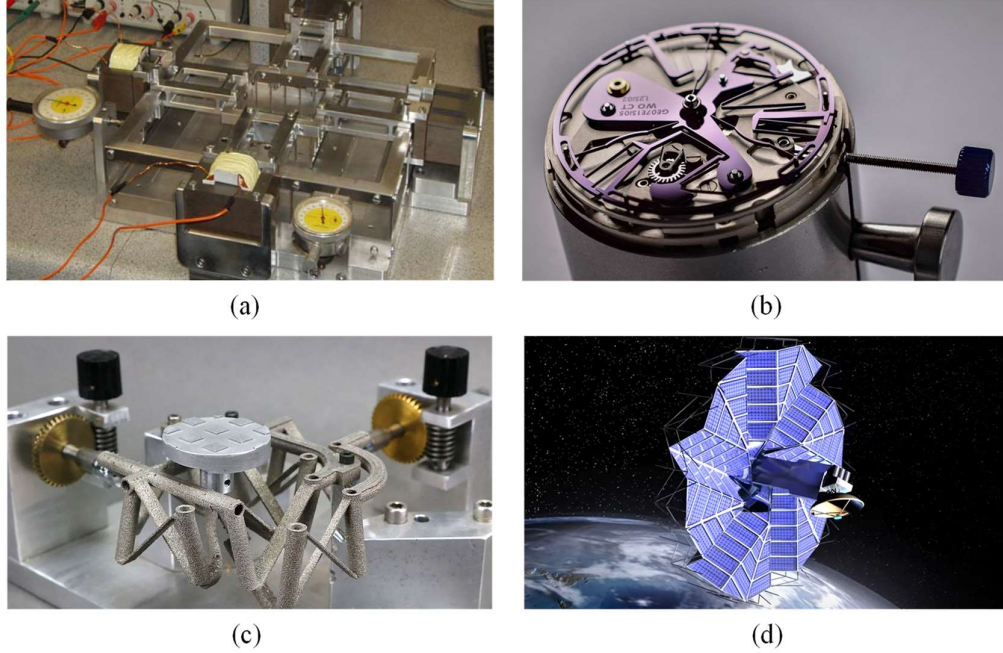
Fig. 1.5. Application examples of CMs: (a) XY compliant parallel manipulator [48], (b) compliant monolithic sprung balance and escapement in mechanical watch [49], (c) compliant pointing mechanism for space applications [51], (d) origami-based solar panel for satellites [52].

For the CMs with deflection larger than 10% of the beam length, the previous modelling methods are inappropriate and lead to larger errors. The elliptic integral solution is considered as the most accurate method to describe the large deformation of thin beams with axial elongation and shear neglected [58, 59]. Although the elliptic integral solutions are not straightforward and easy [53], they are capable to predict the large deflections of thin beams with multiple inflection points, any kinds of end loads and any beam end angles [58]. For the initial designs of CMs with large deflections, a more efficient method is in need.

The Pseudo-rigid-body model (PRBM) provides a relatively simple approach to describe the large and nonlinear deflection of CMs with acceptable loss of accuracy [45, 53]. The core

concept of the PRBM is to model the deflection of flexible parts utilizing rigid-body components with equivalent force-displacement characteristics [45]. Thus, CMs can be analyzed with traditional rigid-body mechanism theories, such as those found in references [60, 61]. A typical example of the PRBM is that a planar fixed-free flexible beam with external load applied on its end can be replaced with a rigid link that is pinned to a fixed link. The stiffness of the flexible planar beam is described by an equivalent pseudo-pivot with torsional spring [53, 62].

Finite element analysis (FEA) is another important tool for modeling CMs. There are a number of powerful commercial FEA software products available in the market with professional technique supports, Such as COMSOL Multiphysics®, ABAQUS®, ANSYS®. The FEA method can predict and describe the deflections in various levels and corresponding stiffness nonlinearity with high accuracy, but it is not suitable for parametric design [53]. It is more used as a verification method [63, 64] of the analytical models introduced above or a way to finely tune the design for optimal performance [65].

Taking advantages of that the deflections and stiffness characteristics of CMs can be predicted and described with the modelling methods introduced, more complex CMs can be developed and synthesized to achieve desired functions and static/dynamic performance. Several synthesis principles of CMs have been developed. The synthesis approach of freedom and constraint topology (FACT) is mainly utilized for developing CMs with desired degrees of freedoms while motions in other directions are constrained [53, 66]. It helps the designers to rapidly generate complex flexural concepts with visualization of the permitted and constrained motions in specified directions through geometric entities [66, 67]. This FACT approach particularly benefits the design of precision compliant structures, such as precision motion stages [68], nano-manipulators [69], micro positioners [70], etc. The limitation of this FACT method is that it mainly focuses on the kinematic flexures with certain DOFs without considering the stiffness and dynamic characters of the CMs designed [53].

Topology optimization is another approach in the synthesis of CMs. It is normally used in the design of a flexible structure with a specified output displacement in response to the input force [71]. A trade-off between the flexibility and stiffness should be achieved for some CMs that are expected to be flexible enough for easy deformation while be able to supply sufficient force for desired tasks. The topology optimization method is particularly suitable for tackling this

problem [53]. Compliant pliers are typical application cases of this synthesis method [72, 73]. In addition, some novel compliant structures which might be out of the designers' capability can be generated with this method. However, the optimal solutions obtained are generally not unique and they depend on the mesh strategy and loading conditions [53].

Rigid body replacement method is one of the most practical and user-friendly approaches to synthesize CMs [53, 74]. This method normally starts with an existing rigid-body mechanism with desired functions. The rigid members and joints are then fully or partially replaced with equivalent alternatives in the flexural forms while the desired functions are kept unchanged. One major limitation of this synthesis is that not all rigid-body mechanisms can be replaced with CMs due to the constrained motion strokes of the flexural parts [53]. One successful example of this rigid body replacement method in the synthesis of CMs is that the traditional bicycle derailleur is partially replaced with compliant components for better performance and reduced weight [75].

Based on the modularity principle, CMs can also be synthesized and designed utilizing building blocks as subcomponents to achieve desired static/dynamic characters or other functions [76]. A large group of individual compliant structures with basic functions have been summarized in a building block library [53]. The wide variety of compliant building blocks provide the engineers opportunities to generate original designs based on their special requirements and creation capabilities [53]. The design and manipulation on the force-displacement characteristics of the CMs is possible with this building-block approach. For example, tri-stability and even quad-stability can be obtained with the integration of multiple bi-stable compliant building blocks [77]. In particular, this building-block method enables the compensation of different stiffness from individual compliant building blocks to achieve novel stiffness features such as static balancing which is focused in this research.

1.4 Statically balanced compliant mechanisms

SBCMs are special cases of CMs with zero force and zero stiffness in a certain displacement range. They are able to stay in equilibrium in the continuous displacement range, which is composed of infinite stable positions. Therefore, SBCMs can also be seen as infinite-stable CMs according to the characters of the multi-stable CMs [30]. SBCMs are energy free from

the energy perspective [78]. Therefore, the SBCM can be stimulated with weak external disturbing with just a small amount of energy.

Taking these CMs with opposite stiffness as building blocks, various SBCMs have been synthesized based on the compensation between the positive stiffness and negative stiffness [76]. Kuppens P.R. et al. developed a SBCM in which the positive stiffness of a compliant parallelogram was compensated with the negative stiffness provided by post-buckled beams arranged in a V shape [79]. In this device, the negative-stiffness beams were pre-loaded to buckle by a bi-stable compliant structure which could switch between the two stable positions for loading and unloading. Barel M. Y. et al. introduced locking hooks in various forms to pre-stress the negative-stiffness beams to ensure a permanent static balancing [80]. The relatively simple structures of the hooks benefit SBCM in MEMS scales in particular. Inspired by the bendy straw, Wang S. et al. designed a SBCM composed of a thin-wall bellow and an axially paced balancer [81]. The positive stiffness of the compliant bellow was compensated with the negative stiffness of the balancer. A multi-stable CM have positive stiffness and negative stiffness in different displacement segments. Chen G. et al. [82] and Tolou N. et al. [83, 84] proposed SBCMs synthesized with two well-designed multi-stable CMs. The static balancing could be achieved in the displacement range where the multi-stable compliant building blocks owned opposite stiffness.

SBCM can also be constructed based on the concept that the horizontal section of the force-displacement of constant-force CMs (as shown in Fig. 1.6(b)) is pulled down to the zero-force position by preloading the constant-force CMs. Based on this idea, Pluimers P. J. et al. preloaded a constant-force CM precisely with bi-stable compliant beams and static balancing was obtained [85]. Their design was verified and demonstrated with a statically balanced compliant gripper. Tolou N. [86], Gallego J. A. [87] and Kuppens P. R. et al. [88] creatively constructed the SBCMs by connecting two identical constant-force CMs with opposite constant forces in series. This method can also be seen as the concept that the constant positive force of a CM is balanced to zero by the constant negative force provided by an identical CM which is pre-stressed. Chen G. introduced the method of preloading a constant-force CM simply by the gravity force of a mass for static balancing [82]. Dunning D.G. et al. developed a compliant precision stage in the same method [89]. However, this gravity-force preloading approach is limited only to the application conditions in the vertical direction.

In addition to the SBCMs with translational force-displacement relationship, static balancing can also be achieved in the torque-angle relationship of CMs with rotational motions. Kuppens P.R. et al. reported a rotational SBCM which is composed of two positive-stiffness beams and two V-shaped post-buckled negative-stiffness beams [79]. In the statically balanced flexural pivot introduced by Yang Q. et al., the positive stiffness of leaf springs was compensated by the negative stiffness from a pair of compressed springs [90]. Bilancia P. et al. developed a rotational SBCM and the rotational static balancing was achieved based on the compensation between the positive stiffness of a compliant spiral spring and the negative stiffness provided by two pined-pined post-buckled compliant beams [91].

1.5 Motivations

In summary, the main motivations of this doctoral research are listed as follows.

1) Environmental vibrational sources are normally in the low frequency range at 10^0-10^1 Hz levels [8, 25, 31, 32, 92]. However, the majority of vibrational energy harvesters reported in the literature work in the much higher frequency range even with a narrow bandwidth [30]. This frequency gap between the energy harvesting devices and the accessible vibrational sources is still to be filled for improving dynamic performance of vibrational energy harvesters.

2) A wide variety of structural methodologies have been proposed for PVEHs in the literature. Due to their common bending deformations of flexural members, the mechanical structures of PVEHs are CMs in nature. A review on the mechanical structures of PVEHs from the perspective of CMs is necessary for the design of an effective structure for PVEHs. However, such a review is still not reported.

3) SBCMs can provide structural solutions for the challenge mentioned in the point 1). Due to the static balancing over a finite range and the overall stiffness nonlinearity, SBCMs are sensitive to ultra-low wide bandwidth frequencies with weak accelerations. However, only a limited number of researches explored the application of SBCMs into vibrational energy harvesting and lacked comprehensive and in-depth study [93, 94]. Our work focuses on a more comprehensive investigation on using SBCMs for vibrational energy harvesting, including a

guideline of quick structural design, and analytical modelling and experimental verifications in particular.

4) Despite traditional mechanisms (or integration of traditional mechanisms and compliant mechanisms) based quasi-zero-stiffness oscillators have been reported for vibrational energy harvesting at ultra-low wide bandwidth frequencies, their complex structures restrict their practical applications [95, 96]. By contrast, the structural simplicity of SBCMs makes them friendly in fabrication, applications and miniaturization.

5) Analysing the limited number of publications on SBCM-based vibrational energy harvesting, it is observed that all theoretical analysis and experimental testing are based on harmonic excitations. However, most environmental vibrations have mixed or irregular frequencies with weak accelerations. Applications of the SBCM-based vibrational energy harvesters targeting practical vibrational sources have not been discussed and demonstrated in the literature yet.

6) MEMS vibrational energy harvesters based on traditional linear oscillators have high resonant frequencies (at the 10^2 Hz level) due to the size effect [97] and narrow effective frequency bandwidths [98, 99]. This leads to low energy harvesting efficiencies. The frequency limitation imposed by the size effect of MEMS vibrational energy harvesters needs to be broken for the application of MEMS vibrational energy harvesters in vibrational conditions with ultra-low wide bandwidth excitation frequencies.

1.6 Thesis aim and layout

1.6.1 Objectives

Targeting on the existing problems in the field of vibrational energy harvesting, SBCMs are investigated as the structural solution to address performance issues of the vibrational energy harvesters. SBCMs outperforms their traditional linear and nonlinear counterparts due to their ultra-low and wide frequency bandwidth dynamic response and other advantages in fabrication, practical application and miniaturization. PVEHs are focused throughout this research for a demonstration. It should be emphasized that other energy conversion mechanisms, such as electromagnetic, electrostatic and triboelectric, can also be combined with the SBCM for vibrational energy harvesting, not limited to piezoelectric effect only.

A design guideline will be first proposed to facilitate the quick design of the SBCM based on the analysis on its static balancing behavior. The more accurate force-displacement relationship with stiffness nonlinearity is then analysed using FEA tools. Subsequently, the dynamic displacement response of the SBCM under harmonic base excitations will be analytically modelled based on the fitted polynomials of the force-displacement relationships. Numerical methods will also be adopted for checking the accuracy of the analytical model. In addition, the static and dynamic characteristics of the SBCM and its applicability in vibrational energy harvesting will be verified experimentally using a prototype fabricated. Finally, the application cases of the SBCM in different dimensions will be demonstrated based on FEA simulations. COMSOL Multiphysics® in version 5.5 is used throughout the research for FEA simulations.

1.6.2 Layout

In order to present the research on SBCMs and the application for PVEHs in a logic and comprehensive way, the rest of the thesis is organized as follows:

In chapter 2, a large variety of structural methodologies of PVEHs in the literature are reviewed and categorized into five groups from the perspective of CMs. This work helps to form an overall view on the development status and research trends of mechanical structures utilized in PVEHs. Several CMs are proposed for PVEHs in different structural configurations as inspirations and references to prompt the development of this research field. Characteristics of five most commonly used piezoelectric materials in PVEHs are summarized and compared. Energy generation capabilities of reported PVEHs are assessed and illustrated first in a volume-normalized power density graph. Without breaking the logic of the thesis, this review work is presented as a separate chapter to highlight its contribution of the first systematic discussion on the application of CMs in PVEHs

Chapter 3 selects one specific SBCM as the main structure for the PVEH based on the comparison of two possible SBCMs. These SBCMs are synthesized with different stiffness components following the stiffness compensation principle. The development procedure of this SBCM is proposed as a design guideline in the form of a flow chart based on a quick design equation. Utilizing the tool of FEA simulations, the more accurate force-displacement curve of the SBCM is obtained. This special force-displacement relationship is fitted and described with

a 5th order polynomial, providing the theoretical basis for the following analysis on the dynamic response of the SBCM under harmonic base excitations. Influence from the geometric parameters on the force-displacement characteristics of the SBCM is also discussed.

Chapter 4 analyses the dynamic performance of the SBCM base-excited by the harmonic excitations. The analytical model which describes the relative displacement amplitude-excitation frequency character of the SBCM is created based on the averaging method and the fitted force-displacement polynomials. The dynamic response of the SBCM in different mono-stable and static-balancing modes are also explored and compared. With the assistance of COMSOL Multiphysics®, the dynamic response of the SBCM under sinusoidal base excitation with ultra-low frequencies and low accelerations is verified by FEA simulations. In addition, settings of this dynamic FEA model is summarized and introduced as a tutorial for researchers interested in this simulation work.

Chapter 5 experimentally demonstrates the applicability of the SBCM in vibrational energy harvesting with a prototype. The prototype is fabricated in the assembling form with tunable length of the positive-stiffness beams. A preliminary SBCM-based PVEH is created with PVDF films attached on the positive-stiffness beams for electric energy generation. The force-displacement characteristics of the prototype are tested with Texture Analyser in static experiments. Dynamic experiments with harmonic base excitations are conducted with a permanent magnet shaker (electrodynamic shaker). Both the displacement responses and electric outputs in the dynamic experiments are captured and critically analysed.

Chapter 6 explores two application cases of the SBCM for vibrational energy harvesting in macro and micro scales. The integration of the macro SBCM in an oceanic drifter for harvesting vibrational energy from ocean waves is first considered. A FEA model of the preliminary SBCM-based PVEH with PVDF films is created in COMSOL. Based on the excitation of drifter motion patterns corresponding to two typical ocean waves, the dynamic displacement response and the electric energy outputs of the SBCM-based PVEH are simulated in time-domain. In the second application case, the SBCM is miniaturized into the MEMS scale as the main structure of the micro vibration energy harvesters for powering low-energy-cost sensors and circuits on chip. The dynamic response of the miniaturized SBCM under harmonic base excitation is analysed based on FEA simulations. A conceptual MEMS-scale SBCM structure

is proposed as a structural example suitable for the practical fabrication and attachment of piezo-materials with MEMS technologies.

Chapter 7 is a conclusion chapter. The contributions and conclusions of this research are summarized. Those aspects which are not fully explored and discussed in this thesis are explained and they will be part of the work in the future.

Chapter 2 A Review on Piezoelectric Vibrational Energy Harvesters from the Aspect of Compliant Mechanisms

For the purpose of enhancing the dynamic performance of PVEHs with advanced CMs, a comprehensive review on the mechanical structures of PVEHs in the literature to date is necessary. This review work helps to form an in-depth understanding on the development status and research trends of the mechanical structures adopted for PVEHs. According to the literature survey based on the Core Collection of Web of Science with topic keywords: (*energy harvest**) AND (*piezoelectric*) AND (*vibration*) AND (*wide bandwidth*) OR (*large bandwidth*) OR (*broad bandwidth*), growing attentions have been drawn over the past 10 years as reflected from the number of articles published from 2010 to 2020 as shown in Fig. 2.1. A wide variety of structural methodologies have been proposed for PVEHs in the literature. However, a review on the mechanical structures of PVEHs from the aspect of CMs has not been conducted by other researchers yet. This is mainly because the mechanical structures of PVEHs are CMs in nature, which has not been widely studied in the relevant research community. Without breaking the overall logic of this thesis, the review work is organized as a separate chapter to highlight this contribution which could not be clearly illustrated within limited length of a sub-section. The review work in this section has been published as a review article titled as "*A review on vibration-based piezoelectric energy harvesting from the aspect of compliant mechanisms*" in the journal of Sensors and Actuators A: Physical.

The review work contains two main parts. Section 2.1 introduces the PVEHs in the literature following a structural categorization summarized. Serval CMs suitable for PVEHs in the corresponding structure groups are proposed. Section 2.2 compares several typical piezoelectric materials commonly used in vibrational energy harvesting. Energy generation capabilities of the PVEHs based on these piezo-materials are summarized and compared.
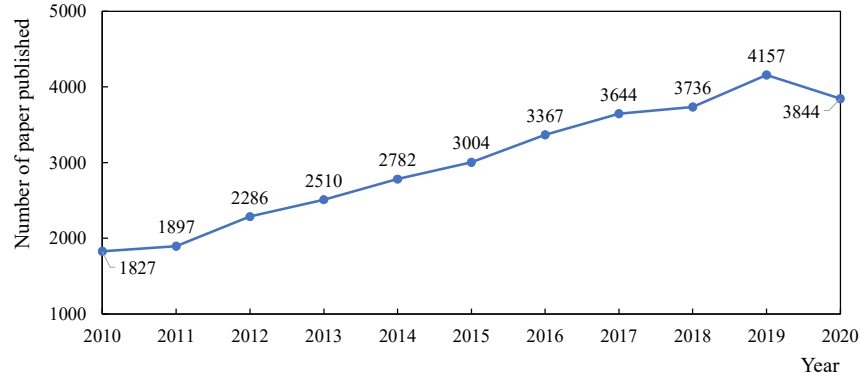
Fig. 2.1. The number of articles published on PVEHs targeting a wide frequency bandwidth (years 2010 - 2020).

2.1 Mechanical structures of PVEHs in the literature

According to their structural features, PVEHs in the literature are analyzed and categorized into five configurations, namely mono-stable structures, multi-stable structures, multi-degrees-of-freedom structures, frequency up-conversion structures and stress optimization structures. This structural categorization is graphically illustrated in Fig. 2.2. Detailed discussion on these structural configurations in the following sections are organized based on this structural logic. The compatibility of each configuration to MEMS process is also assessed. At the end of each section, several CMs suitable for PVEHs are proposed as inspirations and references for researchers in this area.
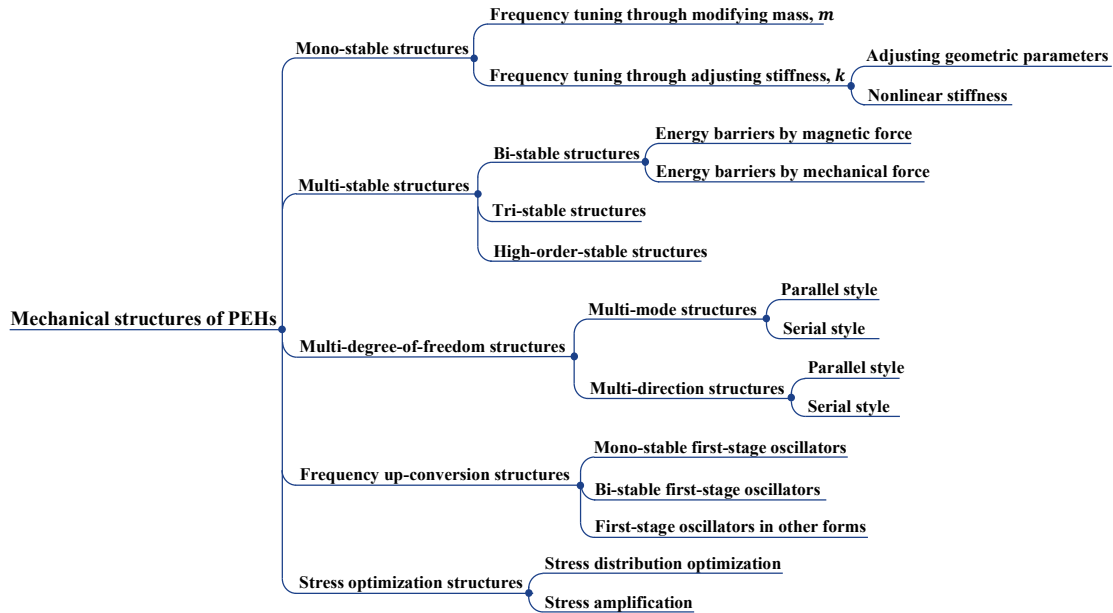
Fig. 2.2. Categorization of PVEHs reported in the literature based on their structural characteristics.

2.1.1 Mono-stable structures

Mono-stable oscillators have single stable positions. Once the external stimulation stops, mono-stable oscillators eventually return to their equilibrium positions after the dynamic energy is damped off. PVEHs in this configuration maximize the energy generation by resonance, normally in their first-order natural mode with the lowest resonant frequency and lowest stimulating energy requirement. Cantilever beams and clamped-clamped beams are typical examples of the mono-stable oscillators. Mono-stable PVEHs can be described as mass-spring vibration systems and their resonant frequency, f_r, can be calculated with the equation [13, 100]:

$$f_r = \frac{1}{2\pi}\sqrt{\frac{k}{m}} \tag{2.1}$$

where m represents the mass of this harvesting device, and k is the stiffness coefficient. For given mono-stable oscillators, their resonant frequencies are determined, while the excitation frequencies spread in a low and wide frequency range [8, 25]. According to the Eq. 2.1, there are two methods to tune and match the resonant frequencies of the mono-stable oscillators with excitation frequencies: (i) modifying the mass, m, and (ii) adjusting the stiffness, k, as shown schematically in Fig. 2.3.
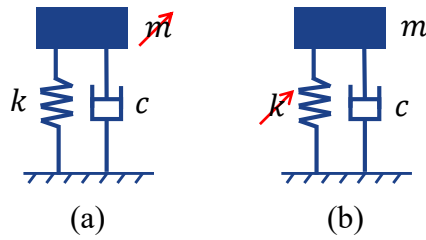
Fig. 2.3. Two main methods for tuning the resonant frequencies of mono-stable PVEHs: (a) modifying the mass, m, and (b) adjusting the stiffness, k.

a) Frequency tuning through modifying proof mass

According to Eq. 2.1, a larger mass leads to a lower resonant frequency when the stiffness coefficient is given. Based on this principle, researchers attach proof masses on mono-stable PVEHs to lower their resonant frequencies [101-103]. Taking the geometric position of the proof mass into consideration, as indicated in Fig. 2.4.
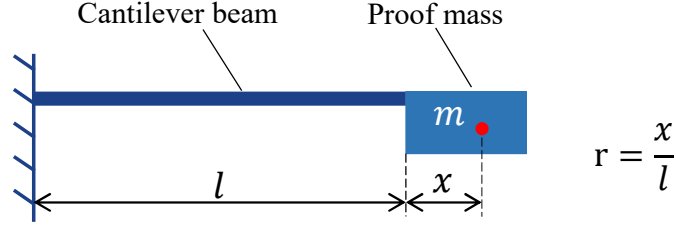
Fig. 2.4. Cantilever beam with tip mass.

The resonant frequency equation (Eq. 2.1) can be rewritten as [13, 104]:

$$f_r = \frac{1}{2\pi} \sqrt{\frac{E\omega h^3}{12ml^3} \cdot \frac{r^2 + 6r + 2}{8r^4 + 14r^3 + \frac{21}{2}r^2 + 4r + \frac{2}{3}}} \tag{2.2}$$

where E is the Young's modulus of the material used for the cantilever, w, h, and l are the width, thickness and length of the cantilever respectively. r is the ratio between the position of tip mass gravity centre, x, and the length of the cantilever, l, which is x/l. m represents the proof mass, while the cantilever mass is neglected.

According to Eq. 2.2, a proof mass closer to the clamped end results in a high resonant frequency, while a proof mass further from the clamped end leads to a low resonant frequency. Mass distribution in the direction perpendicular to the cantilever has no effect on the natural frequencies. Wu X. et al. experimentally verified this frequency tuning method and achieved a wide frequency range from 130 Hz to 180 Hz through adjusting the position of the mass center in their cantilever prototype with tip mass [105]. In a similar piezoelectric cantilever, Somkuwar R. et al. deployed two cylindrical masses in the tip container for automatic frequency tuning when the cylindrical masses changed their relative positions [106]. An auto-tuned resonant frequency range of 22 Hz to 35 Hz was observed in experiments. Instead of utilizing solid masses, Jackson et al. filled the mass cavity with a liquid and used this to change the mass center of gravity [107]. This mass-center-tuning approach has also been adopted by other researchers for widening the effective frequency range of PVEHs [108, 109].

CMs have medium level of flexibility between rigid parts and liquids, and they can be alternative solutions to change the mass gravity center for broadening the response frequency bandwidth. Under vibrational excitations, the CM-based proof mass in the piezoelectric cantilever can change its gravity center under the action of centrifugal force. The CM-based proof mass can be fabricated monolithically with 3D printing technology. The response

frequency range can also be controlled based on the well-designed compliant structures of the proof mass. One possible structure of the compliant proof mass for PVEHs is proposed and illustrated in Fig. 2.5. This compliant tip mass has 3D structures made of flexible materials, such as plastics or rubber.

Cantilever beam   Flexible proof mass   Flexible proof mass

Cantilever beam

(a)   (b)
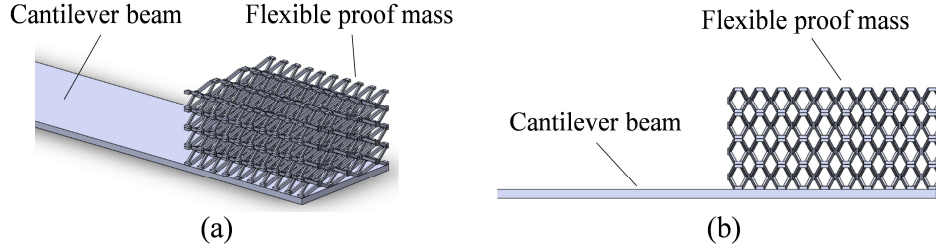
Fig. 2.5. Cantilever beam with deformable tip proof mass based on the concept of CMs for PVEH in (a) the isometric view and (b) the side view.

b) Frequency tuning through adjusting stiffness

In addition to the modification of proof mass, adjusting the stiffness is the second way for frequency tuning of mono-stable PVEHs. Stiffness is determined by several factors, including geometric parameters, loading conditions etc. Following content is organized based on these factors in this sub-section.

- Stiffness adjustment with geometric parameters

Cantilever beams with rectangular cross sections are widely adopted for mono-stable PVEHs. The stiffness coefficient, k, of such cantilever beams can be calculated with the equation [13]:

$$k = \frac{3EI}{l^3} = \frac{Ewh^3}{4l^3} \tag{2.3}$$

where I is the cross-section moment of inertia. According to this equation, the stiffness of a cantilever beam can be modified through changing geometric parameters (w, h and l), when the structural material (represented by Young's modulus E in this equation) is chosen. Length, l, and thickness, h, are more influential due to their third-order power.

Jackson N. et al. reduced the resonant frequency of a MEMS PVEH to 28.5 Hz by reducing the cantilever thickness to 5 μm [110], while the device strength might be weakened. Berdy D. F. et al. adopted a meandered cantilever in their PVEH for lowering the effective frequency to

49.7 Hz [111] and this structure can be seen as a typical example and it is shown in Fig. 2.6. In order to further reduce the natural frequencies of meandered cantilever beams, Apo D. J. et al. replaced straight branches with arc-based shapes [112]. Numerical models demonstrated that the frequency reduction reached up to 40%. This frequency lowering concept has also been taken by other researchers in their devices [113-115].
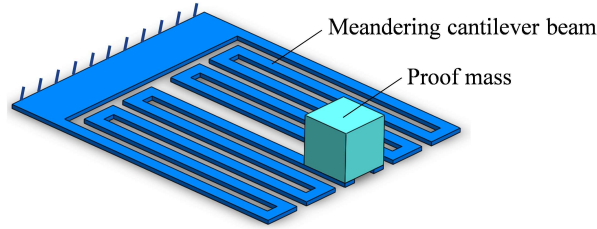
Fig. 2.6. Meandered cantilever beams for PVEH [111].

- Nonlinear stiffness

During vibrating, loading condition and stress distribution inside PVEHs change dynamically due to the geometric deformation, which brings a nonlinear stiffness. This stiffness nonlinearity broadens the working frequency range of mono-stable PVEHs. To describe this nonlinear vibration, a cubic term is introduced in the differential equation of motion of a mass-damping-stiffness oscillating system under a harmonic vibration, as presented in Eq. 2.4. This equation is also called Duffing equation [13, 116].

$$m\ddot{x} + c\dot{x} + kx + \alpha x^3 = A\sin(\omega t) \tag{2.4}$$

where x is the oscillating displacement. $A\sin(\omega t)$ is the external sinusoidal excitation and ω indicates the excitation frequency. $\dot{x}, \ddot{x}$ are the first and second differentiation of x with respect to time, t, which represent speed and acceleration respectively. x^3 represents the stiffness nonlinearity of the vibration system. Constant coefficients, m, c, k, α and A, are system mass, damping rate, linear stiffness coefficient, nonlinear stiffness coefficient and excitation amplitude, respectively. In general, a nonlinear stiffness coefficient, α, determines the nonlinearity of this oscillating system. Corresponding to different nonlinear stiffness coefficient, α, the displacement response, x, with respect to excitation frequency, f, is graphically shown in Fig. 2.7.
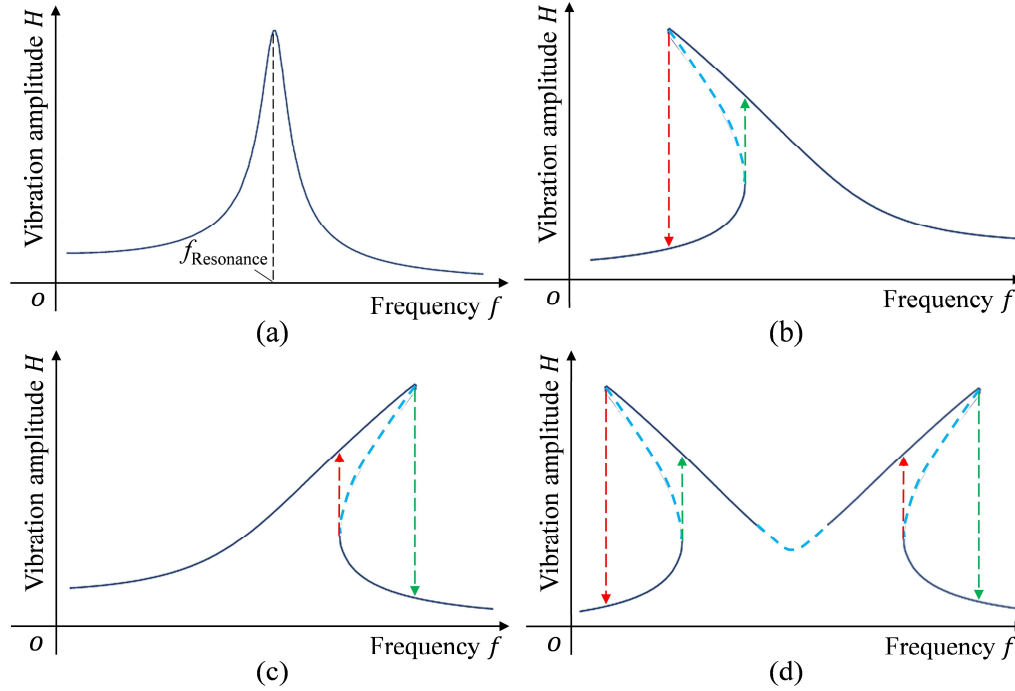
Fig. 2.7. Frequency response of mechanical oscillators with (a) $\alpha = 0$ (linear stiffness); (b) $\alpha < 0$ (nonlinear stiffness representing spring softening effect); (c) $\alpha > 0$ (nonlinear stiffness representing spring hardening effect); (d) internal resonance.

When the nonlinear stiffness coefficient, α, is zero, Duffing equation (Eq. 2.4) describes the oscillation of a linear mono-stable oscillator (e.g. cantilever beams) under sinusoidal excitations. In this case, the relative displacement, x, reaches maximum at the resonance frequency with a sharp tip in the displacement-frequency curve as shown in Fig. 2.7(a). When α is non-zero, frequency hysteresis emerges. If α is negative, the displacement response curve bends towards lower frequency domain, which is called stiffness softening, as indicated in Fig. 2.7(b). Conversely, a positive α leads to stiffness hardening and the frequency response curve bends towards the higher frequency region, as illustrated in Fig. 2.7(c). For both stiffness softening and hardening, bended displacement response curves indicate a wider frequency bandwidth, however this depends on frequency sweeping directions. It should be noted that the dashed lines indicate unstable oscillation conditions that cannot be reached, while the solid lines represent the stable oscillation conditions [117]. The internal resonance is also a nonlinear vibration phenomenon [118]. In addition to duffing nonlinear oscillations, internal-resonance-based structures have been introduced in the field of energy harvesting to broaden the frequency bandwidth [119-123]. As shown in Fig. 2.7(d), the displacement response curve of the internal-resonance-based oscillator bends towards both higher and lower frequency ranges,

which leads to a fairly broadened frequency bandwidth regardless of the frequency sweeping directions.

Based on the concept of stiffness nonlinearity, various approaches are reported in the literature for widening the response bandwidth of PVEHs. Nonlinear stiffness can be caused by geometric restrictions. A typical structure of this method is a clamped-clamped beam [124] which bends and stretches during oscillation, as shown in Fig. 2.8. Tensional stress generated along the beam results in a hardening stiffness. Gafforelli G. et al. provided an in-depth analysis on the stiffness nonlinearity of clamped-clamped PVEHs [124]. Marzencki M. et al. utilized the clamped-clamped mono-stable structure in a MEMS harvester [125]. Similar research [126, 127] was also carried out by Leadenham S. et al. and Hajati A. et al.
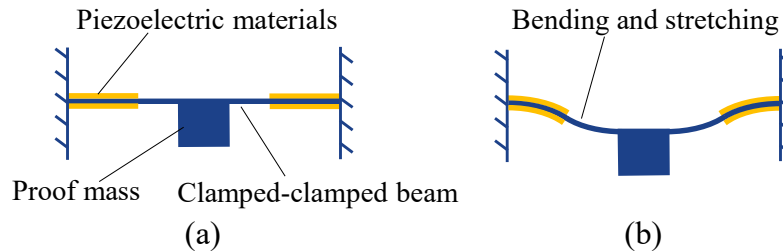
Fig. 2.8. The clamped-clamped beam [124] in its (a) original position and (b) the deformed mode with bending and stretching.

Preloading is the second solution to create stiffness nonlinearity and it can be applied by either mechanical forces or magnetic coupling. Fig. 2.9 shows schematic structures of mono-stable cantilevers with different preloading methods. During oscillation, the dynamically changing preloading conditions causes stiffness nonlinearity. Masana R. et al. investigated the influence from the axial preloading on the stiffness nonlinearity and the broad effective bandwidth was achieved in experiments [128]. Stanton S. C. et al. preloaded a piezoelectric cantilever by interacting magnetic forces for wide working frequency bandwidth [129]. Both stiffness softening and hardening could be achieved with the same device through adjusting the relative position of the magnets distributed. Tang L. et al. utilized an oscillating magnet to interact with the tip magnet of the cantilever to achieve stiffness-softening nonlinearity [130]. The concept of preloading-based stiffness nonlinearity to broaden the working bandwidth has also been reported in [131-133].
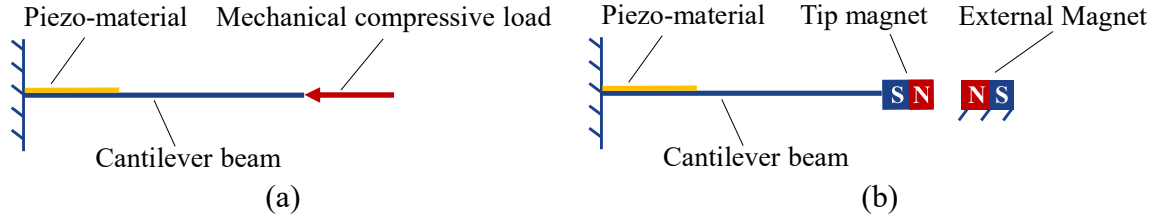
Fig. 2.9. Schematic structures of mono-stable piezoelectric cantilevers with (a) mechanical [134] and (b) magnetic pre-loading [135].

In the typical structure of PVEHs based on internal resonance phenomenon, a primary nonlinear oscillator is connected with a linear auxiliary oscillator as illustrated in Fig. 2.10(a). The nonlinear structures as shown in Fig. 2.9 can be options for the primary oscillators. Xiong L. et al. employed the nonlinear structure as shown in Fig. 2.9(b) as the primary oscillator in their L-shaped PVEH with the internal resonance [122, 123]. Xie Z. et al. reported a T-shaped PVEH device that used a clamped-sliding nonlinear beam as the primary oscillator in connection with a linear cantilever [121]. Chen L. et al. [119] and Jiang W. et al. [120] also developed internal-resonance-based PVEHs for wide bandwidth energy harvesting. Structures with nonlinear energy sinks (NES) can respond to a wide range of excitation frequencies and they have also been adopted for PVEHs [136-142]. Different from the connecting sequence of linear and nonlinear oscillators in those internal-resonance-based structures [119-123], nonlinear oscillators (acting as NESs) are mounted on the linear (primary) oscillators in the NES-based structures as shown in Fig. 2.10(b). Under certain conditions, the vibrational energy is irreversibly pumped from the primary oscillator to the coupled nonlinear oscillators [143]. In the NES-based PVEH developed by Zhang Y. et al. [138], a prepressed clamped-clamped beam was connected to a linear primary oscillator. Xiong L. et al., utilized a piezoelectric cantilever with a magnetic tip interacting with adjacent magnets as the nonlinear oscillator in their NES-based PVEH [139].
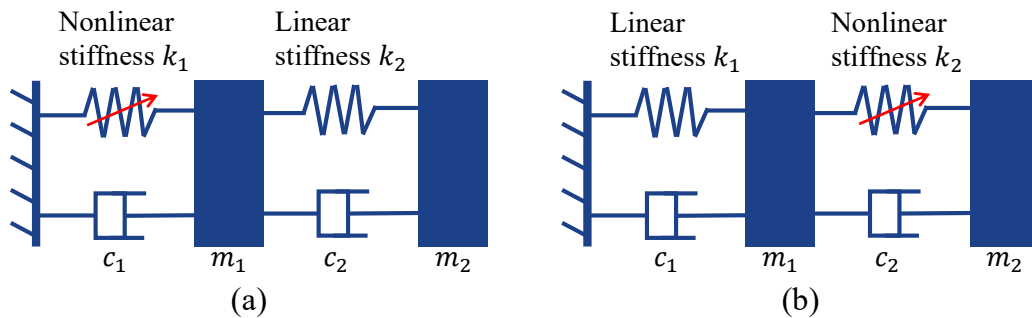
Fig. 2.10. Schematic structures of nonlinear oscillators based on (a) internal resonance [119] and (b) NESs [143]

Mono-stable PVEHs interacting with stoppers also exhibit stiffness nonlinearity. However, the stiffness hardening happens sharply rather than gradually in this case. A typical structure of this nonlinear PVEH with a mechanical stopper and its characteristic curve of stiffness are given in Fig. 2.11(a). The stiffness of the system is hardened from k_1 up to k_2 once the vibrating cantilever hits the stopper. Therefore, the overall system owns a piecewise-linear stiffness, as shown in Fig. 2.11(b). Olszewski O. et al. developed a PVEH to harvest energy from wires carrying AC current and the frequency bandwidth was broadened by 250% through introducing a mechanical stopper [28]. Halvorsen E. et al. achieved a wide effective bandwidth based on the stiffness-hardening nonlinearity caused by a piezoelectric cantilever coupling with a mechanical stopper [144]. The concept of stoppers have also been utilized in MEMS scale to broaden the working bandwidth of the micro PVEHs [145] [146].
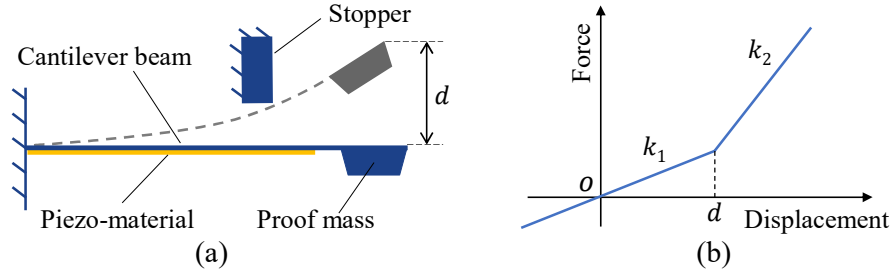
Fig. 2.11. A nonlinear PVEH with a mechanical stopper [147] (contact aided CM [148]): (a) schematic structure; (b) piecewise-linear stiffness coefficient.

c) Discussion

With special design, CMs exhibit stiffness nonlinearity. Howell L. et al. carried out a systematic research on nonlinear compliant structures [45]. Hao G. et al. proposed a framework for designing CMs with nonlinear stiffness and several nonlinear compliant structures were presented [149]. These nonlinear flexures provide references and inspirations for the design of nonlinear PVEHs. In addition, mono-stable oscillators are generally simple. They provide basic elements and theoretical foundations for the design of PVEHs in more complex configurations in the following sections. The CMs can be designed using the methods introduced in Section 1.3, targeting vibrational energy harvesting. More specifically, these design methods include freedom and constraint topology, topology optimization, rigid body replacement and synthesis using building blocks.

2.1.2 Multi-stable structures

Multi-stable structures can stay in balance in multiple positions. Each stable position represents local potential-energy minimum and it is also called the potential energy well. One potential energy barrier exists between every two adjacent potential energy wells, indicating the energy required for the oscillator to jump from one stable position to another. Schematic graphs of potential energy patterns for mono-stable and multi-stable types are given in Fig. 2.12. According to the number of stable positions, multi-stable configurations are sub-defined as bi-stable, tri-stable, quad-stable etc. The presence of multiple stable positions brings PVEHs diverse vibrating behaviors. Depending on the excitation magnitude of environmental vibrational, multi-stable oscillators vibrate in three manners, i.e. intra-well, chaotic and inter-well vibrations respectively [150].
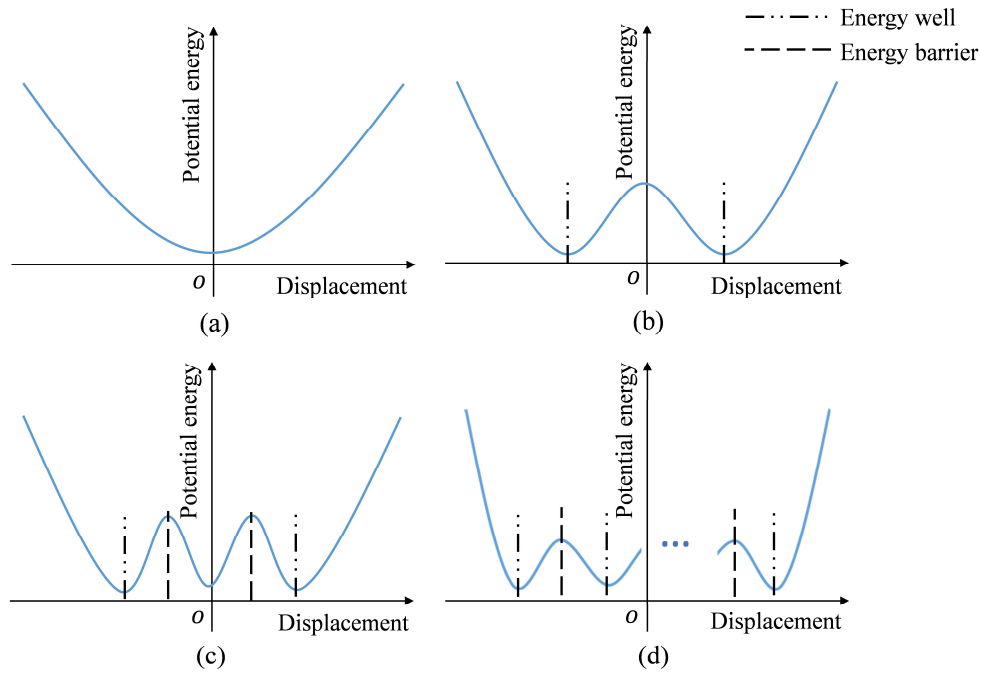
Fig. 2.12. Schematic potential energy graph of multi-stable structures: (a) mono-stable, (b) bi-stable, (c) tri-stable and (d) higher-order-stable.

a) Bi-stable structures

The essence of designing a bi-stable oscillator is to create an energy barrier between two potential energy wells. This energy barrier represents the work required of a resistance force

against the vibrating motion and it can be created with either magnetic forces or mechanical forces.

Both attractive and repulsive magnetic forces can be utilized in the construction of bi-stable PVEHs and the typical structures are schematically shown in Fig. 2.13. A piezoelectric cantilever with a tip magnet is repelled from its original mono-stable position by attractive forces (type I as shown in Fig. 2.13(a)) or repulsive forces (type II as shown in Fig. 2.13(b)) from closely located fixed magnets. Erturk A. et al. experimentally verified that the bi-stable PVEH in type I outperformed its mono-stable counterparts due to the concept of high-energy orbits [29]. Zhou S. et al. optimized the orientation of two external magnets by introducing a small tilt to enhance the dynamic performance of the bi-stable PVEH [151]. Lan C. et al. lowered the potential energy barrier between two potential energy wells by imposing an extra small magnet in between of two magnets in type-I structure [152]. Ferrari M. et al. designed a bi-stable energy harvester based on structural type II [153]. Yang W. et al. proposed a hybrid resonator with internal resonance through replacing the fixed tip magnet in type-II structure with a moveable magnet connected with a spring [154]. A MEMS harvester in bi-stable style II has been fabricated by Baglio S. et al. on a die (7 mm × 7 mm) [155].
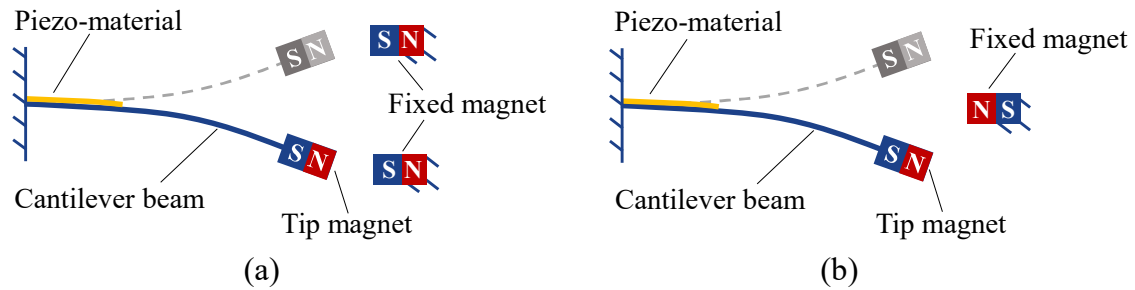
Fig. 2.13. Schematic structures of magnetic bi-stable energy harvesters based on (a) attractive magnetic forces (type I) [29] and (b) repulsive magnetic forces (type II) [156].

Bi-stable PVEHs can also be achieved purely mechanically with bi-stable mechanisms. Fig. 2.14(a) shows a post-buckled beam with two stable positions by axial preloading [157]. Fig. 2.14(b) presents a bi-stable pre-shaped compliant beam. Both of these two structures have been adopted in the construction of bi-stable PVEHs. The difference between them is that pre-shaped bi-stable structure is stress-free in its original stable position, while the post-buckling type stores stress energy in both stable positions.

Cottone F. et al. created a bi-stable energy harvester in the past-buckling type [157]. Sneller A. et al. attached a proof mass in the central part of the post-buckled clamped-clamped beam to enhance its dynamic performance [158]. With the similar doubly clamped bi-stable beam, Zhu Y. et al. further introduced magnetic forces through the central poof mass to prompt the energy generation [159]. Andò B. et al. theoretically verified the advantages of a purely mechanical bi-stable structure for PVEHs in the MEMS scale [160]. Xu R. et al. fabricated a doubly clamped bi-stable energy harvester successfully in the MEMS scale [161]. For the pre-shaped bi-stable structure, it has been widely researched in the area of CMs [162-164], but the application for PVEHs is rare. This is mainly because of the large positive stiffness at the initial position, which corresponds to a high resonant frequency.
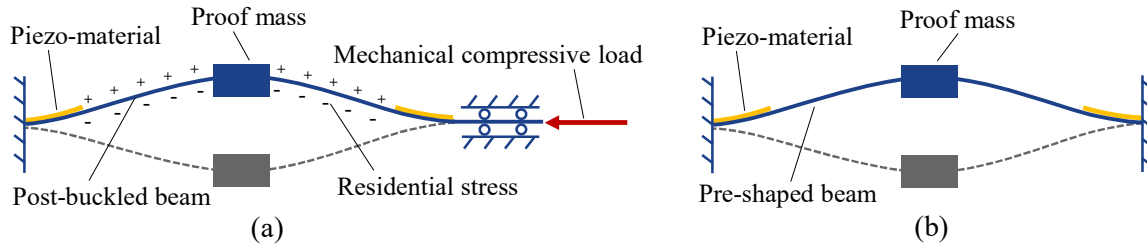
Fig. 2.14. Purely mechanical bi-stable structures for PVEHs in (a) the post-buckling type [157] and (b) the pre-shaped type.

Bi-stability can also be achieved with pre-curved planar compliant structures in the application of PVEHs [2]. Due to the flexibility of the carbon fiber epoxy, a pre-curved composite plate stays in balance in this original shape and can jump to the second stable position with the opposite curvature, as shown in Fig. 2.15. This pre-curved composite plate can also be seen as
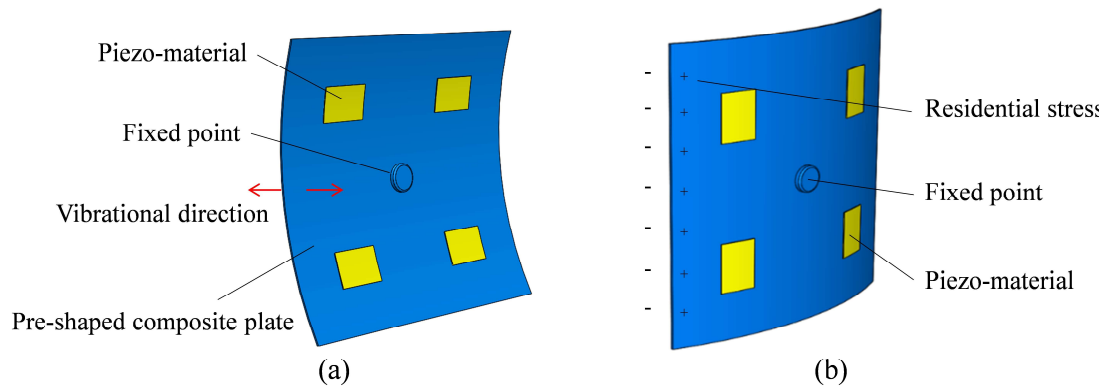
Fig. 2.15. Schematic structure of the bi-stable pre-shaped composite plate [2]. (a) The first/original stable position; (b) The second stable position with residential stress. ("−" here indicates the compressive stress and "+" indicates the tensile stress)

a special case of the pre-shaped type (in Fig. 2.14(b)) in 3D. Arrieta A. et al. and Betts D. et al. conducted in-depth research on the bi-stable PVEHs utilizing the pre-shaped composites [165, 166]. Arrieta A. fixed one edge of the pre-curved composite plate, instead of its central point, in a cantilevered manner in the PVEH developed [167].

b) Tri-stable structures

A tri-stable oscillator has three equilibrium positions. Under external excitations, the tri-stable oscillator can jump among the three energy wells (as shown in Fig. 2.12) in a more complex manner compared with the bi-stable oscillators. The dynamic response of the tri-stable oscillator can be enhanced with shallower potential energy wells [168, 169] and/or a wider distance between two adjacent energy wells [170]. Theoretically, tri-stability could be created either magnetically or mechanically. However, current tri-stable PVEHs in the literature are all based on magnetic forces. The structure based on repulsive magnetic forces is more preferable due to the reduced number of external magnets utilized. The schematic structure of such a magnetic tri-stable harvester is illustrated in Fig. 2.16. Kim P. et al. [171] and Li H. et al. [169] investigated the influence of the geometric distribution of external magnets on the multi-stability of a cantilever-magnet device. Zhou S. et al. carried out continuous and in-depth research on tri-stable piezoelectric energy harvesting [172, 173]. Mei X. et al. applied a tri-stable energy harvester to scavenge energy from rotational vibrations of a rolling vehicle wheel [174]. A wide frequency bandwidth of a tri-stable PVEH with the structure in Fig. 2.16 was theoretically and experimentally proved [175].
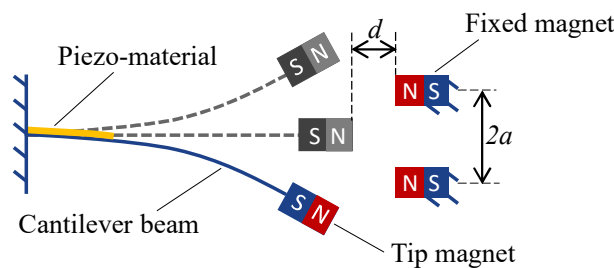
Fig. 2.16. Schematic structure of a tri-stable PVEH utilizing repulsive magnetic force [169].

c) High-order-stable structures

In order to further enhance the dynamic advantages of multi-stable oscillators in vibrational energy harvesting, oscillators with high-order stabilities, such as quad-stable, penta-stable structures, have been introduced in PVEHs. Following the structural principle of the multi-stable PVEHs utilizing magnetic forces, Fig. 2.17 illustrates the schematic structure of a piezo-magneto-elastic quad-stable harvester. Four energy wells appear with three energy barriers created with magnetic repulsive forces. Zhou Z. et al. carried out both theoretical analysis and experiments on the piezo-magnetic quad-stable energy harvesters [176, 177]. A wide effective frequency bandwidth with weak excitation has been verified experimentally. Wang C. et al. adopted attractive magnetic force to create potential energy barriers in their magnetic quad-stable PVEH [178].
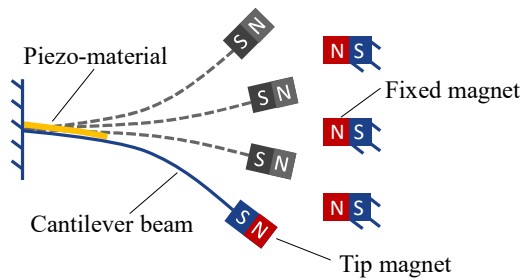
Fig. 2.17. Schematic structure of a quad-stable PVEH based on repulsive magnetic force [177].

Huang D. et al. theoretically analyzed the dynamic response of a penta-stable PVEH with complex inter-well vibration modes responding to external vibrations [150]. Zhou Z. et al. developed a penta-stable PVEH in the cantilever-magnet configuration which contained a piezoelectric cantilever with tip magnet and four external magnets [179]. Kim P. et al. proposed a method to create penta-stability with a bimorph cantilever beam attached with a soft magnetic tip and only two external magnets [180].

d) Discussions

In summary, the spirit of designing a multi-stable PVEH is creating multiple equilibrium positions isolated by potential energy barriers along the vibrating trace. In those multi-stable PVEHs based on magnetic forces, the presence of multiple magnets leads to a complex structure and difficulty in miniaturization. Taking advantages of multi-stable CMs, multi-stable

PVEHs can also be achieved entirely mechanically and monolithically through the deformation of flexible segments. In addition, the monolithic characteristic of multi-stable CMs is also beneficial for PVEHs in miniaturization using MEMS manufacture technologies. According to my knowledge, PVEHs based on multi-stable CMs (except bi-stable type) have not been reported yet. Howell has conducted systematic research on multi-stable CMs [45, 181]. Chen G. et al. introduced a design principle on multi-stable CMs through the synthesis of several single bi-stable compliant structures [57, 77, 182]. Based on their research, some examples of multi-stable CMs suitable for PVEHs are presented in Fig. 2.18. A tri-stable compliant structure is shown in Fig. 2.18(a) and a quad-stability CM is illustrated in Fig. 2.18(b). These multi-stable CMs provide structural potions in constructing multi-stable PVEHs.
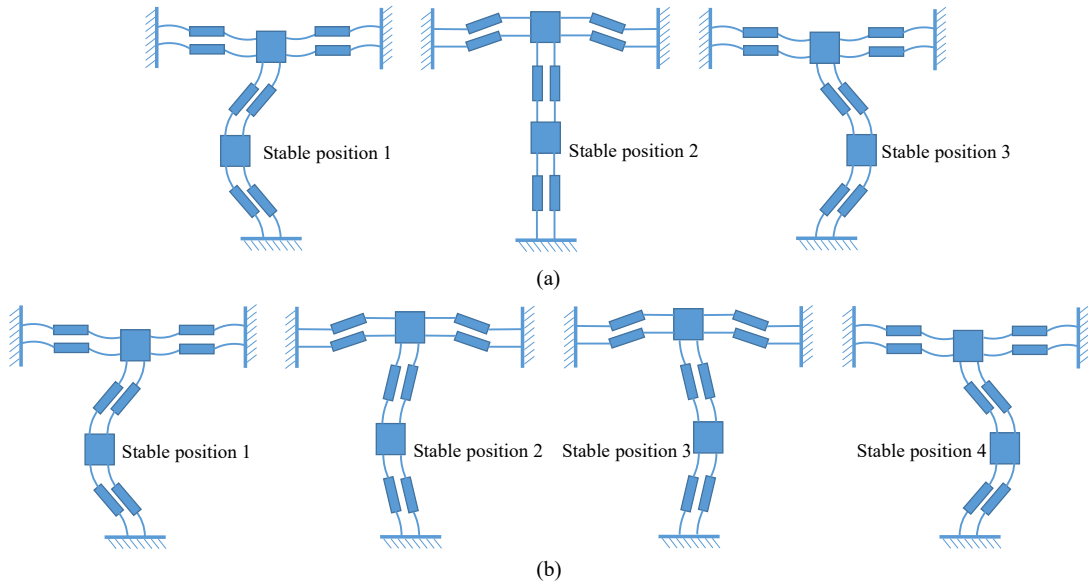
Fig. 2.18. Multi-stable compliant structures suitable for PVEHs [77]. (a) Tri-stable compliant structure; (b) Quad-stable compliant structure.

If the number of stable positions keeps increasing to infinite and the height of energy barriers declines to zero, such a structure will be able to stay stable in a continuous range, which can be seen as the infinite-stable type. The corresponding potential energy pattern is schematically shown in Fig. 2.19.
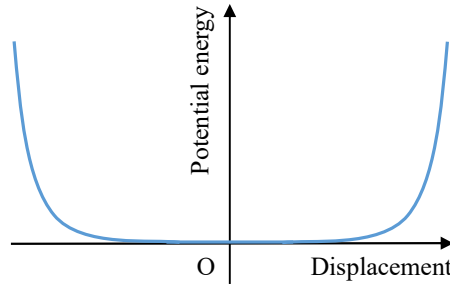
Fig. 2.19. Schematic potential energy pattern of the infinite-stable structure.

The idea of applying SBCMs in PVEHs has been proposed and explored by researchers. Pellegrini S. theoretically discussed the application of the SBCMs in PVEHs [93]. However, only conceptual ideas were provided and no specific structural design, comprehensive dynamic analysis, or experimental validation was reported. Mariello M. et al. tested the performance of a SBCM-based PVEH under wind excitation [94]. However, this study lacks design guidelines and in-depth theoretical analysis on the dynamic performance, and the experiment results were preliminary. Quasi-zero-stiffness oscillators were developed for the purpose of vibration isolation in [183-185] and they share similar static force-displacement characters with SBCMs. However, their structural complexity is not beneficial for practical applications, monolithic fabrication, and miniaturization. Wang K. et al. proposed the combination of a quasi-zero-stiffness mechanism with sliding-triboelectric generators to scavenge energy from ultra-low-frequency vibrations [95]. The dynamic performance of this harvester was reported theoretically, but no experimental verification was given due to the structural complexity of the conceptual design. Yang T. et al. also introduced a quasi-zero-stiffness structure for vibrational energy harvesting [96], but no prototypes and experiments were provided to verify their theory because of the same challenges in terms of complex structures.

Liu C. et al. explored the application of a quasi-zero-stiffness device in vibrational energy harvesting with theoretical analysis and experiments [186]. CMs can be partially compliant or fully compliant. The structure introduced in [186] contained compliant parts partially while some parts are still traditional mechanisms in principle. The employed buckled beams are connected to the frame using pinned-pinned constraints, which makes the resulting structure very difficult to fabricate monolithically and in miniaturized scales. Static experiments on the device were not performed to verify a quasi-zero stiffness and research on its dynamic performance was not complete. According to the reports in the literature, the application of SBCMs in the field of vibrational energy harvesting is still in the conceptual stage. More in-

depth and comprehensive research on the performance of SBCMs in vibrational energy harvesting is still an open issue. This research on SBCMs for vibrational energy harvesting aims to fill this gap. The SBCM structure proposed in this research is a fully compliant mechanism. This distinguishes the SBCM design from the structure in [186]. The SBCM is more attractive in monolithic fabrication and miniaturization.

2.1.3 Multi-degrees-of-freedom structures

To widen the effective frequency range and increase the energy output of PVEHs, several mono-stable oscillators can be integrated in one single device. These mono-stable oscillators resonate simultaneously or individually, leading to multiple degrees of freedom in the system level. Based on their main purposes, multi-degree-of-freedom (multi-DoF) PVEHs can be sorted into two groups, i.e. multi-mode type for broadening the effective frequency bandwidth and multi-direction type aiming at scavenging vibrational energy from different directions.

a) Multi-Mode structures

A continuous frequency range can be approximately represented by a group of isolated frequency points from this range. Based on this concept, a wide effective frequency bandwidth can be simply achieved by integrating several individual mono-stable oscillators in parallel (Fig. 2.20(a)) or in series (Fig. 2.20(b)). The serial type can also be seen as a single resonator with multiple resonant modes at different frequencies. Xue H. et al. and Farokhi H. et al. numerically achieved a wide operating frequency bandwidth based on the multi-mode PVEHs in array type [187, 188]. Shahruz S. expanded the working frequency bandwidth by integrating several piezoelectric cantilevers with different geometric parameters arranged in parallel [189]. Al-Ashtari W. constructed a PVEH with three piezoelectric cantilevers for broadening the efficient frequency bandwidth [190]. Similar structures in Fig. 2.20(a) have also been reported in [191-193]. Connecting mono-stable resonators in series is the second structural approach of multi-mode PVEHs. Hu Y. et al. developed a PVEH containing three stages of cantilever units in a folded series way corresponding to resonant frequencies [194]. Tang X. et al. reported a dual-mass PVEH which connected two single degree of freedom systems in series [195]. Tadesse Y. et al. attached piezoelectric crystals along a slim cantilever beam to create multiple

resonant modes [196]. Gong L. et al. proposed a folded structure for the construction of a multi-mode harvester [197].
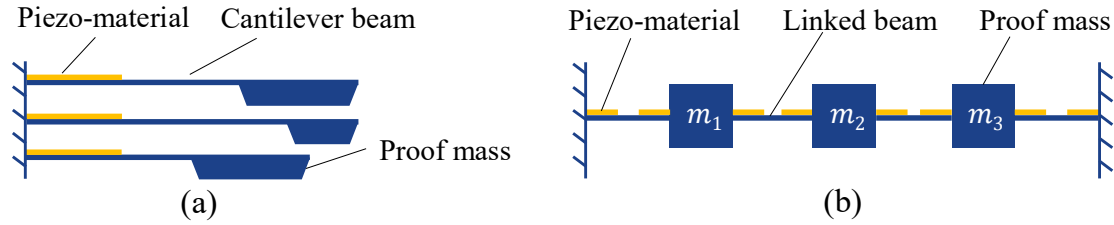
Fig. 2.20. Schematic structures of multi-mode PVEHs in (a) the parallel style [189] and (b) the serial style [198].

b) Multi-direction structures

In real world, environmental vibrations not only spread along a wide frequency spectrum, but also come from various directions. In order to enhance the energy scavenging efficiency from vibrations in different directions, multi-direction PVEHs have also been investigated. The schematic structures of the multi-direction PVEHs in parallel type and in series type are given in Fig. 2.21. Zhou S. et al. developed a multi-direction harvester which consisted several piezoelectric beams linked in series and in a zigzag shape [199]. Hu G. et al. proposed an interesting twisted piezoelectric cantilever beam for harvesting vibrational energy in two perpendicular directions [200]. This structure can be seen as the serial style in Fig. 2.21(b). Yang Z. et al. utilized a doubly clamped elastic rod which was sensitive to vibrations from arbitrary directions in the vertical plane in the reported multi-direction PVEH [201]. Chen R. et al. developed a dandelion-like PVEH to capture energy from ambient vibrations in different directions based on the parallel structural mode in Fig. 2.21(a), which was verified experimentally [202].
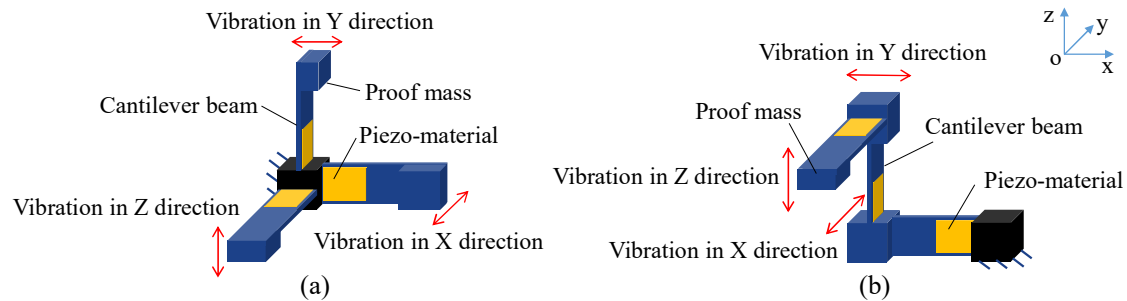
Fig. 2.21. Schematic structures of multi-direction PVEHs in (a) the parallel style [202] and (b) the serial style [11].

c) Discussion

Multi-mode and multi-direction configurations share the same constructing concept which is integrating mono-stable oscillators in parallel or in series. The main difference between them is that multi-mode configuration is aimed at broadening the effective frequency bandwidth, while the multi-direction configuration targets on scavenging vibrational energy from multiple directions. The multi-degree-of-freedom PEVHs show reasonable energy harvesting performance with simple construction principles based on mono-stable oscillators. The concept of CMs can benefit the multi-degree-of-freedom PVEHs by monolithic design and fabrication. Existing multi-degree-of-freedom CMs [203] would provide inspirations and references.

2.1.4 Frequency up-conversion structures

Resonance significantly amplifies vibrational amplitudes of oscillators. However, the energy generation efficiency of PVEHs can still be low due to the low-frequency deformation cycle of the piezoelectric elements under low-frequency environmental excitations. Targeting on this issue, frequency-up-conversion structures are proposed to trigger higher-frequency vibration of the piezoelectric elements by the environmental vibrations with low frequencies. The frequency-up-conversion PVEHs are composed of two stages of oscillators, i.e. first-stage oscillators (driving oscillators) and second-stage oscillators (energy-generation oscillators). The low-frequency oscillation of the first-stage oscillator triggers the high-frequency oscillation of the second-stage oscillator by mechanical impact or magnetic forces. The frequency-up-conversion feature is illustrated in Fig. 2.22. From this aspect, frequency-up-conversion devices can also be seen as frequency amplifiers. In the literature, first-stage
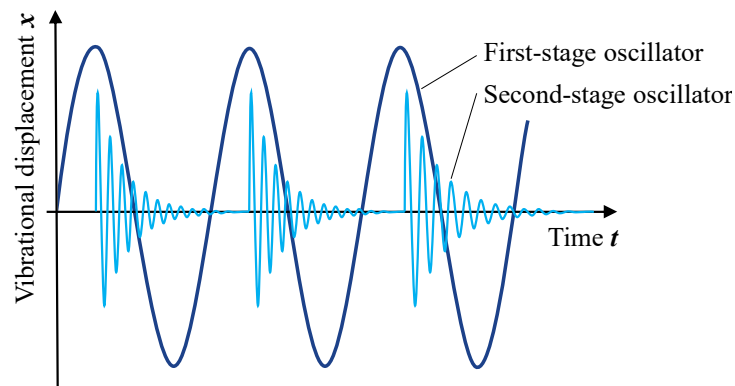
Fig. 2.22.Vibrations of both stages of oscillators of a frequency-up-conversion structure subject to time.

oscillators are reported in various forms, while second-stage oscillators are mainly mono-stable resonators with high resonance frequencies.

a) Mono-stable first-stage oscillators

Cantilever beams are adopted as first-stage oscillators in frequency-up-conversion PVEHs due to their structural simplicity. Two interaction manners, i.e. mechanical impact (Fig. 2.23(a)) and magnetic interaction (Fig. 2.23(b)) between the first- and second-stage cantilevers in such PVEHs are schematically shown in Fig. 2.23. Gu L. utilized a cantilever beam as the driving oscillator in between of two more rigid piezoelectric cantilevers as second-stage oscillators in his frequency-up-conversion harvester [204]. Mechanical impact among the cantilever beams triggers higher-frequency oscillation. Ferrari M. et al. also achieved frequency-up conversion by mechanical impact in their energy harvester [205]. Liu H. et al. successfully fabricated a frequency-up-conversion PVEH in the structure shown in Fig. 2.23(a) in the MEMS scale [206][28]. Tang Q. et al. adopted the magnetic interaction, instead of the mechanical impact, between tip magnets of the two stages of oscillators for frequency up-conversion [207, 208]. Magnetic interaction was also adopted by Wickenheiser A. et al. [209] and Chen S. et al. [210] in the frequency-up-conversion PVEHs.
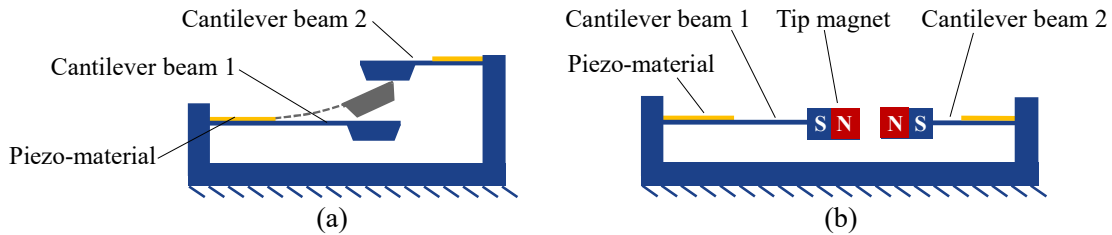
Fig. 2.23. Schematic structures of frequency-up-conversion harvesters utilizing cantilevers as first-stage oscillators. (a) Coupling through mechanical impact; (b) Coupling through magnetic interactions [208].

b) Bi-stable first-stage oscillators

Bi-stable oscillators are also preferable for first-stage oscillators in frequency-up-conversion PVEHs due to their unique dynamic performance introduced earlier. Two distributing manners of bi-stable structures as first-stage oscillators are schematically shown in Fig. 2.24. Second-stage oscillators can be mounted on the base (in Fig. 2.24(a)) or on the proof mass of the first-stage oscillator (in Fig. 2.24(b)). Andò B. et al. adopted a clamped-clamped bi-stable compliant

beam as the first-stage oscillator and two piezoelectric cantilever beams as the second-stage
oscillators in their frequency-up-conversion harvester [211, 212]. Jung S. et al. attached
second-stage piezoelectric cantilevers on the central proof mass of the first-stage bi-stable
beam instead of on the frame to achieve frequency up-conversion in their PVEH [213], as
shown in Fig. 2.24(b). Inspired by the auditory hair bundle structure, Kim G. et al. developed
a bi-stable compliant mechanism as the first-stage oscillator for the frequency up-conversion
harvester [214].
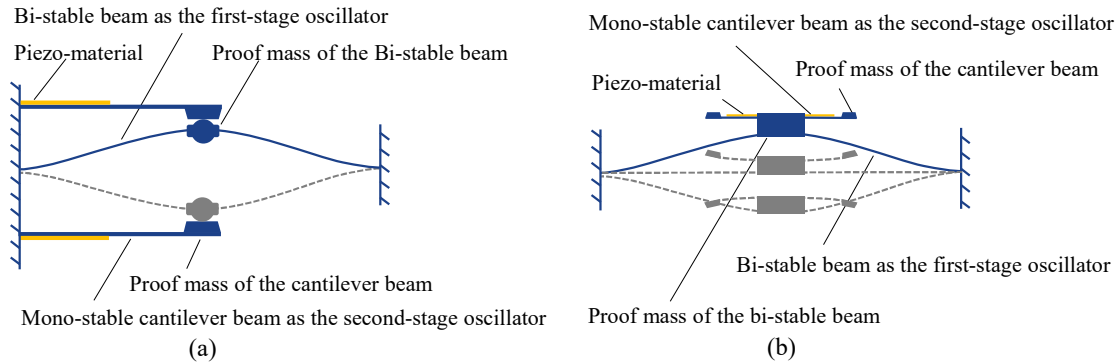
Fig. 2.24. Schematic structures of frequency-up-conversion harvesters utilizing bi-stable resonators as first-stage
oscillators. (a) Two stages of oscillators are distributed separately [212]; (b) The second-stage oscillators are
mounted on the first-stage oscillator [213].

c) First-stage oscillators in other forms

In addition to mono-stable or bi-stable oscillators, first-stage oscillators can be in other forms.
Yeo H. et al. utilized an eccentric rotor (as the first-stage oscillator) to stimulate six circularly
arranged PZT beams (as the second-stage oscillators) to scavenge the energy from low-
frequency vibration sources [215]. Pillatsch P. et al. adopted a rotating pendulum as the first-
stage oscillator [216]. The second-stage piezoelectric cantilever was triggered by the magnetic
interaction between the magnets attached on both stages of oscillators. Fan K. et al. adopted
rolling elements (cylinder or ball) as first-stage oscillators [217, 218]. The second-stage
piezoelectric cantilevers were triggered by magnetic coupling forces between the tip magnets
and rolling elements under external excitations. Hara M. et al. used a micro metal ball guided
by a cylindrical hole as the first-stage oscillator in their frequency-up-conversion harvester in
MEMS scale [219]. Under environmental excitation, the metal ball was stimulated to impact
the piezoelectric cantilever beam arranged above for energy generation at a higher frequency.

d) Discussion

Frequency-up-conversion PVEHs improve the energy generation efficiency through amplifying the low excitation frequencies up to higher resonant frequencies of energy-generating oscillators. Drawbacks of current frequency-up-conversion harvesters in the literature include complex assembling process, large volume, difficulties in miniaturization etc. CMs with the frequency-up-conversion character can be solutions for these problems. Tolou N. et al. proposed several CMs with such frequency-amplifying functions [220, 221], which can be utilized as main structures in PVEHs. The frequency-amplifying CMs in literature include frequency-doubler [220] and frequency-quadrupler [222]. The schematic structure of the frequency-doubler and its working concept are introduced in Fig. 2.25. Higher frequency amplifying ratio can be achieved by simply connecting multiple frequency-doubler in series.
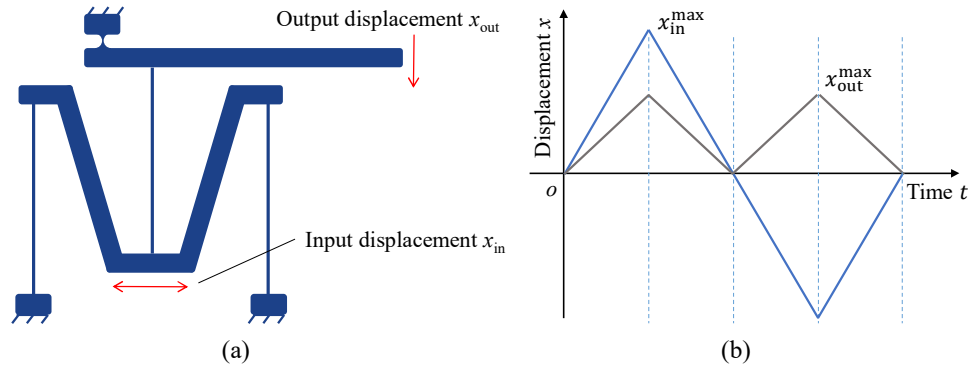
Fig. 2.25. (a) Schematic structure and (b) the displacement of input and output points with respect to time of the frequency doubling compliant structure proposed by Tolou et al. [221]

2.1.5 Stress optimization structures

Mechanical stress is critical for PVEHs because it is basically required by the piezoelectric effect. Therefore, operations on mechanical stress, such as optimizing stress distribution and maximizing stress generation, provide new approaches to enhance the energy generation performance of PVEHs.

a) Stress distribution optimization

The stress concentration around the clamped end is a commonly existing problem for cantilever oscillators, while the stress is nearly zero at the free end. The unevenly distributed stress leads

to a low energy conversion efficiency and short life-durance of the device. Targeting this problem, piezoelectric cantilevers with optimized shapes, such as triangular, trapezoidal etc. were proposed for PVEHs. The trapezoidal piezoelectric cantilever is shown schematically in Fig. 2.26. Roundy S. et al. reported that a cantilever PVEH in the trapezoidal shape could double the energy output compared with that in a rectangular shape [198]. Goldschmidtboeing F. et al. reported that triangular-shaped cantilever beams had larger tolerable excitation amplitude and higher power output than rectangular cantilever beams for PVEHs [223]. In MEMS scale, Jackson N. et al. compared the performance of PVEHs with cantilever beams in trapezoidal, wide rectangular and narrow rectangular shapes through both finite-element simulation and experiments [224]. Trapezoidal beams showed more balanced characteristics in power density and frequency bandwidth. In addition to the shape optimization, a specific CM was designed and connected with the free end of the traditional rectangular cantilever beam for a more uniform stress distribution [225].
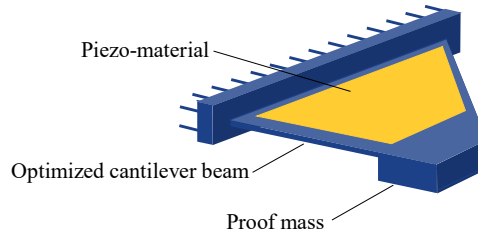
Fig. 2.26. Piezoelectric cantilever in trapezoidal shape for the optimized stress distribution [226].

b) Stress amplification

In the scenario where energy is scavenged from mechanical impacts, impulsive force applied on piezoelectric stacks is expected to be multiplied for a higher energy generation efficiency. A compliant structure with stress-amplifying function is schematically shown in Fig. 2.27. Based on the deformation of compliant joints and lever principle, the input load will be multiplied with a certain ratio (determined by geometric parameters) and then applied on piezoelectric stacks. Zhang Y. et al. developed a compliant load amplifier in a pedal PVEH to maximize voltage outputs [227]. Wen S. et al. designed a force-amplification CM for harvesting energy from human walking [228]. Feenstra J. et al. replaced the strap buckle of a backpack with a piezoelectric stress-amplifier to scavenge energy from wearers' motions [229]. Cao D. et al. designed a compliant force amplifier to increase the force applied on the piezoelectric stack for harvesting energy from the pressure fluctuation in pipeline systems

[230]. Such stress-amplifying structures harvesting energy from impact forces in MEMS scales have not been in the literature yet.
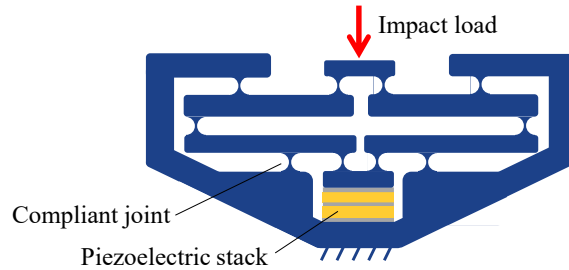
Fig. 2.27. Schematic structure of a compliant stress amplifier for PVEH from impact loads.

2.2 Comparison and selection of piezoelectric materials for the integration with CMs in vibrational energy harvesting

In addition to mechanical structures, piezoelectric materials also play critical roles in PVEHs. Popular piezoelectric materials for PVEHs include PZT (Pb[ZrxTi1-x]O3), KNN (K0.5Na0.5NbO3), ZnO, AlN and PVDF (Polyvinylidene fluoride). Main characteristics of these piezo-materials are summarized in Table 2.1 for a clear comparison. The comparison shows that PVDF has the best flexibility compared with other piezo-materials, although its piezoelectric property is moderate. Therefore, PVDF would be the best choice to integrate with CMs for vibrational energy harvesting and therefore this material will be used in this research.

Due to their specific physical characteristics, different piezo-materials have been utilized in PVEHs with different structures, sizes and application scenarios. Since the energy generation capability varies from a device to another, a common assessment criterion is needed. The metric of Normalized Power Density (NPD), *Power/(volume·frequency·acceleration²)*, considering the device volume, excitation frequencies and stimulating accelerations, is proposed here for comparing the energy generation capability of the PVEHs in the literature. The volume of the PVEH device is an important parameter because it qualitatively reflects structural configurations (which have been introduced above), fabrication techniques used, application conditions etc. The NPD of different PVEHs utilizing different piezo-materials versus the device volume is plotted in Fig. 2.28 to illustrate their relationship. Volume here is the active volume of devices. A large amount of data on energy generating performance of PVEHs has been collected and summarized [7, 111, 231], however, it has not been organized

in a such way. Initial data of PVEHs from literature are listed in Table 2.1. Note that inaccuracy exists in this NPD-Volume graph due to the three main reasons: 1) the authors may calculate device volumes in different ways because no standard is established for this yet [232]. 2) The same piezo-material can be fabricated in various forms which shows different performances. 3) The number of samples is limited since not all publications on PVEHs provide sufficient figures wanted. Therefore, this NPD-Volume graph of PVEHs shows the NPD-Volume tendency and relationship qualitatively.

Table 2.1. Comparison of piezo-materials widely used in PVEHs.

PZT ($Pb[Zr_xTi_{1-x}]O_3$)	1. Excellent piezoelectric properties.[233] 2. High Curie temperatures [8]	1. Lead contained in PZT is toxic. [234] 2. Polarization process is required for piezoelectric effect. [235, 236]
KNN ($K_{0.5}Na_{0.5}NbO_3$)	1. Lead-free perovskites ceramics. [237, 238] 2. High piezoelectric constants, good Young's modulus, moderate dielectric properties and Curie temperatures.[238-240]	High leakage current density caused by element loss because of the thermalization problem.[7]
ZnO	Good semiconducting properties; multiple forms are available. [241]	1. Moderate piezoelectric properties [242] 2. ZnO is unstable and reacts with other IC materials; 3. It is hard to reproduce its properties. [243]
AlN	1. Compatible to MEMS process. Various operations can be done on it.[7, 243] 2. Excellent physical properties: high thermal conductivity, high breakdown voltage, high resistivity and corrosion resistance[243, 244]. 3. Biocompatible[245, 246].	1. Moderate piezoelectric properties[7, 242]. 2. Residual stress in AlN during fabrication has an influence on the piezoelectric performance. [247]
PVDF (Polyvinylidene fluoride)	1. Outstanding flexibility, low density, good stability, tough.[248] 3. Available in the market for easy applications.	1. Poling process is required[249-251]. 2. Moderate piezoelectric properties.[7, 248]

Based on this NPD-Volume graph, several conclusions are drawn. 1) PZT owns relatively the most stable power generating capability across a wide device volume range. It also represents the largest NPD among all these piezo-materials. Because of its outstanding performance, PZT has the highest popularity. 2) AlN shows higher power density in a larger device size. 3) The NPD of KNN and ZnO has a tendency to decline when the device volume increases. 4) Around the device volume of 100 mm^3, the NPD of PVDF varies among different PVEHs. In addition,

mono-stable cantilever beams are still the most popular structural type for PVEHs in the literature. according to the column of mechanical structures in Table 2.2.
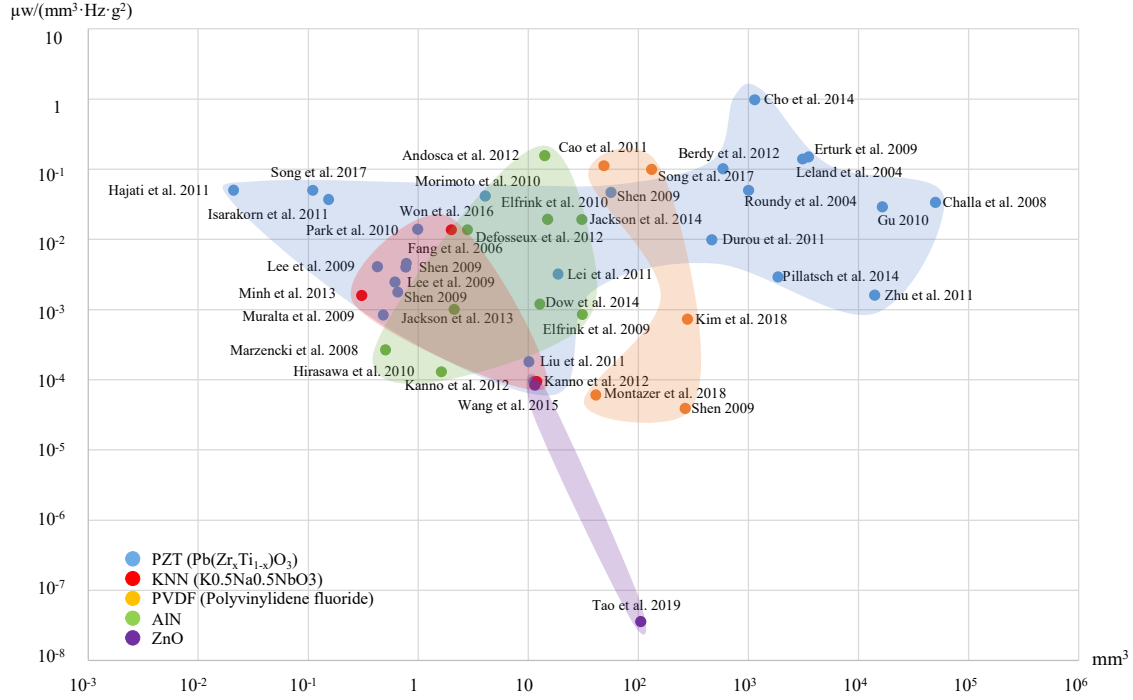
Fig. 2.28. NPD-Volume graph of PVEHs.

2.3 Summary

This Chapter systematically reviewed the state-of-the-art structural methodologies of PVEHs in the literature, for gaining a better understanding on the structural design of PVEHs. The mechanical structures of PVEHs were analysed and categorized into five groups, namely mono-stable structures, multi-stable structures, multi-degree-of-freedom structures, frequency-up-conversion structures and stress-optimization structures. Several CM concepts in different structural categories were first proposed as mechanical structures for PVEHs, which would be both references and inspirations for researchers in the related area.

In addition to mechanical structures, piezoelectric materials directly determine the energy generating capability of PVEHs. The metric of NPD was introduced to compare and assess the energy generation capability of PVEHs with different piezo-materials and in different scales. Based on the data collected in the literature, the NPD-Volume graph on PVEHs was first drawn. PVEHs with PZT owned the highest NPD among all piezo-materials discussed here and stable

energy generation in a large volume range. The energy generating performance of PVDF is moderate, but its mechanical flexibility is outstanding. Therefore, PVDF films can be reasonable options for the combination with CMs in PVEHs.

According to this review, the majority of the PVEHs in the literature work in the high frequency spectrum although wide frequency bandwidths have been achieved with various structural methodologies. These structures also have limitation in miniaturization due to the size effect, i.e. smaller sizes lead to higher resonating frequencies [97]. The ideal PVEHs would be sensitive to ultra-low wide bandwidth frequencies with weak accelerations and friendly to fabrication and miniaturization. However, such performances have not been fully achieved. The SBCM investigated in this thesis provides a structural solution for creating ideal vibrational energy harvesters.

Table 2.2. Energy generation capability of PVEHs from literature.

Number	Power (µW)	Acceleration (g)	Volume (mm³)	Frequency (Hz)	NPD (µW/mm3/HZ/g²)	Piezoelectric materials	Mechanical structures (corresponding sections in this review)	Source
1	118	0.2	588	49.7	1.01E-01	PZT	Mono-stable (section 1.2)	Berdy et al. 2012[111]
2	29.3	0.05	3106	27	1.40E-01	PZT	Mono-stable (section 1.1)	Leland et al. 2004[102]
3	23900	1	3520	45.6	1.49E-01	PZT	Mono-stable (section 1.1)	Erturk et al. 2009[103]
4	375	0.25	1000	120	5.00E-02	PZT	Mono-stable (section 1.1)	Roundy et al. 2004[101]
5	0.0855	1	10.1	47	1.80E-04	PZT	Nonlinear Mono-stable (section1.2.2)	Liu et al. 2011[145]
6	257	1	56.4	97.6	4.67E-02	PZT	Mono-stable (section 1.1)	Shen 2009[252]
7	2.13	2	0.652	461.15	1.77E-03	PZT	Mono-stable (section 1.1)	Shen 2009[252]
8	0.32	0.75	0.769	183.8	4.02E-03	PZT	Mono-stable (section 1.1)	Shen 2009[252]
9	280	0.08	50000	26	3.37E-02	PZT	Nonlinear mono-stable (section1.2.2)	Challa et al. 2008[253]
10	0.0233	0.25	0.11	68	4.98E-02	PZT	Mono-stable (section 1.2.1)	Song et al. 2017[113]
11	240	0.4	14025	67	1.60E-03	PZT	Mono-stable (section 1.1)	Zhu et al. 2011[254]
12	13.98	1	18.6	235	3.20E-03	PZT	Mono-stable (section 1.1)	Lei et al. 2011[255]
13	1.11	0.39	0.99	528	1.40E-02	PZT	Mono-stable (section 1.1)	Park et al. 2010[256]
14	43	2	1850	2	2.91E-03	PZT	Frequency up-conversion (section 4)	Pillatsch et al. 2014[216]
15	1530	0.4	16416^e	20.1	2.90E-02	PZT	Frequency up-conversion (section 4)	Gu 2010[204]
16	2.16	1	0.78	608	4.55E-03	PZT	Mono-stable (section 1.1)	Fang et al. 2006[257]
17	2.765	2.5	0.425	255.9	4.07E-03	PZT	Mono-stable (section 1.1)	Lee et al. 2009[258]
18	1.288	2	0.612	214	2.46E-03	PZT	Mono-stable (section 1.1)	Lee et al. 2009[258]
19	1	1	11.9	892	9.42E-05	PZT	Mono-stable (section 1.1)	Kanno et al. 2012[239]
20	13	1	0.153	2297	3.70E-02	PZT	Mono-stable (section 1.1)	Isarakorn et al. 2011[259]
21	15300	0.69	1140	29	9.72E-01	PZT	Mono-stable (section 1.1)	Cho et al. 2014[232]
22	1.4	2	0.48	870	8.38E-04	PZT	Mono-stable (section 1.1)	Muralta et al. 2009[260]
23	5.3	0.5	4.05	126	4.15E-02	PZT	Mono-stable (section 1.1)	Morimoto et al. 2010[261]

Table 2.2. Energy generation capability of PVEHs from literature.

Number	Power (µW)	Acceleration (g)	Volume (mm³)	Frequency (Hz)	NPD (µW/mm3/HZ/g²)	Piezoelectric materials	Mechanical structures (corresponding sections in this review)	Source
24	22	4	0.021	1300	5.04E-02	PZT	Nonlinear Mono-stable (section1.2.2)	Hajati et al. 2011[127]
25	13.9	0.2	464	76	9.85E-03	PZT	Mono-stable (section 1.1)	Durou et al. 2010[262]
26	0.731	1	0.306	1509	1.58E-03	KNN	Mono-stable (section 1.1)	Minh et al. 2013[263]
27	3.62	1	2.01	132	1.36E-02	KNN	Mono-stable (section 1.1)	Won et al. 2016[264]
28	1.1	1	11.22	1036	9.46E-05	KNN	Mono-stable (section 1.1)	Kanno et al. 2012[239]
29	1.25	1	11.5	1300.1	8.36E-05	ZnO	Mono-stable (section 1.1)	Wang et al. 2015[265]
30	0.00046	0.5	105.125	489.9	3.57E-08	ZnO	Multi-mode (Section 3.1)	Tao et al. 2019[266]
31	3.5	0.2	30.7	149	1.91E-02	AlN	Mono-stable (section 1.1)	Jackson et al. 2014[224]
32	60	2	31	572	8.46E-04	AlN	Mono-stable (section 1.1)	Elfrink et al. 2009[267]
33	0.62	0.275	2.8	214	1.37E-02	AlN	Mono-stable (section 1.1)	Defosseux et al. 2012[268]
34	0.18	1	1.63	853	1.29E-04	AlN	Mono-stable (section 1.1)	Hirasawa et al. 2010[269]
35	6.9	0.2	15	599	1.92E-02	AlN	Mono-stable (section 1.1)	Elfrink et al. 2010[270]
36	0.8	2	0.504	1495	2.65E-04	AlN	Mono-stable (section 1.1)	Marzencki et al. 2008[271]
37	128	1	14.16	58	1.56E-01	AlN	Mono-stable (section 1.1)	Andosca et al. 2012[272]
38	34.78	2	12.76	572	1.19E-03	AlN	Mono-stable (section 1.1)	Dow et al. 2014[273]
39	0.669	1	2.125	315	9.99E-04	AlN	Mono-stable (section 1.1)	Jackson et al. 2013[274]
40	18.56	1.75	280	30	7.21E-04	PVDF	Mono-stable (section 1.1)	Kim et al. 2018 [275]
41	40.9	1	41.19	164	6.05E-05	PVDF	Mono-stable (section 1.1)	Montazer et al. 2018[276]
43	1.0688	1	267	102.9	3.89E-05	PVDF	Mono-stable (section 1.1)	Shen 2009[252]
44	100.833	0.431	48.7	100	1.11E-01	PVDF	Mono-stable (section 1.1)	Cao et al. 2011[277]
45	112.8	0.5	132.6	34.4	9.89E-02	PVDF	Mono-stable (section 1.1)	Song et al. 2017[278]

Note: Estimated Figures based on original publications are marked with 'e'.

Chapter 3 Design of Statically Balanced Compliant Mechanisms

SBCMs achieve zero force and zero stiffness in a limited displacement range and show stiffness nonlinearity in the wider displacement range. This unique stiffness characteristic distinguishes SCBMs from the linear or nonlinear oscillators in the literature reviewed in Chapter 2. This Chapter introduces the design principle of the SBCMs. One suitable SBCM is selected from two possible structures. The diverse force-displacement relationships of the SBCM is obtained and analysed based on FEA simulations, which also forms a foundation for the dynamic modelling in the next Chapter.

3.1 Design principle of the SBCM

SBCMs are energy free from the energy perspective. This is because the external force required for the desired motion of the SBCM is zero in the static-balancing displacement range and thus the work exerted by the external force is zero in the whole system level. In order to achieve this energy-free character, the mechanical energy consumed in the deformation procedure of the compliant structures can be compensated by the mechanical energy stored in the mechanism in advance and the imported mechanical energy is zero [279, 280]. Strain energy contained in the whole device keeps constant and it flows between the constructive stiffness components.

It is common to see CMs with positive stiffness, such as V-shaped compliant beams [281], the parallelogram flexure [55], the double parallelogram flexure [54], etc. Mechanical energy is consumed in the deformation process of the positive-stiffness CMs. However, some other CMs own negative stiffness. Fixed-guided bi-stable compliant beams [162, 282], post-buckled fixed-guided compliant beams [55, 283] are typical examples of these negative-stiffness CMs. In the deformation process of these negative-stiffness CMs in its displacement range with negative stiffness, mechanical energy is released.

A typical SBCM is constructed based on the stiffness compensation principle [78, 279] whereby the stiffness of the positive-stiffness component and that of the negative-stiffness component are balanced with each other so that a zero effective stiffness is achieved. A further requirement for the static balancing is that the force-displacement curves of the positive- and negative-stiffness components should be symmetric about the horizontal axis. This makes SBCMs distinguished from constant-force CMs [149, 284, 285] where the stiffness stays zero in a certain displacement range and the corresponding force keeps constant (not necessary to be zero). The requirements for static balancing in a certain displacement range can be described with the two equations as follows:

$$F_+(x) + F_-(x) = 0 \tag{3.1}$$

$$k_+(x) + k_-(x) = 0 \tag{3.2}$$

where $F_+(x)$ and $F_-(x)$ are the external forces exerted on the positive- and negative-stiffness components, respectively. $k_+(x)$ and $k_-(x)$ are corresponding stiffness expressions of these two stiffness components. They can be obtained with the first derivation of force-displacement equations. For SBCMs, both of the Eqs. (3.1) and (3.2) have to be fulfilled, while Eq. (3.2) is the only requirement for constructing constant-force CMs.

As alternative expressions of the Eqs. (3.1) and (3.2), Fig. 3.1 schematically shows the requirements on the construction of the SBCMs and constant-force CMs in the form of graphs. Both SBCMs and constant-force CMs have zero stiffness based on the stiffness compensation principle as shown in Fig. 3.1(c). For SBCMs, the force-displacement curves of the positive- and negative-stiffness components have to be symmetric about the horizontal axis as shown in Fig. 3.1(a), while this is not necessarily required for constant-force CMs. Constant-force CMs own constant force in their functional displacement ranges. This brings another approach on the design of SBCMs by taking the constant-force CMs as building blocks. Static balancing can be achieved when the force of the constant-force CM is compensated by another constant force in the opposite direction. The constant force in the opposite direction can be provided by preloading [284], gravity forces [82], etc.

In summary, both SBCMs and constant-force CMs are designed based on the stiffness compensation principle. Symmetric force-displacement curves are required for static balancing while this is not necessary for constant-force CMs. In addition, constant-force CMs can be utilized as building blocks for the construction of SBCMs.
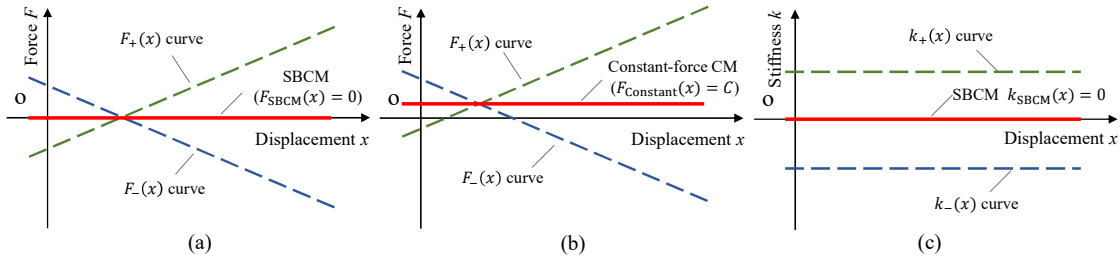
Fig. 3.1. Schematic graphs of (a) force-displacement curves of positive-stiffness component, negative-stiffness component and the SBCM constructed, (b) force-displacement curves of positive-stiffness component, negative-stiffness component and constant-force CM constructed and (c) curves of positive stiffness, negative stiffness and zero stiffness obtained.

3.2 Preliminary designs of the SBCM and structure selection

Based on the stiffness compensation principle introduced, various SBCMs can be designed utilizing different positive- and negative-stiffness components [283]. Two preliminary SBCM structures are proposed based on the synthesis concepts mentioned earlier and they are introduced and compared in this section. The SBCM structure which is more suitable for the practical application in vibrational energy harvesting is selected between the two structures. It is noteworthy that there might be more SBCMs suitable for vibrational energy harvesting and they will be explored in the future work.

3.2.1 SBCM structure 1

The first SBCM structure achieves static balancing based on the direct stiffness compensation between a positive-stiffness component and a negative-stiffness component (as shown in Fig. 3.2(a)). The positive-stiffness component consists of a pair of symmetrically distributed double parallelograms and the negative-stiffness component is composed of 2 pairs of clamped-guided post-buckled compliant beams arranged in bi-symmetry. The positive- and negative-stiffness components are connected together with the sharing mass block.

In terms of the positive-stiffness component, alternatives include leaf springs [45, 281] and diamond leaf springs [90, 281]. Leaf springs have the simplest structure while the un-desired parasite motion perpendicular to the effective displacement exists. Diamond leaf springs provide approximate linear motions with alleviated parasite motions. However, the

translational motion perpendicular to the functional direction and the rotational motion of the diamond leaf springs are not restricted. The double parallelogram outperforms its counterparts by tackling these issues [54]. The linear translational motion of a double parallelogram is valid in a large displacement range without causing over-constraint or significant error motions. Another advantage is that it permits the vertical translational motion only and other 5 DOF are restricted. The capability to restrict un-desired motions is preferable. This is because the negative-stiffness components normally have more DOF [286], such has rotation, horizontal translational motion, in addition to the desired motion. Therefore, the double parallelogram is adopted here for the construction of the positive-stiffness component.

Since both the positive- and negative-stiffness components have zero force at the origin point, the requirement zero-force equation (Eq. (3.1)) will be automatically fulfilled when the zero-stiffness equation (Eq. (3.2)) is satisfied with well-selected geometric parameters. No further operation is required for static balancing. In addition, the force-displacement curves of both positive- and negative-stiffness components are symmetric about the origin point. Therefore, the fore-displacement curve of the SBCM synthesized is also symmetric about the origin point.
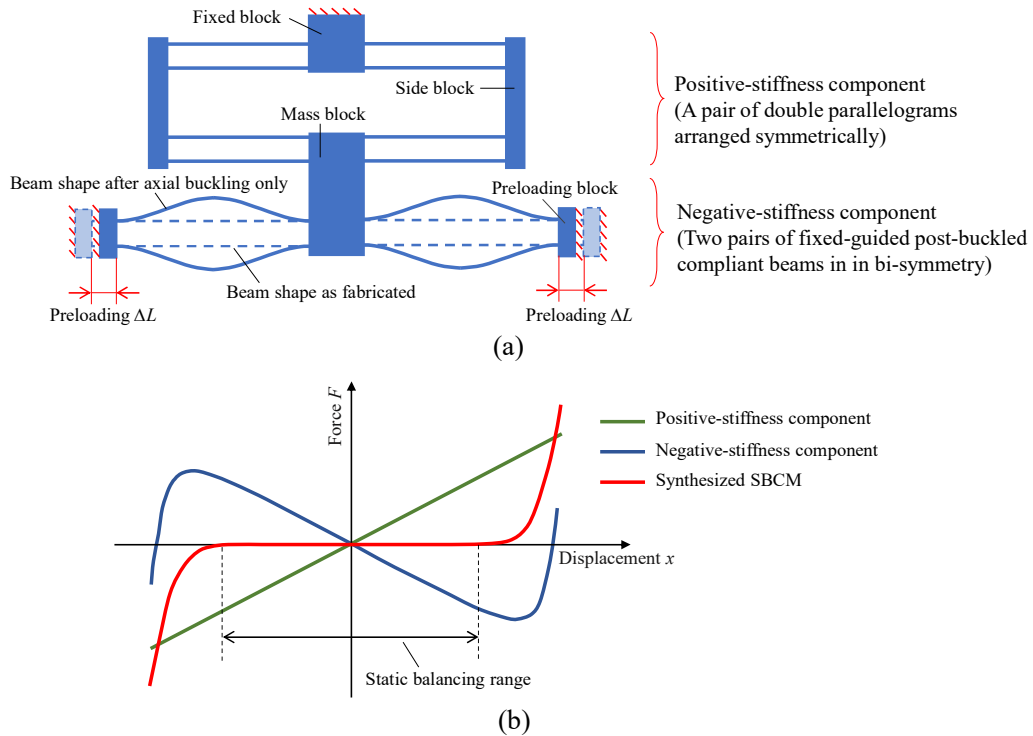
Fig. 3.2. (a) The schematic structure and (b) force-displacement curves of the SBCM structure 1 and its positive- and negative-stiffness components. (Coloured curves)

The force-displacement curves of the SBCM structure 1 and its positive- and negative-stiffness components are schematically presented in Fig. 3.2(b).

3.2.2 SBCM structure 2

The second SBCM structure is designed taking a constant-force CM as the constructive component and its constant force is compensated by preloading. The structure of the constant-force CM [284] is schematically shown in Fig. 3.3(a). The double parallelograms are also adopted here for the construction of the positive-stiffness component due to the advantages mentioned earlier. The negative-stiffness component is composed of four inclined fixed-guided compliant beams [162, 282] which are symmetrically arranged. The positive- and negative-stiffness components are connected with a common mass block.

The force-displacement curves of the constant-force CM and the positive- and negative-stiffness components are schematically shown in Fig. **3.3** (b). As indicated in Fig. 3.3(b), the force-displacement curve of the negative-stiffness component can be divided into three parts by points 1, 2 and 3. In the starting small displacement range (between points 1 and 2), the negative-stiffness component owns positive stiffness. Once the inclined fixed-guided compliant beams are bucked, the stiffness turns negative sharply in the central displacement range (between points 2 and 3). In the displacement range from point 3 forward, the stiffness turns to positive again. Synthesized with a well-designed positive-stiffness component, a constant force is achieved in the displacement range between points 2 and 3 (considering the inherent stiffness nonlinearity, the actual constant-force range is smaller than the negative-stiffness displacement range).

Taking the constant-force CM as a building block, the static balancing can be achieved by compensating the constant force in the form of preloading. The schematic structure of the SBCM based on this principle is shown in Fig. 3.3(c). The positive-stiffness component is preloaded by pressing the fixed block downward for a certain displacement of ΔL. As a result, the inclined fixed-guided beams are buckled and the mass block moves to the new position in the static-balancing displacement range. The corresponding force-displacement curves of this preloading procedure are schematically in Fig. 3.3(d). The bottom light blue line represents the compensation force imposed by preloading on the positive-stiffness component.

(a)

(b)

(c)

(d)
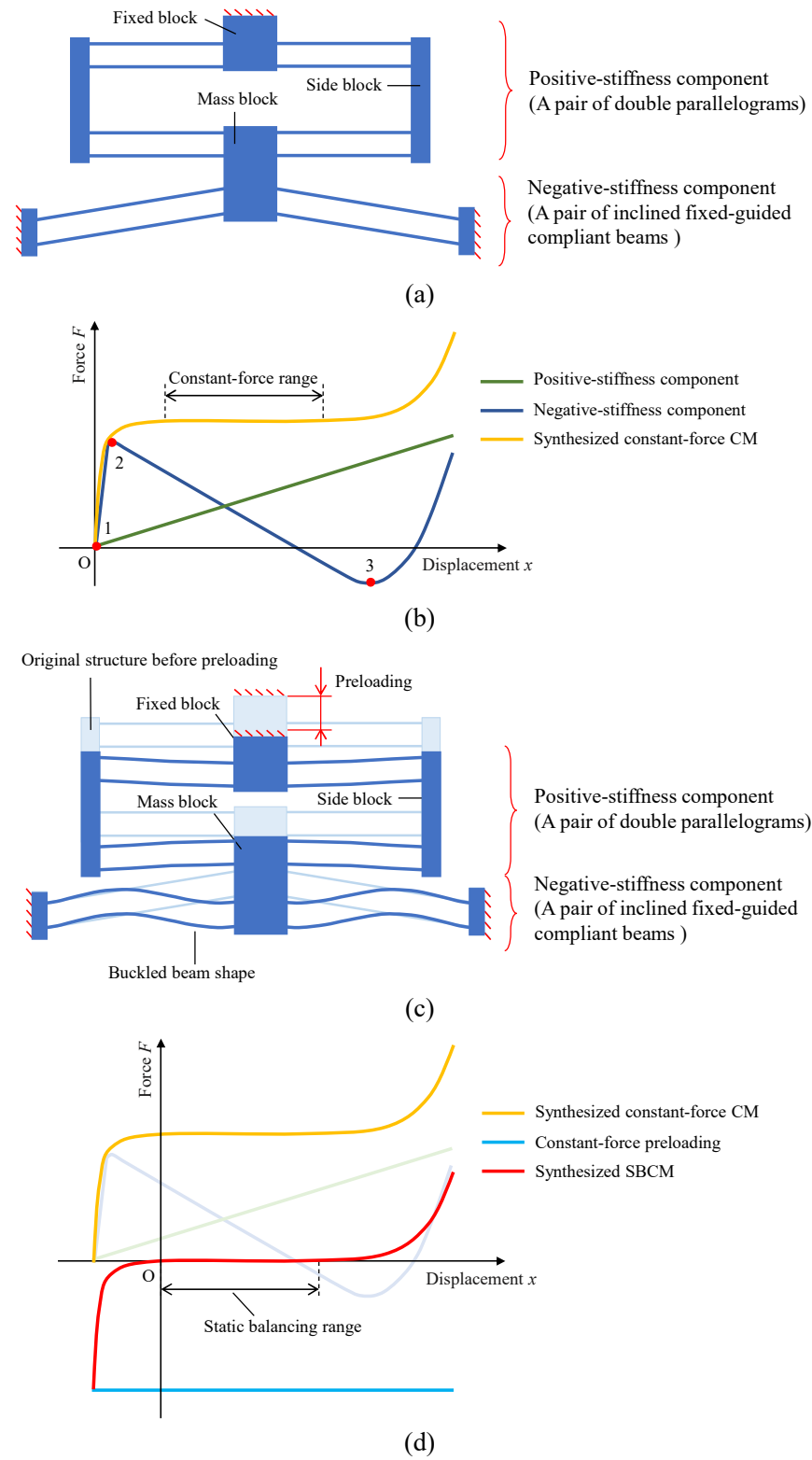
Fig. 3.3. (a) The schematic structure and (b) force-displacement curves of the constant-force CM and its positive-and negative-stiffness components; (c) The schematic structure and (d) force-displacement curves of the SBCM achieved by preloading on the constant-force CM. (Coloured curves)

52

According to the research in the literature about the inclined fixed-guided compliant beams, the force-displacement curve of the negative–stiffness beams is not symmetric about any axes or points (as shown in Fig. 3.3(b)) [162]. Therefore, the force-displacement curve of the SBCM eventually synthesized is not symmetric. In addition, the design of the SBCM based on this principle contains two steps, namely, design of the constant-force CM and preloading on the constant-force for static balancing.

3.2.3 Structural comparison and selection
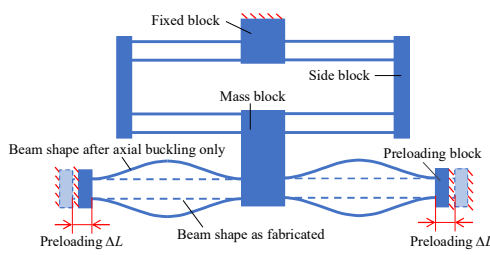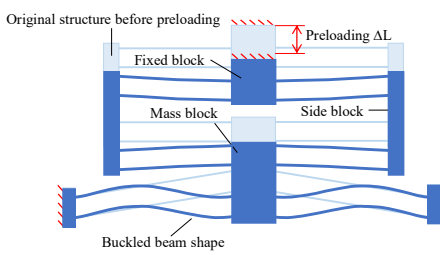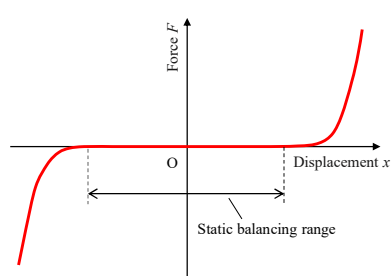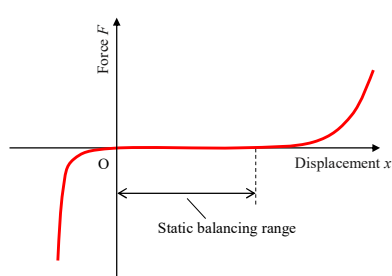
The two SBCM structures proposed in Section 3.2.1 and 3.2.2 are compared in Table 3.1. Based on the comprehensive comparison from the perspectives of theoretical analysis, fabrication and application etc., the first SBCM structure is selected in this research for the application in vibrational energy harvesting. The main reasons are summarized as follows:

1) The first SBCM structure has relatively simpler design procedure, where only Eq. (3.2) has to be satisfied. Static balancing is automatically achieved when the geometric parameters are well designed or tuned. For the second SBCM structure, both requirement equations (Eqs. (3.1) and (3.2)) have to be fulfilled, leading to a more complex design process. A constant-force CM is first developed. The constant force is then compensated by further operations for static balancing. Compared with the second SBCM, the first SBCM structure is then friendlier in fabrication and applications.

2) The force-displacement curve of the first SBCM structure is symmetric about the origin point. This character benefits the modelling and analysis of the static and dynamic performance of the SBCM. This is preferable in particular at the investigation stage on the SCBM in vibrational energy harvesting. The second SBCM structure has asymmetric force-displacement curve. Special dynamic performance is expected from this structure, while this could not represent general characteristics of the SBCM and might cause confusions.

3) For the first SBCM structure, the mass block theoretically stays at the same origin position regardless of the preloading (in static-balancing and mono-stable conditions). However, the preloading will determine the original position of the second SBCM for static balancing. An accurate preloading displacement, ΔL, is required. Since a small preloading displacement error will lead to large force difference around in static-balancing condition. Due to the fact that

preloading errors always exist, a perfect static-balancing condition may never be achieved and always a constant-force condition with a force value (minus or positive) very close to zero is obtained.

4) In the first SBCM structure, preloading has to be applied at two positions (axial preloading on the negative-stiffness beams), while preloading at only one position is needed in the second SBCM structure. This feature of the first SBCM might increase the structural complexity and cause preloading asymmetry on left/right-hand side of the structure. However, this problem is solvable with measurement tools with high accuracy or well-designed preloading structures.

Table 3.1. Comparison of the two SBCM structures.

Structural type	SBCM structure 1	SBCM structure 2
Structures		
force-displacement curves		
Features from the application perspective	• Eq. (3.2) is the only requirement equation to satisfy. Eq. (3.1) is fulfilled automatically; • Force-displacement curve is symmetric about the origin point; • Preloading, ΔL, does not influence the origin position of the mass block; • Preloading in two positions is required.	• Both Eqs. (3.1) and (3.2) have to be satisfied; • Force-displacement curve is asymmetric; • Preloading, ΔL, determines the origin position of the mass block; • Preloading is needed in one position.

3.3 Design guideline of the selected SBCM

As introduced in section 3.2.1, the SCBM proposed consists of a pair of double parallelograms as the positive-stiffness component and a pair of post-buckled clamped-guided beams as the negative-stiffness component, which is shown in Fig. 3.4. All the stiffness components are arranged in the symmetrical manner.
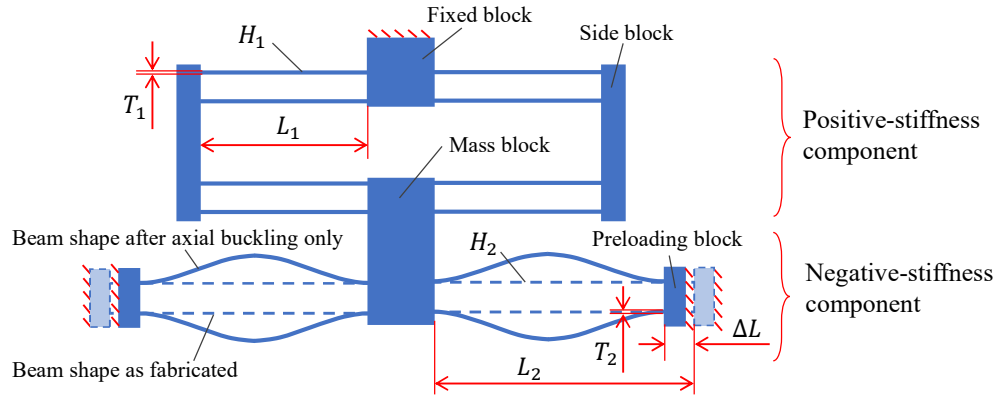
Fig. 3.4. Schematic structure of the SBCM proposed in this work for the PVEH.

The development process of this SBCM is summarized in a form of flow chart as shown in Fig. 3.5, which is used as a design guideline. All parameters and equations in Fig. 3.5 are elaborated in Sections 3.3.1 and 3.3.2. Geometric parameters are preliminarily selected and narrowed down with the quick design equation. The length of the positive-stiffness beams is finely adjusted for static balancing with the trial-and-error method after the prototype is machined and assembled. The influence from the piezoelectric materials has also been considered in the procedure in the cases of developing SBCM-based PVEHs. Therefore, piezoelectric materials are first attached and then the device is tuned for static balancing. The positive- and negative-stiffness components in this design are introduced in the following sub-sections.
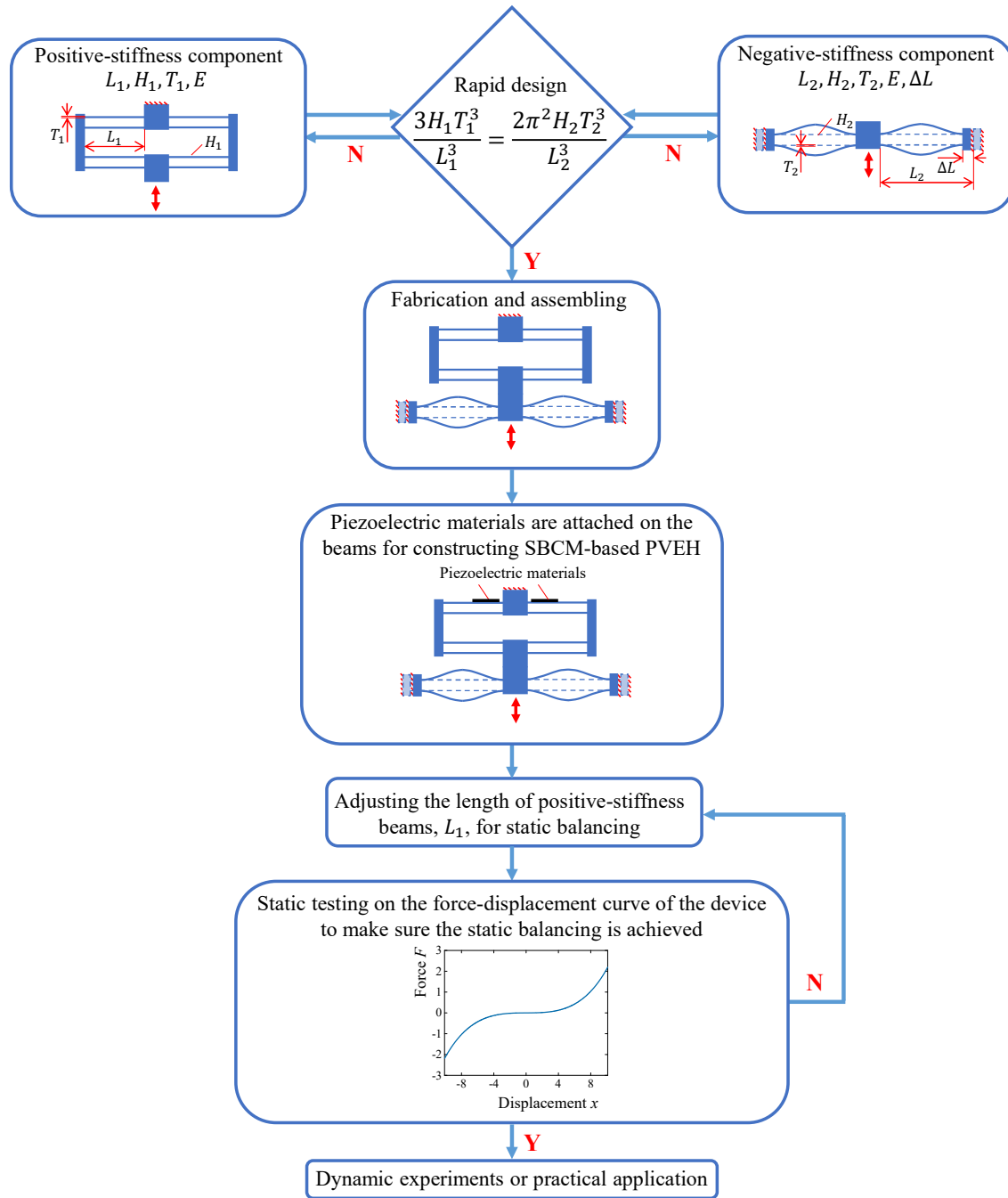
Fig. 3.5. Design guideline of the PVEH based on the SBCM.

3.3.1 Positive-stiffness component

Fig. 3.6(a) illustrates a double parallelogram mechanism with positive stiffness in the analysed displacement range. It has relatively simple structure to design and fabricate. Due to the coupling of four compliant beams, the movable mass can perform a reliable linear motion in the vertical direction in a large displacement range and its parasite motions are eliminated to a large extent [287]. Based on the Euler's equation, Awtar described the force-displacement relationship of such structure with a simplified linear equation [54]:

$$F_1(y_1) = \frac{aEI_1}{L_1^3} y_1 \tag{3.3}$$

where $F_1(y_1)$ is the external force applied on the movable mass block in the vertical direction and y_1 is the corresponding displacement in the same direction. L_1 is the length of the identical compliant beams, and E is the Young's modulus. All compliant beams have identical rectangular cross-sections with the beam (in-plane) thickness, T_1, beam width (out-of-plane thickness), H_1. $I_1 = H_1 T_1^3/12$ is the second moment of area of the compliant beams and a is a constant coefficient that is equal to 12 [54]. It is noteworthy that Eq. (3.3) reflects the linear portion of the force-displacement relationship while the slight stiffness nonlinearity [26, 27] is neglected.
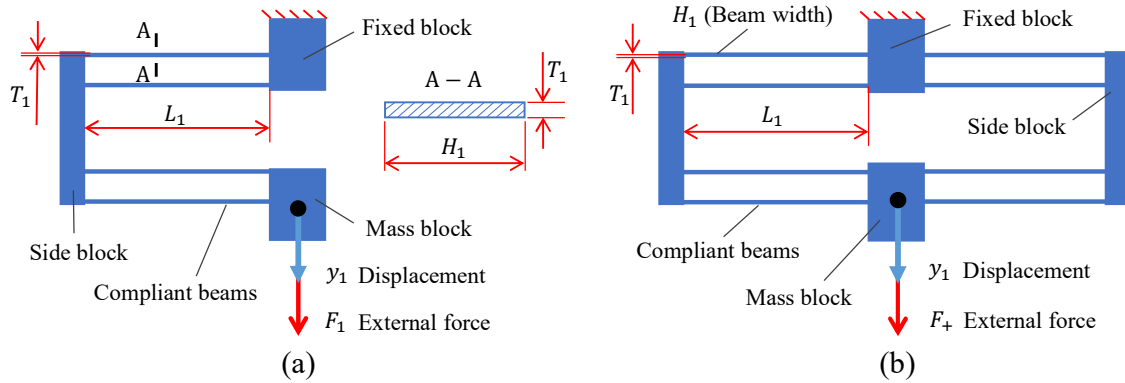
Fig. 3.6. Schematic structures of (a) the double parallelogram mechanism [54] and (b) the positive-stiffness component of the SBCM.

In order to further restrict the parasite motions and enhance the dynamic stability of the structure under vibration, two double parallelograms are connected in parallel acting as the positive-stiffness component in the SBCM proposed, as schematically shown in Fig. 3.6(b). Based on Eq. (3.3), the force-displacement relationship and stiffness of the positive-stiffness component can be easily derived and expressed with Eqs. (3.4) and (3.5).

$$F_+(y_1) = \frac{24EI_1}{L_1^3} y_1 \qquad (3.4)$$

$$k_+ = \frac{24EI_1}{L_1^3} \qquad (3.5)$$

3.3.2 Negative-stiffness component

The post-buckled fixed-guided compliant beams with negative stiffness are schematically illustrated in Fig. 3.7(a) [283, 288]. Both the rotational motion and the horizontal translational motion of the movable mass block are restricted. The negative-stiffness property is achieved through beam buckling with axial preloading of a displacement of Δl. The schematic force-displacement curve of this compliant structure is shown in Fig. 3.7(b). In the overall displacement range, the negative-stiffness compliant structure shows bi-stability with two stable equilibrium positions (marked as points 1 and 5) and one unstable equilibrium position (the origin position marked as point 3). The stiffness is negative in the displacement range between points 2 and 4 and it turns positive beyond this range. $\pm U$ is the limit for the corresponding displacement range with the negative stiffness. In the negative-stiffness range, Frederik [288] described the force-displacement relationship of this post-buckled fixed-guided compliant structure with an approximate closed-form equation (Eq. (3.6)) with the displacement range defined with Eq. (3.7).

$$F_2(y_2) = -\frac{8\pi^2 EI_2}{L_2^3} y_2 \qquad (3.6)$$

$$U = \pm 2L_2 \sqrt{\frac{\Delta L}{3L_2}} \qquad (3.7)$$

where $F_2(y_2)$ is the external force applied on the movable mass block, y_2 is the displacement of the movable mass block in the vertical direction, and L_2 is the length of the beams that have rectangular cross-sections with the (in-plane) thickness of T_2 and the width (out-of-plane thickness) of H_2. The second moment of area of the compliant beams is $I_2 = H_2 T_2^3/12$. It should be noted that the nonlinear contribution of Δl has been neglected in Eq. (3.6) due to its limited influence on the accuracy [288]. In addition, the negative stiffness is independent of the buckling direction of the compliant beams.

In order to better restrict the rotational motion of the movable mass block [286] and increase the structural stability, the final negative-stiffness component integrates two pairs of the post-buckled fixed-guided compliant beams, as shown in Fig. 3.7(c), for constructing the SBCM. Note that the two negative-stiffness beams on the left/right hand side are buckled to opposite directions to avoid interference between the buckled beams. This can be achieved with manual guiding or tiny pre-curvature of the beams in real operation. In this way, the positive-stiffness and negative-stiffness components are interacted with forces in the vertical direction only and undesired internal torques are avoided for a symmetric stress distribution in the SBCM. Based on Eq. (3.6), the force-displacement relationship and the stiffness of the negative-stiffness component can be easily derived:

$$F_-(y_2) = -\frac{16\pi^2 EI_2}{L_2^3} y_2 \tag{3.8}$$

$$k_- = -\frac{16\pi^2 EI_2}{L_2^3} \tag{3.9}$$
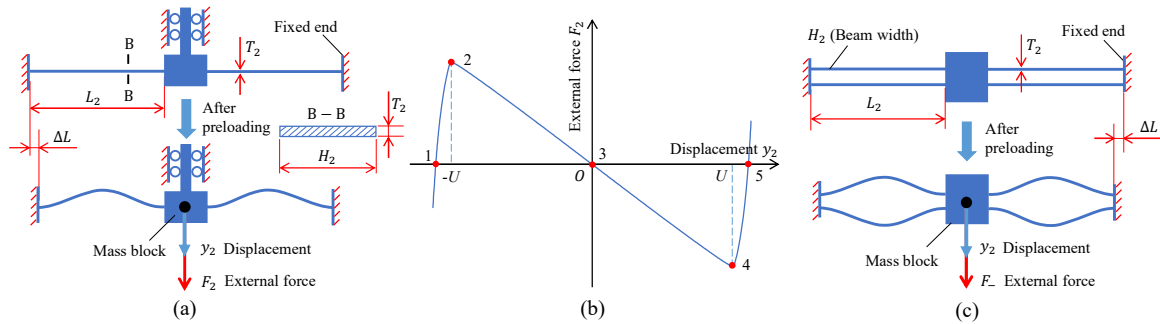
Fig. 3.7. (a) Schematic structure of the post-buckled fixed-guided compliant beams with negative stiffness [288]; (b) Schematic force-displacement curve of the post-buckled fixed-guided compliant beams; (c) Schematic structure of the negative-stiffness component for the SBCM.

3.3.3 Synthesis of the SBCM

In the final SBCM proposed in this work, the positive-stiffness component and the negative-stiffness component are connected together with a common movable mass block, as shown

. As mentioned in Section 3.1, Eqs. (3.1) and (3.2) have to be fulfilled at the same time for achieving static balancing. Since both the positive-stiffness and negative-stiffness components have zero force at the origin position (it is noteworthy that negative-stiffness component is

unstable at this position), Eq. (3.2) will be the only requirement to meet for the structure proposed for static balancing. Eq. (3.10) is obtained when Eqs. (3.5) and (3.8) are substituted into Eq. (3.2).

$$\frac{3H_1T_1^3}{L_1^3} = \frac{2\pi^2 H_2 T_2^3}{L_2^3} \tag{3.10}$$

Eq. (3.10) can be utilized as the guideline for the quick design of the SBCM based on the stiffness compensation principle. This close-form equation helps to narrow down the possible geometric parameters of the stiffness components with different materials and sizes. It should be noted that errors between this quick design and the actual results exist. Further refinement on the geometric parameters using a trial-and-error method is needed to achieve a more accurate static balancing.

3.4 FEA modeling of the SBCM

3.4.1 2D FEA model of the SBCM

In order to verify the static balancing characteristic of the SBCM proposed, A FEA model of the SBCM is first created with the assistance of COMSOL Multiphysics® 5.5. Since the structural features of the SBCM can be fully described in a plane and the design can be achieved with uniform thickness in the direction perpendicular to the plane, the SBCM is created with a 2D model instead of a 3D model for efficient computing with less time and memory consumed in the FEA simulations.

The 2D FEA model of the SBCM in COMSOL is shown in Fig. 3.8. An outer frame is added considering the real fabrication of the prototype in the later research stages. In addition to the geometric parameters presented in Fig. 3.4, the dimensions of the outer frame are preliminary selected and marked in Fig. 3.8. and the geometric parameters of inner structures can be finely adjusted. It should be noted gravity force of the SBCM device is not considered in this 2D FEA model. When the SBCM is arranged horizontally, the gravity force of the mass block does not influence the achievement of static balancing. This is because the gravity force is perpendicular to the functional direction in which static balancing exists. When the SBCM device is arranged vertically, which is the case in our experiments, the gravity force affects our static balancing

design. The mass block is pulled away from its origin and the SBCM is changed into a constant-force CM. However, the gravity force of the mass block can be compensated by a slight lift of the fixed block, which can be regarded as a preloading on the linear positive-stiffness component. This is the method that will be used in the following experiments in Chapter 5 for verification. In FEA simulations, the gravity force is not considered for simplification.

In the FEA model of the SBCM, the four negative-stiffness beams are designed with a pre-curvature with the a radius of 5000 mm, which is much larger than the dimensions of the structure as indicated in Fig. 3.8. Due to the large dimensional difference, it is acceptable to still regard the negative-stiffness beams as straight beams and the inaccuracy introduced by the pre-curvature can be neglected. There are two folds of meaning for this pre-curvature in the FEA simulation. Firstly, for straight beams, the buckling direction is uncertain when it is pressed to buckle. This uncertainty will lead to divergence in FEA simulations. Therefore, a pre-curvature is given at the negative-stiffness beams for convergence in FEA simulations. Secondly, the buckling directions of the negative-stiffness beams on the same side of the device are expected to be in the opposite directions to avoid interference of the beams as mentioned earlier. In FEA simulations, the designed pre-curvatures guide the negative-stiffness beams to buckle in the desired directions.
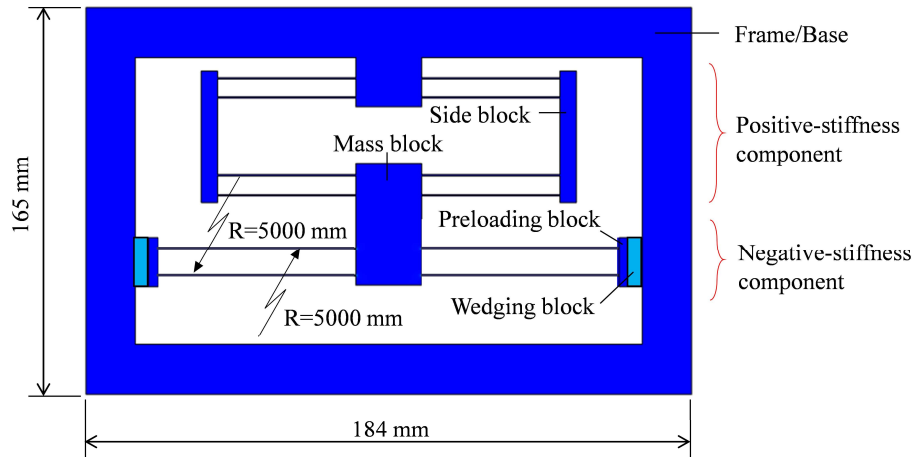
Fig. 3.8. 2D FEA model of the SBCM in COMSOL

3.4.2 Settings for the static FEA simulation

Settings in COMSOL for achieving static balancing with the SBCM structure are summarized and presented in this section as references for the researchers facing the same challenges in this

area. Since basic setting tutorials of COMSOL are widely available, the guidance provided here is mainly focused on this specific simulation issue in this research, i.e. achieving static balancing with the SBCM. In order to obtain the force-displacement curve of the SBCM, there are two stationary steps contained in the simulation study. The first stationary step is preloading on the negative-stiffness beams and the second step is making the movable mass block travel along the targeted displacement range.

In the first step, the negative-stiffness beams are axially preloaded with displacement ΔL to buckle in order to obtain negative stiffness as described in Section 3.3.2, In the FEA simulation, the preloading is achieved by introducing a wedging block between the frame and the preloading on each side of the SBCM as indicated in Fig. 3.8. For a clear illustration on the relative positions of the preloading block, the wedging block and the frame, the preloading part of the SBCM model is shown in a larger scale in Fig. 3.9. In the original condition, the right boundary (boundary 2) of the wedging block and the inner boundary (Boundary 1) of the frame are collinear. The preloading block and the wedging block are overlapped. The distance between the left boundary (Boundary 3) of the wedging block and the right boundary (Boundary 4) of the preloading block is ΔL, which is also the preloading distance applied on the negative-stiffness beams in simulation.
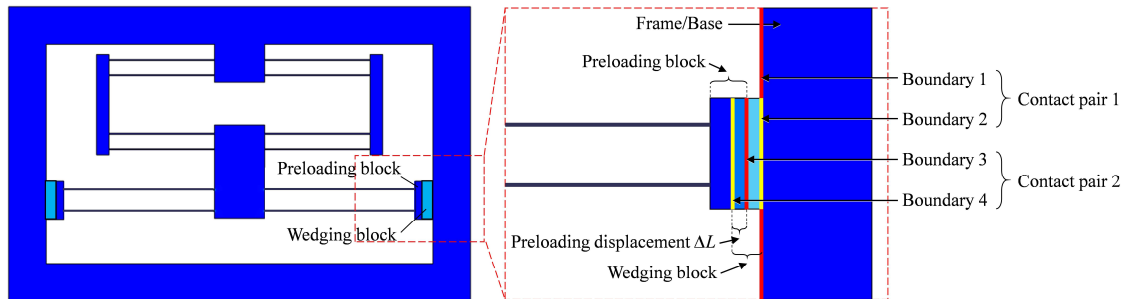
Fig. 3.9. Relative positions of the preloading block, the wedging block and the frame.

In this stationary step, "Contact" and "Adhesion" functions are the core settings to complete preloading. Boundary 1 and Boundary 2 are defined as a Contact pair, while Boundary 3 and Boundary 4 are defined as Contact pair 2. After the stationary step 1 is computed, two boundaries in each Contact pair are adhered to each other. For an easy understanding, the wedging block is wedged between the preloading block and the frame. In this way, the negative-stiffness beams are axially preloaded with a displacement of ΔL. At the same time,

the three parts are stuck together and this will be passed down to the next stationary step. The relative positions of the three parts after preloading are shown in Fig. 3.10.
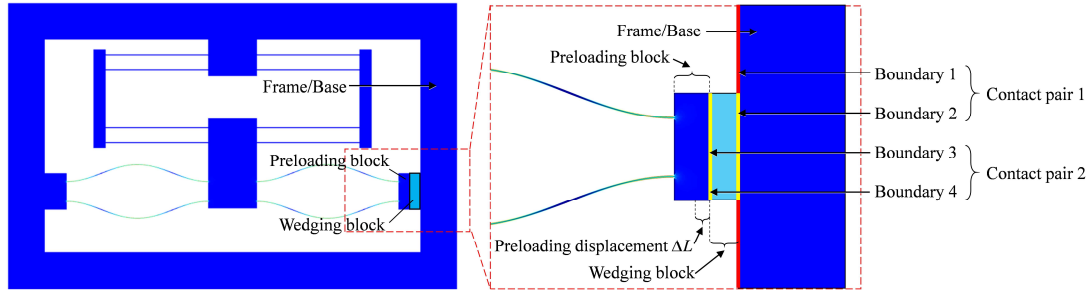
Fig. 3.10. Relative positions of the preloading block, the wedging block and the frame after preloading.

Following the previous step where the negative-stiffness beams are preloaded and buckle, the second stationary step simulates the deformation of the SBCM with the mass block at different positions in the targeted displacement range. The force-displacement relationship of the movable block then can be obtained and plotted. This is mainly achieved by the "Prescribed Displacement" function. Since the SBCM structure is symmetric, the preloading setting introduced above on the left-hand side is the same with that for the right-hand side. Boundaries which will be used in the settings are illustrated in Fig. 3.11.
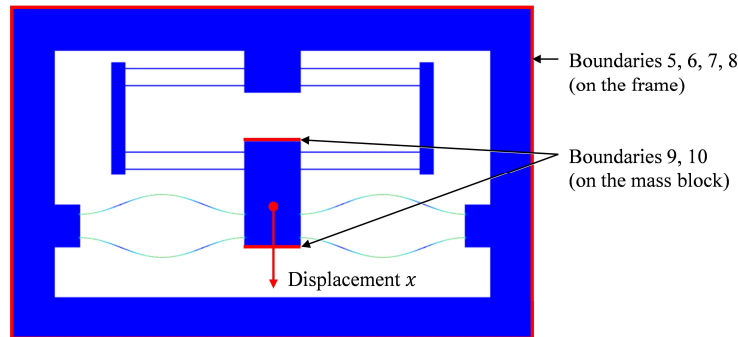
Fig. 3.11. Boundaries of the SBCM in the FEA stationary simulation.

In the FEA model, structural steel is selected as the material of the structure. Its default properties in COMSOL are shown in Table 3.2. Another setting should be noted is plane stress or plane strain approximation, which can be found following the path: "**Solid Mechanics**" → "**Settings**" → "**2D Approximation**" → "**Plane stress**" or "**Plane strain**". Plane strain assumption is utilized in the simulation conditions where all out-of-plane strain components are zero, such as very thick members. Plane stress assumption is more useful when a thin plate

63

is studied. Under this assumption, the material is able to expand or contract in the out-of-plane direction and the transverse stress is zero. The stress analysis is considerably simplified. In this FEA model of the SBCM, the length of the compliant beams is much larger than the thickness. Therefore, plane stress assumption is used in the simulation here. The key settings are introduced in detail in Appendix A. It should be noted that the settings are provided based on COMSOL Multiphysics® and they would be not applicable in other FEA tools.

Table 3.2. Default properties of the Structural Steel in COMSOL.

Material	Density [g/cm³]	Young's Modulus [GPa]	Poisson's Ratio
Structural Steel	7.85	200	0.3

3.4.3 FEA simulation results

Static balancing is achieved in the FEA model of the SBCM structure based on the design guideline as illustrated shown in Fig. 3.5 and using the settings introduced in Section 3.4.2. L_1 is the only geometric parameter to adjust for static balancing when other geometric parameters are selected. This is the same with the procedure in real operation when the prototype is fabricated. The geometric parameters of the SBCM structure in its static-balancing mode are listed in Table 3.3.

Table 3.3. Geometric parameters of the SBCM with static balancing achieved based on FEA simulations.

Positive-stiffness component		Negative-stiffness component	
Length L_1	42 mm	Length L_2	60 mm
Thickness out of plane H_1	15 mm	Thickness out of plane H_2	15 mm
Thickness in plane T_1	0.4 mm	Thickness in plane T_2	0.3 mm
——	——	Preloading ΔL	2 mm

It should be noted that the negative stiffness is valid in a certain displacement range defined by $\pm U$ and the stiffness nonlinearity gets more obvious around the joint points (points 2 and 4 as indicated in Fig. 3.7(b)) between the positive-stiffness and negative-stiffness ranges. Therefore, the displacement range of static balancing is determined by the displacement range of negative stiffness. $\pm 90\% U$ is focused in the following analysis in order to avoid severe stiffness nonlinearity. According to the geometric parameters $L_2 = 60$ mm and $\Delta L = 2$ mm, the

corresponding force-displacement curve in the displacement range from −11.4 mm to 11.4 mm is shown in Fig. 3.12(a). Since it is impractical to get a perfect force-displacement cure with absolute zero force and zero stiffness in the displacement range, the absolute force value smaller than 0.025 N is regarded static balancing in this work. This force value (0.025 N) is determined according to the absolute force limit obtained in the displacement range where the SBCM can stay equilibrium in experiments in Chapter 5. Fig. 3.12(a) shows that the zero-force displacement range is about 4.8 mm (from −2.4 mm to 2.4 mm). The stiffness-displacement curve can also be obtained as the first derivation of the force-displacement curve and it is shown in Fig. 3.12(b).

(a)

(b)
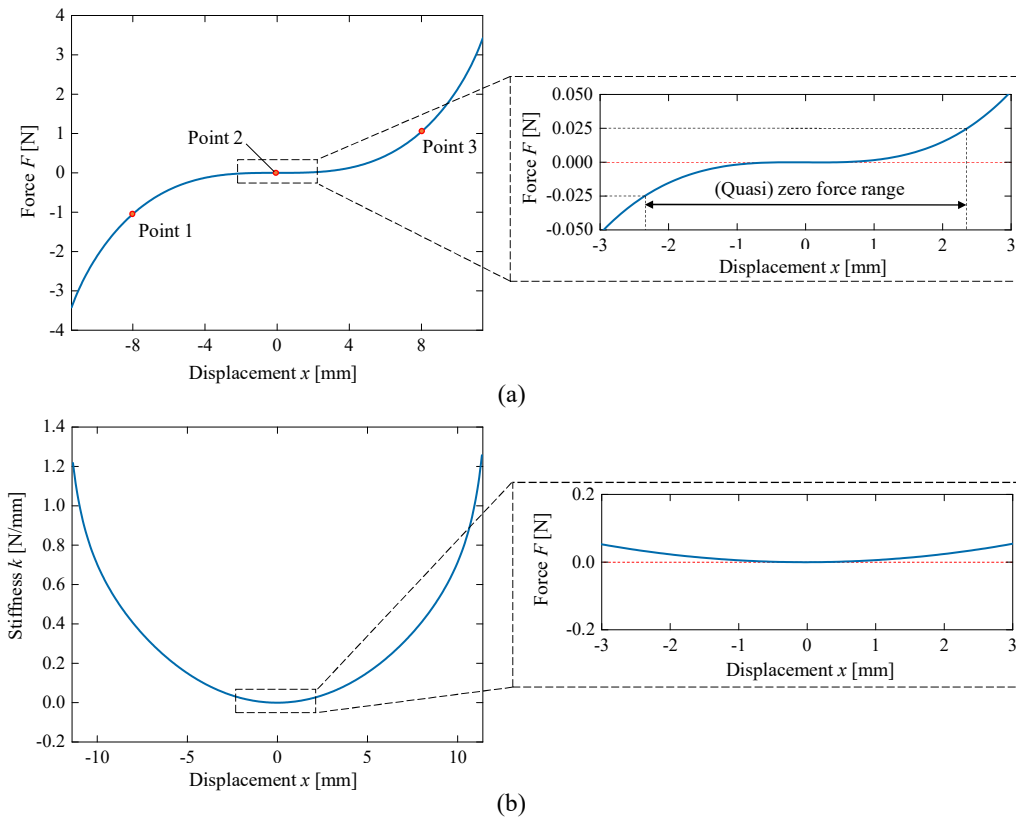
Fig. 3.12. (a) Force-displacement curve and (b) stiffness-displacement curve of the SBCM structure in its static-balancing mode obtained in FEA simulations.

In the static simulation on the SBCM, the deformation of the compliant beams can also be observed in this displacement range. Fig. 3.13 gives three deformation examples of the compliant beams of the SBCM corresponding to the three displacement points marked in Fig. 3.12(a). It should be noted that the interference between the base and side-blocks in Fig. 3.13(a)

does not influence of the simulation results, because no contact properties between these domains are defined in simulations.

The force-displacement relationship of this SBCM can be described by fitting to a polynomial equation. Since the force-displacement curve is symmetric about the origin point, only odd-order terms exist in the static equation (in principle) and the even-order terms are therefore neglected. Utilizing the Polyfit function in MATLAB®, the force-displacement curve of this SBCM structure in its static-balancing mode can be described with a 5th order polynomial as Eq. (3.11). The R^2 coefficient of determination is 99.99%, indicating an accurate fit of this polynomial model to the force-displacement curve obtained from FEA simulations. The force-displacement curve and the fitted polynomial curve are presented and compared in Fig. 3.14.

$$F_{\text{SBCM}}(x) = 0.002194x + 0.001774x^3 + 0.000003362x^5 \tag{3.11}$$

(a) (b) (c)
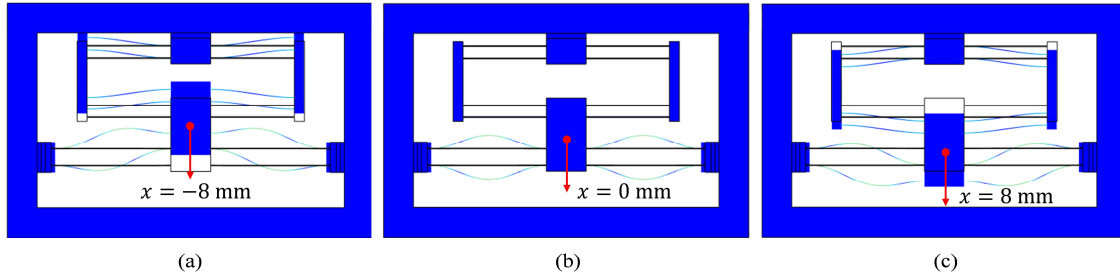
Fig. 3.13. Deformation conditions of the SBCB with displacement of (a) $x = -8$ mm (point 1 in Fig. 3.12(a)), (b) $x = 0$ mm (point 2 in Fig. 3.12 (a)), and (c) $x = 8$ mm (point 3 in Fig. 3.12(a)) in FEA simulations.
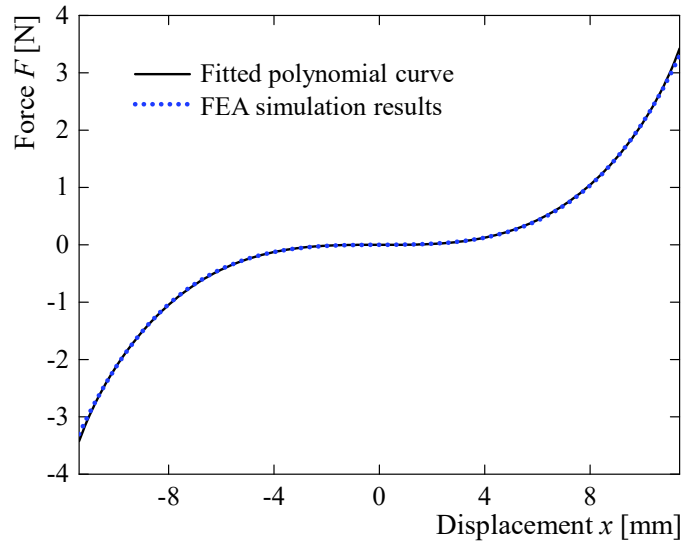
Fig. 3.14. The force-displacement curve of the SBCM in its static-balancing mode and the fitted polynomial curve.

The cubic and quintic terms in Eq. (3.11) reflect the stiffness nonlinearity of the SBCM structure. This stiffness nonlinearity can be caused by the load-dependent effect and large deflection of the compliant beams [45, 46]. The stiffness nonlinearity is critical for the desired dynamic performance of the SBCM structure. Zero stiffness around the origin brings the effective frequency of the device to the ultra-low range. The stiffness nonlinearity broadens the frequency bandwidth by the stiffness hardening effect. Based on this polynomial equation obtained, the dynamic performance of the SBCM structure under harmonic based excitations can be analyzed targeting on the applications in vibrational energy harvesting.

3.5 Force-displacement characteristics of the SBCM

In the FEA simulations, static balancing is achieved with well-adjusted geometric parameters. The change of the geometric parameters will lead to different force-displacement characteristics of the SBCM structure. In this section, the influence from the length of the positive-stiffness beams, L_1, and the preloading displacement, ΔL, on the force-displacement relationship of the SBCM is further investigated based on FEA simulations.

3.5.1 Bi-stability and mono-stability of the SBCM

Static balancing is achieved when the stiffness of the positive-stiffness component is compensated by the stiffness provided by the negative-stiffness component. The un-balanced stiffness of the two stiffness components will lead to either bi-stability or mono-stability. These two force-displacement characteristics can be obtained by adjusting the length of the positive-stiffness beams, L_1, while other geometric parameters in Table 3.3 are unchanged. The force-displacement and stiffness-displacement curves of several examples of the bi-stability and mono-stability corresponding to different L_1 are presented in Fig. 3.15 based on the static FEA simulations. The targeted displacement range is from -11.4 mm to 11.4 mm (which is $\pm 90\%$U corresponding to $\Delta L = 2$ mm).
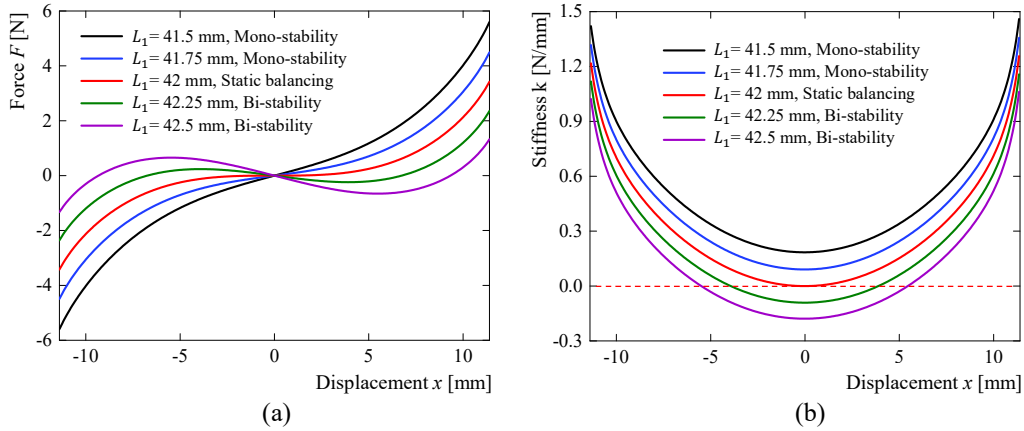
Fig. 3.15. (a) Force-displacement curves and (b) stiffness-displacement curves of the SBCM with different length of the positive-stiffness beams. (Coloured curves)

When L_1 is smaller than 42 mm (e.g. 41.5 mm or 41.75 mm), the stiffness of the positive-stiffness component is larger than the value required to balance the negative stiffness and the SBCM structure shows mono-stability. The black and blue curves in Fig. 3.15(a) are the force-displacement curves of the mono-stable modes. It is shown in Fig. 3.15(b) that the stiffness-displacement curves of the mono-stable modes are above zero line in the whole displacement range and stiffness nonlinearity can be easily observed. When L_1 is larger than 42 mm (e.g. 42.25 mm or 42.5 mm), the stiffness of the positive-stiffness component is smaller than the value needed to compensate the negative stiffness. Bi-stability is then obtained in the whole system level. The purple and green curves in Fig. 3.15(a) indicate the force-displacement relationship of the bi-stable modes. The corresponding stiffness-displacement curves of the SBCM in the bi-stable modes are indicated in same colours in Fig. 3.15(b). In the limited displacement ranges around the origin, the stiffness curves are lower than the zero line. In addition, the stiffness nonlinearity is also obvious in the whole displacement range.

This special feature of the SBCM structure provides an effective method to achieve various force-displacement characteristics with the same device for different applications. In this research, the focus is on the static-balancing mode. A simple comparison with the nonlinear mono-stable mode is performed, whereas the bi-stability is not discussed in this work. However, this SBCM structure can be a new option for the construction of bi-stable energy harvesters. The force-displacement polynomials of the two nonlinear mono-stable modes are obtained by Polyfit function in MATLAB®. Eq.(3.12) describes the mono-stable force-displacement

relationship corresponding to L_1 of 41.75 mm. Eq.(3.13) is the mono-stable force-displacement when L_1 equals to 41.5 mm.

$$F_{\text{SBCM}}(x) = 0.09386x + 0.001795x^3 + 0.000003368x^5 \tag{3.12}$$

$$F_{\text{SBCM}}(x) = 0.1877x + 0.001818x^3 + 0.000003376x^5 \tag{3.13}$$

3.5.2 Static-balancing with different preloading displacements

Base on the linear assumption in Eqs. (3.6) and (3.7) of the fixed-guided post-buckled beams, the axial displacement preloading, ΔL, determines the displacement rang with negative stiffness. The stiffness nonlinearity related to this parameter is not described in the equations. Following this approximation, design of the wider displacement ranges with static balancing starts from the adjustment of ΔL. This concept is investigated based on the FEA simulations with different displacement preloading of 2 mm, 1.5 mm and 1 mm, respectively. Due to the inherent influence of ΔL on the negative stiffness, static balancing is broken when ΔL is changed. The length of the positive-stiffness beams, L_1, is then finely adjusted for static balancing corresponding to each ΔL and the results are presented in Table 3.4. Other geometric parameters of the SBCM structure remain unchanged.

Table 3.4. Displacement preloading, ΔL, on the negative-stiffness beams and length of the positive-stiffness beams, L_1, for static balancing.

Displacement preloading, ΔL [mm]	Length of the positive-stiffness beams, L_1 [mm]
2	42.0
1.5	42.2
1	42.4

The force-displacement and stiffness-displacement curves of the static-balancing modes with different ΔL are obtained from FEA simulations and they are presented in Fig. 3.16. Note that displacement ranges of $\pm 90\% U$, i.e. ± 11.4 mm, ± 9.9 mm and ± 8 mm, are focused in the FEA simulations corresponding to ΔL of 2 mm, 1.5 mm and 1 mm, respectively. This is because the stiffness nonlinearity of the SBCM significantly increases beyond the targeted displacement ranges. The fitted polynomial with degree of 5 cannot fully describe the nonlinear force-displacement relationship, with zero force around the origin in particular, with desired

accuracy. This then would cause inaccuracy in the analytical modelling of the dynamic performance of the SBCM in the following study.
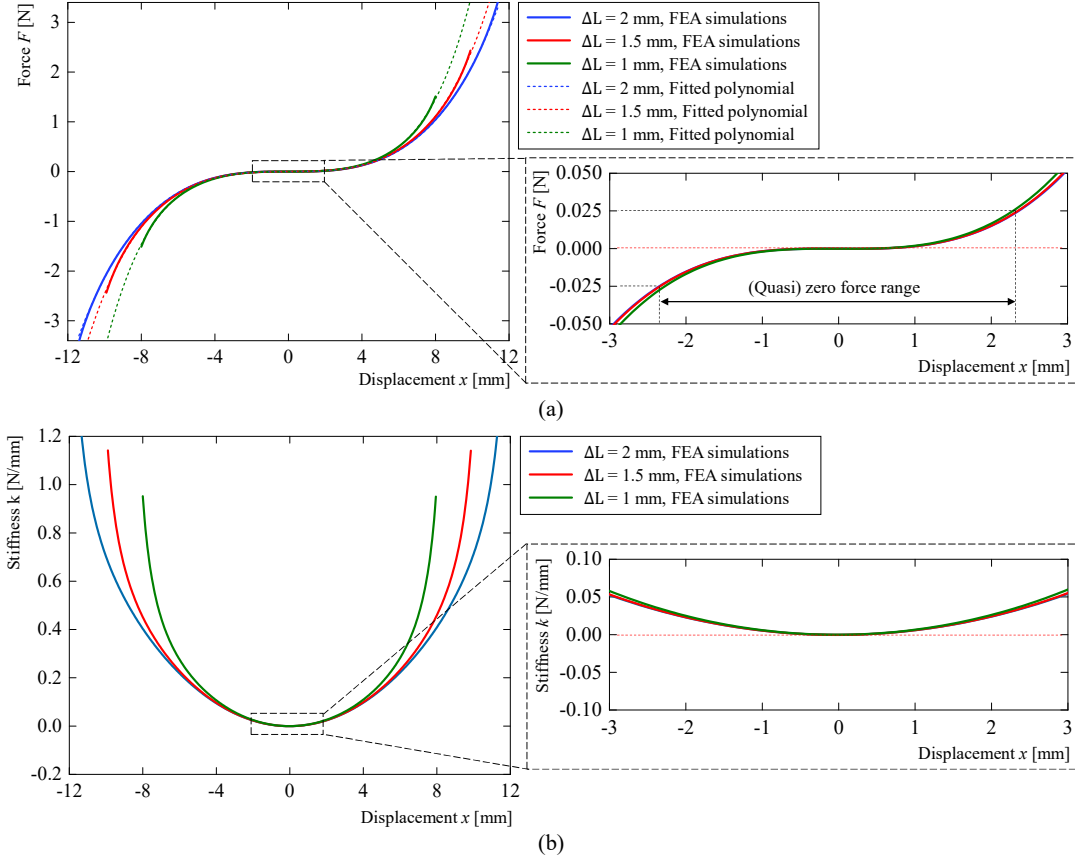
Fig. 3.16. (a) Force-displacement curves and (b) stiffness-displacement curves of the SBCM with ΔL equals to 2 mm, 1.5 mm and 1 mm, respectively, in FEA simulations. (Coloured curves)

The fit 5th order polynomials of the force-displacement curves corresponding to ΔL=1.5 mm and 1 mm are obtained using the Polyfit function in MATLAB® and they are given as Eqs. (3.14) and (3.15). The R^2 coefficients of these two polynomials are 99.98% and 99.96 %, respectively, indicating a reliable fitting accuracy. The force-displacement curves generated based on the polynomials are also plotted in Fig. 3.16(a) for direct comparison. It is shown in Fig. 3.16(a) that all three force-displacement curves have achieved zero force around the origin and the corresponding displacement ranges are almost the same ($\pm$ 2.4 mm). In the wider scale, it is observed that the displacement range corresponding to the same force gradually shrinks when ΔL decreases. It is shown in Fig. 3.16(b) that zero stiffness is achieved around the origin for the three cases. Both requirements of zero force and zero stiffness have been satisfied and

static balancing of the SBCM structure are confirmed with the three different displacement preloading values.

$$F_{SBCM}(x) = 0.006131x + 0.001518x^3 + 0.000008763x^5 \qquad (3.14)$$

$$F_{SBCM}(x) = 0.006428x + 0.001364x^3 + 0.00002171x^5 \qquad (3.15)$$

3.5.3 Stress analysis of the compliant beams

The maximum stress along the compliant beams in the SBCM structure has to be considered to avoid failure of the device in real applications. The extreme values of the internal bending moment occur at the clamping points and halfway of the positive-stiffness beams and post-buckled negative-stiffness beams [288, 289]. The maximum stress on the positive- and negatives-stiffness beams, $|\sigma_1|_{max}$ and $|\sigma_2|_{max}$, can be estimated based on the equations below [55, 288, 289] according to the previous research in the related field:

$$|\sigma_1|_{max} = \frac{3}{2}ET_1\frac{x}{L_1{}^2} \qquad (3.16)$$

$$|\sigma_2|_{max} = 2\pi E\frac{T_2}{L_2}\sqrt{\frac{\Delta l}{L_2}} \qquad (3.17)$$

where x is relative displacement between the movable end and the frame of the positive-stiffness component. It should be noted that the actual maximum stress also depends on the stress concentration in the clamping ends which is not reflected in the stress equations.

The maximum stress along the compliant beams in the SBCM is also analyzed based on the FEA simulations using COMSOL Multiphysics®. Taking the static-balancing mode with $L_1 = 42$ mm and $\Delta L = 2$ mm as an example, the maximum stress along the positive-stiffness beams ($|\sigma_1|_{max}$) and negative-stiffness beams ($|\sigma_2|_{max}$) in the displacement range of ± 11.4 mm from FEA simulations are presented in Fig. 3.17. Structural steel with Young's modulus $E = 200$ GPa and Poisson's ratio μ=0.3 is selected as the material for the compliant beams in the FEA simulations. $|\sigma_2|_{max}$ reaches the maximum value of about 1.07 GPa at the origin position in the targeted displacement range. It gradually decreases to 0.72 GPa when the displacement increases to 11.4 mm in both directions.
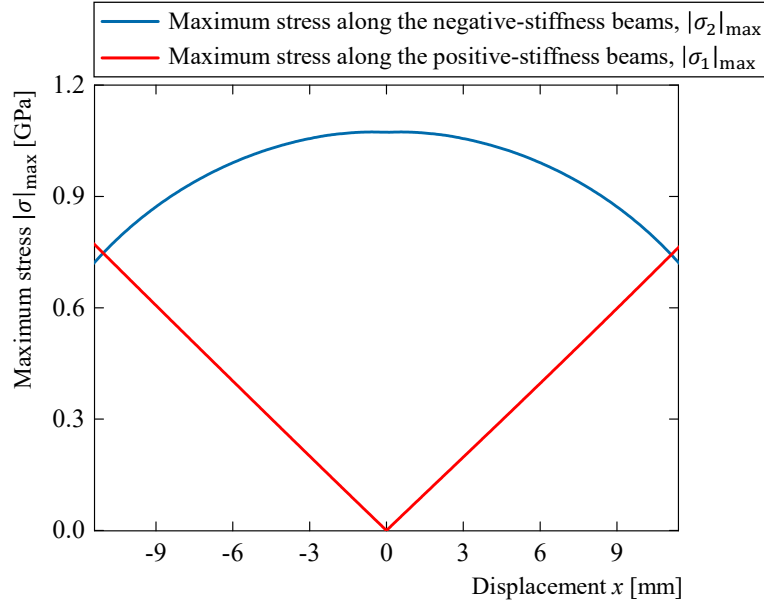
Fig. 3.17. Maximum stress along the positive- and negative-stiffness beams in the displacement range of ± 11.4mm based on FEA simulations. (Coloured curves)

By contrast, $|\sigma_1|_{\max}$ is zero at the origin position and it increases along with the displacement, x, in both directions. $|\sigma_1|_{\max}$ reaches the maximum value of 0.77 GPa at the displacement position of 11.4 mm. The FEA simulation results are confirmed by the analytical results based on Eqs. (3.16) and (3.17) which are 0.78 MPa and 1.08 MPa, respectively. Due to the changing tendency of $|\sigma_1|_{\max}$ and $|\sigma_2|_{\max}$ in the displacement range as shown in Fig. 3.17, $|\sigma_1|_{\max}$ at the displacement limit position and $|\sigma_2|_{\max}$ at the origin position are used for the assessment on the extreme stress conditions of the SBCM structure. Geometric parameters and displacement preloading should be adjusted for a reasonable stress distribution by comparing with the allowable stress strength of the structural materials selected.

3.6 Summary

In this Chapter, the general design principle for SBCMs based on the stiffness compensation between the positive- and negative-stiffness components is presented. An SBCM is proposed and selected from two conceptual SBCM structures for the following study targeting on the application in vibrational energy harvesting. The positive-stiffness component is embodied using a pair of double parallelograms connected in parallel, and the negative-stiffness component is composed of two pairs of post-buckled fixed-guide compliant beams arranged in bi-symmetry. The design guideline of this SBCM based on a quick-design stiffness

compensation closed-form equation is provided. It can guide the design of the SBCM in different sizes and materials.

An FEA model of the SBCM is created in COMSOL Multiphysics®. The essential settings for preloading on the negative-stiffness beams and plotting force-displacement curves in the FEA simulations are introduced as tutorials for researchers facing similar problems. The static balancing is perfectly achieved by finely tuning the geometric parameters in the FEA model. The static-balancing force-displacement relationship is fitted and described with a 5th order polynomial by the Polyfit function in MATLAB®. This fit 5th order polynomial will be utilized in the following dynamic modelling and analysis of this thesis. In addition, both bi-stability and mono-stability are obtained by adjusting the length of the positive-stiffness beams in this FEA model. Static-balancing modes with different force-displacement curves are also simulated by tuning the preloading displacement applied on the negative-stiffness beams.

Chapter 4 Dynamic Modelling and Analysis on the SBCM

The SBCM structure is stimulated to vibrate under environmental excitations in the application of vibrational energy harvesting. Therefore, an accurate description on the dynamic displacement response of the SBCM is critical for the design of SBCM-based vibrational energy harvesters. The dynamic characteristics of the SBCM under harmonic base excitation is analytically modelled in this Chapter. It is based on the static analysis, the fitted 5th order polynomial in particular, of the SBCM in Chapter 3. Analysis methods in this chapter include analytical modelling based on the average method, numerical analysis based on ODE45 Runge-Kutta method in MATLAB® and FEA simulations using COMSOL Multiphysics®. The dynamic displacement response of the SBCM under harmonic base excitations are obtained and assessed.

4.1 Dynamic modelling of the SBCM under harmonic base excitations

Based on the static-balancing force-displacement relationship obtained in the previous chapter, the dynamic performance of the SBCM structure is modelled and analysed in this section. In the application of vibrational energy harvesting, the environmental vibrations are imported into the harvester by the frames/bases. Therefore, the dynamic displacement response of the SBCM under harmonic base excitations is studied. The simplified mechanical analysis model of the SBCM system is illustrated in Fig. 4.1. z is the harmonic displacement of the base and x represents the relative displacement between the base and the mass. The relative displacement, x, directly influences the energy harvesting performance of the device combined with different energy-conversion mechanisms.

Based on the theoretical analysis and FEA simulations in Chapter 3, a 5th order polynomial provides sufficient accuracy to describe the nonlinear force-displacement relationship of the

SBCM structure in this research. In general, the 5th order polynomial of the force-displacement relationship of the SBCM can be written as:

$$F_{SBCM}(x) = \alpha x + \beta x^3 + \gamma x^5 \tag{4.1}$$

where α, β and γ are the coefficients of the odd-order terms, respectively. Under the sinusoidal base excitation, the motion equation of the SBCM can be described as:

$$-m\ddot{z} = m\ddot{x} + c\dot{x} + F_{SBCM}(x) = m\ddot{x} + c\dot{x} + \alpha x + \beta x^3 + \gamma x^5 \tag{4.2}$$

where m is effective mass of the SBCM, c is the equivalent viscous damping constant of the vibrational system. x represents the steady-state relative displacement between the mass block and the outer frame (i.e., base). $\ddot{z}$ is the base excitation acceleration and is assumed to be harmonic as $\ddot{z} = a_0\cos(\omega t)$. The damping of the SBCM structure is generated from various sources, such as air resistance, materials hysteresis, and looseness in clamping parts (when the SBCM device is fabricated in the assembling form). The damping in this system is simply regarded as a linear viscous damping, because this research is focused on the nonlinear stiffness feature of the SBCM structure. This simplification brings efficiency and convenience to the dynamic analytical modelling of the SBCM device [184].

Note that in the dynamic model the contribution from both the distributed mass of the compliant beams and the mass of two side blocks is usually much smaller than that of the moving mass block in the middle, and is therefore neglected in this model for simplification. The motion equation is thus written as:

$$-ma_0\cos(\omega t) = m\ddot{x} + c\dot{x} + \alpha x + \beta x^3 + \gamma x^5 \tag{4.3}$$
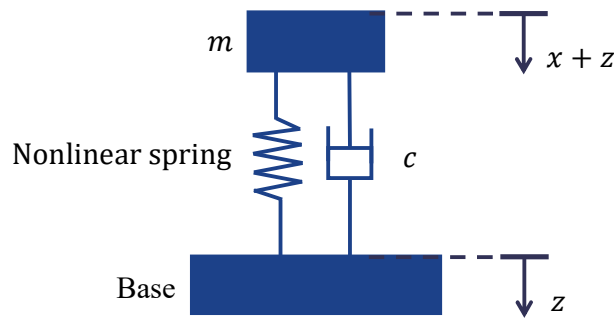
Fig. 4.1. Schematic diagram of the SBCM under base excitation.

To facilitate analysis, Eq. (4.3) can be normalized as:

$$-A_0\cos(\Omega t) = \ddot{X} + 2\zeta\dot{X} + k_1 X + k_2 X^3 + k_3 X^5 \tag{4.4}$$

In Eq. (4.4), these normalized constants and variables are elaborated as follows:

$$\Omega_n = \sqrt{\frac{k_+}{m}}, \qquad A_0 = \frac{a_0}{\Omega_n^2 L_1}, \qquad \Omega = \frac{\omega}{\Omega_n}, \qquad X = \frac{x}{L_1}, \qquad \zeta = \frac{c}{2\sqrt{mk_+}}, \qquad \tau = \Omega_n t,$$

$$k_1 = \frac{\alpha}{k_+}, \qquad k_2 = \frac{\beta L_1^2}{k_+}, \qquad k_3 = \frac{\gamma L_1^4}{k_+}$$

where Ω_n is the resonant frequency of the equivalent linear oscillator; A_0 is the normalized excitation acceleration amplitude; Ω is the normalized excitation frequency; X is the normalized relative displacement; ζ is the damping ratio; τ is the normalized time; k_1, k_2 and k_3 are normalized stiffness coefficients of the odd-order terms, respectively; and k_+ is the positive stiffness defined in Section 3.3.1.

4.1.1 Derivation of the dynamic displacement response modeling

The averaging method is one of the classical methods in analyzing nonlinear oscillations modelled with differential equations [290, 291]. The basic idea of the averaging method is to approximate the original system by the averaged system for an easier study. The dynamic properties of the original system can be inferred by the understanding of the dynamics of the averaged system [290]. The dynamic analysis on the SBCM structure under harmonic base excitation is carried out with the averaging method [292]. The displacement response and velocity response can be assumed as:

$$x(\tau) = H\cos(\Omega\tau + \varphi) \tag{4.5}$$

$$x'(\tau) = -\Omega H\sin(\Omega\tau + \varphi) \tag{4.6}$$

where the amplitude, H, and the phase, φ, of the displacement response, $x(t)$, change slowly and can be considered as functions of the normalized time, τ. Eqs. (4.7) and (4.8) are obtained through differentiating Eqs. (4.5) and (4.6) with respect to time, τ.

$$x'(\tau) = H'\cos(\Omega\tau + \varphi) - \varphi'H\sin(\Omega\tau + \varphi) - H\Omega\sin(\Omega\tau + \varphi) \tag{4.7}$$

$$x''(\tau) = \Omega H'\sin(\Omega\tau + \varphi) - \varphi'\Omega\cos(\Omega\tau + \varphi) - H\Omega^2\cos(\Omega\tau + \varphi) \tag{4.8}$$

Eqs. (4.6) and (4.7) describe the velocity response and therefore Eq. (4.9) can be obtained.

$$H'\cos(\Omega\tau + \varphi) - \varphi'H\sin(\Omega\tau + \varphi) = 0 \tag{4.9}$$

The Substitution of Eqs. (4.5), (4.6) and (4.8) into the Eq. (4.4) yields:

$$H' \sin(\Omega\tau + \varphi) + \varphi'H \cos(\Omega\tau + \varphi) = \Gamma(H, \Omega, \varphi) \tag{4.10}$$

where

$$\Gamma(H, \Omega, \varphi) = -\frac{1}{\Omega}[H\Omega^2 \cos\Phi + 2\zeta\Omega H \sin\Phi - k_1 H \cos\Phi - k_2 H^3 \cos^3\Phi \\ - k_3 H^5 \cos^5\Phi - A_0 \cos(\Phi - \varphi)] \tag{4.11a}$$

$$\Phi(\Omega, \varphi) = \Omega t + \varphi \tag{4.11a}$$

The combination of Eqs. (4.9) and (4.10) leads to:

$$H' = \Gamma(H, \Omega, \varphi)\sin\Phi(\Omega, \varphi) \tag{4.12a}$$

$$\varphi' = \frac{\Gamma(H, \Omega, \varphi)\cos\Phi(\Omega, \varphi)}{H} \tag{4.12b}$$

Because both H and φ change very slowly, it is acceptable that H' and φ' equal to their average values, respectively, over a vibration period.

$$H' = \frac{\Omega}{2\pi}\int_{\tau}^{\tau + \frac{2\pi}{\Omega}} \Gamma(H, \Omega, \varphi)\sin\Phi(\Omega, \varphi)d\tau = \frac{1}{2\pi}\int_{0}^{2\pi} \Gamma(H, \Omega, \varphi)\sin\Phi d\Phi \\ = \frac{A_0}{2\Omega}\sin\varphi - \zeta H \tag{4.13a}$$

$$\varphi' = \frac{\Omega}{2\pi}\int_{\tau}^{\tau + \frac{2\pi}{\Omega}} \frac{\Gamma(H, \Omega, \varphi)\cos\Phi(\Omega, \varphi)}{H}d\tau = \frac{1}{2\pi H}\int_{0}^{2\pi} \Gamma(H, \Omega, \varphi)\cos\Phi d\Phi \\ = -\frac{\Omega}{2} + \frac{k_1}{2\Omega} + \frac{3k_2 H^2}{8\Omega} + \frac{5k_3 H^4}{16\Omega} + \frac{A_0 \cos\varphi}{2\Omega H} \tag{4.13b}$$

At the steady state, $H' = 0$ and $\varphi' = 0$, which brings:

$$\frac{A_0}{2\Omega}\sin\varphi = \zeta H \tag{4.14a}$$

$$\frac{A_0}{2\Omega H}\cos\varphi = \frac{\Omega}{2} - \frac{k_1}{2\Omega} - \frac{3k_2 H^2}{8\Omega} - \frac{5k_3 H^4}{16\Omega} \tag{4.14b}$$

The variable φ can be eliminated through adding the squares of Eqs. (4.14a) and (4.14b), and the relationship between H and Ω is obtained as below:

$$A_0{}^2 = H^2 \left[k_1{}^2 + 4(\zeta^2 - 2k_1)\Omega^2 + \Omega^4 + \frac{3}{2}k_2(k_1 - \Omega^2)H^2 + (\frac{5}{4}k_1k_3 + \frac{9}{16}k_2{}^2 \right.$$
$$\left. - \frac{5}{4}k_3\Omega^2)H^4 + \frac{15}{16}k_2k_3H^6 + \frac{25}{64}k_3{}^2H^8 \right] \tag{4.15}$$

4.1.2 Demonstration with examples

For the most simplistic analysis (i.e., $k_1 = k_2 = k_3 = 0.1$), the normalized force-displacement relationship can be represented in Fig. 4.2(a). As introduced in Section 2.3, ultra-low stiffness exists around the origin equilibrium position and stiffness nonlinearity is evidenced in the wider displacement range. Based on Eq. (4.15), the steady-state relative displacement amplitude, H, with respect to excitation frequencies, Ω, can be represented in Fig. 4.2(b). Different excitation accelerations ($A_0 = 0.1, 0.2, 0.3, 0.4, 0.5$) and a damping ratio ζ of 0.1 are assumed. It is noteworthy that this damping ratio of 0.1 is an arbitrary value. It is used in the dimensionless analysis for a demonstration purpose only. Because of the near-zero stiffness at the origin position, the device is sensitive to ultra-low excitations with low accelerations. The H-Ω curves bend towards the right side, which provides a wider frequency bandwidth. This is due to the stiffness hardening effect as a result of stiffness nonlinearity.
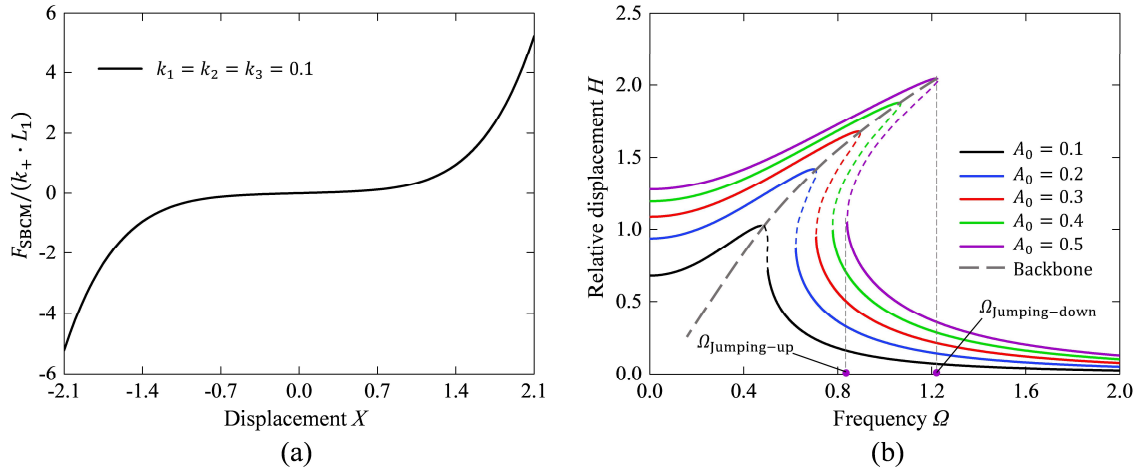
Fig. 4.2. (a) Normalized force-displacement curve of the SBCM and corresponding (b) Steady-state relative displacement amplitude - frequency curves for different accelerations ($\zeta = 0.1$). (Coloured curves)

In a certain frequency range, three relative displacement amplitudes exist corresponding to one single excitation frequency. The oscillations with largest and smallest amplitudes are stable and they are indicated with solid curves. The oscillation with intermediate amplitude is unstable

and it is indicated with dashed curves. This effective frequency bandwidth is determined by the jumping-up frequency, $\Omega_{\text{Jumping-up}}$ (left side limit) and the jumping-down frequency, $\Omega_{\text{Jumping-do}}$ (right side limit), which is indicated in Fig. 4.2(b). It can also be noticed that the relative displacement amplitude and the jumping-up/down frequencies increase along with the acceleration level of the excitation. By connecting the peak points of all the bended H-Ω curves, the backbone of this device with given coefficients is obtained and illustrated with dashed line in Fig. 4.2(b).

A comparison between the analytical results and the numerical results using the ODE23 and ODE45 Runge-Kutta methods in MATLAB® (by solving Eq. (4.4), representing it in the state space form) is presented in Fig. 4.3. The results of the ODE23 and ODE45 Runge-Kutta methods are perfectly matched. A close agreement with an average error percentage of 2.7% between the analytical results and numerical results is observed. A small amplitude jump at $\Omega \approx 0.3$ is noticed from the numerical results causing the largest difference of 0.21 compared with the analytical results. The presence of this phenomenon is confirmed by both ODE23 and ODE45 Runge-Kutta methods. It is likely caused by the super-harmonic oscillation as described in [293]. However, this phenomenon cannot be predicted with an analytical model.
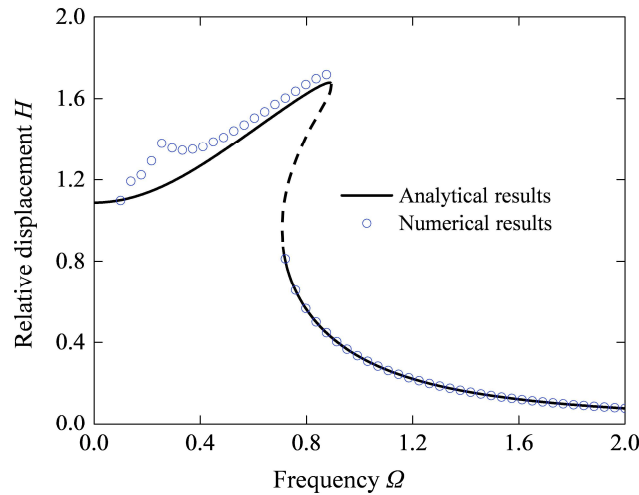
Fig. 4.3. Comparison of the steady-state relative displacement amplitude-frequency results from the analytical solution and the numerical results using the ODE23 and ODE45 Runge-Kutta methods ($A_0 = 0.3, \zeta = 0.1$).

Force-displacement curves are defined by the stiffness coefficients, k_1, k_2 and k_3. When these stiffness coefficients change, different dynamic response corresponding to different force-displacement curves is expected under the same excitation condition. The normalized force-

displacement curves with different coefficients are shown in Fig. 4.4(a) and their corresponding steady-state relative displacement amplitude-excitation frequency curves are illustrated in Fig. 4.4(b) based on Eq. (4.15). In Fig. 4.4, the acceleration, A_0, and the damping ratio, ζ, are assumed to be 0.3 and 0.1, respectively. When the stiffness around the origin position increases due to the changed stiffness coefficients, the static balancing gradually vanishes as observed in Fig. 4.4(a). It is shown that the maximum amplitude decreases while the jumping-down frequency increases in the corresponding dynamic response curves in Fig. 4.4(b). As shown in Fig. 3.15, the tuning of the stiffness characteristic can be achieved by adjusting the length of the positive-stiffness beams, L_1.
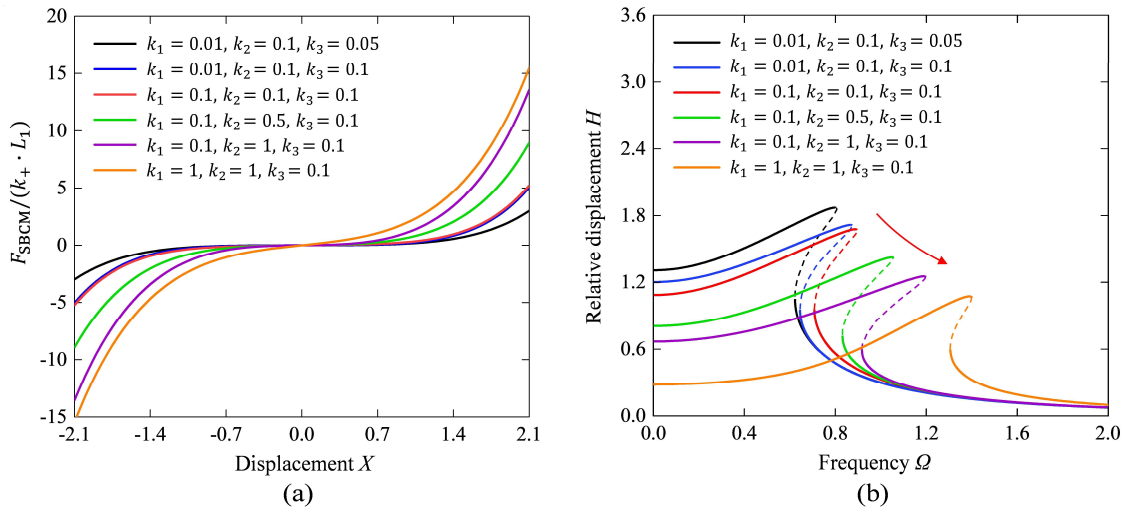
Fig. 4.4. (a) Normalized force-displacement curves with different stiffness coefficients and their corresponding (b) steady-state relative displacement amplitude-excitation frequency curves in the same excitation condition of $A_0 = 0.3, \zeta = 0.1$. The arrow indicates the changing tendency of the maximum amplitude, $H_{\max}$, and the Jumping-down frequency, $\Omega_{\text{Jumping-down}}$. (Coloured curves)

This interesting dynamic character provides a method to match the working frequency range of the SBCM-based energy harvester with the environmental frequencies by finely adjusting the geometric parameters of the device. In this way, the effective frequency bandwidth of the device can be further widened. However, it should be noted that the stiffness coefficients, k_1, k_2 and k_3, cannot be independently adjusted or selected in reality. They are only coefficients of the truncated polynomial of a more accurate expression of the normalized force-displacement relationship of the SBCM structure. The values presented in Fig. 4.4 are symbolically selected for preliminary exploration and demonstration of their influences on the normalized displacement response of the SBCM structure.

4.2 Dynamic analysis on the SBCM with diverse force-displacement relationship

The force-displacement characteristics of the SBCM are described with polynomial equations of degree 5 based on the static FEA simulations as introduced in Chapter 3. The dynamic displacement response of the SCBM with different force-displacement relationships under harmonic base excitations can be predicted and analyzed using the analytical model (Eq. (4.15)). The ODE45 function in MATLAB provides a numerical method to analyze the dynamic displacement performance of the SBCM responding to harmonic base excitations when the force-displacement equations are given. The analytical and numerical results are then compared.

4.2.1 30%-H_{max} frequency bandwidth

A wide effective frequency bandwidth is desired in vibrational energy harvesting. The 3-dB bandwidth is widely used in the assessment of the bandwidth of vibrational energy harvesters [294]. This bandwidth definition is derived from signal processing and it refers to the frequency range over which the signal power is greater than or equal to half of the maximum power achieved [295]. This 3-dB bandwidth definition is not available here to evaluate the effective frequency bandwidth of the SBCM under harmonic base excitation, since no electric output is obtained without energy-conversion capacitors combined in the model. The relative displacement between the base and mass of the SBCM indicates the sensitivity of the structure to environmental vibrations and it determines the energy harvesting performance. Therefore, the definition of 30%-H_{max} frequency bandwidth is introduced from the mechanical aspect.

The 30%-H_{max} bandwidth, $B_{30\%-H_{max}}$, is the frequency range where the oscillator has a relative displacement amplitude larger than 30% of the maximum relative displacement amplitude, H_{max}, under a certain base excitation acceleration. This bandwidth definition is graphically shows in Fig. 4.5. Since the SBCM structure can be combined with various energy-conversion mechanisms, the 30%-H_{max} bandwidth helps to directly assess and compare the effective frequency ranges of the SBCM in different force-displacement relationships without considering the energy-conversion mechanisms. In addition, the bandwidth definition from the mechanical aspect avoids the interference from the energy-conversion components on the

assessment on the structural performance, which is in particular beneficial in the structure-design stage.
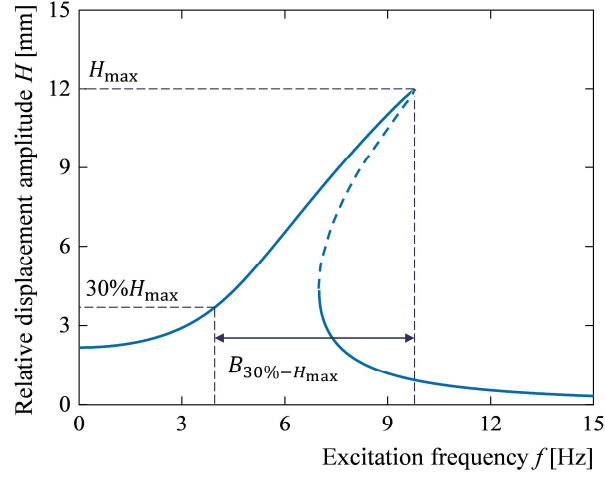
Fig. 4.5. Definition of the 30%-H_{max} bandwidth.

4.2.2 Dynamic response of the SBCM in static balancing

The polynomial equation of Eq. (3.11) describes a static-balancing fore-displacement relationship obtained in FEA simulations with geometric parameters given in Table 3.3. It should be noted that this is one example of many possible static balancing cases with different materials and in various scales. Taking this static-balancing condition as an example, the H-Ω curve of the SBCM under harmonic base excitation can be obtained by substituting the coefficients of the polynomial equation into Eq. (4.15). Compared with the moving mass block in the middle, both the distributed mass of the compliant beams and the mass of two side blocks are much smaller. Therefore, they are neglected here in the dynamic analysis for simplification. Only the mass of the movable mass block is considered as the effective mass of the oscillating system, m. It is calculated as 87.125 g according to the geometric parameters (37 mm × 20 mm × 15 mm) and the material selected ($\rho_{\text{Structural Steel}} = 7.85 \text{ g/cm}^3$). Targeting on the practical vibrational scenarios with low frequencies and weak accelerations, the concerned excitation frequency range is set to be below 20 Hz and the accelerations are 0.1 g, 0.25 g and 0.5 g in the theoretical analysis.

The analytical and numerical results of the displacement response of the SBCM in its static-balancing mode under base harmonic excitation are presented in Fig. 4.6 (corresponding to the accelerations of 0.1 g, 0.25 g and 0.5 g). A close agreement between the analytical results and numerical results are observed for all acceleration values. It is also shown in Fig. 4.6 that the SBCM at its static-balancing status is sensitive to ultra-low excitation frequencies (theoretically starting above 0 Hz) even with a weak acceleration of 0.1 g. This character further confirms the applicability of the SBCM in practical vibrational energy harvesting. In addition, a larger acceleration will lead to a larger response relative displacement amplitude and higher jumping-down frequency. The maximum relative displacement amplitude is about 8.6 mm at 5.6 Hz, 0.1 g and the maximum relative displacement amplitude is about 18 mm at 13.4 Hz, 0.5 g. The effective frequency bandwidth, $B_{30\%-H_{\max}}$, also becomes wider from 5.6 Hz to 9.1 Hz and 13.4 Hz when the acceleration increases.
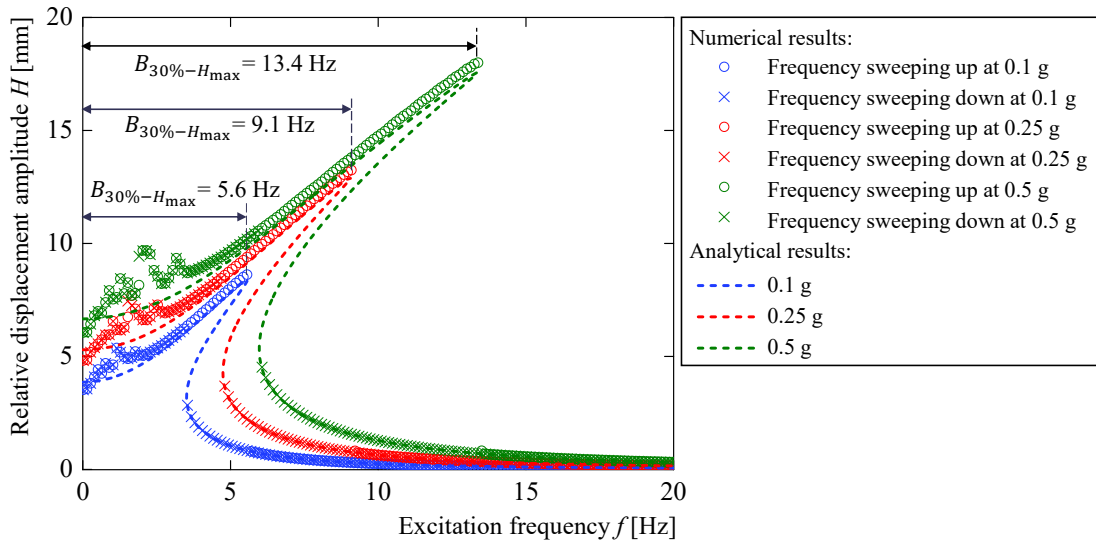
Fig. 4.6. Analytical and numerical results of the dynamic displacement response of the SBCM under harmonic base excitations with different accelerations (A_0 =0.1 g, 0.25 g and 0.5 g). (Coloured curves)

4.2.3 Dynamic response of the SBCM with mono-stability

Section 3.5.1 achieved two nonlinear mono-stable force-displacement relationships of the SBCM by reducing the geometric parameter L_1 (from 42 mm to 41.75 mm and 41.5 mm). Based on the corresponding polynomial force-displacement equations (Eqs. (3.12) and (3.13)), the dynamic displacement response of the SCBM in mono-stable modes can also be predicted and analyzed. The analytical and numerical results are plotted in Fig. 4.7. It should be noted

that bi-stable modes achieved with the same SBCM are not discussed in this section and they are out of the scope of this research.
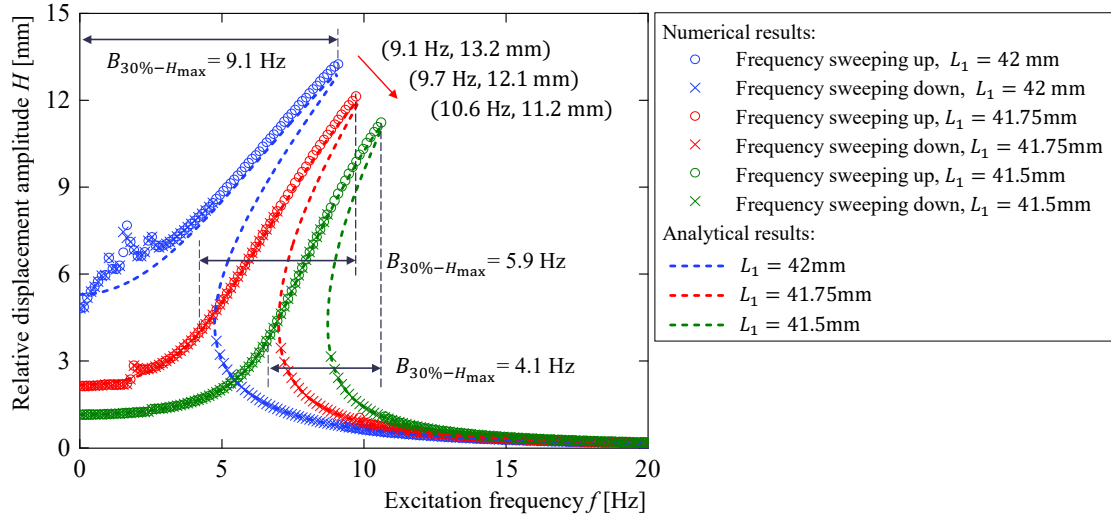
Fig. 4.7. Analytical and numerical results of the dynamic displacement response of the SBCM with static-balancing and mono-stable modes under harmonic base excitation (A_0=0.25 g). Arrow in the graph indicates the changing tendency of the maximum relative displacement amplitude, H_{max}, and the jumping down frequency, $f_{Jumping-down}$. (Coloured curves)

The decrease of the geometric parameter, L_1, leads to a larger stiffness value of the positive-stiffness component. The force-displacement relationship of the SBCM shifts from static balancing to mono-stable modes with an increasing stiffness around the origin position, this is also confirmed by the significant increase of the coefficient of the first-order term of the 5th order polynomial force-displacement equations. In the corresponding dynamic displacement response curves in both analytical and numerical results, the maximum relative displacement amplitude decreases while the jumping-down frequency increases. In addition, the 30%-H_{max} frequency bandwidth decreases and moves towards the higher frequency range as indicated in Fig. 4.7.

4.2.4 Dynamic response of the SBCM in static balancing modes with different displacement preloading

In Section 3.5.2, several static-balancing modes were achieved corresponding to different displacement preloading (ΔL =2 mm, 1.5 mm and 1 mm) on the negative-stiffness beams. Based on the force-displacement curves obtained in FEA simulations and their fitted 5th order

polynomials (Eqs. (3.11), (3.14) and (3.15)), the dynamic displacement response of the SBCM in the three static balancing modes are analyzed and compared. The relative displacement amplitude-excitation frequency curves based on the analytical and numerical models are plotted in Fig. 4.8.
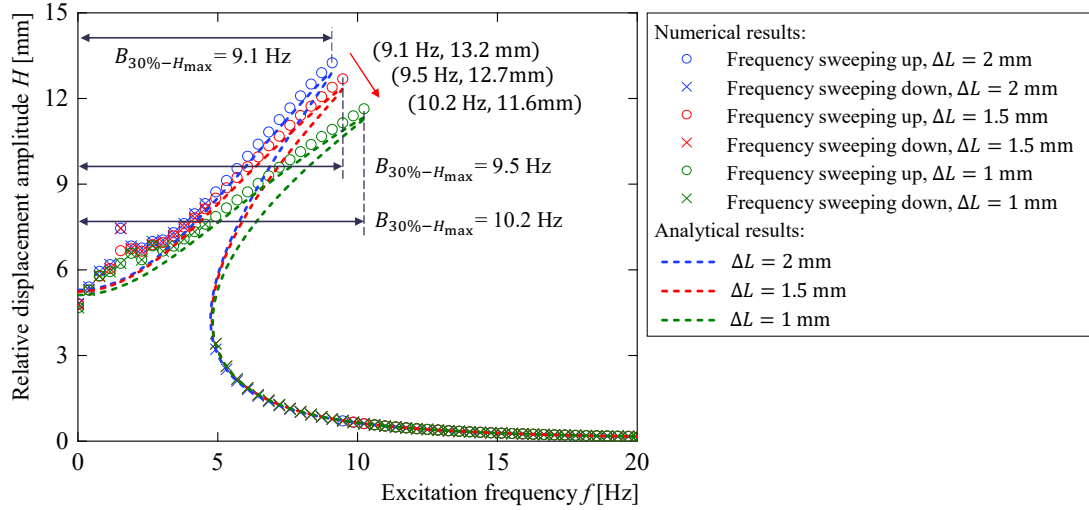
Fig. 4.8. Analytical and numerical results of the dynamic displacement response of the SBCM in static-balancing modes corresponding to different preloading displacement, ΔL =2 mm, 1.5 mm and 1 mm ($A_0 = 0.25$ g). Arrow in the graph indicates the changing tendency of the maximum relative displacement amplitude, H_{max}, and the jumping down frequency, $f_{Jumping-down}$. (Coloured curves)

It is shown in Fig. 4.8 that the three static balancing modes have almost the same relative displacement amplitude at ultra-low excitation frequencies close to 0 Hz. This is due to their close force-displacement curves around the origin position with zero force and zero stiffness. The difference between the displacement response curves becomes more obvious when the excitation frequency increases. The jumping-down frequency $f_{Jumping-down}$ increases from 9.1 Hz to 9.5 Hz and 10.2 Hz corresponding to the static-balancing modes with decreasing ΔL from 2 mm to 1.5 mm and 1 mm. At the $f_{Jumping-down}$ points, the maximum relative displacement amplitude, H_{max}, decreases from 13.2 mm to 12.7 mm and 11.6 mm. A wider 30%-H_{max} bandwidth is then obtained. The 30%-H_{max} bandwidth increases from 9.1 Hz to 9.5 Hz and 10.2 Hz which covers the entire low frequency range below $f_{Jumping-down}$. In summary, it has been verified by analytical and numerical results that the static balancing modes achieved with different ΔL are all sensitive to ultra-low frequencies above 0 Hz. The static balancing mode with smaller ΔL leads to a wider effective frequency bandwidth but lower relative displacement

amplitude. This feature provides approaches to design the SBCM with desired dynamic characteristics according to the application scenarios.

4.3 Dynamic FEA simulation on the SBCM

Based on the 2D FEA model of the SBCM structure, the dynamic displacement response of the SBCM under harmonic base excitations is simulated in time domain in this section. The simulations are carried out at discrete frequencies in an ultra-low frequency range with constant accelerations. The displacement performance of the SBCM is then plotted and analyzed.

4.3.1 Settings for the dynamic FEA simulation

Settings for the FEA simulation on the dynamic performance of the SBCM structure under harmonic excitations in COMSOL Multiphysics® are summarized in this section. They can be used as guidance by researchers who are conducting similar simulation tasks. There are two main steps in the dynamic study corresponding to the operations on the SBCM structure in real. In the first Stationary step, the negative-stiffness beams are axially preloaded by the displacement ΔL. Static-balancing mode of the SBCM structure is then reached with well-tuned geometric parameters in the previous static simulations. Settings in this Stationary step are the same with those introduced in Appendix A and they will not be repeated. In the second Time Dependent step, the SBCM is driven to vibrate by the harmonic base excitations in time domain. "Prescribed Displacement" boundary condition is used for applying base excitations in this Time Dependent step.

Assume that the harmonic base displacement is described as $x = X\sin(2\pi ft)$. X is the displacement amplitude and f is the excitation frequency. The acceleration can be easily derived with the second derivation of the displacement function, which can be described as:

$$a = \ddot{x} = -A\sin(2\pi ft) = -(2\pi f)^2 X\sin(2\pi ft) \qquad (4.16)$$

where A is the acceleration amplitude. Therefore, the relationship between the acceleration amplitude, excitation frequency and displacement amplitude can be presented as:

$$A = (2\pi f)^2 X \qquad (4.17)$$

The time-domain dynamic simulation is carried out at discrete frequencies with constant accelerations. This can be achieved by adjusting the value of the displacement amplitude corresponding to the excitation frequency in the definition table of global parameters as shown in Table B.1. Regarding to a given frequency and an acceleration (e.g. 3 Hz, 0.25 g), one simulation is carried out in the time domain of 20 vibrational periods. The relative displacement amplitude between the mass and the frame, H, the absolute displacement of the base, x_{Base}, and the absolute displacement of the mass, x_{Mass}, are captured and plotted with respect to time, t, based on the dynamic FEA results. These displacement parameters are indicated in Fig. 4.9. These displacement curves of the SBCM obtained from the FEA results are used in the further analysis on the dynamic performance of the SBCM under harmonic base excitations. Core settings of this dynamic simulation are presented in detail in Appendix B. The deformation scale is set to be 1 in COMSOL, which is the real deformation of the compliant parts.
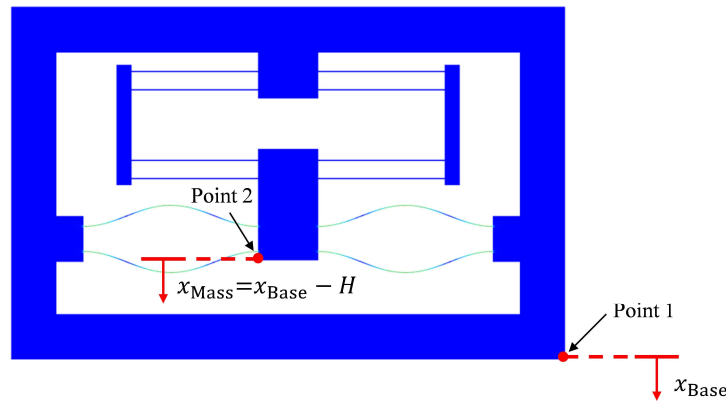
Fig. 4.9. Displacement values concerned in the dynamic FEA simulation and their corresponding points.

4.3.2 Dynamic simulation results

In the dynamic FEA simulations, the SBCM structure in the static-balancing mode is based-excited with ultra-low frequencies with weak accelerations. This is due to the consideration on the practical applications in harvesting energy from vibrations with ultra-low wide bandwidth frequencies with weak accelerations [33, 34, 39]. The excitation frequency range is set from 0.25 Hz to 10 Hz with three acceleration values of 0.1 g, 0.25 g and 0.5 g (1 g equals to 9.8m/s^2). Displacement response (the relative displacement amplitude, H, in particular) is concerned in the dynamic simulations, since it is directly related to the dynamic performance of the SBCM structure. An example of the displacement curves of the SBCM under harmonic base excitation at 5 Hz, 0.5 g in the first 20 periods in the dynamic FEA simulation is presented in Fig. 4.10.

The red curve represents the absolute displacement curve of the base (or base excitation displacement) and its amplitude is 5.07 mm. The blue curve is the absolute displacement response curve of the mass block and its amplitude is about 15.65 mm. The relative displacement between the base and the mass is illustrated as a green curve and the amplitude is about 10.58 mm.
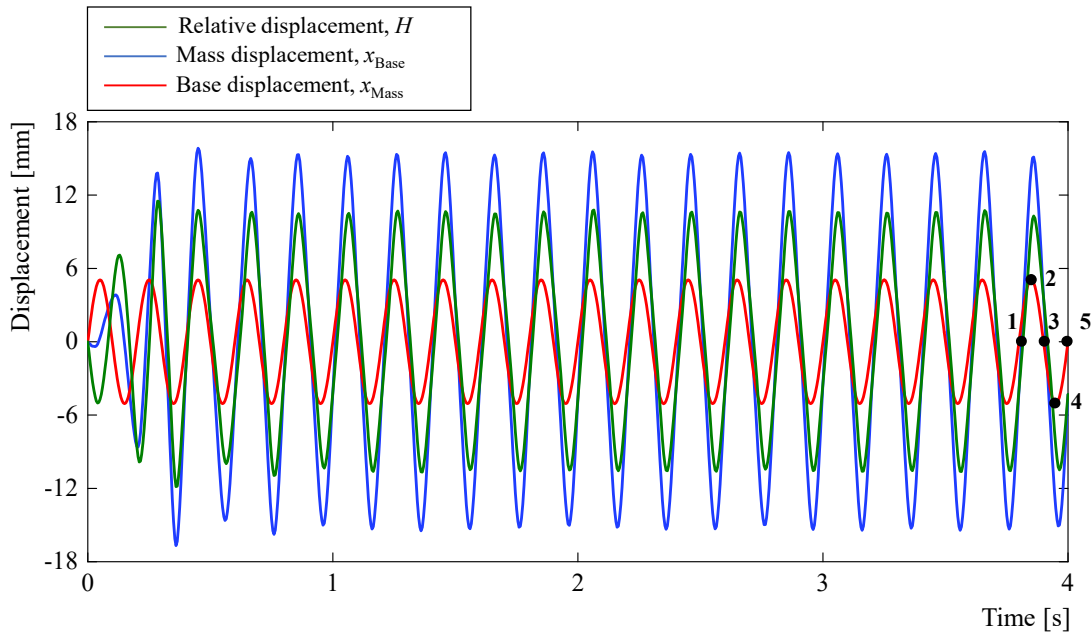
Fig. 4.10. Displacement curves of the SCBM structure in the FEA time-domain simulation at 5 Hz and 0.5 g. (Coloured curves)

The deformation conditions of the SBCM structure under harmonic base excitation in the dynamic FEA simulations is shown in Fig. 4.11. The five graphs (Fig. 4.11(a)-(e)) are corresponding to the five critical time points (points 1 to 5) as marked in Fig. 4.10. The 5 time points represent 3.8 s, 3.85 s, 3.9 s, 3.95 s and 4 s, respectively, in the last oscillation period with excitation frequency of 5 Hz. It is shown that the harmonic base excitation with relatively small displacement amplitude ($x_{\text{Base}} = 5.07$ mm) triggers the more severe oscillation of the mass block with a displacement amplitude (x_{Mass}) of about 15.65 mm. The relative displacement amplitude between the base and mass block can be calculated by $H = x_{\text{Mass}} - x_{\text{Base}}$. The deformation of the compliant beams can be observed directly in Fig. 4.11. From the application perspective, the SBCM can be combined with piezoelectric materials for vibrational energy harvesting by piezoelectric effect due to the dynamic deformation of the compliant beams during oscillation. The relative displacement between the base and the mass also provides the possibility to integrate electromagnetic, triboelectric principles with the

SBCM for vibrational energy harvesting. The energy-conversion mechanism can be selected based on the specific application conditions and requirements for the integration with the SBCM structure.
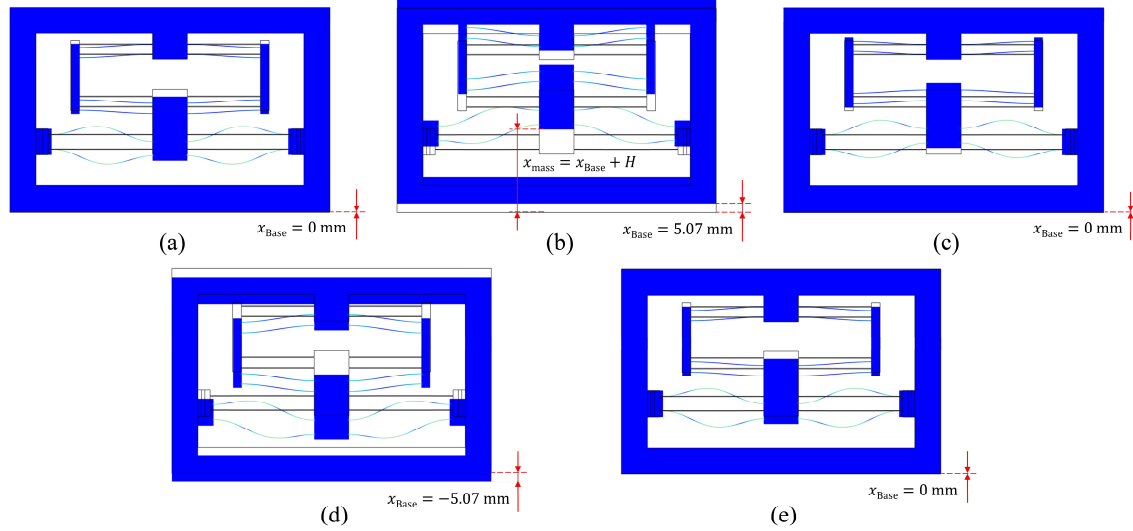
Fig. 4.11. Deformation of the SBCM under harmonic base excitation ($f = 5$ Hz, $A = 0.5$ g) in the FEA simulation corresponding to the time points in Fig. 4.10: (a) point 1 ($t = 3.8$ s); (b) point 2 ($t = 3.85$ s); (c) point 3 ($t = 3.9$s); (d) point 4 ($t = 3.95$ s); (e) point 5 ($t = 4$ s).

The interference between the side blocks and the frame is observed from the 2D FEA model of the SBCM as shown in Fig. 4.11(a). This interference has no influence on the simulation results and it can be ignored in analysis. It is because the interacting conditions between the boundary/surface domains are not defined in the FEA model. The overlapping of the domains will not be considered in the simulation by COMSOL. However, the happening of the interference between the parts during oscillation must be carefully considered and avoided in the prototyping and experimental stages. This will be introduced in the next chapter.

More sets of dynamic simulations with different frequencies and accelerations have been carried out taking the same approach. The relative displacement data are summarized in Table 4.1. It should be noted that only the dynamic response of the SBCM with the force-displacement relationship in Eq. 3.11 is investigated in the FEA simulations. Other force-displacement relationships are not discussed in this method is due to the extreme-high consumption of computing time and memory.

Table 4.1. Dynamic displacement response of the SBCM under harmonic base excitations with different frequencies (0.25 Hz – 10 Hz) and accelerations (0.1 g, 0.25 g and 0.5 g) in FEA simulations.

Base excitation frequency f (Hz)	Relative displacement amplitude H (mm)		
	Acceleration: 0.1 g	Acceleration: 0.25 g	Acceleration: 0.5 g
0.25	4.1	5.4	7.32
0.5	4.36	5.19	6.73
1	4.43	5.86	6.5
2	4.84	6.67	9.4
3	5.93	7.57	9.83
4	1.93	8.04	10.28
5	1.175	1.26	10.58
6	0.748	1.21	5.36
8	0.423	0.53	2.35
10	0.292	0.35	1.45

4.3.3 FEA verification and data analysis

This section compares the FEA results with the analytical and numerical results of the dynamic displacement amplitude of the SBCM under harmonic base excitations. The *H-f* curves based on the dynamic FEA simulations (summarized in Table 4.1) are plotted in Fig. 4.12(a). It is verified by the FEA simulations that the SBCM is sensitive to ultra-low excitation frequencies (starting from 0.25 Hz) with very weak accelerations (e.g. 0.1 g) in a wide frequency range. In addition, a higher excitation acceleration leads to a larger relative displacement amplitude and a wider effective frequency bandwidth. The 30%-H_{max} bandwidth increases roughly from 3 Hz to 4 Hz and 5 Hz when the acceleration increases from 0.1 g to 0.25 g and 0.5 g.

Fig. 4.12(c)-(d) present the comparison on the *H-f* curves of the SCBM obtained from analytical and numerical results and FEA simulations corresponding to accelerations of 0.1 g, 0.25 g and 0.5 g, respectively. A close agreement between the analytical modelling, numerical results with sweeping-down frequencies and FEA simulations is observed for all the accelerations. The accuracy of the dynamic FEA simulation is then confirmed. However, errors between the FEA simulations and numerical and analytical results exist. This is because FEA simulations take more practical influences, such as vibration of the thin beams and side blocks, into consideration. Analytical and numerical methods regard the analysis on the displacement amplitude-excitation frequency relationship as a pure mathematical problem. The larger

displacement amplitudes in the analytical model and numerical simulations with sweeping-up frequencies have not been reached in FEA simulations. This is because the FEA simulation is carried out at discrete frequencies with no vibrational "history" (i.e. vibrational energy from previous oscillation status) considered as the initial condition. In real operation with SBCM prototypes, external disturbing can be applied to the oscillating mass block to stimulate the oscillation with larger amplitudes, while this is not available in FEA simulations.
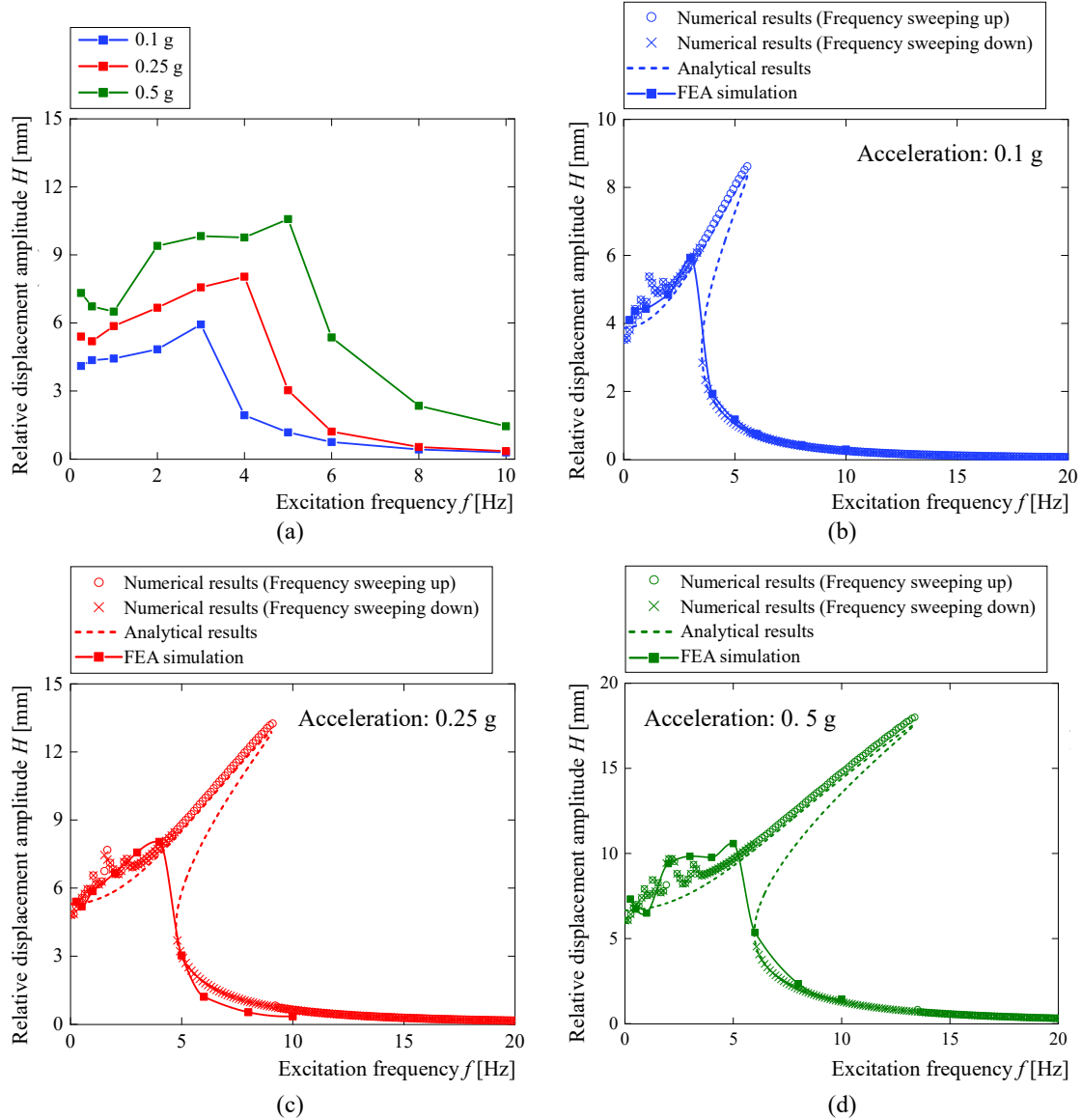
Fig. 4.12. Dynamic relative displacement-excitation frequency curves of the SBCM under harmonic base excitations in the frequency range from 0.25 Hz to 10 Hz based on (a) FEA simulations and the comparison with theoretical results corresponding to accelerations of (b) 0.1 g, (c) 0.25 g and (d) 0.5 g. (Coloured curves)

In summary, dynamic FEA simulations further verify that the SBCM is sensitive to ultra-low wide bandwidth excitation frequencies with weak accelerations. The deformation condition of the compliant beams and oscillation motions of the movable parts can be observed in the dynamic simulations. The dynamic FEA simulation provides another reliable method for analyzing and predicting the dynamic performance of the SBCM under harmonic base excitations with given force-displacement relationships. In addition, more complex simulations can be build up based on the dynamic FEA model. For example, electric outputs under base excitation can be simulated with different electromechanical transducers (e.g. piezoelectric, electromagnetic) integrated in the dynamic model.

4.4 Summary

A dynamic analytical model of the displacement responses of the SBCM to the harmonic base excitations has been derived based on the averaging method. The accuracy of the analytical model is confirmed by the numerical analysis. The relative displacement-excitation frequency characters of the SBCM with different force-displacement relationships are obtained and analyzed based on the analytical and numerical methods. The definition of 30%-H_{max} frequency bandwidth is introduced to assess the effective bandwidth of the SBCM under harmonic base excitations. Using the COMSOL settings provided in this chapter, dynamic FEA simulations on the displacement response of the SBCM have been carried out.

It has been verified by analytical, numerical and FEA results that the SBCM in the static-balancing mode is sensitive to ultra-low wide bandwidth excitation frequencies with very weak accelerations (e.g. 0.1 g). A larger acceleration will cause a wider effective 30%-H_{max} frequency bandwidth and larger relative displacement amplitudes. The dynamic FEA model provides a reliable and visible way to assess the dynamic performance of the SBCM under harmonic base excitations. More complex simulations can be built up based on the dynamic FEA model. For example, electric outputs under base excitations can be simulated with different electromechanical transducers (e.g. piezoelectric) integrated in the dynamic model.

Chapter 5: Prototype and Experiments

This chapter introduces a prototype of the SBCM fabricated in the assembling manner. The static and dynamic characteristics of the SBCM according to the theoretical studies in the previous chapters are experimentally investigated. The applicability of the SBCM in vibrational energy harvesting is demonstrated by integating piezoelectric transducers composed of PVDF films with the compliant beams. Both displacement responses and electricity outputs are obtained under base excitations. Other dynamic features of the SBCM structure, such as dynamic stability, super- and sub-harmonic oscillaitons, are briefly explored and discussed.

5.1 Prototype of the SBCM

5.1.1 Prototype design

A prototype of this SBCM is designed and fabricated following the design guideline as shown in Fig. 3.5 and referring the geometric paramters provided in Table 3.3. 3D model of this SCBM ptototype is created with Solidworks. The model in the front view and the isometric side view is shown in Fig. 5.1. This prototype is designed and fabricated in an assembling mode instead of a monolithic mode. In this investigation research on the SBCM for vibrational energy harvesting, the assembing prototype has several advantages which are summarized as follows:

1) The geometric parameters of both positive- and negative- stiffness beams can be easily tuned for desired force-dispalcement characteristics with the same prototype. However, this is not possible for monolithic prototypes with fixed geometric parameters. Several monolithic prototypes have to be fabricated for achieving different force-displacement relationshipes.

2) All the parts in the SBCM assembly, compliant beams in particular, are replaceable. When failure happens in the protoype, the SBCM strucrture can be easily fixed at a low cost by replaing the broken parts with new ones. By constrast, a local failure of the monolithic prototype will lead to the scrapping of the whole device. This can be expensive in the investigation stage of the research where failure of the device can hardly be avoided.

3) Monolithic prototypes are more expensive in fabrication since special machining tools, such as Wire-cut Electrical Discharge Machine, are needed. The assembling prototypes are relatively more cost-effective. The small parts can be machined in traditonal ways and the thin beams can be cut from metal sheets with the standard thickness [296].

a: Frame
b: Fixed lock
c: Side block
d: Mass block
e: Positive-stiffness beam
f: Preloading block
g: Negative-stiffness beam
h: Pressing finger
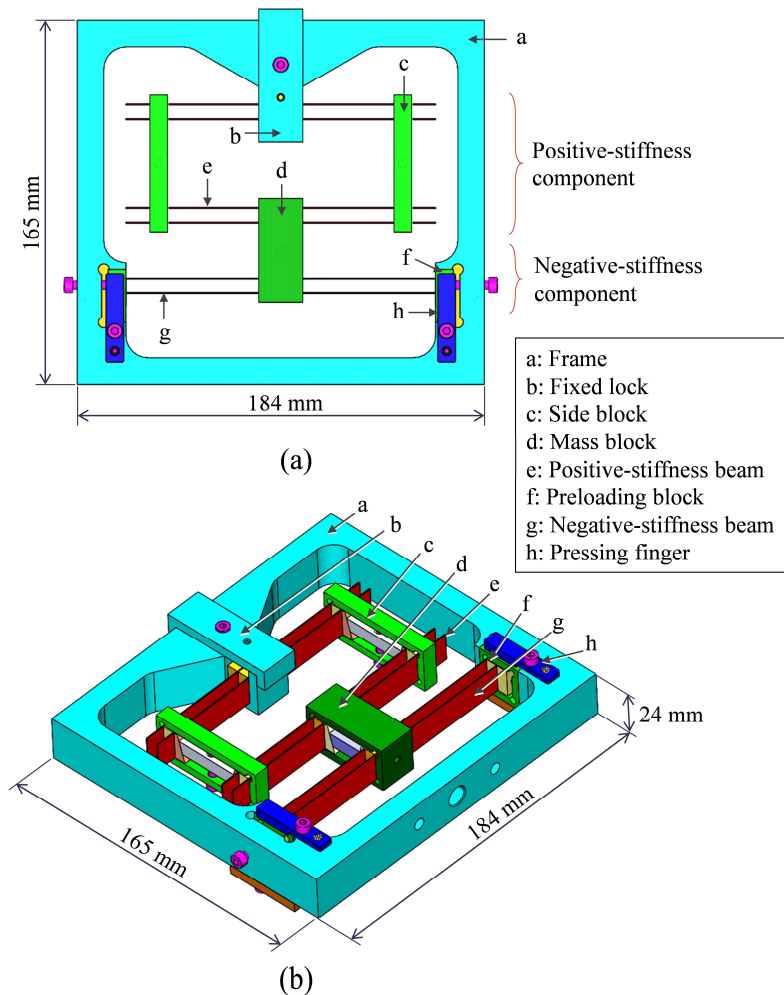
Fig. 5.1. 3D model of the SBCM prototype in (a) front view and (b) isometric side view.

In this SBCM prototype, structures of the side blocks and preloading parts are specially designed and they are introduced here in detail. The sectional drawing of the side block on the right hand side is shown in Fig. 5.2 for a clear illustration. The main function of side blocks has two folds. Firstly, the positive-stiffness beams are solidly clamped and connected by the side blocks in the SBCM structure. Secondly, the effective beam length involved in the system can be controlled by adjusting the position of the side blocks. The side block is composed of a frame, a pulling screw, a central wedge with two slopes (15˚), two side wedges with slopes (15˚) and two spacers as shown in Fig. 5.2. For clamping the positive-stiffness beams, the central wegde is pulled towards the screw which is turned clockwise. Due to the interaction between the slopes, the side wedges are pused simultaneously towards outer directions and the positive-stiffness beams are then clamped. The positive-stiffness beams are released when the screw is tuned anti-clockwise.
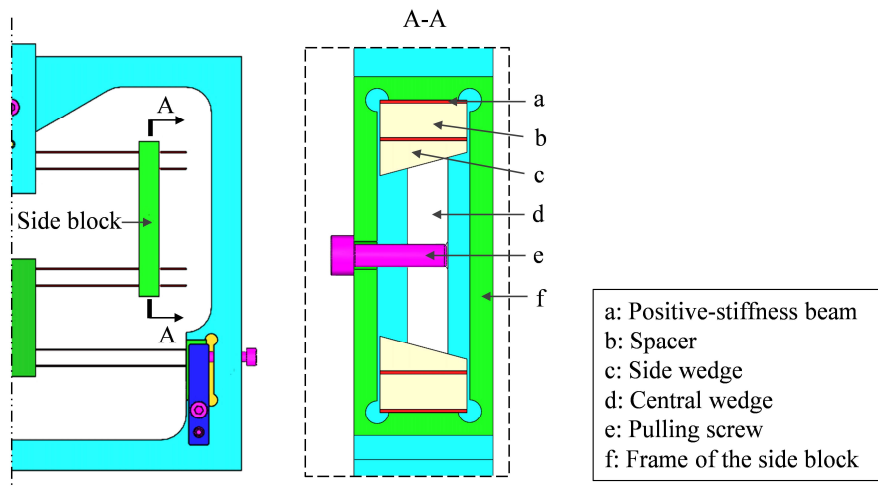
Fig. 5.2. Structure of the side block for clamping positive-stiffness beams.

The structure for preloading the negative-stiffness beams is shown in Fig. 5.3. The pressing fingers indicated in Fig. 5.1 are used to clamp the preloading blocks based on the lever principle after preloading procedure is finished. In Fig. 5.3, the pressing finger is removed in the scaled-up figure for a clear illustration on the preloading strucrture. Due to the symmetry of the SBCM structure, the preloading structure on right hand side is presented. The right ends of the two negative-stiffness beams are clamped by the same preloading block. The side pushing screw pushes the preloading block towards the center of the SBCM strucutre by the desired displacement of ΔL when the screw is turned clockwise. The groove on the outer frame guides the translational motion of the preloading block and restricts other DoF. The negative-stiffness

beams are then preloaded to buckle. When preloading process is completed, the preloading block is then clamped by the pressing finger based on the lever principle.
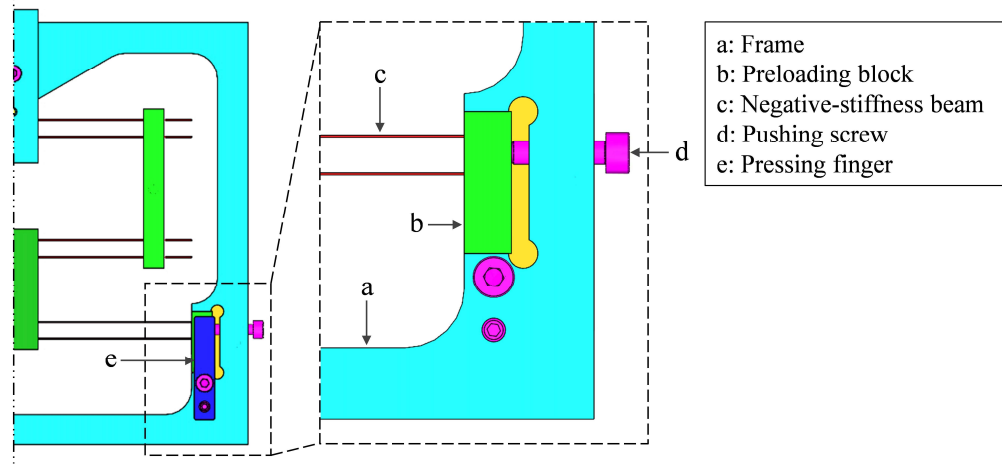
Fig. 5.3. Structure of the preloading parts.

5.1.2 PVDF films utilized as piezoelectric transducers

In order to demonstrate the applicability of the SBCM structure in vibrational energy harvesting, a preliminary SBCM-based PVEH is fabricated with piezoelectric materials integrated in the structure. When the SBCM is stimulated to vibrate under external excitations, electricity can be generated from the piezoelectric transducers by piezoelectric effect. As introduced in Section 2.2, various piezoelectric materials are available in the market [30]. The PVDF (Polyvinylidene fluoride) films are selected in this research because they have significantly

Table 5.1. Key parameters of the PVDF films provided by the supplier (PolyK Technologies).

Properties	Symbol	Values	Unit
Piezo Strain Constant	d_{31}	$23\sim35$	10^{-12} C/N
	d_{33}	$-28\sim-38$	10^{-12} C/N
Piezo Stress Constant	g_{31}	$210\sim220$	10^{-3} Vm/N
	g_{33}	$-330\sim-350$	10^{-3} Vm/N
Dielectric Constant	ε_{r}	$10\sim14$	1
Pyroelectric coefficient	ρ	$26\sim30$	10^{-6} C/m^2K
Electromechanical coupling Factor	k_{31}	$10\sim13$	%
	k_{t}	$12\sim15$	%
Maximum Voltage	E	>100	V/μm

higher flexibility [297] than PZT, which allows them to provide adequate adhesion and appropriate transfer of strain. The energy harvesting is thus at the same pace with the structural response under external excitations. In addtion, PVDF films are also easy for processing [7] and they can be cut into desired shapes by blades. PVDF films are then chosen although PZT has a slight advantage in terms of a higher electromechanical coupling coefficient.

The PVDF films used in this research are from PolyK Technologies. The thickness of the PVDF film is 200 µm (including the sputtered Aluminium electrodes on both sides). The key piezoelectric parameters of the PVDF films provided by supplier are listed in Table 5.1.

5.1.3 Fabrication of the SBCM prototype

Based on the 3D model created in Solidworks, an SBCM prototye is fabricated and assembled as shown in Fig. 5.4. The positive-stiffness beams are made of 65Mn Spring Steel sheets with the standard thickness of 0.4 mm. The negative-stiffness beams are made of the same material but the standard thickness is 0.3 mm. The side blocks, mass block and the frame/base are machined in a CNC machining center and thet are made of Aluminium Alloy 6082T6. The basic properties of these two structural materials are summaried and presented in Table 5.2.

Table 5.2. Properties of the structural materials used in the SBCM prototype.

Material	Density [g/cm3]	Young's Modulus [GPa]	Poisson's Ratio	Yield Strength [MPa]	Tensile Strength [MPa]
65Mn Spring Steel	7.85	190-210	0.27-0.30	≥980	≥785
Aluminium Alloy 6082T6	2.70	71	0.31–0.34	≥280	≥205

Geometric errors of the compliant beams are inevitable in the fabrication and assembling processes. These errors would accumulate and influence the practical stiffness of the positive- and negative- stiffness components. However, the tuneable beam length provides a method to compensate for the stiffness errors caused by the geometric errors, which is done by finely adjusting the effective length of the positive-stiffness beams for static balancing. This feature of the prototype gives a wide dimensional tolerance of the compliant beams in fabrication. The dimensional tolerances of the length and width of all beams are 0.1 mm and 0.05 mm,

respectively. The tolerance of the beam thickness is standard and controlled by the manufacturer of the commercial metal sheets.

A preliminary SBCM-based PVEH is obtianed by integrating piezoelectric materials for electrcity generation in the device. Two pieces of PVDF films (each with a dimension of 20 mm×10 mm×0.2 mm) with Aluminium electrodes are attached on the top surfaces of the upper positive-stiffness beams close to the central fixed block (as indicated in Fig. 5.4). The piezoelctric films are attached in these areas due to the reasons summaried as follows:

1) The maximum stress (from -689 MPa to 689 MPa according to the FEA simulaitons with COMSOL Multiphysics®) along the compliant beams occurs at the clamping points where the curvature is the largest. This is beneficial for energy generation by piezoelectric effect.

2) The length of the positive-stiffness beams is tunned by adjusting the positions of the side blocks for static balancing. These areas close to the central fixed point will not influence the tuning operations.

3) The positive-stiffness beams, and also the piezoelectric materials attached on the beams, are released when the SBCM is not vibraiting. However, the buckled negative-stiffness beams are always stressed independent of the working condition. If the piezoelectric materials are attached on the negaitve-stiffness beams, they will be stressed all the time. This will shorten the lifetime of the piezoelectric materials and also the adhnesive materials.

4) Owing to the small vibrational amplitude of theese areas on the positive-stiffness beams, the vibration of the electric cables connected to these areas will not be too serious. This is beneficial for the working reliability of the SBCM-based harvester.

It should be noted that these beams areas for attaching the PVDF films are still not the optimized positions for the best energy generation performance. However, they are acceptable in the investigation stage for demonstrations. In this research, the adhnesive used to solidly attached the PVDF films on the beam surfaces is cyanoacrylate glue (also called super glue). Since the cyanoacrylate is not conductive [298], the adhnesives pasted between the metal beams and PVDF films also acts as insulating layers. The silver conductive epoxy adhesive (8331) from GM Chemical company is used to attach the electric cables with the upper

electrodes of the PVDF films, while the electric cables are connected with bottom electtodes with the assistance of two small pieces of conductive copper tapes.
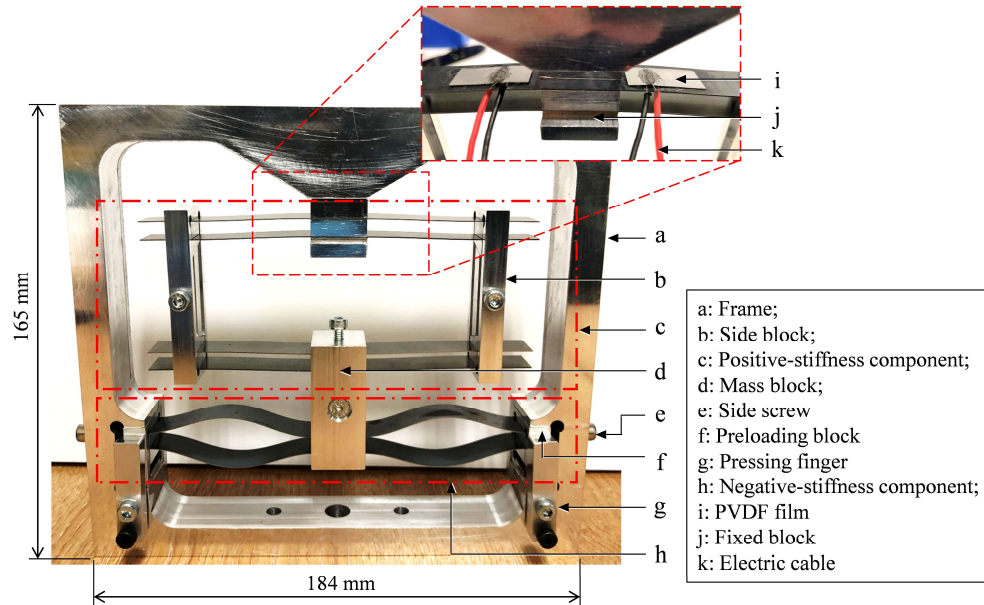
Fig. 5.4. SBCM prototype with PVDF films integrated. (a: Frame of the prototype; b: Side block for clamping the positive-stiffness beams; c: Positive-stiffness component composed of two double parallelograms in parallel; d: Mass block connecting the positive- and negative-stiffness components; e: Side screw for pushing the preloading block; f: Preloading block; g: Negative-stiffness component composed of two pairs of post-buckled fixed-guided beams; h: PVDF film with dimensions of 20 mm × 10 mm × 0.2 mm; i: Fixed block for fixing the positive-stiffness component with the frame; j: Electric cable for output voltage from the piezoelectric film.)

The geometries of the prototype are chosen taking the parameters in Table 3.3 as reference and are narrowed down based on the rapid-design equation, Eq. (3.10), for accommodating the beam thickness tolerance (up to 0.016 mm in this prototype). The gravity force of the mass block and errors from manufacture and assembling are compensated by a slight lift (0.85 mm) of the fixed block of the positive-stiffness component, which can be regarded as the preloading on the positive-stiffness component. Considering the small stiffness influence from the piezoelectric materials and adhesives applied, the prototype is tuned to static balancing over a finite range after the PVDF films are attached on the beams. In the preloading procedure, the negative-stiffness beams on left/right hand sides are preloaded simultaneously and slightly by turning the pushing screws in an altenative progress. The buckling of the negative-stiffness beams are manually guided to the opposite directions. The preloading distance, ΔL, is controlled via using a Vernier caliper with the resolution of 0.01 mm. The preloading blocks are then clamped by the pressing fingers after the desired preloading displacement is reached

in the procedure. The Vernier caliper is also used for controlling the accuracy of the length of the positive stiffness beams by adjusting the positions of the side blocks. The positive-stiffness beams are clamped after the static balancing is observed.

Static balancing is then finally achieved through finely adjusting only the length of the positive-stiffness beams, L_1, which is elaborated in Section 3.5.1. The geometric parameters of this SBCM with static balancing are then obtained as shown in Table 5.3. Comparing Table 5.3 and Table 3.3, we can observe some difference of the geometric parameters between the FEA simulations and static experiments. This is due to the errors from machining [299], assembling [300] and measurement [301], uneven properties in materials [302], additional stiffness introduced by piezo-materials attached [303], etc. According to Fig. 3.17, the maximum stress along the negative-stiffness beams, $|\sigma_2|_{max}$, is larger than $|\sigma_1|_{max}$ of the positive-stiffness beams in the majority displacement range. $|\sigma_2|_{max}$ is then used for checking the extreme stress condition in the SBCM structure. Bases on Eq. (3.17), $|\sigma_2|_{max}$ is calculated to be 1.06 GPa, which is slightly larger than the tensional strength of the 65Mn Spring Steel (> 980 MPa). In the following dynamic experiments, this is acceptable due to the limited testing cycles and the strength allowance of the material.

Table 5.3. Geometric parameters of the SBCM with static balancing in experiment (Note: in parentheses are the FEA dimensions).

Positive-stiffness component		Negative-stiffness component	
Length L_1	40.15 mm (42 mm)	Length L_2	60 mm
Thickness out of plane H_1	15 mm	Thickness out of plane H_2	15 mm
Measured thickness in plane T_1 (average)	0.384 mm	Measured thickness in plane T_2 (average)	0.293 mm
Nominal thickness in plane T_1	(0.4 mm)	Nominal thickness in plane T_2	(0.3 mm)
——	——	Preloading ΔL	2 mm

5.2 Static experiments

The force-displacement characteristic of this SBCM prototype is tested with a texture analyzer (HDplus) and the static testing setup is shown in Fig. 5.5. The probe is connected with the mass block and the reaction force generated on the mass block is measured over the displacement range between -10.1 mm and 10.1 mm at a low speed of 0.2 mm/s. The targeted displacement

range is slightly larger than the maximum relative displacement between the mass block and the frame observed in a preliminary dynamic test. The experimental force-displacement curve of the prototype in its static-balancing mode measured is shown in Fig. 5.6. Without any external force, the mass block can stay in equilibrium in a continuous displacement range of about 2 mm (from −1 mm to 1 mm) around its origin position as illustrated in Fig. 5.6. The corresponding reaction force in this static-balancing displacement range is either zero or very close to zero as reflected in the experimental force-displacement curve. The reaction force increases with the displacement in a wide range in both moving directions and the stiffness becomes nonlinear.
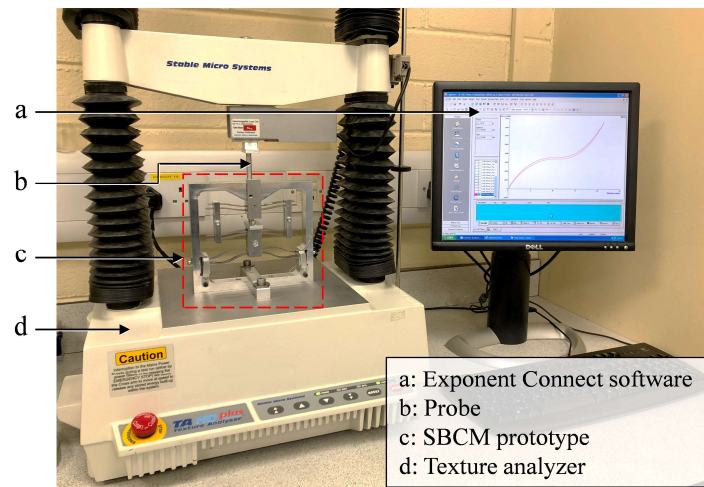
Fig. 5.5. Static experiment setup for testing the force-displacement relationship of the SBCM prototype. (a: Exponent Connect software for controlling the Texture Analyzer and data collecting; b: Probe which connects mass block and guides the displacement of the mass block at a low speed of 0.2 mm/s; c: SBCM prototype; d: Texture Analyzer HDplus.)

Fitting the force-displacement curve with a 5th order polynomial (odd terms only due to the reason explained earlier) with the Polyfit function in MATLAB, the force-displacement equation of the device is then obtained in Eq. (16). The R^2 coefficient of determination is 99.94%, indicating an accurate fit of this polynomial model to the experimental force-displacement curve. Based on this force-displacement equation, the dynamic performance of the prototype can be analyzed and predicted. The force-displacement curve with static balancing achieved in FEA simulations is also plotted in Fig. 5.6 for a comparison purpose. It
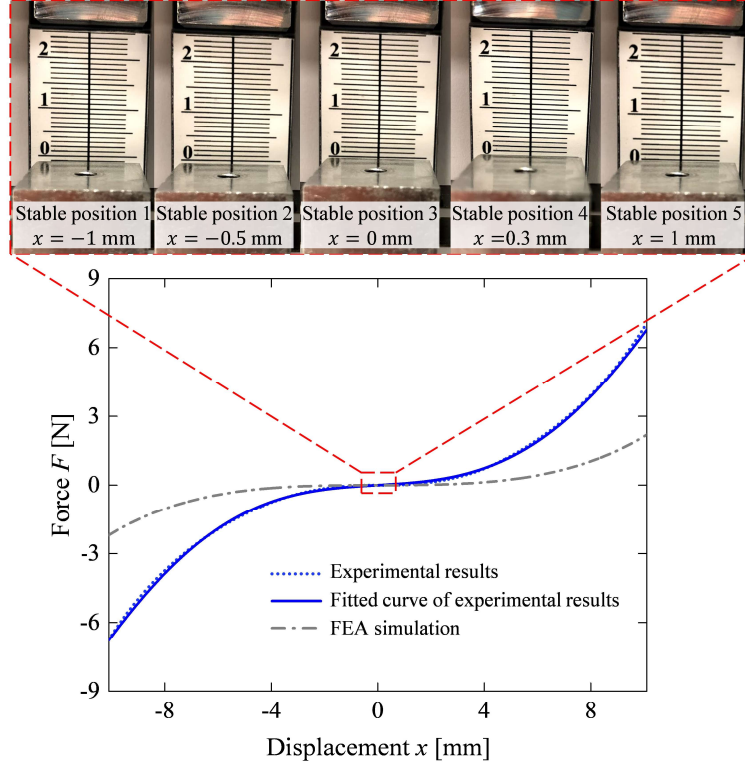
Fig. 5.6. Force-displacement curves of the SBCM prototype and the stable positions of the mass block in the continuous displacement range of about 2 mm (from -1 mm to 1 mm).

is shown that the static experiment has a larger force than the FEA model at the same displacement position. This is also proved by the larger coefficient of the first-order term in Eq. (5.1) than that in Eq. (3.11). This is mainly due to the fabrication errors, assembling inaccuracy, material defects etc. in the real operation while these factors have not been taken into account in FEA simulations.

$$F_{\text{SBCM}}(x) = 0.0685x + 0.00747x^3 - 0.0000152x^5 \tag{5.1}$$

When the length of the positive-stiffness beams is less than 40.15 mm, the positive stiffness is too large to compensate for the negative stiffness so that the prototype shows a mono-stability with stiffness nonlinearity. The force-displacement curves of the prototype with different length of the positive-stiffness beams (L_1= 40.15 mm, 39.5 mm and 39.2 mm) are illustrated and compared in Fig. 5.7.
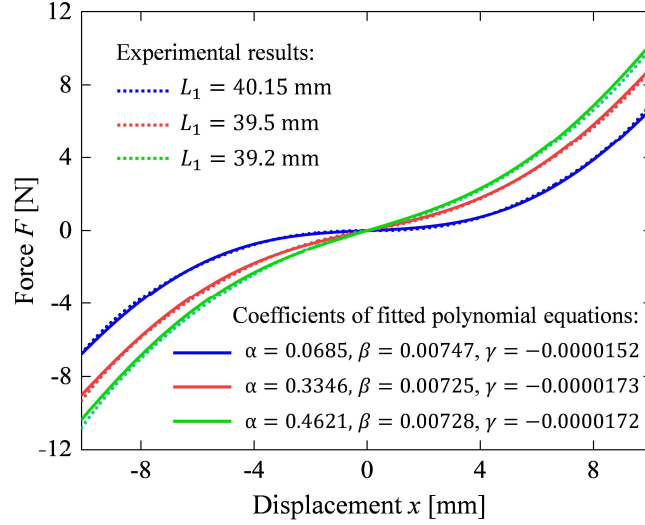
Fig. 5.7. Force-displacement curves of the SBCM prototype with different length of the positive-stiffness beams (L_1= 40.15 mm, 39.5 mm and 39.2 mm) from static testing. (Coloured curves)

It is shown that the static balancing around the origin position is broken when the length of the positive-stiffness beams decreases and the resulting force increases, indicating a larger stiffness of the device. This is also proved by the increasing coefficients of the first-order terms in the fitted polynomial equations in Fig. 5.7. The fitted polynomials of the mono-stable force-displacement curves (corresponding to the length of the positive-stiffness beams of 39.5 mm and 39.2 mm) are given as Eqs. (5.2) and (5.3), respectively. Corresponding to different force-displacement curves, the dynamic responses of the device differ.

$$F_{\text{SBCM}}(x) = 0.3346x + 0.00725x^3 - 0.0000173x^5 \tag{5.2}$$

$$F_{\text{SBCM}}(x) = 0.4621x + 0.00728x^3 - 0.0000172x^5 \tag{5.3}$$

5.3 Dynamic experiments

5.3.1 Experimental hardware apparatus

The experimental hardware apparatus for testing the dynamic performance of the SBCM-based PVEH is shown in Fig. 5.18. The Device is mounted on the platform of the Brüel & Kjær LDS V455 permanent magnet shaker (electrodynamic shaker) which exports harmonic excitations with preset frequencies and accelerations by the platform. Other equipment related to the

shaker includes a piezoelectric DeltaTron 4517-002 accelerometer, a LDS shaker controller and a PA1000L power amplifier. The voltage output from the piezoelectric transducers in the PVEH is recorded and displayed by a PC oscilloscope (Picoscope 3000 series). The steady-state relative displacement amplitude, H, is the main characteristic concerned in the dynamic experiments. The setup for the measurement of H is illustrated in Fig. 5.9 in particular. Because the mass block moves fast at dozens of Hz, the relative displacement amplitude is observed and recorded with a Photron high-speed camera. The Photron Fastcam Viewer is the supporting software of the high-speed camera for setting the parameters and display. A ruler is mounted on the prototype frame and behind the movable mass block. Under base excitation generated by the shaker, the ruler moves together with the device frame. The displacement of the mass block read from the ruler is the relative displacement between the mass and the frame. The average relative displacement amplitude of 5 oscillations after 20 s since the excitation starts is recorded as the steady-state relative displacement, H, in the following analysis.

Because the applicable vibration sources in the ambient environment are normally at low frequencies with low accelerations [8, 25] and the SBCM features a wide response bandwidth in the ultra-low frequency range, the targeted excitation frequency range in the dynamic experiments is set from 6 Hz to 20 Hz. The acceleration range is set from 0.1 g to 0.25 g (1 g = 9.8 m/s^2). The lower frequency limit of 6 Hz is determined by the testing capability of the shaker. Electric characteristics are also measured and recorded in the dynamic experiments to show the applicability of the SBCM in PVEHs.

The internal impedance of the PVDF films can be calculated with the equations [224]:

$$C = \frac{\varepsilon_r \varepsilon_o A}{d} \tag{5.4}$$

$$Z_{\text{in}} = \frac{1}{2\pi f C} \tag{5.5}$$

where C is the capacitance of the piezoelectric components. ε_r is the permittivity of the PVDF film which is regarded as 10 according to Table 5.1. ε_o is the permittivity of the free space and it is defined as 8.85×10^{-12} F/m. A represents the surface area of the piezo-material electrodes and d is the thickness of the PVDF film or the distance between the two electrodes covered on the piezo-material. In the FEA model, the size of each PVDF film is 20 mm $\times$ 15 mm $\times$ 0.2 mm. Z_{in} indicates the internal impedance of the piezoelectric materials and f is the working frequency of the device. Therefore, the internal resistance of each PVDF film

decreases from 100 MΩ to 30 MΩ corresponding to the oscillating frequency from 6 Hz to 20 Hz based on the Eqs. (5.4) and (5.5) [304].

The internal impedance of the PC oscilloscope (Picoscope 3000 series) is $R_{\text{Oscillocope}} = 1$ MΩ according to the product specification. This internal impedance is much lower than that of the PVDF films utilized in the prototype (30 MΩ to 100 MΩ corresponding to the oscillation frequency from 20 Hz to 6Hz). Therefore, the voltage output over the external resistance load $R = 1.12$ MΩ measured by the digital oscilloscope is actually the voltage output over the equivalent load resistance of 0.528 MΩ ($R // R_{\text{Oscillocope}}$). This can be the reason why the voltage output is relatively low (about 1 V). The electric characteristics include RMS voltage across the equivalent load resistance, V_{RMS}, and the average power dissipated on the equivalent load resistance, P_{AVE}.

V_{RMS}, P_{AVE}, can be calculated as follows:

$$V_{\text{RMS}} = \frac{V_{\text{P−P}}}{2\sqrt{2}} \tag{5.6}$$

$$P_{\text{AVE}} = \frac{V_{\text{RMS}}^2}{R} \tag{5.7}$$

where $V_{\text{P−P}}$ is the peak to peak value of the AC voltage measured across the equivalent load resistor. Voltage outputs from both PVDF films are measured and recorded respectively with a PC oscilloscope. Data from the PVDF film with higher voltage outputs are consistently used in the following analysis while the data from the other film are regarded as a reference. It should be noted that the optimal attachment positions and pasting process of PVDF films for piezoelectric effect, and optimal power management circuits [305, 306] have not been considered in the experiments.
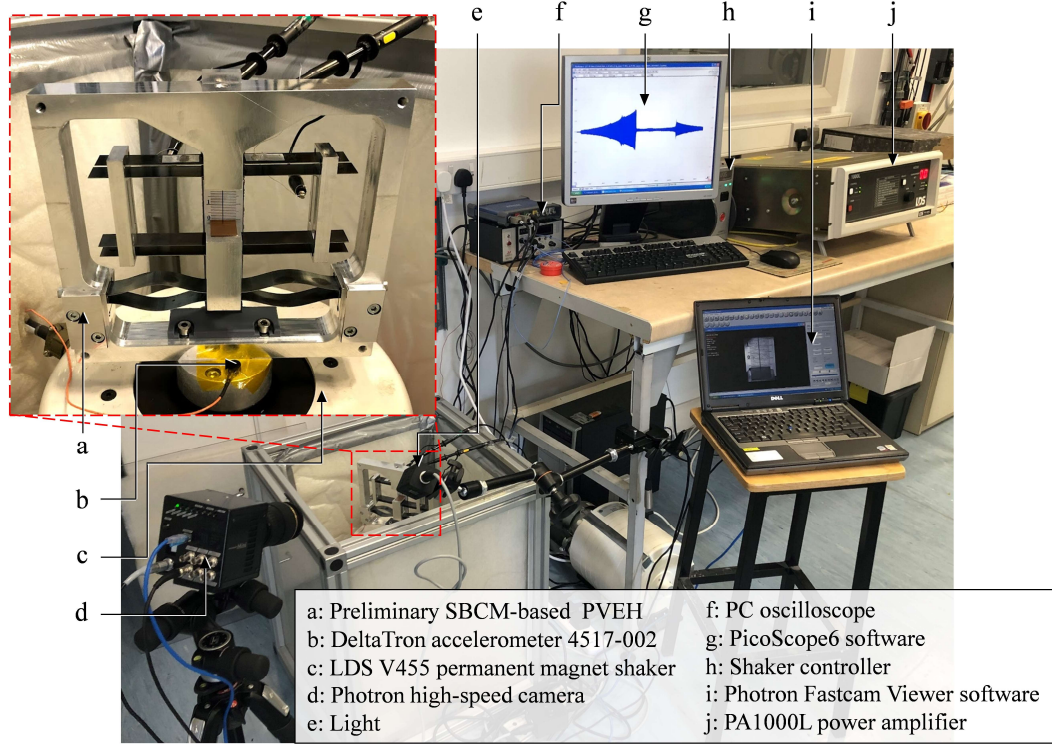
Fig. 5.8. Dynamic experiment setup for testing the displacement and electric response of the SBCM-based PVEH under harmonic base excitations. (a: Preliminary SBCM-based PVEH integrating PVDF films; b: DeltaTron 4517-002 accelerometer; c: LDS V455 permanent magnet shaker; d: Photron high-speed camera for observing the displacement response of the prototype; e: Light for illumination; f: PC oscilloscope (PicoScope 3000 series); g: PicoScope6 software; h: Shaker controller; i: Photron Fastcam Viewer software; j: PA1000L power amplifier.)
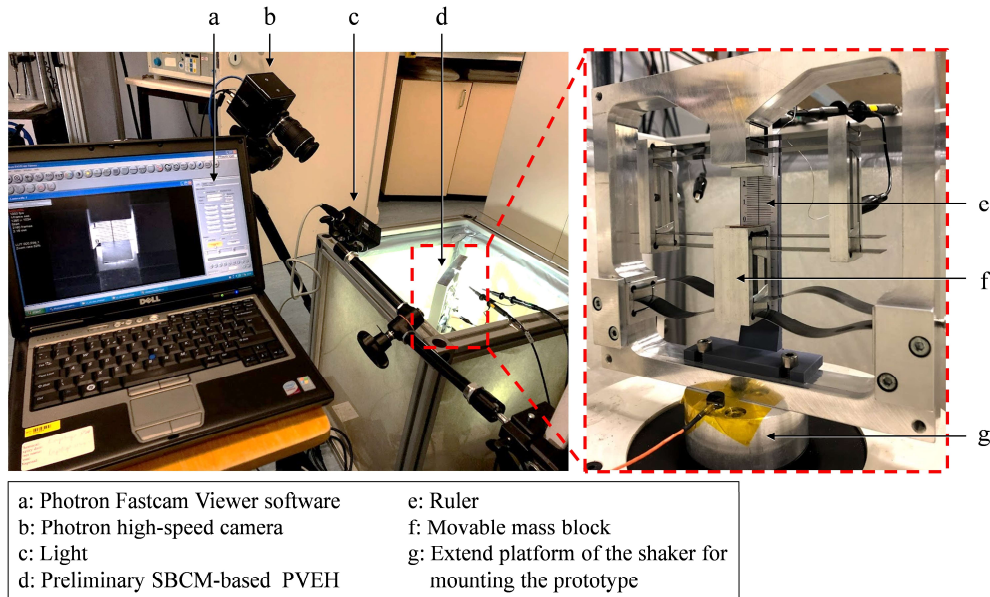
Fig. 5.9. Experimental hardware apparatus for measuring the relative displacement of the movable mass block with respect to the frame using a high-speed camera.

5.3.2 Experimental determination of the damping ratio

The damping ratio of the SBCM-based PVEH is determined experimentally. The experimental setup is shown in Fig. 5.10. In the experiments, the mass block of the SBCM-based PVEH prototype (not necessarily in the static-balancing mode) is stimulated manually to vibrate freely at its natural frequency. The voltage generated from one of the PVDF films is measured and displayed by an oscilloscope. According to the open-circuit voltage curves as shown in Fig. 5.10, the oscillation frequency is roughly f_n =12.5 Hz. In addition, it is shown that half of the oscillation voltage amplitude is damped in 5 periods. The damping ratio can be calculated with the equation [307, 308]:

$$\varepsilon = \frac{c}{c_c} = \frac{1}{2\pi n} \ln \frac{V(t)}{V(t+nT)} \tag{5.8}$$

where $c_c = 2m\omega_n = 2m \cdot 2\pi f_n$ is the critical damping constant [308], n is the number of oscillation periods between two amplitudes measured. Based on the Eq.(5.8), the damping ratio of the SBCM-based PVEH prototype is calculated as 0.022. This experimental value of damping ratio is used in both analytical and numerical models in the following analysis.
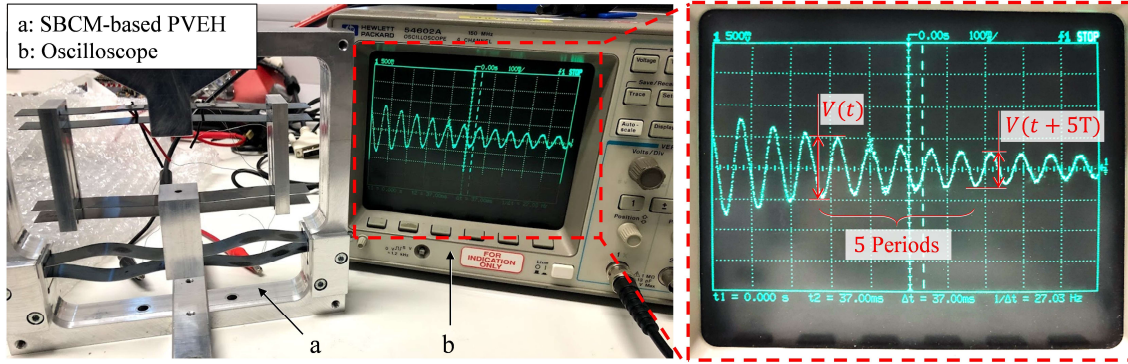
Fig. 5.10. Experimental setup for determination on the damping ratio of the prototype.

5.3.3 Dynamic response of the SBCM under different excitation accelerations

The SBCM-based PVEH in this static-balancing mode (where L_1= 40.15 mm, ΔL= 2 mm) is first tested under the base excitation with different accelerations (A_0=0.1 g, 0.15 g, 0.2 g and 0.25 g) at discrete frequency points. The steady-state relative displacement amplitudes, H, are plotted in Fig. 5.11(a). Taking the case under an excitation acceleration of 0.25 g (the purple lines in Fig. 5.11(a)) as an example, the experimental results are presented in the following

manner. In order to highlight the response of the device with respect to excitation frequencies, data points are connected with two separate curves. The upper-left curve indicates the frequency-sweeping-up tendency while the lower-right curve shows the frequency-sweeping-down tendency. The missing part between the two curves lies in the frequency range defined by the jumping-up/down frequencies. In experiments, the device has two steady-state oscillating states with larger and smaller relative displacement amplitudes in this frequency range. The oscillation can switch between these two states with the external disturbance.
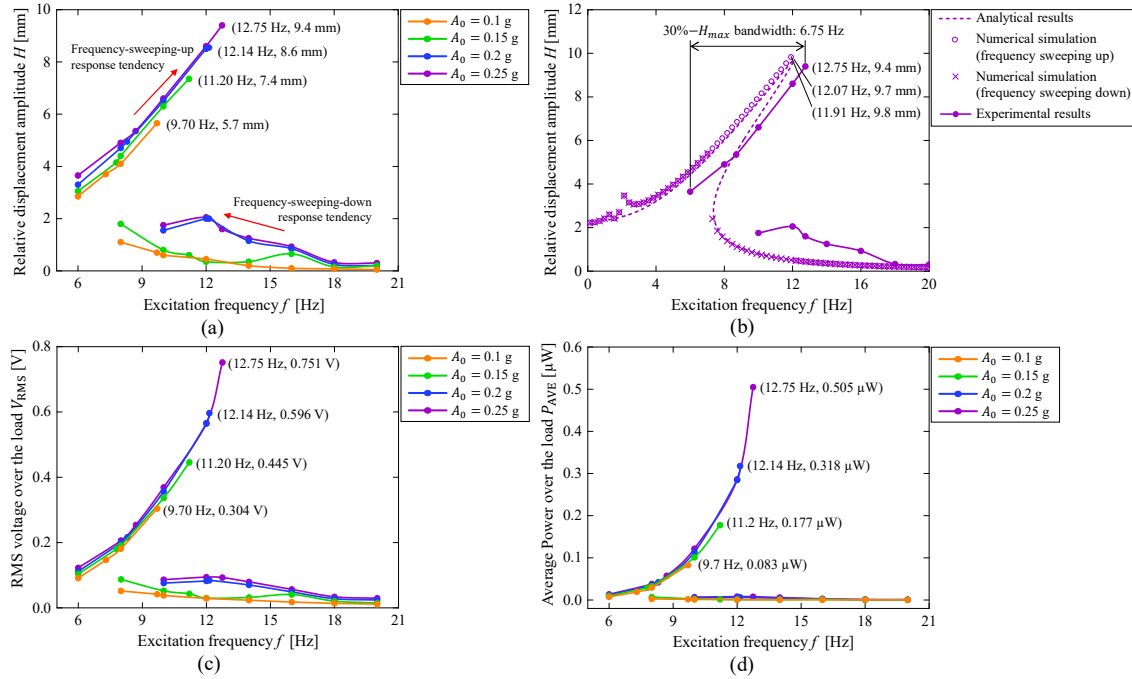
Fig. 5.11. (a) Experimental results of the relative displacement amplitude, H, under base excitation with different accelerations ($A_0 = 0.1$ g, 0.15 g, 0.2 g, 0.25 g); (b) Comparison of the experimental, analytical and numerical results of the relative displacement amplitude, H, under the excitation condition of $A_0 = 0.25$ g; Electric characteristics: (c) RMS voltage across the resistance, V_{RMS}, (d) Average power dissipated on the external resistance, P_{AVE}, in the dynamic experiments with different accelerations ($A_0 = 0.1$ g, 0.15 g, 0.2g, 0.25 g). (Colours curves)

As shown in Fig. 5.11(a), a relative displacement amplitude of 2.9 mm between the frame and the mass block has been observed when the excitation acceleration is 0.1 g at a frequency of 6 Hz. The relative displacement amplitude, H, increases along with the excitation frequency with the same acceleration of 0.1 g, and it reaches 5.7 mm at the jumping-down frequency, $f_{Jumping-down}$, of 9.7 Hz. Comparing the overall displacement data in Fig. 5.11(a), both H and $f_{Jumping-down}$ increase with the excitation acceleration, A_0. The maximum relative

displacement amplitude, H_{max}, of 9.4 mm in the experiments has been observed at the jumping-down frequency of 12.75 Hz with an acceleration of 0.25 g.

This dynamic displacement response can also be predicted analytically and numerically using the simplified experimental force-displacement equation (Eq. (5.1)). The corresponding analytical result is obtained based on Eq. (4.15) and the numerical simulation is carried out with the ODE45 Runge-Kutta solver in MATLAB. The damping ratio of the SBCM is 0.022 which is determined experimentally.

The analytical, numerical and experimental results in the condition of $A_0 = 0.25$ g are presented in Fig. 5.11(b) for direct comparison. Both numerical and analytical results show that the SBCM responds to ultra-low excitation frequencies theoretically starting from above 0 Hz. The close agreement with an average error percentage of 3.8% between the analytical and numerical results is shown in Fig. 5.11(b), which further verifies the accuracy of the dynamic analytical model created in Chapter 4. Errors between the experimental results and the theoretical models exist. Compared with the theoretical results, the experimental $f_{Jumping-down}$ is about 0.8 Hz higher. The experimental H_{max} is 9.4 mm which is only 0.3 mm and 0.4 mm smaller than the analytical and numerical values respectively. It is interesting to observe that the experimental curves look like a horizontal translation of the theoretical curves towards the right direction. Based on the report in [292], this "translation phenomenon" may be caused by the larger actual stiffness of the stiffness components during vibration, while the static stiffness is tested with a very low speed (0.2 mm/s).

Three electric indices, V_O, V_{RMS}, and P_{RMS}, are shown in Fig. 5.11(c)-(e). They show the same tendency with respect to the excitation acceleration, A_0, and also reach the maximum (V_O=1.879 V, V_{RMS}=0.751 V, P_{RMS}=0.505 μW) under 12.75 Hz and 0.25 g. For a given excitation acceleration, there are also two curves indicating the electric output tendency corresponding to frequency sweeping-up/down conditions. The electric outputs obtained in experiments are relatively low for practical application. This can be attributed to non-optimized factors, such as attachment positions, pasting process of the PVDF films and power management circuits.

It is observed from Fig. 5.11(a) that the SBCM-based PVEH has large displacement responses to all excitation accelerations from 6 Hz to the jumping-down frequencies in the experiments. According to the traditional 3-dB bandwidth definition in the signal processing area [295], the frequency bandwidth of the SBCM-based PVEH prototype based on the power output in Fig. 5.11(e) is less than 2 Hz and the actual effective frequency range of the device is highly underestimated. In order to objectively evaluate the dynamic performance of the SBCM, the definition of 30%-H_{max} frequency bandwidth is introduced in this research from the mechanical aspect. The 30%-H_{max} bandwidth refers to the frequency range where the oscillator has a relative displacement amplitude, H, larger than 30% of the maximum relative displacement amplitude, H_{max}, under a certain base excitation acceleration, as introduced in Section 5.3.1.

Based on this definition, the experimental 30%-H_{max} bandwidth of the SBCM under 0.25 g is larger than 6.75 Hz (a relative displacement amplitude larger than 30% of the H_{max} is expected when the frequency is lower than 6 Hz) as indicated in Fig. 5.11(b). According to the analytical results in Fig. 5.10(b), the theoretical 30%-H_{max} bandwidth is 8.73 Hz (from 3.34 Hz to 12.07Hz) under 0.25 g. Note that the lower frequency limit is 6 Hz in experiments, while displacement response to frequencies lower than 6 Hz can be provided in analytical and numerical results. The influence on the dynamic displacement response from the electromechanical coupling is neglected here because the electric energy dissipated in the circuit is very small (about only 0.5 µW).

5.3.4 Dynamic response of the SBCM with different force-displacement relationship under the same base excitations

Dynamic performance of the SBCM with different force-displacement characteristics (as shown in Fig. 5.7) has also been tested under the same excitation acceleration of 0.2 g. The corresponding experimental results are summarized and presented in Fig. 5.12. Fig. 5.12(a) shows that in the low-frequency range from 6 Hz to 12.14 Hz, the device in its static-balancing mode has a larger displacement response than that in its two distinct mono-stable modes. When the stiffness of the device around its origin position increases, corresponding to the decrease of the length of the positive-stiffness beams, L_1, $f_{Jumping-down}$ of the oscillator increases from

12.14 Hz to 14.5 Hz and 15.5 Hz, while $H_{\max}$ at this $f_{\text{Jumping-down}}$ decreases from 8.6 mm to 7.9 mm and 7.3 mm.
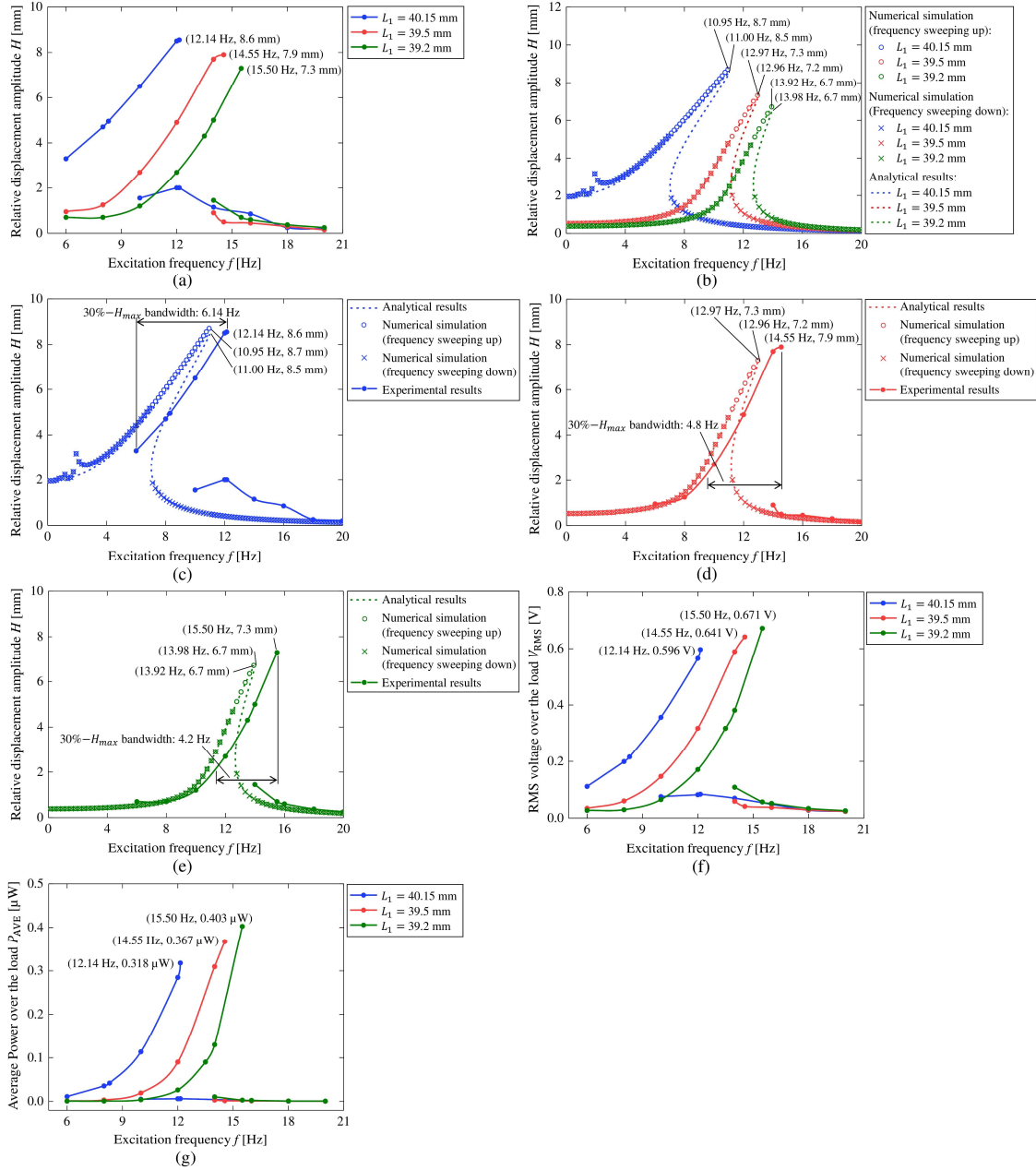
Fig. 5.12. (a) Experimental results, (b) analytical results and numerical simulation of the relative displacement amplitude, H, of the SBCM-based PVEH with different length of the positive-stiffness beams; Comparison of the experimental, analytical and numerical results of the relative displacement amplitude, H, for each length of the positive-stiffness beams: (c) L_1= 40.15 mm, (d) L_1= 39.5 mm and (e) L_1= 39.2 mm; Experimental results of (f) RMS voltage across the resistance, V_{RMS}, and (g) Average power dissipated on the resistance, P_{AVE}, of the SBCM-based PVEH with different length of the positive-stiffness beams. (The excitation acceleration is 0.2 g for all the graphs and curves are coloured.)

The changing tendency of $f_{\text{Jumping-do}}$ and $H_{\max}$ with respect to the change of the force-displacement relationship in experiments is consistent with that in the numerical and analytical results as shown in Fig. 5.12(b). Expected agreement between the numerical and analytical results of the dynamic displacement response is also observed with average error percentages of 3.8%, 0.4% and 0.2% corresponding to the static balancing mode and the two mono-stable modes respectively. For the three force-displacement cases, the experimental values of $f_{\text{Jumping-do}}$ are slightly higher than the theoretical results by less than 1.6 Hz. In terms of $H_{\max}$, the experimental values are almost equal to or 0.6 mm larger than the theoretical results. The "translation phenomenon" is also observed in the static balancing case under 0.2 g as shown in Fig. 5.12(c). For the two mono-stable cases shown in Fig. 5.12(d) and (e), the experimental curves have smaller inclined angles with respect to the horizontal axis due to larger actual stiffness of the stiffness components as mentioned earlier.

In addition, it is predicted analytically and numerically that the device in its static-balancing mode has great displacement responses to the excitation frequencies lower than 6 Hz (which is beyond the frequency limit in experiments). However, the displacement responses corresponding to the two mono-stable modes in this frequency range is almost zero. The experimental 30%-$H_{\max}$ frequency bandwidths of the device with different force-displacement relationships are indicated in Fig. 5.12(c)-(e), respectively. It is shown that, the experimental 30%-$H_{\max}$ bandwidth decreases from 6.14 Hz to 4.8 Hz and 4.2 Hz and this bandwidth moves towards the higher frequency range when the device stiffness around its origin position increases. According to the analytical results in Fig. 5.12(c)-(e), the theoretical 30%-$H_{\max}$ bandwidth of the device shows the similar tendency and it decreases from 7.82 Hz to 4.01 Hz and 3.31 Hz.

However, an opposite tendency of the maximum values of electric characteristics (V_{RMS}, and P_{AVE} at the corresponding jumping-down frequencies) is observed in Fig. 5.12(f)-(h). They increase with the stiffness of the device around the origin. This can be explained by the following reason. The SBCM structure has higher jumping-down frequencies when the stiffness around the origin increases. The increased jumping-down frequency leads to a decreased internal impedance of the PVDF film according to Eq. (5.5). However, the equivalent external impedance of the circuit remains constant. Therefore, the voltage output across the equivalent external impedance in the electric circuit is then relatively increases, which is

measured and observed by the digital oscilloscope. The availability of tuning the working frequency range of the SBCM-based energy harvester by adjusting the length of the positive-stiffness beams provides a solution to track the environmental excitation frequencies for an improved energy harvesting performance.

5.3.5 Comparison with a linear cantilever oscillator

The performance of a linear piezoelectric cantilever with tip mass is dynamically tested for comparison in order to highlight the dynamic advantages of the SBCM in vibrational energy harvesting. The experimental setup is shown in Fig. 5.13. The upper positive-stiffness beam with PVDF films in the SBCM is used as the linear piezoelectric cantilever directly. Therefore, the electric parameters remain the same in the comparison experiments. An Aluminium block is fixed on the cantilever tip for lowering the resonant frequency of the oscillator. The dimension of the cantilever beam is $50 \, \text{mm} \times 15 \, \text{mm} \times 0.4 \, \text{mm}$, while dimension of the Aluminium tip mass is $24 \, \text{mm} \times 24 \, \text{mm} \times 10 \, \text{mm}$.
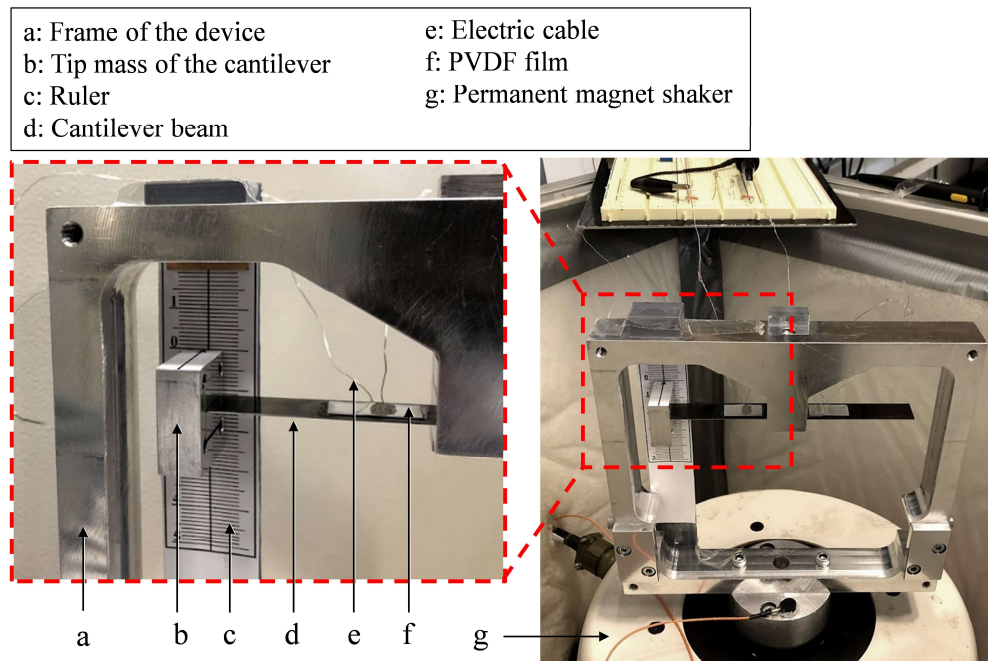
Fig. 5.13. Experimental setup for the dynamic testing on the piezoelectric cantilever with tip mass.

The outer frame of the SBCM is used for supporting the cantilever oscillator on the shaker. A ruler is mounted on the outer frame and behind the tip mass for indicating the relative displacement amplitude under base excitations. Using the same approach in the previous

dynamic experiments in Section 5.3.3 and Section 5.3.4, the relative displacement amplitudes of the tip mass block of the linear oscillator is observed and recorded by the high-speed camera. The electric outputs from the piezoelectric transducer is displayed and recorded using the PC digital oscilloscope. Due to the frequency limits of the shaker and the natural frequency of the linear oscillator of about 23.7 Hz (which is experimentally obtained), the targeted frequency range in the experiments is set to be from 6 Hz to 30 Hz. The excitation acceleration in experiments is 0.2 g.

The experimental results of the relative displacement amplitudes and electric outputs of the piezoelectric cantilever are summarized and plotted in Fig. 5.14. The experimental results of the SBCM-based PEVH under the same excitation acceleration are presented in the corresponding figures for comparison. It is shown in Fig. 5.14(a) that the cantilever oscillator has a very sharp displacement amplitude peak of 11.3 mm at 23.7 Hz which is the natural frequency of the cantilever. The corresponding 30%-H_{max} bandwidth is then very narrow and it is only about 0.7 Hz. In spite of the slightly lower maximum relative displacement amplitude of 8.6 mm, the SBCM structure has a 30%-H_{max} bandwidth of about 6.14 Hz (from 6 Hz to 12.14 Hz), which is 8 times wider. The advantages of the SBCM in ultra-low wide bandwidth frequencies are further confirmed by the comparison with the linear cantilever. It should be noted that compliant beams in the SBCM and the cantilever deform in different modes. This is the reason why the cantilever has larger maximum relative displacement amplitude than that of the SBCM. In addition, the relative displacement amplitude-excitation frequency curve of the cantilever slightly bends towards right side. This is caused by the small stiffness nonlinearity of the cantilever during large-deflection oscillations [28].

The electric outputs of the piezoelectric cantilever reach the maximum ($V_{RMS} =$ 2.336 V and $P_{AVE} = 2.437$ μW) at the resonant frequency of 23.7 Hz. The maximum electric outputs are much higher than those of the SBCM-based PVEH. The large electric outputs are caused by the higher deformation rate of the piezoelectric materials at 23.7 Hz. However, a slight shift from the resonant frequency will lead to a dramatic drop of the electric outputs due to the very narrow bandwidth. In addition, the electric outputs of the piezoelectric cantilever in the lower frequency range (from 6 Hz to 12 Hz) is almost zero, while electric outputs are obtained from the SBCM-based PVEH in this frequency range. Therefore, the SBCM-based PVEH is more preferable for practical applications then the harvesters based on linear oscillators.
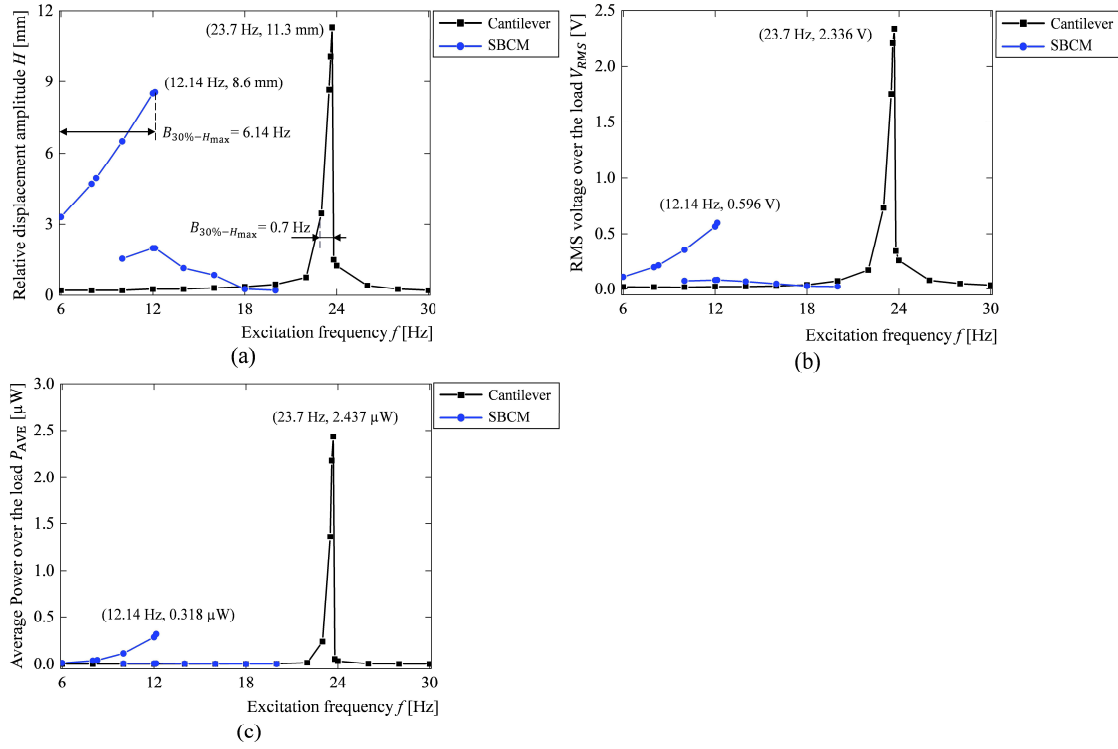
Fig. 5.14. Comparison on the experimental results of (a) relative displacement amplitude between the base and mass block, (b) RMS voltage across the resistance, V_{RMS}, and (c) Average power dissipated on the resistance, P_{AVE}, of the SBCM-based PVEH and piezoelectric cantilever oscillator (0.2 g).

5.3.6 Vibration stability of the SBCM in experiments

A phenomenon observed in experiments related to the vibration stability is that the buckling direction of the negative stiffness beams can snap from one direction to the opposite direction in violent vibration conditions as shown in Fig. 5.15. This is because the buckled negative-stiffness beams are bi-stable CMs. The original buckling shape is one of the two stable modes. When the relative displacement between the mass and the frame is large enough under severe excitation, the negative-stiffness beams turn from pressed condition into stretched condition. The buckling direction of the negative-stiffness beams might change randomly to the opposite (undesired) direction when the beams are pressed again in the oscillating process. The vibration phenomenon should be avoided due to the two main reasons. Firstly, the randomly changing buckling directions might lead to the interference of the negative-stiffness beams. Secondly, the asymmetric buckling directions on left/right hand side of the device will lead to the asymmetrically distributed stress along the compliant beams on left and right hand sides. This

is because internal torque will be generated and applied on the mass block when the negative-stiffness beams on left/right hand sides buckle to the asymmetric directions [286].
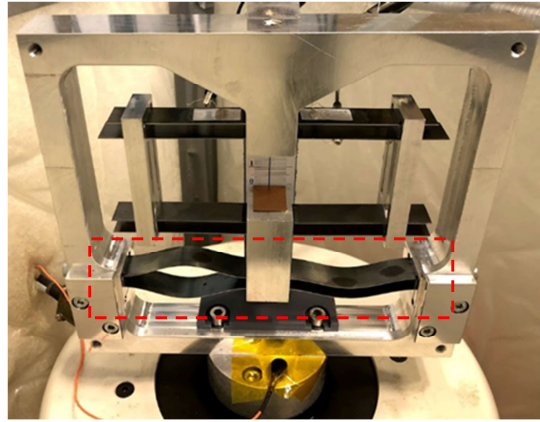
Fig. 5.15. Change of the buckling direction of the negative-stiffness beams in violent vibration conditions.

In order to prevent this undesired phenomenon and keep the buckling directions of the negative-stiffness beams in the symmetric pattern in the oscillation process, the excitation accelerations are limited to a certain level (amplitude smaller than 0.25 g) in experiments. Although the base excitation is not very large, the SBCM developed shows good sensitivity to ultra-low wide bandwidth frequencies in experiments. The expected dynamic characteristics of the SBCM are verified.

The vibration stability of the SBCM structure with asymmetric buckling directions of the negative-stiffness beams was also explored in a quick testing. The suspended mass block was stimulated to vibrate manually and the oscillation motion was observed and recorded with a high-speed camera. The asymmetric buckling directions of the negative-stiffness beams are shown in Fig. 5.16(a) and (b) which are compared with the symmetric buckling direction as shown in Fig. 5.16(c)). Fig. 5.17 presents the orientations of the mass block at three displacement positions (i.e. $x = 5 \text{ mm}, 0 \text{ mm and} - 5 \text{ mm}$) corresponding to the three buckling conditions recorded by the high-speed camera in the testing. It was observed that the suspended mass block oscillated straightly up and down in the vertical direction as indicated in Fig. 5.17(a) to (c) and Fig. 5.17(d) to (f). It was the same with the oscillation condition where the buckling directions of the negative-stiffness beams were symmetric as shown in Fig. 5.17(g) to (i). No rocking or wobbling motion of the mass block was observed.

(a)   (b)   (c)
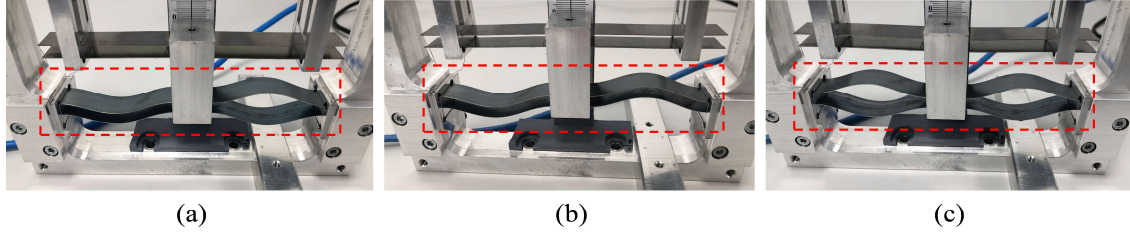
Fig. 5.16. (a)Type-I asymmetric, (b) Type-II asymmetric, and (c) symmetric buckling directions of the negative-stiffness beams on left/right hand side of the SBCM structure.

(a)   (b)   (c)

(d)   (e)   (f)

(g)   (h)   (i)
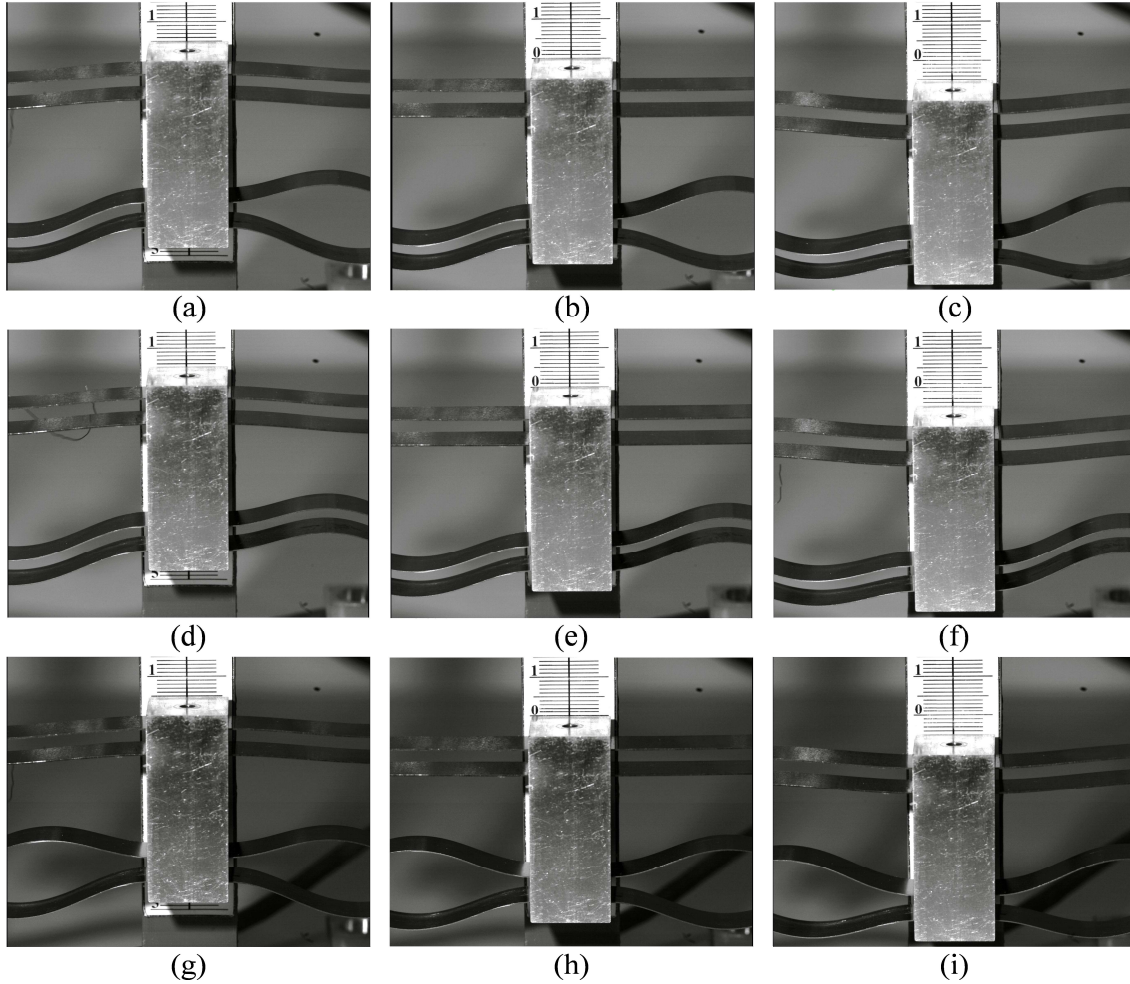
Fig. 5.17. Orientation of the mass block in the SBCM with Type-I asymmetric buckling directions of the negative-stiffness beams at displacement of (a) 5 mm, (b) 0 mm, (c) −5 mm; Orientation of the mass block in the SBCM with Type-II asymmetric buckling directions of the negative-stiffness beams at displacement of (a) 5 mm, (b) 0 mm, (c) −5 mm; Orientation of the mass block in the SBCM with symmetric buckling directions of the negative-stiffness beams at displacement of (a) 5 mm, (b) 0 mm, (c) −5 mm. (Recorded by the high-speed camera)

This is because the positive-stiffness component (two double parallelograms connected in parallel) has one degree of freedom in the vertical direction only and other motions (including

the rotation of the suspended mass) are restricted. Guided by the positive-stiffness component, the suspended mass block vibrates straightly in the vertical direction only and does not wobble regardless of symmetricity of the buckling direction of the negative stiffness beams. In this research, two main measures are adopted to keep the mass block vibrating straightly in the vertical direction. Firstly, the negative-stiffness component is designed to be in a bi-symmetrical pattern (using four beams). Secondly, the positive-stiffness component acts as guiding part which permits the vertical motion only and restricts other motions.

5.3.7 Super-harmonic and sub-harmonic oscillations

In the dynamic experiments, interesting oscillation phenomena, i.e. super-harmonic and sub-harmonic oscillations [309], have been observed at certain frequencies. Voltage-output curves recorded by PC oscilloscope clearly show the change of the response frequencies of the device compared with the excitation frequencies due to these two subtle oscillation phenomena. Two examples of super/sub-harmonic oscillations are marked in their corresponding voltage-frequency curves in Fig. 5.18(a). The super-harmonic oscillation happens at 6.5 Hz and 0.2 g when the length of the positive-stiffness beams is 39.2 mm and the preloading is 1.8 mm. The voltage across the internal resistance of the digital oscillloscope in the time domain is shown in Fig. 5.18(b). In this case, the oscillation frequency of the mass block is twice of the base excitation frequency. This is further verified with the fast Fourier transformation (FFT) graph of the super-harmonic oscillation as shown in Fig. 5.18(d) and there are two voltage peaks at 6.49 Hz and 12.99 Hz, respectively. The sub-harmonic oscillation appears at 12.14 Hz and 0.2 g over the lower relative displacement amplitude domain when the device is in the static-balancing mode. The oscillation frequency of the mass block is half of the base excitation frequency. The voltage of the sub-harmonic oscillation in time domain is shown in Fig. 5.18(c). Two voltage peaks can be seen at 6.08 Hz and 12.13 Hz respectively in the FFT graph in Fig. 5.18(e).

Although the force-displacement relationship of the SBCM has odd-order nonlinearity, it is observed in the experiments that the oscillation frequencies of super-harmonic and sub-harmonic are twice and half of the base excitation frequency. This seems contradictory. However, this may be explained by the findings in [309] where super/sub-harmonic oscillations with odd frequency ratios can only be generated from force-displacement relationship with
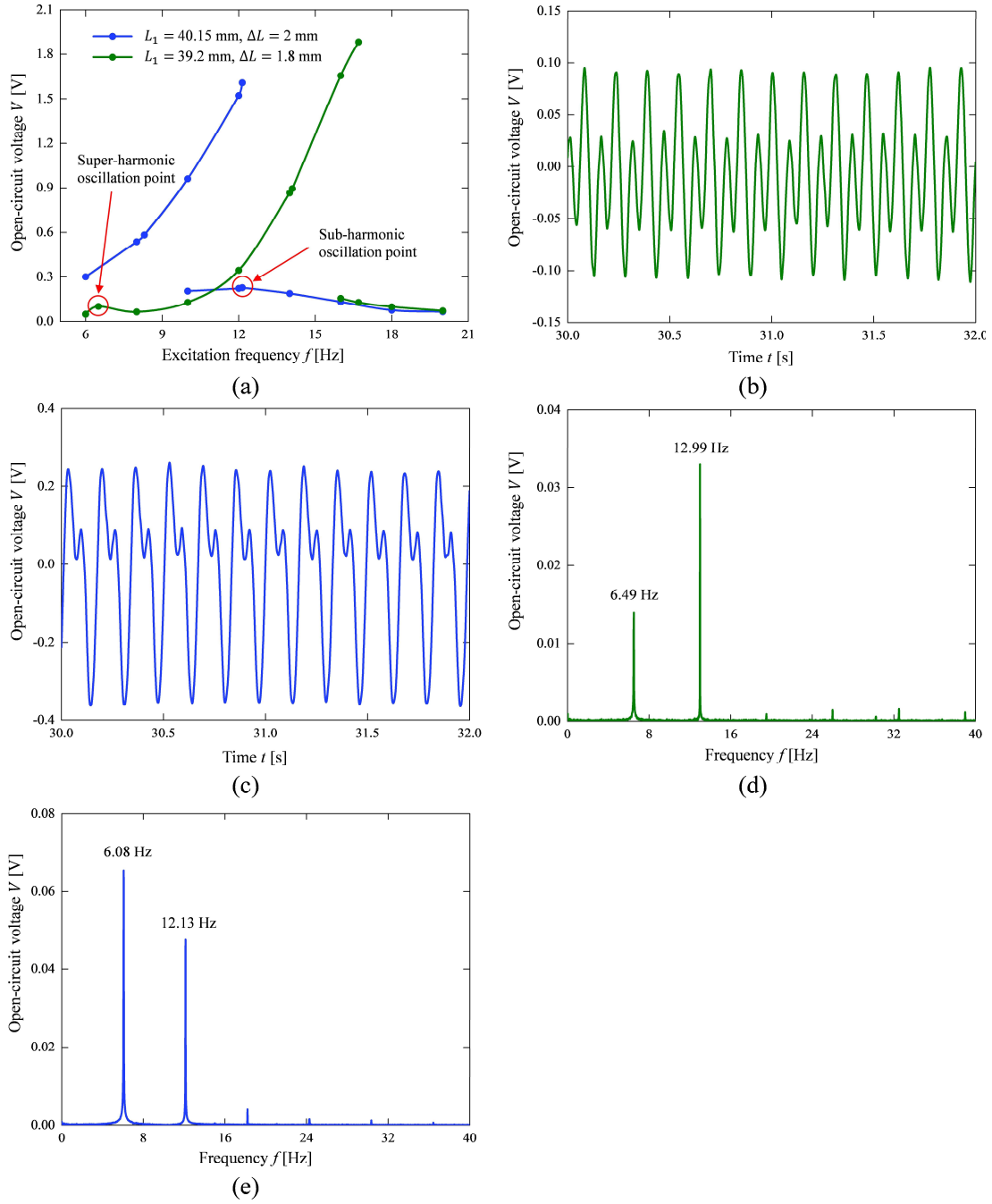
Fig. 5.18. (a) The voltage of the prototype with two sets of geometric parameters (static balancing: $L_1 = 40.15$ mm, $\Delta L = 2$ mm; Mono-stable: $L_1 = 39.2$ mm, $\Delta L = 1.8$ mm) with respect to excitation frequency; (b) The voltage of super-harmonic oscillation of the prototype at 6.5 Hz, 0.2 g ($L_1 = 39.2$ mm, $\Delta L = 1.8$ mm) in time domain; (c) The voltage of sub-harmonic oscillation of the prototype at 12.14 Hz, 0.2 g ($L_1 = 40.15$ mm, $\Delta L = 2$ mm) in time domain; (d) Fast Fourier Transform of the super-harmonic oscillation voltage in frequency domain. (e) Fast Fourier Transform of the sub-harmonic oscillation voltage in frequency domain. (Coloured curves)

odd-order nonlinearity, while super/sub-harmonic oscillations with even frequency ratios can be generated from force-displacement relationship with either odd-order or even-order nonlinearity [309]. For the nonlinearity order of 5, the frequency ratio of super/sub-harmonic oscillation can be 2 or 1/2, respectively, which is observed in the dynamic experiments. Neglecting the even-order terms in the fitted force-displacement curve from experimental results may be another possible reason that the super-harmonic and sub-harmonic resonances are of order 2 and half, respectively. Compared with the voltage outputs at adjacent frequencies in Fig. 5.18(a), super/sub-harmonic oscillations have higher voltage outputs which is favorable in energy harvesting. Note that those super-harmonic and sub-harmonic oscillation phenomena are trivial to compromise our claim of ultra-low wide bandwidth energy harvesting.

5.4 Remarks

In the dynamic experiments, it has been verified that the SBCM developed in this thesis has a wide bandwidth in the ultra-low frequency range with low excitation accelerations. The applicability of this SBCM in PVEHs has also been preliminarily demonstrated with the electric outputs from the integrated PVDF films. Based on the overall review on the dynamic experiments, the following issues should be highlighted, which remain unexplored or not fully explored.

1) Limitations exist in the dynamic experiments using the shaker. For example, the excitation scenarios of frequencies lower than 6 Hz and random excitations could not be applied in experiments. The sensitivity of the SBCM to harmonic base excitations with low accelerations and low frequencies below 6 Hz was explored and verified by FEA simulations in Section 4.3. The FEA simulation results can be seen as supplementary proof of the theory in the ultra-low frequency range. The dynamic performance of the SBCM under irregular vibrations will be investigated by FEA simulations in the next chapter.

2) It is noted that the optimal attachment positions and pasting process of PVDF films, power-management circuit design and optimization were not considered in the piezoelectric energy harvesting demonstration. Nonlinear oscillators for PVEH requires more complex interface circuits [310]. Therefore, the obtained electric outputs may not be optimized. However, an optimized circuit will not be able to improve the power by a significant order either despite

being able to make it more regularized, which can have an impact on micro-nano systems and even in IoT or edge computing hardware.

3) Other possible improvement points include displacement measurement, beam length adjustment, preloading approach and miniaturization. More specifically, laser micrometers can be used for more accurate displacement measurement instead of the high-speed camera. The length of the positive-stiffness beams can be micro-tuned with a well-designed displacement-reduction mechanism. In addition, preloading process can be completed more efficiently with bi-stable compliant mechanisms using the method as reported in [79], which is beneficial for both miniaturization and monolithic fabrication. With further optimized design, the SBCM proposed can be fabricated with MEMS technology.

4) The definition of 30%-H_{max} bandwidth has been proposed for the evaluation on the dynamic performance of this new type of nonlinear SBCM-based PVEH considering the high displacement response at the start of excitation. Its frequency response can be underestimated based on the traditional 3-dB bandwidth principle given from the signal processing aspect.

5) Due to its outstanding compatibility, the SBCM developed in this research can be combined with other energy conversion mechanisms, such as electromagnetic, electrostatic, triboelectric, and not limited to piezoelectric harvesters. The low frequency systems typically correspond to built infrastructure systems which are degrading [311] and requires significant attention in terms of monitoring. Considering the structure as a mechanical and unknown filter, with uncertainties, the harvested energy can be used as not only for health monitoring of such structures but also for analyses of extreme value responses [312, 313]. The proposed system can thus work as a controllable device in this regard, for detection of anomalies and other features of interest, along with system identification in some circumstances. Then, the low frequency harvesting with nonlinearity as a calibrated control mechanism can give rise to estimates of the structure linked to its lifetime performance, risk and related intervention options.

6) This research is mainly focused on the dynamic displacement response of the SBCM under harmonic base excitations. The electric output of the SBCM-based PVEH is presented as a demonstration only and it is not modelled in this research. Modelling on the electric output of the SBCM-based energy harvesters combined with various energy-conversion mechanisms will be a part of the future work referring the prior outstanding work in this field [314-316].

7) No static/fatigue failure of the compliant beams was observed in both static and dynamic experiments with the preloading displacement of 2 mm, although theoretical analysis (in Section 3.5.3) and FEA results suggested that the maximum stress of the negative stiffness beams was beyond the tensile strength of the material (in Section 5.1.3). It is noted that the loading cycle times of the compliant beams in experiments are very limited and smaller than their actual fatigue life. This is acceptable in this research as a demonstration. For the static condition, the actual maximum stress along the deformed beams is smaller than the yield strength of the material, which is not accurately modelled in this research. The static/fatigue strength of the SBCM structure will be carefully checked before practical applications in the future.

5.5 Summary

An SBCM prototype is fabricated in an assembling manner and its detailed structures are introduced in this chapter. The static and dynamic characteristics of the SBCM are experimentally verified using the prototype fabricated. The applicability of the SBCM in vibrational energy harvesting is demonstrated by integrating piezoelectric transducers which are composed of PVDF films. Both displacement responses and electric outputs of the SBCM-based PVEH under harmonic base excitations are presented and analyzed. Comparison experiments with a linear piezoelectric cantilever is also carried out. In addition, influence of the buckling symmetry of the negative-stiffness beams on the dynamic stability of the mass block is tested. Conclusions are drawn and summarized as follows based on the experiments.

1) Fabricating the SBCM prototype in the assembling manner is reasonable in this investigation study. It not only reduces the cost in fabrication and maintenance, but also allows fine adjusting of the geometric parameters for desired static and dynamic characteristics.

2) Static experiments show that the SBCM in the static balancing mode owns a unique force-displacement relationship. It stays in equilibrium in a limited continuous displacement range (from -1 mm to 1 mm in the experiments) around the origin and shows stiffness nonlinearity in the wider displacement range.

3) It is verified experimentally that the SBCM is sensitive to ultra-low frequencies (starting from 6 Hz due to the frequency limit of the shaker) with weak accelerations (from 0.1 g to 0.25

g) in a wide bandwidth (larger than 6.75 Hz at 0.25 g). This is further emphasized by the comparison with a cantilever oscillator which a very narrow effective bandwidth in the higher frequency range. Therefore, the SBCM provides a practical structural solution in enhancing the dynamic performance of vibrational energy harvesters.

4) The SBCM also has reliable vibrational stability independent of the buckling directions of the negative stiffness beams. This is due to the guiding function of the positive-stiffness component.

Chapter 6 Application Case Studies

It has been verified analytically, numerically and experimentally that the SBCM structure proposed is sensitive to ultra-low wide bandwidth frequencies with weak excitations in previous chapters. The SBCM structure also owns advantages of easy fabrication and good scalability due to the general features of CMs. The unique static and dynamic features of the SBCM are independent of the dimensions. This enables the SBCM to be applied in various scenarios in different scales. Two application examples of the SBCM in different dimensions are demonstrated in this chapter using FEA simulations with COMSOL Multiphysics®. The first application scenario is that the macro SBCM (with dimensions given in Chapter 3) is integrated inside a Lagrangian oceanic drifter for harvesting vibrational energy from ocean waves. The second application example is that the SBCM is miniaturized into MEMS scale for vibrational energy harvesting. The static and dynamic characters of the SBCM structure in both macro and micro scales in these two application cases are presented and assessed in the following sections.

6.1 Application in oceanic drifters for harvesting energy from ocean waves

In the context of climate change, there are surging requirements on monitoring and predicting the evolution of the oceans for preserving the ocean environment and its bio-diversity [317, 318]. In order to collect the relevant oceanographic data, such as ocean currents, temperature, salinity, etc., Lagrangian drifters are commonly used [319] and such an oceanic drifter is shown in Fig. 6.1. These oceanic drifters are expected to be self-powered because they are ocean-widely distributed for a long period. Self-powering can reduce the expenses in the maintenance tasks of battery replacement and expand the working life time. Solar energy [320] and wind energy [321] have already be captured and utilized to power drifters. However, sunlight is not available over the night and in cloudy days and wind turbines introduce negative impacts on the dynamic behavior of the drifters [318]. Ocean waves can be ideal additional energy sources.

It is because ocean waves contain a massive amount of power at Tera-watt level (10^{12} W) [322] which is sufficient for powering sensors and circuits. In addition, they are ubiquitous regardless of the time, locations and weather for a continuous energy supply.
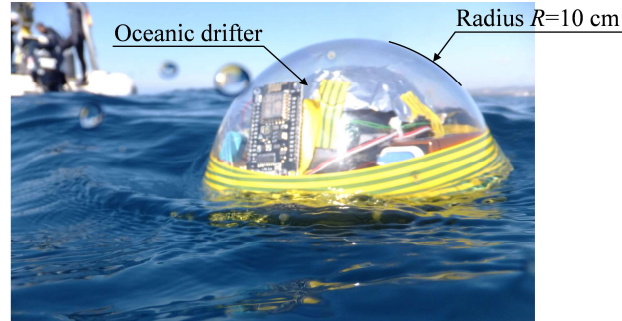
Fig. 6.1. A Lagrangian Drifter developed by Polytechnic University of Catalonia [323].

Ocean waves are mainly wind-generated vibrations on the ocean surface. Their movement features in mixed ultra-low frequencies with small accelerations (typically below few Hz and 1g) [324-326], which makes energy harvesting from the wave motions challenging. Current ocean wave energy harvesters are mainly based on linear oscillators [327, 328], such as pendulums, cantilevers, etc. These traditional structures respond to specific resonant frequencies with very narrow bandwidth, leading to limited energy harvesting capability. The SBCM provides a practical structural solution in this application scenario because of its sensitivity to ultra-low frequencies with weak acceleration in a wide frequency range as introduced in the previous chapters. The applicability of the SBCM into oceanic drifters for harvesting energy from ocean waves is investigated and discussed in this section based on FEA simulation in COMSOL Multiphysics®.

FEA results in Section 4.3 confirm that the SBCM structure responds to harmonic vibrations at ultra-low frequencies (starting from 0.25 Hz) with weak acceleration (0.25 g). As compensations, this section focuses on the dynamic response of the SBCM to more complex excitations, i.e. drifter motion patterns induced by ocean wave excitations with mixed ultra-low frequencies and weak accelerations. In addition, the electric energy generation capability of the SBCM-based harvester integrated in the ocean drifter is demonstrated by introducing PVDF films in the FEA model. Both the displacement response and the electric output from the FEA results are presented and analyzed. The FEA simulations in this section are also

supplement verifications of random excitation condition for dynamic experiments in Chapters 4 and 5 where only harmonic excitations were considered.

6.1.1 Motion patterns of oceanic drifters induced by ocean waves

A drifter floating on the ocean surface has motions in six DOF [325]. The movement in the vertical direction (gravity direction) contains most vibrational energy. The SBCM has only one DoF in the functional direction and other degrees of freedom are restricted as introduced in Chapter 3. Therefore, the SBCM is supposed to be installed vertically inside the drifter to align its sensitive direction with the drifter vertical motion for optimum dynamic performance. Only the vertical motion patterns of the drifter are thus considered in the following FEA simulations. The outer diameter of the spherical drifter is 20 cm in this case study. Dimensions of the SBCM are then kept identical with those shown in Table 3.3. In the future application, the rectangular outer frame of the SBCM structure can be replaced with the spherical frame of the drifter for a better integration. In the FEA simulations here, the shape of the outer frame is not changed because it has no influence on the dynamic performance of the SBCM.

The vertical motion curves of the drifter excited by ocean waves are generated with OrcaFlex®. OrcaFlex® is a powerful software for the dynamic analysis on the offshore marine systems [329]. In the settings, the external diameter of the drifter is 20 cm and its mass is 3.63 kg. Two typical ocean waves are considered and the relevant parameters are listed in Table 6.1. The ocean wave A is composed of two airy sub-waves with different amplitudes and frequencies. The ocean wave B is in the Jonswap type which is very close to the real ocean waves. The vertical motion patterns of the drifter induced by these two ocean waves and their frequency spectrum curves by FFT are presented in Fig. 6.2. The Jonswap wave has smaller amplitudes but denser vibrations compared with the synthesized ocean wave. It is shown in Fig. 6.2(a) that the maximum vertical displacement amplitude of the drifter reaches 1.2 m driven by the synthesized airy wave (wave A). Two dominant frequencies of 0.3 Hz and 1.25 Hz are observed in the frequency spectrum as shown in Fig. 6.2(c). The displacement amplitude of the drifter reaches the maximum of 0.7 m when it is excited by the Jonswap ocean wave (wave B) as shown in Fig. 6.2(b). Mixed dominant frequencies around the ultra-low frequency of 0.25 Hz are observed in the frequency spectrum corresponding to the Jonswap wave as shown in Fig. 6.2(d). The maximum acceleration corresponding to the synthesized airy wave is 0.25g while the maximum acceleration corresponding to the irregular Jonswap wave is about 0.8 g. These

drifter motion patterns are imported into COMSOL Multiphysics® as the base excitation singles applied on the SBCM for investigating its dynamic responses. The original data corresponding to these drifter motions patterns are given in Appendix C.

Table 6.1. Parameters of the ocean waves in OrcaFlex®.

Wave	Sub-wave contained	Model	R/I	Direction [°]	Significant Wave Height [m]	Significant. Wave Period [s]
A	1	Airy	Regular	0°	0.7 m	3.5 s
	2	Airy	Regular	0°	1.5 m	8 s
B	1	Jonswap	Irregular	0°	0.8 m	3 s
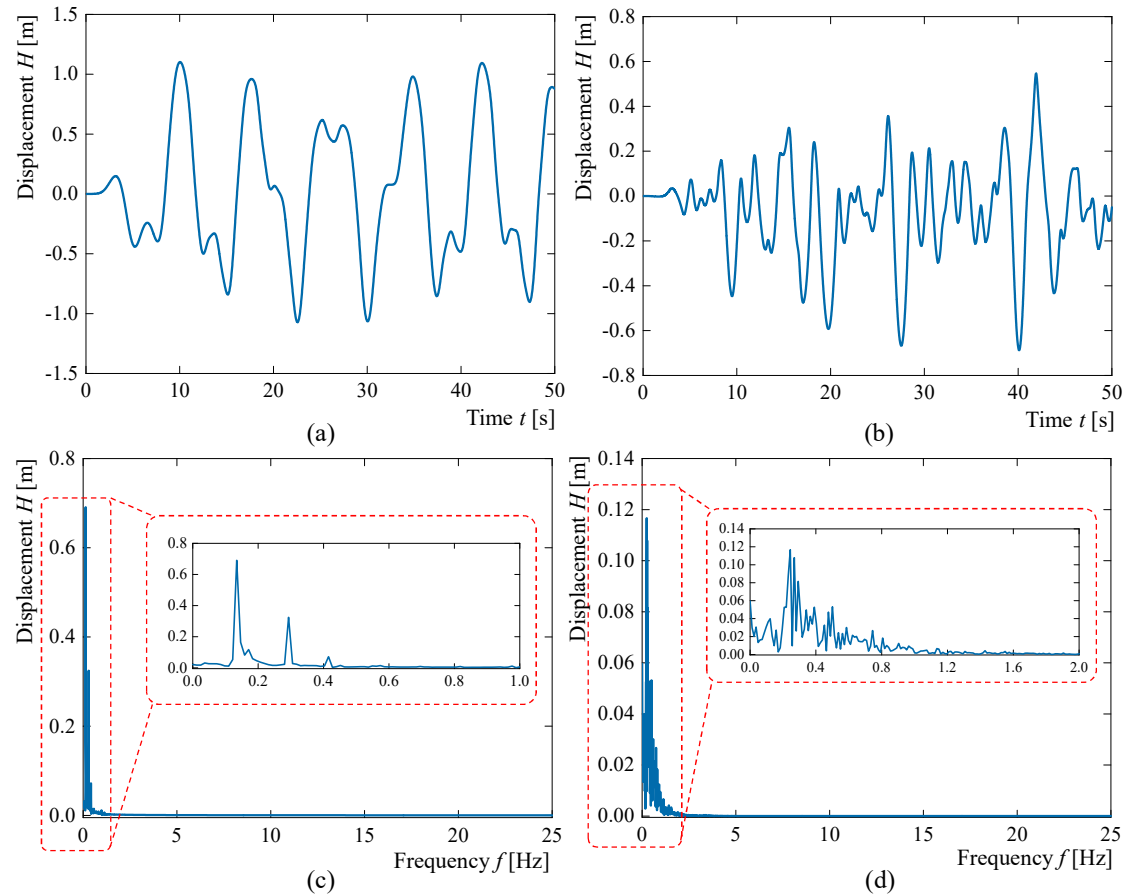
Fig. 6.2. Vertical motion patterns of the oceanic drifter induced by the (a) Synthesized airy ocean wave and the (b) Jonswap ocean wave (Note: These drifter motion data corresponding to different ocean waves are from EnABLES Transnational Access Project (No. 106) collaborating with UPC in Spain). Frequency spectrum curves of the drifter vertical motion patterns by FFT corresponding to the (c) synthesized airy wave and the (d) Jonswap ocean wave.

6.1.2 FEA model with integrated PVDF films

A Preliminary SBCM-based PVEH is created with piezoelectric materials attached on the flexural beams. PVDF films are adopted here as piezoelectric materials for the consistency with the prototype presented in Chapter 5. Two PVDF films are added on the positive-stiffness beams in the near-root area close to the central fixed block. These PVDF films are symmetrically arranged to keep the internal force on the left/right hand side balanced. The FEA model of the SBCM-based PVEH with PVDF materials (each with dimensions of 20 mm × 15 mm × 0.2 mm) is shown in Fig. 6.3. The influence from the PVDF films on the stiffness of the compliant beams is small though, it is not negligible. The length of the positive-stiffness beams, L_1, is finely tuned from 42 mm to 42.15 mm in the trial and error method for static balancing. Other geometric parameters remain unchanged. The force-displacement curve obtained in the FEA simulation is shown in Fig. 6.4. The fitted 5th order polynomial of the force-displacement relationship is also given in Eq.(6.1). The R^2 coefficient of this polynomial fitting is 99.98 % indicating a high accuracy.
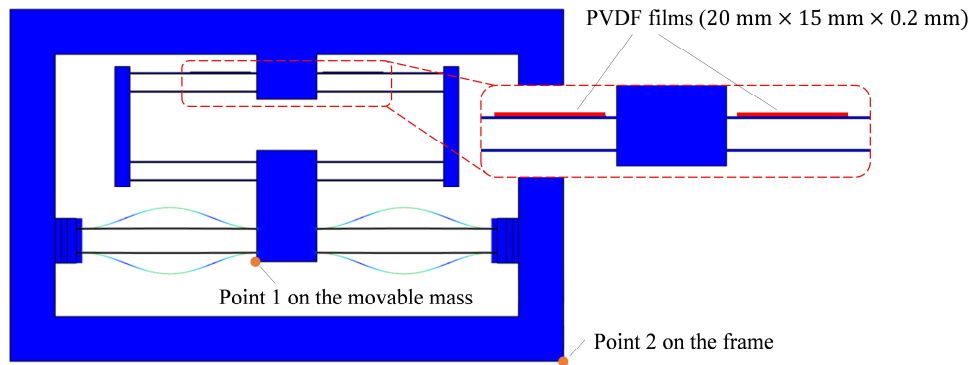
Fig. 6.3. FEA model of the SBCM with PVDF material added for voltage output demonstration.

$$F_{SBCM}(x) = 0.01233x + 0.001678x^3 + 0.000008239x^5 \qquad (6.1)$$

Electric energy is expected to be generated from the piezoelectric materials in the SBCM-based PVEH under base excitations. The coupling among multiple physics, i.e. solid mechanics, electrostatics and electrical circuit, has to be considered in the FEA model. The detailed settings for this FEA simulation task in COMSOL Multiphysics® are summarized and introduced in the next section. The settings can be used as tutorials for the researchers interested in this work or facing similar simulation problems.
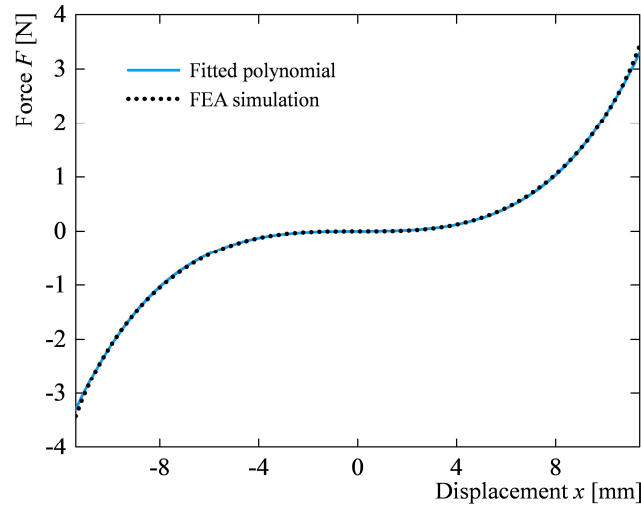
Fig. 6.4. Force-displacement curve of the SBCM with PVDF films added in the FEA model.

6.1.3 Settings for multi-physics FEA simulations on the SBCM structure excited by oceanic drifter displacement patterns

The SBCM-based PVEH is base-excited by oceanic drifter displacement patterns imported from external sources in the FEA model in COMSOL Multiohysics®. PVDF films integrated in the SBCM structure are bended together with the compliant beams when the mass block is excited to vibrate. Electric outputs are then generated from the PVDF materials by the piezoelectric effect. Both relative displacement responses and electric outputs of the SBCM-based PVEH in the FEA results are obtained and recorded for further analysis.

This multi-physic FEA model in time domain includes two Study Steps which are similar with those introduced in Section 4.3.1. In the first Stationary Step, static balancing is achieved by preloading the negative-stiffness beams to buckle. In the second Time Dependent Step, the 2D model of the SBCM-based PVEH is base-excited based on the imported drifter displacement patterns. The common settings in this FEA model have been introduced in the previous chapters and they are not repeated here. There are two main setting tasks to address for desired simulation results. They are settings for base-exciting the SBCM-based PVEH with imported displacement data from external sources and settings for coupling the multiple physics for relative displacement responses and electric outputs. The basic settings, such as creation of the geometries, selection of the materials, meshing, are not introduced here due to the widely available tutorials online. Detailed settings of the two setting tasks are summarized and presented in Appendix D in detail.

6.1.4 Selection of the external load resistance in the FEA model

The selection of the load resistance in the electric circuit of the FEA model is discussed in this sub-section. The equivalent electric circuit of the SBCM-based PVEH is schematically shown in Fig. 6.5. According to the theory that the maximum power output is obtained when the external load resistance is equal to the internal impedance, the optimum load resistance can be predicted with the Eqs. (5.4) and (5.5). The permittivity of the PVDF film, ε_r, is 9.3 in the default settings in COMSOL Multiphysics®. The permittivity of the free space, ε_o, is 8.85×10^{-12} F/m. In the FEA model, the size of each PVDF film is 20 mm $\times$ 15 mm $\times$ 0.2 mm. Therefore, the optimum external resistance of the circuit is theoretically calculated as 130 MΩ based on the Eqs. (5.4) and (5.5) [304] when the working frequency is 5 Hz.
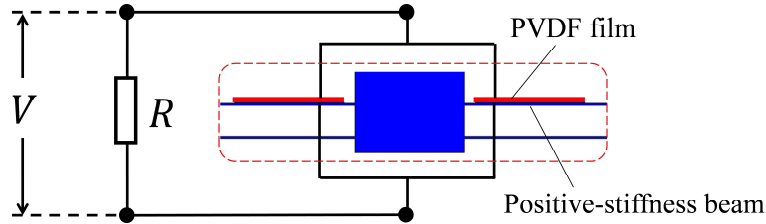
Fig. 6.5. Equivalent circuit of the SBCM-based PVEH in FEA simulation.

The optimum resistance can also be determined based on the FEA simulation in a targeted resistance range. The targeted resistance range is set from 0.1 MΩ to 1000 MΩ in the simulation study according to the theoretical optimum resistance of 130 MΩ. The SBCM-based PVEH with a given load resistor in the electric circuit is under sinusoidal base excitation at 5 Hz, 0.5 g in the time-domain simulation. The voltage across the external resistor in time domain is obtained and recorded. An example of the voltage output curve across the load resistance of 1 MΩ in the first 20 periods is presented in Fig. 6.6. The RMS voltage, V_{RMS}, is calculated based on the voltage curve in the last 10 periods where steady-state oscillation is assumed to be reached. The average power, P_{AVE}, can then be obtained based on Eq. (5.7). The RMS voltage and average power corresponding to a series of discrete external resistance are obtained and summarized in Table 6.2 using the same calculating method.
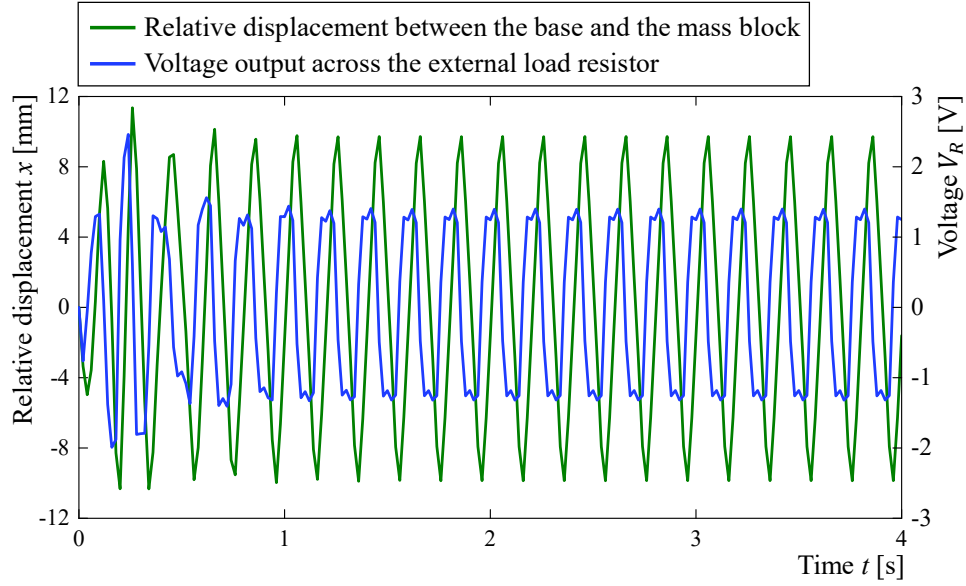
Fig. 6.6. Voltage output over the load resistance of 1 MΩ under and relative displacement between the base and mass of the SBCM-based PVEH the harmonic base excitation in FEA simulation at 5 Hz, 0.5 g. (Coloured curves)

Curves of V_{RMS} and P_{RMS} with respect to the external resistance are plotted in Fig. 6.7 based on the data in Table 6.2. It is shown that V_{RMS} increases along with the external resistance, while the increasing rate gradually decreases. P_{RMS} increases long with the external resistance at the beginning. It reaches the maximum of about 98.66 µW when the external resistance is 140 MΩ. The P_{RMS} starts to decrease when the resistance increases in the range larger than 140 MΩ. Therefore, 140 MΩ is the optimal resistance for the SBCM-based PVEH under the harmonic base excitation frequency of 5 Hz.

A close agreement between the theoretical result (130 MΩ) and the FEA result (140 MΩ) of the optimal external resistance in the electric circuit of the SBCM-based PVEH is observed. The relatively small error can be caused by the dynamic coupling between the mechanical structures and the piezoelectric transducers in the FEA model, which is not considered in the theoretical approximation equation. However, it is also observed in FEA simulations that the voltage output across such optimal external resistances in 100 MΩ level is around 100 V, which is unrealistic. In addition, the electrical circuit utilized in the FEA model is basic and linear, which is not suitable for a nonlinear energy harvester [330]. For the application scenario of harvesting energy from ocean waves with mixed and changing frequencies, an advanced power management circuit is required. However, the design of the optimal nonlinear circuits is out of the scope of this research. Therefore, an external resistance of 1 MΩ, which is the same with

the resistance adopted in dynamic experiments in Chapter 5, is used here to preliminarily demonstrate the energy generation capability of the SBCM-based PVEH excited by oceanic drifter displacement patterns using FEA simulations.

Table 6.2. RMS voltage, V_{RMS} and average power, P_{AVE}, of the SBCM-based PVEH versus external resistance in FEA simulations with the sinusoidal base excitation condition of 5 Hz, 0.5 g.

Resistance [MΩ]	RMS voltage [V]	Average power [µW]	Resistance [MΩ]	RMS voltage [V]	Average power [µW]
0.1	0.12	0.15	120	107.99	97.18
0.5	0.6	0.73	130	112.99	98.21
1	1.21	1.46	140	117.53	98.66
10	12.04	14.49	150	121.63	98.63
50	56.12	62.98	200	137.09	93.96
90	89.67	89.35	500	164.16	53.9
100	96.37	92.88	1000	169.94	28.88
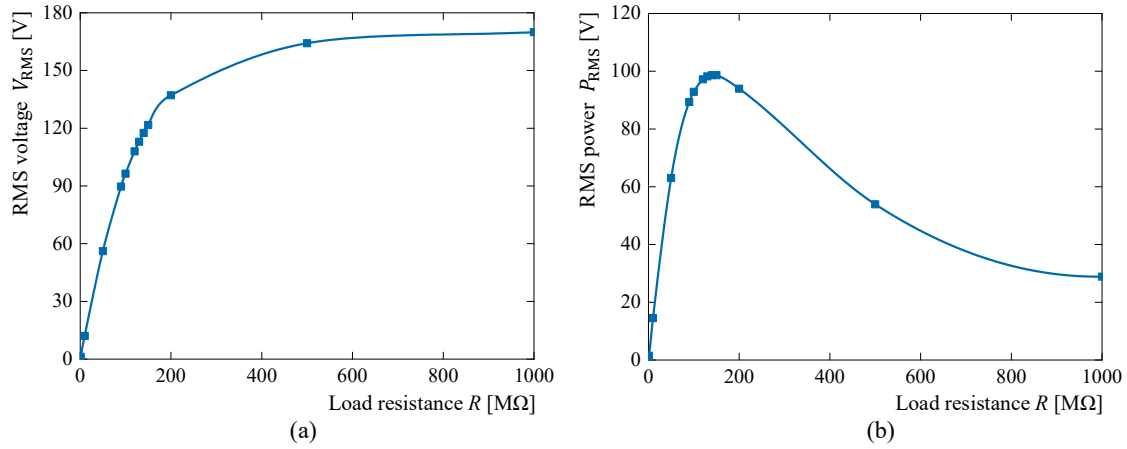
Fig. 6.7. (a) RMS voltage, V_{RMS}, and (b) Average power, P_{AVE}, curves of the SBCM-based PVEH versus the external resistance in FEA simulations with the sinusoidal base excitation condition of 5 Hz, 0.5 g.

6.1.5 FEA results of displacement responses

The FEA simulations on the SBCM-based PVEH under base excitations with imported drifter displacement patterns are conducted in time domain. The displacement responses in the FEA results corresponding to two drifter motion patterns (as shown in Fig. 6.2(a) and (b)) are presented in Fig. 6.8. It is shown in Fig. 6.8(a) and (c) that the absolute displacement curves of

the base and mass are almost overlapped with each other. It is because that the displacement amplitudes of the drifter motion patterns are in meter level and they are much larger than the dimensions of the SBCM device. The relative displacement curves between the frame and the mass block are thus presented separately in Fig. 6.8(b) and (d) for clear illustration. The maximum relative displacement amplitude between the base and mass of the SBCM in the excitation condition of the synthesized airy ocean wave (regular wave) is about 9 mm. In the excitation condition of the Jonswap ocean wave (irregular wave), the maximum relative displacement amplitude reaches about 10 mm.
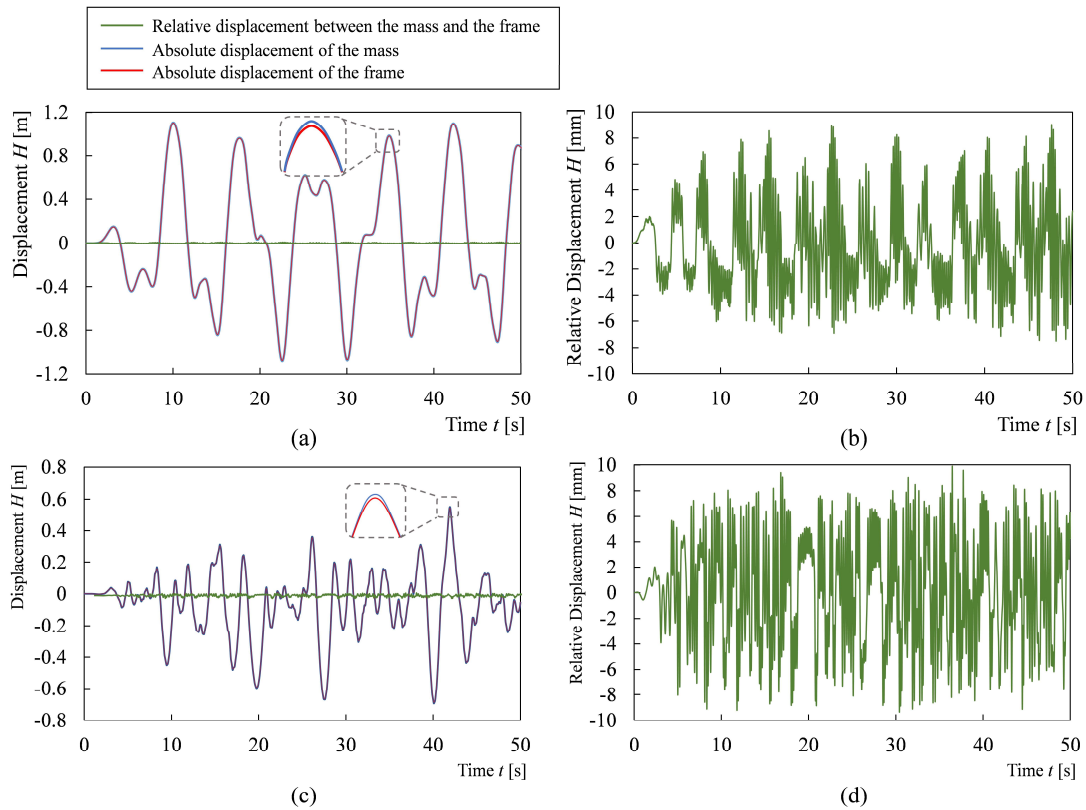
Fig. 6.8. FEA results of the displacement response of the SBCM-based PVEH. (a) Absolute displacements of the frame and mass block and (b) the relative displacement between the frame and the mass block excited by the drifter motion pattern corresponding to ocean wave A; (c) Absolute displacements of the frame and mass block and (d) the relative displacement between the frame and the mass block excited by the drifter motion pattern corresponding to ocean wave B. (Coloured curves)

The large relative displacement between the base and mass (up to 10 mm) in the FEA results confirms the applicability of the SBCM structure in the integration with oceanic drifter. Since the drifter displacement patterns are induced by regular and irregular ocean waves with ultra-low frequencies (mixed frequencies around 0.3 Hz) and weak accelerations (less than 0.8 g here), it is reasonable to conclude that the SBCM structure is sensitive to irregular displacement

base excitations with mixed and ultra-low frequencies with weak accelerations. In particular, the FEA simulations based on irregular displacement patterns compensate the dynamic simulations in Chapter 4 and dynamic experiments in Chapter 5 where only harmonic base excitations are focused. The FEA simulations and previous experimental results lead to a joint conclusion that the SBCM structure responds to both regular and irregular vibrations with ultra-low wide bandwidth frequencies and weak accelerations. Deformation of the compliant beams validates the electric generation of the integrated PVDF films by the piezoelectric effect.

6.1.6 FEA results of electric outputs

Electrical potential difference is generated at the two electrodes of the PVDF films by piezoelectric effect when the PVDF films are bended together with the compliant beams under base excitations. Electric current flows in the circuit and voltage across the external load resistor, V_R, can be measured. The V_R curves with respect to time corresponding to the two oceanic drifter displacement patterns are plotted in Fig. 6.9 based on the FEA results. The relative displacement curves between the mass and the frame are also plotted in the same figures as references to highlight the relationship between the deformation of the beams and the electric energy generated by PVDF films. It is shown in Fig. 6.9(a) that the AC voltage reaches the maximum of 1.37 V in the excitation condition corresponding to the synthesized airy wave. The maximum instantaneous power is about 1.87 µW according to Fig. 6.9(b). In the excitation condition corresponding to the Jonswap ocean wave, the maximum AC voltage is about 1.53 V (as shown in Fig. 6.9(c)) and the maximum instantaneous power is about 2.34 µW (as shown in Fig. 6.9(d)).

The electric outputs and instantaneous power dissipated over the load resistor are obtained in the FEA results corresponding to both the synthesized airy wave and the Jonswap wave. The FEA simulations demonstrate a successful integration of the SBCM-based PVEH in to an oceanic drifter for harvesting energy from ocean waves. The relatively low electric outputs can be attributed to the ultra-low frequencies and weak accelerations of the vibrational sources (ocean waves A and B), the un-optimized electric circuits and not fully defined coupling of the multiple physics. In spite of the low electric outputs, the FEA simulations are still reliable in predicting the trends of the electric energy harvested from the ocean waves. The FEA

simulations also provide guidance and reference for the future experiments and real applications of the SBCM-based PEVH into an oceanic drifter.
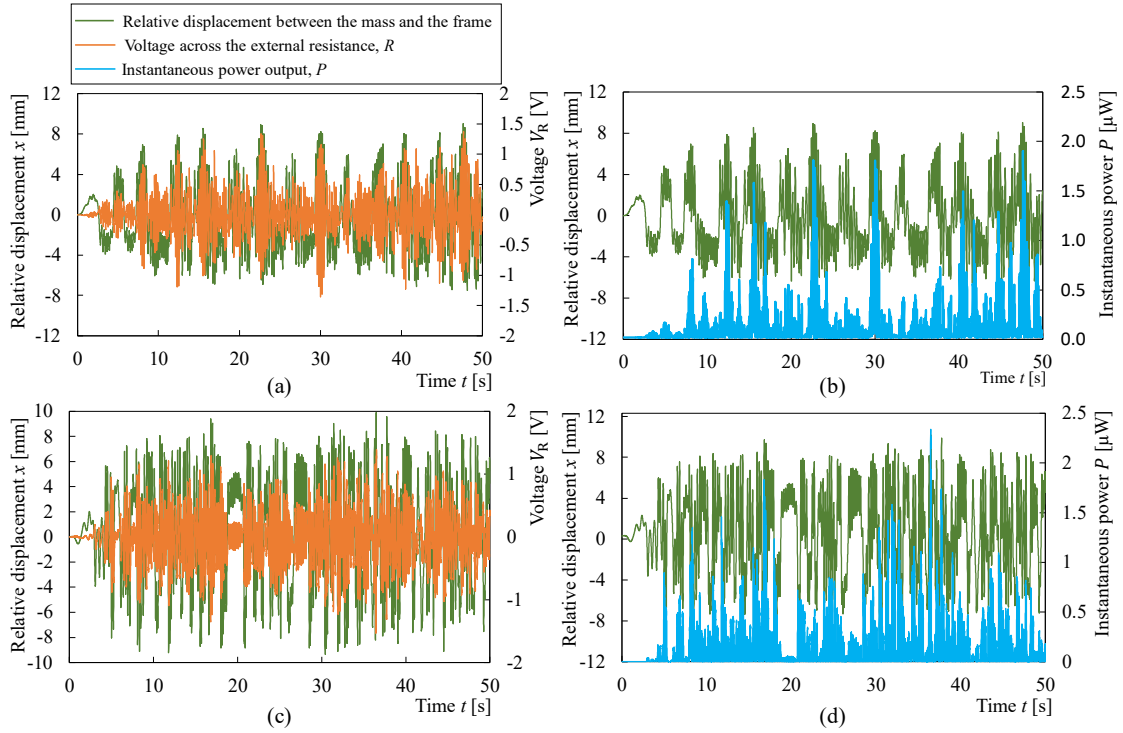
Fig. 6.9. (a) Voltage output across the external resistor and (b) instantaneous power generated over the external resistor together with the relative displacement between the base and mass under the base excitation of oceanic drifter displacement pattern induced by the synthesized airy ocean wave (wave A in Table 6.1) in time domain; (c) Voltage output across the load resistance and (d) instantaneous power generated over the external resistance together with the relative displacement between the base and mass under the base excitation of oceanic drifter displacement patterns induced by the Jonswap ocean wave (wave B in Table 6.1) in time domain. (Coloured curves)

6.1.7 Remarks

The applicability of the SBCM-based PVEH in harvesting energy from ocean waves is demonstrated by FEA simulations in this section. The displacement patterns of the oceanic drifter induced by two typical ocean waves, i.e. a synthesized airy wave and a Jonswap wave, are imported to the FEA model in COMSOL Multiphysics® as base excitation signals. Both the displacement response performance and the electric outputs of the SBCM-based PVEH have been explored in the time domain simulations. The core settings for importing external

displacement patterns as base excitation signals and obtaining electric outputs from piezoelectric materials integrated in the SBCM structure are introduced in detail.

FEA results show that the SBCM proposed is sensitive to both regular and irregular vibrations with mixed ultra-low frequencies and weak accelerations. Expected relative displacement response and electric outputs are obtained in the FEA simulations. Corresponding to the synthesized airy wave (wave A in Table 6.1), the maximum relative displacement between the frame and the mass is about 9 mm. The maximum voltage across the external resistor of 1 MΩ is about 1.37 V and the maximum instantaneous power dissipated over this load is about 1.87 µW. Corresponding the Jonswap ocean wave (wave B in Table 6.1), the maximum relative displacement reaches the maximum of about 10 mm. The maximum voltage output and instantaneous power are 1.53 V and 2.34 µW, respectively.

The buckling direction of the negative-stiffness beams of the SBCM structure did not change under a base excitation condition with the maximum acceleration of 0.8 g in FEA simulations. This is because the negative-stiffness beams are slightly pre-curved as indicated in Fig. 3.8. The pre-curvature helps to keep the buckling direction of the negative-stiffness beams unchanged during oscillation. Another method is to use stoppers to restrict the vibration of the movable mass block in a limited displacement range. The negative-stiffness beams could not get stretched so change of the bucking direction of the beams over the functional displacement range could be avoided. In addition, the stoppers would further improve the dynamic performance of the PVEHs based on the research in [28, 144].

It is noteworthy that the FEA simulation with the irregular displacement pattern can also be regarded as a complement case for the dynamic simulations and experiments in Chapters 4 and 5, where only harmonic base excitations are considered. A comprehensive investigation on the dynamic performance of the SBCM base-excited by both regular and irregular vibrations is then presented in this research. Therefore, the SBCM outperforms linear oscillators [327, 328], such as pendulums and cantilevers, in harvesting vibrational energy from ocean waves.

Limitations exist in this application case study in ocean wave energy harvesting based on FEA simulations. Firstly, in addition to the vertical translational motion, the in-plane rotational motion of the drifter would also contribute to the displacement response of the device and then the electric generation by centrifugal force. However, the rotational motion of the drifter was

not considered in the simulations. This is because the integration of the rotational motion would significantly increase the model complexity and computational cost. Secondly, the electric circuit utilized in the FEA model is linear and simple. An advanced nonlinear electric circuit is required for this SBCM-based PVEH under irregular base excitations. To address these shortages, an enhanced FEA model which includes all types of effective excitations and an advanced electric circuit will be created in the future work.

It should also be noted that this section is originally from EnABLES TA project (No.106: Simulation on the SBCM structure for ocean drifters). This project is collaborated with Polytechnic University of Catalonia in Spain. The settings of the FEA models in COMSOL Multiphysics® are obtained and summarized based on the assistance of the COMSOL Support service.

6.2 Miniaturized SBCM in a MEMS scale for vibrational energy harvesting

One ultimate goal for powering low-energy-cost sensors and electronics is that the vibrational energy harvesters can be integrated on a single chip [331]. This requires the vibrational energy harvesters to be miniaturized significantly and fabricated by MEMS technologies. MEMS vibrational energy harvesters have been reported in the literature [98, 99]. However, these micro oscillators normally have narrow working bandwidths and high natural frequencies due to their linear stiffness and the size effect [97]. These drawbacks lead to a poor energy harvesting performance and make the traditional MEMS-scale vibrational energy harvester less attractive in practical applications.

The SBCM provides a structural solution to these issues of the MEMS-scale vibrational energy harvesters based on its unique static and dynamic characteristics as presented in the previous chapters. In addition, the SBCM structure is friendly to miniaturization. It is because all the solid/compliant parts are contained in a single plane and it thus can be fabricated monolithically. The SBCM structure is miniaturized in the MEMS scale in this section as the main structure of vibrational energy harvester on chip. Both the static and dynamic performances of the MEMS-scale SBCM are investigated based on FEA simulations. Note that the detailed fabrication process and techniques of the micro SBCM from the perspective of MEMS technologies are not focused in this section.

6.2.1 Design of the SBCM in a MEMS scale

The miniaturized SBCM structure in the MEMS scale is designed following the guideline as shown in Fig. 3.5. Key geometric parameters of the 2D FEA model of the MEMS-scale SBCM created in COMSOL Multiphysics® are illustrated in Fig. 6.10. The footprint size of the SBCM is 16 mm × 8 mm, which is 128 mm². The thickness of the model is set as 0.5 mm. Silicon is chosen as the structural material of the MEMS-scale SBCM model. This MEMS-scale SBCM then can be fabricated using a silicon wafer with a standard thickness of 525 µm. Static balancing is finally achieved by finely adjusting the geometric parameters of the compliant beams. These geometric parameters are listed in Table 6.3. Note that this set of geometric parameters is one example of the many possible geometric solutions for achieving static balancing of the MEMS-scale SBCM device. The geometric parameters can be determined based on the specific application conditions. The following analysis is carried out based on the static balancing achieved corresponding to the geometric parameters listed in Table 6.3.
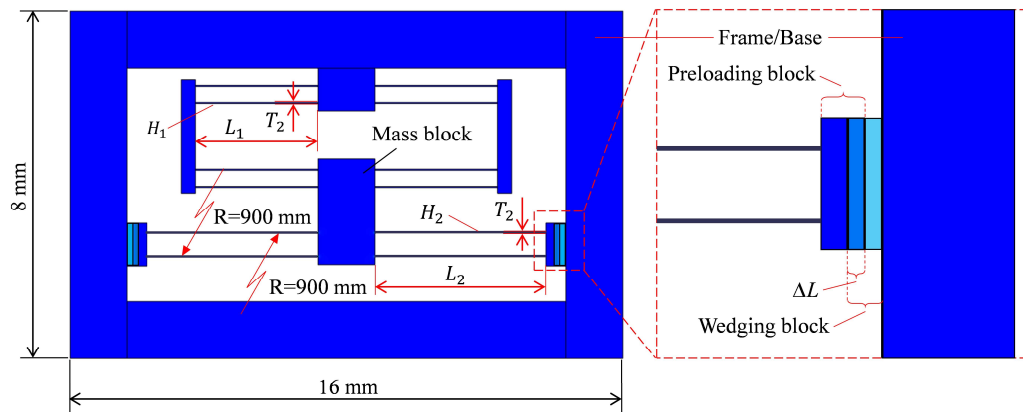
Fig. 6.10. 2D FEA model of the miniaturized SBCM in the MEMS scale and key geometric parameters.

Table 6.3. Geometric parameters of the MEMS-scale SBCM with static balancing achieved.

Positive-stiffness component		Negative-stiffness component	
Length L_1	4.286 mm	Length L_2	6 mm
Thickness out of plane H_1	500 µm	Thickness out of plane H_2	500 µm
Thickness in plane T_1	20 µm	Thickness in plane T_2	15 µm
———	——	Preloading ΔL	30 µm

The force-displacement curve of the MEMS-scale SBCM can be obtained based on the static FEA simulation as introduced in Section 3.4. The targeted displacement range, $\pm 90\% U$, in this simulation is from -0.4 mm to 0.4 mm, where U can be calculated according to Eq. (3.7). The force-displacement curve in the FEA results is shown in Fig. 6.11. The fitted 5th order polynomial of the force-displacement curve is obtained using the Polyfit function of MATLAB® and it is given in Eq. (6.2). The R^2 coefficient of determination is 99.97% indicating a high fitting accuracy. The fitted polynomial curve is also plotted in Fig. 6.11 for direct comparison. Based on the analysis on the stress distribution of the SBCM in Section 3.5.3, it is shown that the maximum stress, σ_{max}, happens at the central and clamped positions of the buckled negative-stiffness beams when the mass block stays at its origin point. The σ_{max} is calculated as 155 MPa based on the Eq. (3.17) and the geometric parameters listed in Table 6.3. It is smaller than the maximum allowable stress of 200 MPa of silicon [220]. The Dynamic performance of the SBCM in the MEMS scale under harmonic base excitation are analyzed based on the force-displacement character obtained.

$$F_{\text{SBCM}}(x) = 0.00002656x + 0.001574x^3 + 0.01771x^5 \tag{6.2}$$
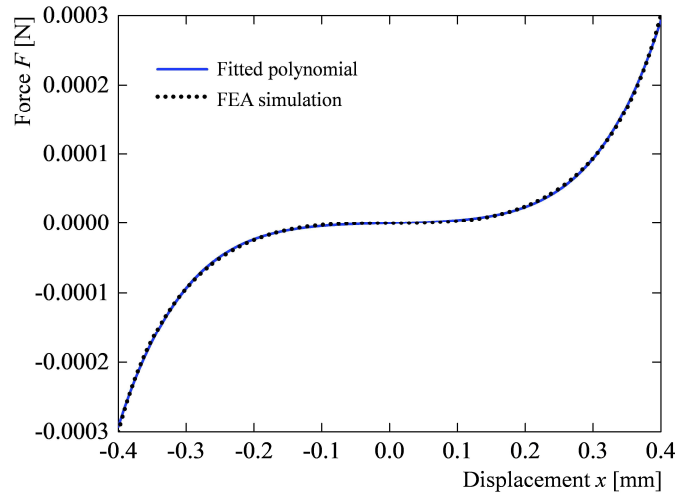
Fig. 6.11. Force-displacement curves of the SBCM in MEMS scale based on the FEA simulations and fitted 5th order polynomial equation.

6.2.2 Dynamic displacement response of the MEMS-scale SBCM in FEA simulations

The dynamic displacement response of the MEMS-scale SBCM under harmonic base excitations is studied using the FEA method as introduced in Section 4.3. In each FEA

simulation, the micro SBCM model is base-excited by harmonic vibrations with discrete frequencies in the targeted range from 0.25 Hz to 50 Hz. The excitation acceleration is set as 0.3 g, which is weak. The relative displacement between the mass block and the frame is then obtained from the FEA results. One example of the relative displacement curve corresponding to the base excitation condition of 20 Hz and 0.3 g is plotted in Fig. 6.12. The relative displacement amplitude, H, is calculated based on the last 10 oscillations which are regarded as steady-state oscillations. The relative displacement amplitude, H, corresponding to the discrete frequencies, f, in the targeted frequency range are obtained and summarized in Table 6.4 based on the FEA simulations. The H-f relationship based on Table 6.4 is represented as discrete data points connected by a solid curve as shown in Fig. 6.13. In addition, the dynamic displacement response of the MEMS-scale SBCM can be theoretically predicted based on the force-displacement polynomial Eq. (6.2). The analytical result is obtained based on the dynamic displacement response model as introduced in Section 4.1 and the numerical model is obtained using ODE45 Runge-Kutta method in MATLAB®. The H-f curves based on the analytical and numerical results are also plotted in Fig. 6.13 for direct comparison.

Table 6.4. Dynamic displacement response of the MEMS-scale SBCM under harmonic base excitations with discrete frequencies from 0.25 Hz to 50 Hz in FEA simulations. (Acceleration: 0.3 g)

Base excitation frequency f [Hz]	Relative displacement amplitude H [mm]
0.25	0.205
5	0.218
10	0.209
15	0.225
20	0.248
25	0.213
30	0.057
35	0.049
40	0.046
50	0.034

A close agreement between the FEA, analytical and numerical results is observed in the frequency range from 0.25 Hz to 25 Hz in Fig. 6.13. In the frequency range higher than 25 Hz, the relative displacement amplitude, H, from the FEA simulations did not reach larger values. This is because no vibrational energy is imported into the oscillation system in the initial condition. Therefore, vibrations with larger amplitudes cannot be stimulated. The close

agreement between the analytical and numerical results is observed in the overall frequency range as shown in Fig. 6.13. The maximum error percentage between the two theoretical methods is 13.7 %, which happens around 11.5 Hz. The errors are caused due to the super-harmonic oscillation phenomenon which is predicted by the numerical analysis while this can be predicted by the dynamic analytical model. According to the analytical and numerical results based on the fitted 5th order polynomial, the maximum relative displacement amplitude, H_{max}, reaches 0.76 mm and 0.77 mm at the jumping frequency, $f_{Jumping-down}$, of 154.79 Hz and 152.92 Hz, respectively. A wide 30%-H_{max} bandwidth of about 137.24 Hz is observed according to the analytical curve. It is concluded based on the FEA, analytical and numerical results in Fig. 6.13 that the SBCM in the MEMS scale is sensitive to a wide range of excitation frequencies starting from an ultra-low value of 0.25 Hz with a weak acceleration of 0.3 g.
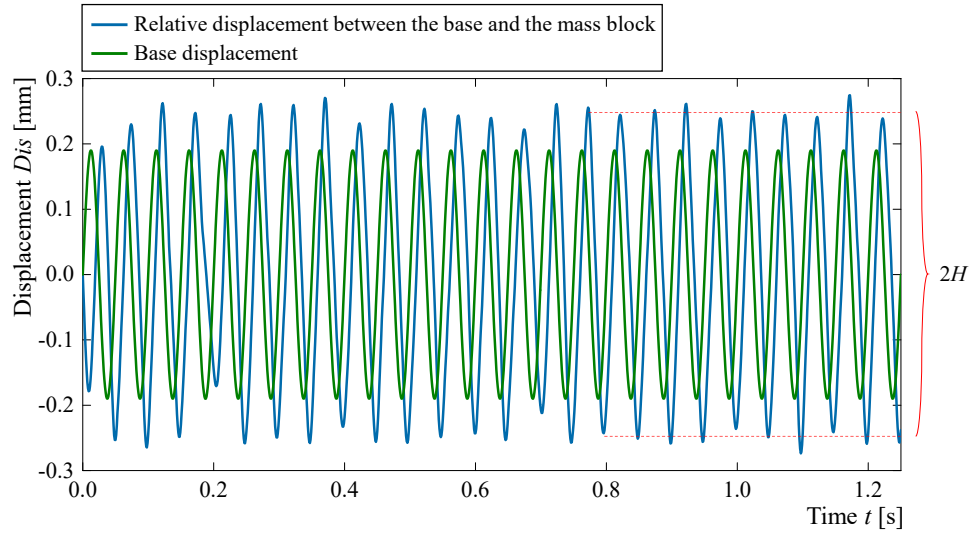
Fig. 6.12. The relative displacement curve between the base and mass block of the SBCM in the MEMS scale corresponding to the excitation condition of 20 Hz and 0.3 g. (Coloured curves)

However, it should be noted that this 30%-H_{max} bandwidth is corresponding to the force-displacement relationship described by the fitted 5th order polynomial (Eq. (6.2)) in the displacement range from -0.4 mm to 0.4 mm. The actual force-displacement relationship of the MEMS-scale SBCM becomes more nonlinear when the relative displacement is beyond $\pm U$. Consequently, the actual dynamic characteristic would be different when the relative displacement is beyond $\pm U$. In order to describe the force-displacement relationship in whole displacement range more accurately, fitted polynomials with higher order (e.g. 7th, 9th order) are required. In addition, both the analytical model and numerical model should also be updated.
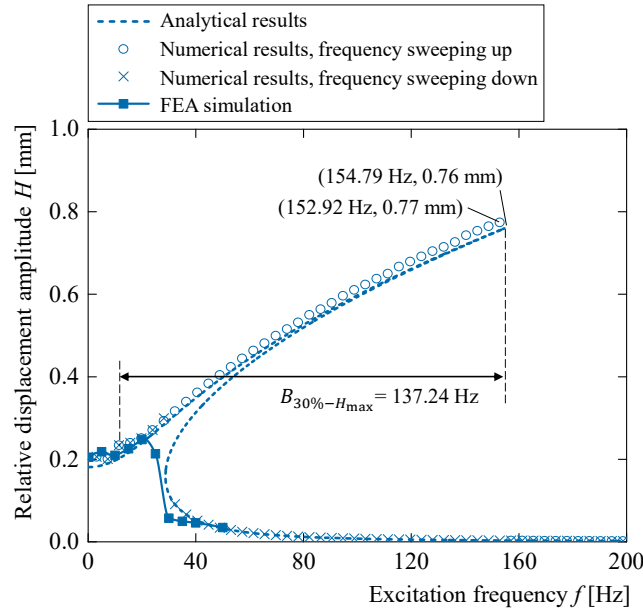
Fig. 6.13. Relative displacement amplitude-excitation frequency curves of the SBCM in the MEMS scale based on the FEA, analytical and numerical results.

6.2.3 A preliminary structural concept of the MEMS-scale SBCM

It has been experimentally demonstrated in Chapter 5 that the SBCM structure in macro scale is applicable for the combination with piezoelectric materials (PVDF films) in vibrational energy harvesting. The PVDF films were manually attached on upper surfaces of the positive-stiffness beams in this experimental demonstration. The MEMS-scale SBCM structure (as shown in Fig. 6.10) shares the same design principle and static/dynamic characteristics with the macro SBCM structure. It is in particular fabrication-friendly with MEMS technologies due to its in-plane and monolithic structure. In the application of the MEMS-scale SBCM in vibrational energy harvesting based on piezoelectric effect, the piezoelectric materials (e.g. AlN [274] and ZnO [266]) and electrode materials (e.g. Titanium and Aluminium [304, 332]) should be attached on the beams' surfaces perpendicular to the bending direction for the best energy generation performance. However, these surfaces of the SBCM structure (as shown in Fig. 6.10) are vertical in the MEMS fabrication process. It is challenging to deposit the piezoelectric and electrode materials in the designated order and with the desired crystal orientation on the lateral walls. Targeting on this problem, a SBCM structure concept based on the stiffness compensation principle is preliminarily proposed and schematically illustrated in Fig. 6.14. This SBCM structure would be suitable for the deposition of piezoelectric and

electrode materials on the beam surfaces in MEMS fabrication process for most energy generation.

In addition, the approach of preloading on the negative-stiffness beams should be carefully considered in the MEMS-scale SBCM structures. Several preloading methods used in MEMS devices have been reported in the literature [80, 333]. Kuppens et al. successfully preloaded a Si beam for achieving negative stiffness with residual film stress by thermal oxidation of silicon in their MEMS device [333]. Barel et al. used hooks to achieve permanent preloading on the negative-stiffness beams [80]. The preloading process was conducted by external shaking or shock on the MEMS device. However, these two preloading methods are permanent. Bi-stable CMs provide an alternative preloading approach, which is reversible. The switch between preloading and unloading on the negative-stiffness beams can be easily achieved by the snap through of the bi-stable CMs. This consequently leads to the switch between the static-balancing mode and mono-stable mode of the MEMS-scale SBCM structure. When the external excitations are severe, the negative-stiffness beam can be un-loaded in advance and the overall oscillator then has large stiffness and a high resonant frequency. This helps to avoid breaking the slim beams and failure of the oscillating device. The applicability of the bi-stable CMs in preloading the negative-stiffness beams has been experimentally verified with a macro SBCM prototype by Kuppens et al. [79] The preloading method based on bi-stable CMs is also adopted in the schematic MEMS-scale SBCM structure as presented in Fig. 6.14.
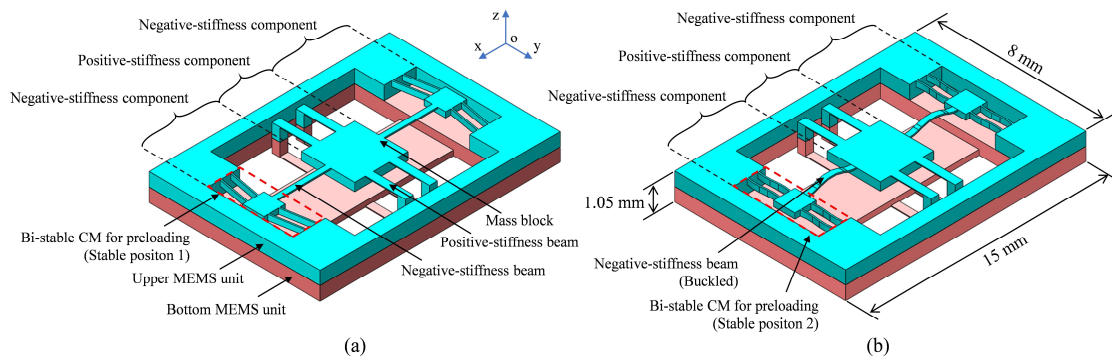
Fig. 6.14. The preliminary structural concept of the micro SBCM for fabrication with MEMS technologies. (a) The MEMS-scale SBCM structure before preloading; (b) The MEMS-scale SBCM structure after preloading.

The conceptual SBCM structure for MEMS fabrication is composed of positive- and negative-stiffness components, which are connected by the central sharing movable mass block. The positive-stiffness component consists two double parallelogram mechanisms in parallel. The

143

positive-stiffness beams are located in two planes of two MEMS units instead of the identical plane. The structure of the positive-stiffness component allows the vibration in the vertical direction only and restricts other un-desired motions. The negative-stiffness component consists of two fixed-guided post-buckled beams in parallel. Preloading on the negative-stiffness beams is achieved by the snap through of the bi-stable CMs from stable position 1 (as shown in Fig. 6.14(a)) to stable position 2 (as shown in Fig. 6.14(b)). Static balancing is then obtained with well-designed geometric parameters of the positive- and negative-stiffness components. Depositing piezoelectric and electrode materials on the beams' surfaces with most stress generation is then feasible with MEMS technologies for vibrational energy harvesting based on the piezoelectric effect. However, one drawback of this conceptual structure is that some basic MEMS assembling operations are required in the fabrication process.

It should be noted that the preliminary structural concept of the MEMS-scale SBCM proposed in this sub-section is demonstrated for the integration of piezoelectric materials for vibrational energy harvesting. Its structural details are still not fully considered or optimized for MEMS fabrication. It is one of many possible MEMS structures of the SBCM-based PVEHs. The structure can vary when the SBCM concept is utilized in vibrational energy harvesting combining with other energy conversion mechanisms, such as electromagnetic, electrostatic and triboelectric.

6.2.4 Remarks

A miniaturized SBCM structure in the MEMS scale is demonstrated in this section. It is aimed at the future integration of the MEMS-scale SBCM on chip as the main structure of vibrational energy harvesters for powering low-energy-cost sensors and circuits. Both the static and dynamic characteristics of the micro SBCM are investigated based on a 2D FEA model in COMSOL Multiphysics®. Static balancing is achieved by finely tuning the geometric parameters of the FEA SBCM model. The analytical, numerical and FEA results verify that the MEMS-scale SBCM is sensitive to ultra-low wide bandwidth excitation frequencies with a weak acceleration. This micro SBCM structure provides a structural solution for effectively lowering the working frequencies of MEMS oscillators to the ultra-low frequency range. It breaks the working frequency limit imposed by the size effect, i.e. smaller sizes lead to higher resonating frequencies [97]. This would significantly improve the dynamic performance of the

vibrational energy harvesters in the MEMS scale. In addition, a conceptual structure of the MEMS-scale SBCM is proposed for the integration of piezoelectric materials by MEMS technologies for vibrational energy harvesting.

It should be noted that this section mainly focuses on the theoretical analysis on the static and dynamic performance of the micro SBCM, while the optimization of geometric parameters and MEMS fabrication technologies are not concentrated. The issues which are not fully discussed are summarized as remarks as follows.

1) The minimum in-plane thickness of the negative-stiffness beams, T_2, of this micro SBCM (as shown in Fig. 6.10) is 15 µm. This might be challenging in MEMS fabrication process due to the large length-thickness ratio. However, the existing micro structures in the literature [333] with similar dimensions confirm the fabrication possibility of such thin beams with MEMS technologies. In the MEMS-scale CM [333] successfully fabricated by Kuppens et al., the length of a compliant beams is 8.673 mm, the in-plane thickness is 24 µm and the out-of-plane thickness is 525 µm (which is a standard thickness of the silicon wafer). In the frequency doubling mechanism [220] fabricated by Machekposhti et al. with MEMS techniques, the length of the compliant beam reaches 22.52 mm, while the in-plane thickness is between 18.75 µm and 24.25 µm. The out-of-plane thickness of the device is 525 µm. A long and thin compliant beam is also seen in the MEMS gravimeter [334] fabricated by Middlemiss et al. The beam length is about 5 mm. Its in-plane thickness and out-of-plane thickness are 5 µm and 200 µm, respectively. These MEMS examples with compliant beams provide references for the fabrication of the MEMS-scale SBCM for vibrational energy harvesting.

2) Optimizing the geometric parameters of the MEMS-scale SBCM for static balancing can be challenging and expensive. This is because the geometric parameters are fixed and cannot be tuned after the monolithic device is fabricated. In addition, the integration of the energy conversion components introduces more design and fabrication complexity. Therefore, sophisticated theoretical designs, high fabrication precision, a large amount of performance testings are required by the successful fabrication of the MEMS-scale SBCM for vibrational energy harvesting.

3) Like the SBCM in macro scale, the MEMS-scale SBCM can also be combined with various energy conversion mechanisms, such as piezoelectric, electromagnetic, electrostatic and

triboelectric. The structural concept of the MEMS-scale SBCM in Section 6.2.4 is proposed considering the combination with piezoelectric effect for vibrational energy harvesting. MEMS SBCMs with diverse structures are to be designed and developed for the integration with different energy conversion mechanisms.

4) The power output from the SBCM-based PVEHs in the MEMS scale is expected at the µW level. This is mainly due to the limit of the energy generation capability of piezoelectric materials. However, the SBCM-based PVEH in the MEMS scale has an ultra-wide bandwidth (up to 100 Hz) in the ultra-low frequency range (above 0 Hz) as indicated in this section. Theoretical analysis and FEA simulations in this section have verified this feature. The working bandwidth of the traditional MEMS-scale PVEHs in literature is much narrower than the frequency bandwidth of the SBCM-based PVEHs in the MEMS scale.

6.3 Summary

This chapter investigates the application of the SBCM structure in both macro and micro scales in vibrational energy harvesting. In the first section, the applicability of the macro SBCM in harvesting vibrational energy from ocean waves is demonstrated with FEA simulations. Integration of the SBCM with an oceanic drifter is considered. The drifter displacement patterns in the vertical direction induced by two typical ocean waves (based on the simulation with Orcaflex®) are imported into the FEA model as base excitation signals. These two ocean waves are a synthesized airy wave (which is regular) and a Jonswap wave (which is irregular). PVDF films are added as piezoelectric transducers in the FEA model for electric outputs under base excitations. The core setting procedures in the FEA simulations are introduced as tutorials and references for researchers interested in this simulation work. The displacement and electric responses of the SBCM-based PVEH are obtained from the FEA results.

In the second section, the SBCM is miniaturized in the MEMS scale for the integration on chip. The MEMS-scale SBCM can be adopted as the main structure of micro vibrational energy harvesters for powering low-energy-cost sensors and circuits. The static and dynamic characteristics of the MEMS-scale SBCM are investigated with FEA simulations and also theoretically analyzed. A conceptual MEMS-scale SBCM structure is proposed considering the

deposition of piezoelectric materials and electrode materials with MEMS techniques for vibrational energy harvesting by piezoelectric effect.

Several conclusions are drawn based on the application case study of the SBCM in both micro and macro scales in this chapter. They are summarized as follows:

1) When static balancing is achieved, the SBCM is sensitive to ultra-low wide bandwidth frequencies with low accelerations regardless of the dimensions and scales. This is verified by the FEA, analytical and numerical results.

2) The SBCM responds to both regular and irregular vibrations with ultra-low wide bandwidth frequencies and weak accelerations. The FEA and theoretical results in this Chapter prompts the experiments in labs and future applications in the open sea of the SBCM-based PVEH in spite of the low electric outputs according to the FEA simulations.

3) The macro SBCM is an effective structural option for vibrational energy harvesters for harvesting energy from ocean waves which have mixed ultra-low frequencies in a wide frequency range with weak accelerations.

4) When miniaturized, the SBCM concept can be of particular interest to researchers active in energy harvesting for MEMS technology. It would provide inspirations on the design of vibrational energy harvesters in the MEMS scale. A conceptual MEMS-scale SBCM structure is proposed in this chapter while the prototype is not fabricated. The design of diverse MEMS-scale SBCM structures for the combination with different energy conversion mechanisms and the fabrication with MEMS technologies will be part of the future work.

Chapter 7 Conclusions and Future Work

In my thesis, a systematic review on state-of-the-art structural methodologies of the PVEHs from the aspect of CMs is first carried out. The frequency gap between the energy harvesting devices and the accessible vibrational sources is observed and targeted as a main issue to be addressed. Therefore, an SBCM structure is proposed as a structural solution to improve the dynamic performance of the vibrational energy harvesters. This SBCM is designed based on the stiffness compensation principle and is composed of a positive-stiffness component and a negative-stiffness component. The positive-stiffness component is embodied using a pair of double parallelogram mechanisms connected in parallel, while the negative-stiffness component is embodied by two pairs of post-buckled fixed-guide compliant beams arranged in bi-symmetry. Static balancing has been perfectly tuned with an FEA model of this SBCM.

A dynamic analytical model of the displacement responses of the SBCM to the harmonic base excitations has been derived based on the averaging method. This starts from describing the nonlinear force-displacement relationship from nonlinear FEA simulations with a 5th order polynomial equation taking into account of odd-order terms only. The accuracy of the dynamic analytical model is confirmed by the numerical analysis. Utilizing an SBCM prototype and setting up an experimental hardware apparatus, comprehensive experiments have been conducted for verifying the analytical model and for critical analysis on the limitations in analytical modelling and experiments. The static and dynamic characteristics of this SBCM are finally investigated analytically, numerically and experimentally, confirming the ultra-low wide bandwidth responses of the SBCM under weak excitations for vibrational energy harvesting.

The applicability of the SBCM in PVEHs is demonstrated with the integration of PVDF films as piezoelectric transducers in dynamic experiments and FEA simulations. Two application cases of the SBCM in macro and micro scales in vibrational energy harvesting are also

investigated. The integration of a macro SBCM in an oceanic drifter for harvesting vibrational energy from ocean waves is first discussed. The displacement and electric responses of the SBCM-based PVEH excited by drifter displacement patterns corresponding to regular and irregular ocean waves are analyzed based on FEA simulations. In the second application case, a miniaturized SBCM in a MEMS scale is considered as the main structure of MEMS-scale vibrational energy harvesters on chip. The static and dynamic characteristics of the MEMS-scale SBCM are explored with nonlinear FEA simulations. A conceptual MEMS-scale SBCM is proposed for the integration of piezoelectric materials by MEMS technologies.

7.1 Contributions

Several outcomes are generated throughout my doctoral research. They can be seen as contributions in the field of structural design and dynamic analysis of vibrational energy harvesters, which are listed as follows:

1) The mechanical structure for vibrational energy harvesting in nature is a CM. A structural categorization of the PVEHs is proposed based on a systematic review on state-of-the-art mechanical structures of PVEHs in the literature. The structures of the PVEHs are categorized into 5 groups, i.e. mono-stable structures, multi-stable structures, frequency-up-conversion structures and stress-optimization structures. This structural categorization helps researchers to form a clear overview and better understanding on the structural methodologies of the current PVEHs. In addition, several CMs are first proposed in different configurations as inspirations and references for the structural design of PVEHs.

2) The metric of Normalized Power Density (NPD), is introduced to compare and assess the energy generation capability of PVEHs with different piezo-materials and in different scales. Based on the data collected in the literature, the NPD-Volume graph of PVEHs is first presented. This NPD-Volume graph provides references for researchers on the piezo-material selection, structural design of their PVEHs.

3) The design guideline of the SBCM based on a stiffness compensation closed-form equation is provided. It is presented as a flow chart. Such a detailed design guideline of the SBCM has

not been reported in the literature based on my knowledge. It can guide the rapid design of the SBCM in different sizes and materials.

4) A dynamic analytical model describing the displacement response of the SBCM to harmonic base excitations is derived based on the averaging method. This analytical model helps to predict the dynamic performance of the SBCM in an efficient way with desired accuracy. The model accuracy has been verified by numerical analysis, FEA simulations and dynamic experiments.

5) Detailed setting tutorials of the FEA simulations on the SBCM in COMSOL Multiphysics® 5.5 are summarized and presented. These FEA simulations include the static simulation on the force-displacement relationship of the SBCM, dynamic simulation on the displacement response of the SBCM under regular and irregular base excisions in time domain, dynamic simulation with imported displacement patterns, and multi-physics simulation integrating piezoelectric materials with the SBCM structure. These tutorials are generated and summarized based on the simulating practices and assistance from COMSOL Support. They might be helpful to those researchers who are facing similar FEA simulation tasks.

6) A successful application case of the SBCM in harvesting energy from regular and irregular ocean waves is demonstrated by FEA simulations with displacement responses and electric outputs obtained. The integration of the SBCM-based PVEH into an oceanic drifter is considered in the FEA simulations. This application demonstration provides an effective solution to improve the dynamic performance of the oceanic vibrational energy harvesters.

7) The miniaturized SBCM in the MEMS scale breaks the frequency limit imposed by the size effect, i.e. smaller sizes lead to higher resonating frequencies [97], by its sensitivity to ultra-low wide bandwidth frequencies with weak accelerations. This would inspire the researchers in relevant fields with the development of more effective MEMS vibrational energy harvesters by adopting this SBCM structure.

7.2 Conclusions

The main conclusions based on my doctoral research are drawn as follows:

1) When static balancing is tuned, the SBCM stays in equilibrium in a finite displacement range around the origin. In the wider displacement range, stiffness nonlinearity appears. This unique force-displacement is verified by both experiments and FEA simulations. With the same device, bi-stability and mono-stability can also be obtained by adjusting the length of the positive-stiffness beams.

2) The SBCM structure is sensitive to regular and irregular vibrations with ultra-low wide bandwidth frequencies (theoretically starting above 0 Hz) and low accelerations, according to the analytical model, numerical analysis, FEA simulations and experiments. The SBCM is thus considered as an ideal structural solution for enhancing the dynamic performance of the vibrational energy harvesters.

3) The SBCM structure is transferable to different scales, while the static and dynamic characteristics of the SBCM is regardless of the dimensions of the device based on the theoretical analysis and FEA simulations.

4) The dynamic performance of the SBCM is directly related to the force-displacement relationship of the SBCM as described in the analytical model, while the force-displacement relationship is defined by the geometric parameters of the SBCM. This feature offers an approach to match the effective frequency range of the SBCM with the frequencies of environmental vibrations by adjusting the length of the positive-stiffness beams for a better energy harvesting performance.

5) The SBCM structure is applicable as the main structure of PVEHs by integrating piezoelectric materials in the device. This has been demonstrated with a prototype and a FEA model of the SBCM-based PVEH. Note that the SBCM can be combined with various energy conversion mechanisms, e.g. electromagnetic, electrostatic and triboelectric, not limited to piezoelectric type only.

6) The SBCM is friendly to fabrication and miniaturization. This is because the static-balancing mode of the SBCM with stiffness nonlinearity is achieved purely by the deformation of the compliant beams, without using any accessory parts such as magnets [335, 336] or spiral springs [154, 337]. This enables the miniaturization of the SBCM as the main structure of the MEMS vibrational energy harvesters for powering low-energy-cost sensors and circuits on chip.

7.3 Future work

My doctoral research and the outcomes would facilitate the development of the SBCM-based vibrational energy harvesters. However, these are not sufficient yet to support the immediate application of the SBCM-based vibrational energy harvesters in powering the low-energy-cost sensors and circuits. Future research work will be conducted from the following aspects:

1) The SBCM structure will be further optimized. The length of the positive-stiffness beams can be micro-tuned with a well-designed displacement-reduction mechanism. In addition, the preloading process on the negative-stiffness beams can be completed more efficiently with bi-stable CMs using the method as reported in [79], which is beneficial for both miniaturization and monolithic fabrication. The positions of the positive- and negative-stiffness components in a SBCM structure can be re-arranged for the combination with different energy-conversion mechanisms. The eventual SBCM will be fabricated in a monolithic form instead of in the assembling manner.

2) An optimal nonlinear electric circuit will be utilized for this nonlinear oscillator for maximized electric power generation. The integration techniques of the electromechanical transducers with the SBCM structure will be optimized for the best energy-conversion performance. For example, the attachment positions and pasting process of PVDF films on the compliant beams of the SBCM structure should be optimized. The electric output model of the SBCM-based vibrational energy harvesters will be established corresponding to different energy-conversion mechanisms.

3) Integrated with the optimized electric circuits and electromechanical transducers, dynamic experiments on the SBCM-based vibrational energy harvesters will extend from labs to real vibrational scenarios. The most accessible vibration sources include ocean waves, human motions and vehicle vibrations, etc.

4) The SBCM will be miniaturized and prototyped with MEMS technologies. It will be used as the main structure of MEMS vibrational energy harvesters. The structure of the MEMS-scale SBCM may have to be re-designed and optimized from the perspective of MEMS techniques for the integration of different electromechanical transducers. The MEMS-scale

SBCM with diverse structures are expected. Static and dynamic testing on the MEMS-scale SBCM-based vibrational energy harvesters will be conducted.

5) Diverse SBCM structures will be designed and developed based on the stiffness compensation principle. The SBCM structure proposed here is one example of many possible forms. The static balancing can also be achieved by the integration of various positive- and negative-stiffness components as building blocks which can be arranged in different relative positions.

6) Inspired by the research from Xiong et al. [122], Zhang et al. [140] and Hu et al. [338] on vibrational energy harvesters based on internal resonance, nonlinear energy sinks and stoppers, the SBCM structure can also be utilized as a nonlinear coupling resonator in such devices. The introduction of the SBCM structure would further enhance the energy harvesting performance of these nonlinear vibrational energy harvesters.

References

[1]   Faber, J. A., Arrieta, A. F. & Studart, A. R. 2018. Bioinspired spring origami. *Science,* 359**,** 1386-1391.

[2]   Emam, S. A. & Inman, D. J. 2015. A review on bistable composite laminates for morphing and energy harvesting. *Applied Mechanics Reviews,* 67**,** 060803.

[3]   Kelly, K. 2009. *Out of control: The new biology of machines, social systems, and the economic world*, Hachette UK.

[4]   Golpîra, H., Khan, S. a. R. & Safaeipour, S. 2021. A review of logistics internet-of-things: Current trends and scope for future research. *Journal of Industrial Information Integration***,** 100194.

[5]   Kamalinejad, P., Mahapatra, C., Sheng, Z., Mirabbasi, S., Leung, V. C. & Guan, Y. L. 2015. Wireless energy harvesting for the Internet of Things. *IEEE Communications Magazine,* 53**,** 102-108.

[6]   Bogue, R. 2014. Towards the trillion sensors market. *Sensor review*.

[7]   Todaro, M. T., Guido, F., Mastronardi, V., Desmaele, D., Epifani, G., Algieri, L. & De Vittorio, M. 2017. Piezoelectric MEMS vibrational energy harvesters: Advances and outlook. *Microelectronic Engineering,* 183**,** 23-36.

[8]   Li, H., Tian, C. & Deng, Z. D. 2014. Energy harvesting from low frequency applications using piezoelectric materials. *Applied physics reviews,* 1**,** 041301.

[9]   Pressler, M. W. More earthquakes than usual? Not really. *KidsPost (Washington Post: Washington Post). pp. C,* 10**,** 2010.

[10]   Roundy, S., Wright, P. K. & Rabaey, J. M. 2003. Energy scavenging for wireless sensor networks. *Norwell.* Springer.

[11]   Blad, T., Machekposhti, D. F., Herdser, J., Holmes, A. & Tolou, N. Vibration Energy Harvesting from Multi-Directional Motion Sources. 2018 International Conference on Manipulation, Automation and Robotics at Small Scales (MARSS), 2018. IEEE, 1-9.

[12]   Erturk, A. & Inman, D. J. 2011. *Piezoelectric energy harvesting*, John Wiley & Sons.

[13]   Kazmierski, T. J. & Beeby, S. 2014. *Energy harvesting systems*, Springer.

[14]   Podder, P., Constantinou, P., Mallick, D., Amann, A. & Roy, S. 2017. Magnetic tuning of nonlinear MEMS electromagnetic vibration energy harvester. *Journal of Microelectromechanical Systems,* 26**,** 539-549.

[15] Beeby, S. P., Torah, R., Tudor, M., Glynne-Jones, P., O'donnell, T., Saha, C. & Roy, S. 2007. A micro electromagnetic generator for vibration energy harvesting. *Journal of Micromechanics and microengineering,* 17**,** 1257.

[16] Yang, B., Lee, C., Xiang, W., Xie, J., He, J. H., Kotlanka, R. K., Low, S. P. & Feng, H. 2009. Electromagnetic energy harvesting from vibrations of multiple frequencies. *Journal of Micromechanics and Microengineering,* 19**,** 035001.

[17] Roy, S., Mallick, D. & Paul, K. 2019. MEMS-based vibrational energy harvesting and conversion employing micro-/nano-magnetics. *IEEE Transactions on Magnetics,* 55**,** 1-15.

[18] Torres, E. O. & Rincón-Mora, G. A. 2008. Electrostatic energy-harvesting and battery-charging CMOS system prototype. *IEEE Transactions on Circuits and Systems I: Regular Papers,* 56**,** 1938-1948.

[19] Tvedt, L. G. W., Nguyen, D. S. & Halvorsen, E. 2010. Nonlinear behavior of an electrostatic energy harvester under wide-and narrowband excitation. *Journal of Microelectromechanical systems,* 19**,** 305-316.

[20] Basset, P., Galayko, D., Paracha, A. M., Marty, F., Dudka, A. & Bourouina, T. 2009. A batch-fabricated and electret-free silicon electrostatic vibration energy harvester. *Journal of Micromechanics and Microengineering,* 19**,** 115025.

[21] Fan, F.-R., Tian, Z.-Q. & Wang, Z. L. 2012. Flexible triboelectric generator. *Nano energy,* 1**,** 328-334.

[22] Niu, S., Liu, Y., Wang, S., Lin, L., Zhou, Y. S., Hu, Y. & Wang, Z. L. 2013. Theory of sliding-mode triboelectric nanogenerators. *Advanced materials,* 25**,** 6184-6193.

[23] Wang, Z. L. 2015. Triboelectric nanogenerators as new energy technology and self-powered sensors–Principles, problems and perspectives. *Faraday discussions,* 176**,** 447-458.

[24] Seddik, B. A., Despesse, G., Boisseau, S. & Defay, E. 2012. *Strategies for wideband mechanical energy harvester*, InTech Rijeka, Croatia.

[25] Kim, S.-G., Priya, S. & Kanno, I. 2012. Piezoelectric MEMS for energy harvesting. *MRS bulletin,* 37**,** 1039-1050.

[26] Zhao, X., Shang, Z., Luo, G. & Deng, L. 2015. A vibration energy harvester using AlN piezoelectric cantilever array. *Microelectronic Engineering,* 142**,** 47-51.

[27] Hosseini, R., Hamedi, M., Im, J., Kim, J. & Dayou, J. 2017. Analytical and experimental investigation of partially covered piezoelectric cantilever energy

harvester. *International Journal of Precision Engineering and Manufacturing,* 18**,** 415-424.

[28] Olszewski, O. Z., Houlihan, R., Blake, A., Mathewson, A. & Jackson, N. 2017. Evaluation of vibrational PiezoMEMS harvester that scavenges energy from a magnetic field surrounding an AC current-carrying wire. *Journal of Microelectromechanical Systems,* 26**,** 1298-1305.

[29] Erturk, A. & Inman, D. J. 2011. Broadband piezoelectric power generation on high-energy orbits of the bistable Duffing oscillator with electromechanical coupling. *Journal of Sound and Vibration,* 330**,** 2339-2353.

[30] Liang, H., Hao, G. & Olszewski, O. Z. 2021. A review on vibration-based piezoelectric energy harvesting from the aspect of compliant mechanisms. *Sensors and Actuators A: Physical***,** 112743.

[31] Khan, F. U. 2016. Review of non-resonant vibration based energy harvesters for wireless sensor nodes. *Journal of Renewable and Sustainable Energy,* 8**,** 044702.

[32] Covaci, C. & Gontean, A. 2020. Piezoelectric energy harvesting solutions: A review. *Sensors,* 20**,** 3512.

[33] Khusainov, R., Azzi, D., Achumba, I. E. & Bersch, S. D. 2013. Real-time human ambulation, activity, and physiological monitoring: Taxonomy of issues, techniques, applications, challenges and limitations. *Sensors,* 13**,** 12852-12902.

[34] Antonsson, E. K. & Mann, R. W. 1985. The frequency content of gait. *Journal of biomechanics,* 18**,** 39-47.

[35] Satkunskiene, D., Grigas, V., Eidukynas, V. & Domeika, A. 2009. 487. Acceleration based evaluation of the human walking and running parameters. *Journal of Vibroengineering,* 11.

[36] Galchev, T., Mccullagh, J., Peterson, R. L. & Najafi, K. 2010. A vibration harvesting system for bridge health monitoring applications. *Proc. PowerMEMS,* 1**,** 179-182.

[37] Jang, S., Jo, H., Cho, S., Mechitov, K., Rice, J. A., Sim, S.-H., Jung, H.-J., Yun, C.-B., Spencer Jr, B. F. & Agha, G. 2010. Structural health monitoring of a cable-stayed bridge using smart sensor technology: deployment and evaluation. *Smart Structures and Systems,* 6**,** 439-459.

[38] Sazonov, E., Li, H., Curry, D. & Pillay, P. 2009. Self-powered sensors for monitoring of highway bridges. *IEEE Sensors Journal,* 9**,** 1422-1429.

[39] Munk, W. H. 1951. Origin and generation of waves. Scripps Institution of Oceanography La Jolla Calif.

[40] Brown, A. C. & Paasch, R. K. 2021. The Accelerations of a Wave Measurement Buoy Impacted by Breaking Waves in the Surf Zone. *Journal of Marine Science and Engineering,* 9**,** 214.

[41] Maamer, B., Boughamoura, A., El-Bab, A. M. F., Francis, L. A. & Tounsi, F. 2019. A review on design improvements and techniques for mechanical energy harvesting using piezoelectric and electromagnetic schemes. *Energy Conversion and Management,* 199**,** 111973.

[42] Paul, K., Amann, A. & Roy, S. 2020. Tapered nonlinear vibration energy harvester for powering Internet of Things. *Applied Energy***,** 116267.

[43] Tousif, S. M. & Çelik-Butler, Z. Array of linear and nonlinear electrostatic energy harvesters for broadband energy harvesting. 2019 IEEE Sensors Applications Symposium (SAS), 2019. IEEE, 1-6.

[44] Zhu, J., Wang, A., Hu, H. & Zhu, H. 2017. Hybrid electromagnetic and triboelectric nanogenerators with multi-impact for wideband frequency energy harvesting. *Energies,* 10**,** 2024.

[45] Howell, L. L. 2001. *Compliant mechanisms*, John Wiley & Sons.

[46] Lobontiu, N. 2002. *Compliant mechanisms: design of flexure hinges*, CRC press.

[47] Hao, G. & Kong, X. 2012. A novel large-range XY compliant parallel manipulator with enhanced out-of-plane stiffness.

[48] Hao, G. 2013. Simplified PRBMs of spatial compliant multi-beam modules for planar motion. *Mechanical Sciences,* 4**,** 311-318.

[49] Semon, G., Ypma, W. J. B., Weeke, S. L. & Tolou, N. 2020. Device for Timepiece, Clockwork Movement and Timepiece Comprising Such a Device. Google Patents.

[50] Merriam, E., Jones, J., Magleby, S. & Howell, L. 2013. Monolithic 2 DOF fully compliant space pointing mechanism. *Mechanical Sciences,* 4**,** 381-390.

[51] Greenberg, H., Gong, M., Magleby, S. & Howell, L. 2011. Identifying links between origami and compliant mechanisms. *Mechanical Sciences,* 2**,** 217-225.

[52] Zirbel, S. A., Lang, R. J., Thomson, M. W., Sigel, D. A., Walkemeyer, P. E., Trease, B. P., Magleby, S. P. & Howell, L. L. 2013. Accommodating thickness in origami-based deployable arrays. *Journal of Mechanical Design,* 135.

[53] Howell, L. L., Magleby, S. P. & Olsen, B. M. 2013. *Handbook of compliant mechanisms*, John Wiley & Sons.

[54] Awtar, S., Slocum, A. H. & Sevincer, E. 2007. Characteristics of beam-based flexure modules.

[55]   Awtar, S. 2003. *Synthesis and analysis of parallel kinematic XY flexure mechanisms.* Massachusetts Institute of Technology.

[56]   Kong, K., Chen, G. & Hao, G. 2019. Kinetostatic modeling and optimization of a novel horizontal-displacement compliant mechanism. *Journal of Mechanisms and Robotics,* 11**,** 064502.

[57]   Chen, G. & Ma, F. 2015. Kinetostatic modeling of fully compliant bistable mechanisms using Timoshenko beam constraint model. *Journal of Mechanical Design,* 137**,** 022301.

[58]   Zhang, A. & Chen, G. 2013. A comprehensive elliptic integral solution to the large deflection problems of thin beams in compliant mechanisms. *Journal of Mechanisms and Robotics,* 5.

[59]   Kimball, C. & Tsai, L.-W. 2002. Modeling of flexural beams subjected to arbitrary end loads. *J. Mech. Des.,* 124**,** 223-235.

[60]   Uicker, J. J., Pennock, G. R. & Shigley, J. E. 2011. *Theory of machines and mechanisms*, Oxford University Press New York.

[61]   Norton, R. L. & Mccarthy, J. M. 2003. Design of machinery. American Society of Mechanical Engineers Digital Collection.

[62]   Saxena, A. & Kramer, S. N. 1998. A simple and accurate method for determining large deflections in compliant mechanisms subjected to end forces and moments.

[63]   Rad, F. P., Vertechy, R., Berselli, G. & Parenti-Castelli, V. 2016. Analytical compliance analysis and finite element verification of spherical flexure hinges for spatial compliant mechanisms. *Mechanism and Machine Theory,* 101**,** 168-180.

[64]   Meng, Q., Li, Y. & Xu, J. 2014. A novel analytical model for flexure-based proportion compliant mechanisms. *Precision Engineering,* 38**,** 449-457.

[65]   Sun, Y., Zhang, D., Liu, Y. & Lueth, T. C. 2020. Fem-based mechanics modeling of bio-inspired compliant mechanisms for medical applications. *IEEE Transactions on Medical Robotics and Bionics,* 2**,** 364-373.

[66]   Hopkins, J. B. & Culpepper, M. L. 2010. Synthesis of multi-degree of freedom, parallel flexure system concepts via Freedom and Constraint Topology (FACT)–Part I: Principles. *Precision Engineering,* 34**,** 259-270.

[67]   Yu, J., Li, S., Su, H.-J. & Culpepper, M. 2011. Screw theory based methodology for the deterministic type synthesis of flexure mechanisms.

[68]   Hao, G. 2013. Towards the design of monolithic decoupled XYZ compliant parallel mechanisms for multi-function applications. *Mechanical Sciences,* 4**,** 291-302.

[69]   Culpepper, M. L. & Anderson, G. 2004. Design of a low-cost nano-manipulator which utilizes a monolithic, spatial compliant mechanism. *Precision engineering,* 28**,** 469-482.

[70]   Du, E., Cui, H. & Zhu, Z. 2006. Review of nanomanipulators for nanomanufacturing. *International Journal of Nanomanufacturing,* 1**,** 83-104.

[71]   Frecker, M., Ananthasuresh, G., Nishiwaki, S., Kikuchi, N. & Kota, S. 1997. Topological synthesis of compliant mechanisms using multi-criteria optimization.

[72]   Pedersen, C. B., Buhl, T. & Sigmund, O. 2001. Topology synthesis of large-displacement compliant mechanisms. *International Journal for numerical methods in engineering,* 50**,** 2683-2705.

[73]   Dirksen, F., Berg, T., Lammering, R. & Zohdi, T. I. 2012. Topology synthesis of large-displacement compliant mechanisms with specific output motion paths. *Pamm,* 12**,** 801-804.

[74]   Olsen, B. M., Issac, Y., Howell, L. L. & Magleby, S. P. Utilizing a classification scheme to facilitate rigid-body replacement for compliant mechanism design.   International Design Engineering Technical Conferences and Computers and Information in Engineering Conference, 2010. 475-489.

[75]   Mattson, C. A., Howell, L. L. & Magleby, S. P. 2004. Development of commercially viable compliant mechanisms using the pseudo-rigid-body model: case studies of parallel mechanisms. *Journal of intelligent material systems and structures,* 15**,** 195-202.

[76]   Hoetmer, K., Herder, J. L. & Kim, C. J. A building block approach for the design of statically balanced compliant mechanisms.   International Design Engineering Technical Conferences and Computers and Information in Engineering Conference, 2009. 313-323.

[77]   Chen, G., Gou, Y. & Zhang, A. 2011. Synthesis of compliant multistable mechanisms through use of a single bistable mechanism. *Journal of Mechanical Design,* 133**,** 081007.

[78]   Herder, J. L. 2001. *Energy-free Systems. Theory, conception and design of statically*.

[79]   Kuppens, P., Bessa, M., Herder, J. & Hopkins, J. 2021. Monolithic binary stiffness building blocks for mechanical digital machines. *Extreme Mechanics Letters,* 42**,** 101120.

[80]   Barel, M., Machekposhti, D. F., Herder, J., Tolou, N. & Sitti, M. Permanent Preloading by Acceleration for Statically Balancing MEMS Devices.   2018 International Conference on Reconfigurable Mechanisms and Robots (ReMAR), 2018. IEEE, 1-11.

[81]   Wang, S., Yang, X., Chen, Y. & Ma, J. 2021. A theoretical design of a bellow-shaped statically balanced compliant mechanism. *Mechanism and Machine Theory,* 161**,** 104295.

[82]   Chen, G. & Zhang, S. 2011. Fully-compliant statically-balanced mechanisms without prestressing assembly: concepts and case studies. *Mechanical Sciences,* 2**,** 169-174.

[83]   Tolou, N., Henneken, V. A. & Herder, J. L. Statically balanced compliant micro mechanisms (SB-MEMS): Concepts and simulation. International Design Engineering Technical Conferences and Computers and Information in Engineering Conference, 2010. 447-454.

[84]   Tolou, N., Estevez, P. & Herder, J. L. Collinear-type statically balanced compliant micro mechanism (SB-CMM): experimental comparison between pre-curved and straight beams. International Design Engineering Technical Conferences and Computers and Information in Engineering Conference, 2011. 113-117.

[85]   Pluimers, P. J., Tolou, N., Jensen, B. D., Howell, L. L. & Herder, J. L. A compliant on/off connection mechanism for preloading statically balanced compliant mechanisms. International Design Engineering Technical Conferences and Computers and Information in Engineering Conference, 2012. American Society of Mechanical Engineers, 373-377.

[86]   Tolou, N. 2012. Statically Balanced Compliant Mechanisms for Micro-Precision.

[87]   Gallego Sánchez, J. 2013. Statically Balanced Compliant Mechanisms: Theory and Synthesis.

[88]   Kuppens, P., Bessa, M., Herder, J. L. & Hopkins, J. 2021. Compliant Mechanisms That Use Static Balancing to Achieve Dramatically Different States of Stiffness. *Journal of Mechanisms and Robotics,* 13**,** 021010.

[89]   Dunning, A. 2011. Design of a zero stiffness six degrees of freedom compliant precision stage.

[90]   Yang, Q., Bi, S. & Liu, T. Static balancing of flexural pivots with two symmetrically arranged pre-compressing springs. IOP Conference Series: Materials Science and Engineering, 2020. IOP Publishing, 012121.

[91]   Bilancia, P., Smith, S. P., Berselli, G., Magleby, S. P. & Howell, L. L. 2020. Zero Torque Compliant Mechanisms Employing Pre-buckled Beams. *Journal of Mechanical Design,* 142.

[92] Wang, H., Jasim, A. & Chen, X. 2018. Energy harvesting technologies in roadway and bridge for different applications–A comprehensive review. *Applied energy,* 212**,** 1083-1094.

[93] Sergio, P. P. 2012. Neutrally stable vibration energy harvesting. *Master's thesis, Delft University of Technology, Delft, Netherlands*.

[94] Mariello, M., Blad, T., Mastronardi, V., Madaro, F., Guido, F., Staufer, U., Tolou, N. & De Vittorio, M. 2021. Flexible piezoelectric AlN transducers buckled through package-induced preloading for mechanical energy harvesting. *Nano Energy,* 85**,** 105986.

[95] Wang, K., Zhou, J., Ouyang, H., Chang, Y. & Xu, D. 2021. A dual quasi-zero-stiffness sliding-mode triboelectric nanogenerator for harvesting ultralow-low frequency vibration energy. *Mechanical Systems and Signal Processing,* 151**,** 107368.

[96] Yang, T., Cao, Q. & Hao, Z. 2021. A novel nonlinear mechanical oscillator and its application in vibration isolation and energy harvesting. *Mechanical Systems and Signal Processing,* 155**,** 107636.

[97] Deng, J., Rorschach, K., Baker, E., Sun, C. & Chen, W. 2014. Topology optimization and fabrication of low frequency vibration energy harvesting microdevices. *Smart Materials and Structures,* 24**,** 025005.

[98] Saadon, S. & Sidek, O. 2011. A review of vibration-based MEMS piezoelectric energy harvesters. *Energy Conversion and Management,* 52**,** 500-504.

[99] Tan, Y., Dong, Y. & Wang, X. 2016. Review of MEMS electromagnetic vibration energy harvester. *Journal of Microelectromechanical Systems,* 26**,** 1-16.

[100] Rao, S. S. 2007. *Vibration of continuous systems*, Wiley Online Library.

[101] Roundy, S. & Wright, P. K. 2004. A piezoelectric vibration based generator for wireless electronics. *Smart Materials and structures,* 13**,** 1131.

[102] Leland, E. S., Lai, E. M. & Wright, P. K. A self-powered wireless sensor for indoor environmental monitoring. Wireless Networking Symposium, University of Texas at Austin Department of Electrical & Computer Engineering, 2004.

[103] Erturk, A. & Inman, D. J. 2009. An experimentally validated bimorph cantilever model for piezoelectric energy harvesting from base excitations. *Smart materials and structures,* 18**,** 025009.

[104] Thomson, W. 2018. *Theory of vibration with applications*, CrC Press.

[105] Wu, X., Lin, J., Kato, S., Zhang, K., Ren, T. & Liu, L. 2008. A frequency adjustable vibration energy harvester. *Proceedings of PowerMEMS***,** 245-248.

[106] Somkuwar, R., Chandwani, J. & Deshmukh, R. 2018. Wideband auto-tunable vibration energy harvester using change in centre of gravity. *Microsystem Technologies,* 24**,** 3033-3044.

[107] Jackson, N., Stam, F., Olszewski, O. Z., Doyle, H., Quinn, A. & Mathewson, A. 2016. Widening the bandwidth of vibration energy harvesters using a liquid-based non-uniform load distribution. *Sensors and Actuators A: Physical,* 246**,** 170-179.

[108] Shin, Y.-H., Choi, J., Kim, S. J., Kim, S., Maurya, D., Sung, T.-H., Priya, S., Kang, C.-Y. & Song, H.-C. 2020. Automatic resonance tuning mechanism for ultra-wide bandwidth mechanical energy harvesting. *Nano Energy,* 77**,** 104986.

[109] Schaufuss, J., Scheibner, D. & Mehner, J. 2011. New approach of frequency tuning for kinetic energy harvesters. *Sensors and Actuators A: Physical,* 171**,** 352-360.

[110] Jackson, N., Olszewski, O. Z., O'murchu, C. & Mathewson, A. 2018. Ultralow-frequency PiezoMEMS energy harvester using thin-film silicon and parylene substrates. *Journal of Micro/Nanolithography, MEMS, and MOEMS,* 17**,** 015005.

[111] Berdy, D. F., Srisungsitthisunti, P., Jung, B., Xu, X., Rhoads, J. F. & Peroulis, D. 2012. Low-frequency meandering piezoelectric vibration energy harvester. *IEEE transactions on ultrasonics, ferroelectrics, and frequency control,* 59**,** 846-858.

[112] Apo, D. J., Sanghadasa, M. & Priya, S. 2014. Vibration modeling of arc-based cantilevers for energy harvesting applications. *Energy Harvesting and Systems,* 1**,** 57-68.

[113] Song, H.-C., Kumar, P., Maurya, D., Kang, M.-G., Reynolds, W. T., Jeong, D.-Y., Kang, C.-Y. & Priya, S. 2017. Ultra-low resonant piezoelectric MEMS energy harvester with high power density. *Journal of Microelectromechanical Systems,* 26**,** 1226-1234.

[114] Liu, H., Lee, C., Kobayashi, T., Tay, C. J. & Quan, C. 2012. Piezoelectric MEMS-based wideband energy harvesting systems using a frequency-up-conversion cantilever stopper. *Sensors and Actuators A: Physical,* 186**,** 242-248.

[115] Le Scornec, J., Guiffard, B., Seveno, R. & Le Cam, V. 2020. Frequency tunable, flexible and low cost piezoelectric micro-generator for energy harvesting. *Sensors and Actuators A: Physical***,** 112148.

[116] Kovacic, I. & Brennan, M. J. 2011. *The Duffing equation: nonlinear oscillators and their behaviour*, John Wiley & Sons.

[117] Brennan, M., Kovacic, I., Carrella, A. & Waters, T. 2008. On the jump-up and jump-down frequencies of the Duffing oscillator. *Journal of Sound and Vibration,* 318**,** 1250-1261.

[118] Nayfeh, A. H. 2000. *Nonlinear interactions: analytical, computational and experimental methods*, Wiley.

[119] Chen, L.-Q. & Jiang, W.-A. 2015. Internal resonance energy harvesting. *Journal of Applied Mechanics,* 82.

[120] Jiang, W.-A., Chen, L.-Q. & Ding, H. 2016. Internal resonance in axially loaded beam energy harvesters with an oscillator to enhance the bandwidth. *Nonlinear Dynamics,* 85**,** 2507-2520.

[121] Xie, Z., Wang, T., Kwuimy, C. K., Shao, Y. & Huang, W. 2019. Design, analysis and experimental study of a T-shaped piezoelectric energy harvester with internal resonance. *Smart Materials and Structures,* 28**,** 085027.

[122] Xiong, L., Tang, L. & Mace, B. R. 2016. Internal resonance with commensurability induced by an auxiliary oscillator for broadband energy harvesting. *Applied Physics Letters,* 108**,** 203901.

[123] Xiong, L., Tang, L. & Mace, B. R. 2018. A comprehensive study of 2: 1 internal-resonance-based piezoelectric vibration energy harvesting. *Nonlinear Dynamics,* 91**,** 1817-1834.

[124] Gafforelli, G., Xu, R., Corigliano, A. & Kim, S.-G. 2014. Modeling of a bridge-shaped nonlinear piezoelectric energy harvester. *Energy Harvesting and Systems,* 1**,** 179-187.

[125] Marzencki, M., Defosseux, M. & Basrour, S. 2009. MEMS vibration energy harvesting devices with passive resonance frequency adaptation capability. *Journal of Microelectromechanical Systems,* 18**,** 1444-1453.

[126] Leadenham, S. & Erturk, A. 2015. Nonlinear M-shaped broadband piezoelectric energy harvester for very low base accelerations: primary and secondary resonances. *Smart Materials and Structures,* 24**,** 055021.

[127] Hajati, A. & Kim, S.-G. 2011. Ultra-wide bandwidth piezoelectric energy harvesting. *Applied Physics Letters,* 99**,** 083105.

[128] Masana, R. & Daqaq, M. F. 2011. Electromechanical modeling and nonlinear analysis of axially loaded energy harvesters. *Journal of vibration and acoustics,* 133.

[129] Stanton, S. C., Mcgehee, C. C. & Mann, B. P. 2009. Reversible hysteresis for broadband magnetopiezoelastic energy harvesting. *Applied Physics Letters,* 95**,** 174103.

[130] Tang, L. & Yang, Y. 2012. A nonlinear piezoelectric energy harvester with magnetic oscillator. *Applied Physics Letters,* 101**,** 094102.

[131] Yu, L., Tang, L. & Yang, T. 2020. Piezoelectric passive self-tuning energy harvester based on a beam-slider structure. *Journal of Sound and Vibration,* 489**,** 115689.

[132] Chen, Y. & Yan, Z. 2020. Nonlinear analysis of axially loaded piezoelectric energy harvesters with flexoelectricity. *International Journal of Mechanical Sciences,* 173**,** 105473.

[133] Sebald, G., Kuwano, H., Guyomar, D. & Ducharne, B. 2011. Experimental Duffing oscillator for broadband piezoelectric energy harvesting. *Smart materials and structures,* 20**,** 102001.

[134] Masana, R. & Daqaq, M. F. 2013. Response of duffing-type harvesters to band-limited noise. *Journal of Sound and Vibration,* 332**,** 6755-6767.

[135] Lin, J.-T., Lee, B. & Alphenaar, B. 2010. The magnetic coupling of a piezoelectric cantilever for enhanced energy harvesting efficiency. *Smart materials and Structures,* 19**,** 045012.

[136] Vakakis, A. 2001. Inducing passive nonlinear energy sinks in vibrating systems. *J. Vib. Acoust.,* 123**,** 324-332.

[137] Jiang, X., Mcfarland, D. M., Bergman, L. A. & Vakakis, A. F. 2003. Steady state passive nonlinear energy pumping in coupled oscillators: theoretical and experimental results. *Nonlinear Dynamics,* 33**,** 87-102.

[138] Zhang, Y., Tang, L. & Liu, K. 2017. Piezoelectric energy harvesting with a nonlinear energy sink. *Journal of Intelligent Material Systems and Structures,* 28**,** 307-322.

[139] Xiong, L., Tang, L., Liu, K. & Mace, B. R. 2018. Broadband piezoelectric vibration energy harvesting using a nonlinear energy sink. *Journal of Physics D: Applied Physics,* 51**,** 185502.

[140] Zhang, Y., Lu, Y. & Chen, L. 2019. Energy harvesting via nonlinear energy sink for whole-spacecraft. *Science China Technological Sciences,* 62**,** 1483-1491.

[141] Xiong, L., Tang, L., Liu, K. & Mace, B. R. 2020. Effect of Electromechanical Coupling on Dynamic Characteristics of a Piezoelectric Nonlinear Energy Sink System. *Journal of Vibration Engineering & Technologies***,** 1-13.

[142] Li, X., Zhang, Y.-W., Ding, H. & Chen, L.-Q. 2019. Dynamics and evaluation of a nonlinear energy sink integrated by a piezoelectric energy harvester under a harmonic excitation. *Journal of Vibration and Control,* 25**,** 851-867.

[143] Ding, H. & Chen, L.-Q. 2020. Designs, analysis, and applications of nonlinear energy sinks. *Nonlinear Dynamics,* 100**,** 3061-3107.

[144] Blystad, L.-C. J. & Halvorsen, E. 2011. A piezoelectric energy harvester with a mechanical end stop on one side. *Microsystem technologies,* 17**,** 505-511.

[145] Liu, H., Tay, C. J., Quan, C., Kobayashi, T. & Lee, C. 2011. Piezoelectric MEMS energy harvester for low-frequency vibrations with wideband operation range and steadily increased output power. *Journal of Microelectromechanical systems,* 20**,** 1131-1142.

[146] Liu, H., Lee, C., Kobayashi, T., Tay, C. J. & Quan, C. 2012. A new S-shaped MEMS PZT cantilever for energy harvesting from low frequency vibrations below 30 Hz. *Microsystem technologies,* 18**,** 497-506.

[147] Soliman, M., Abdel-Rahman, E., El-Saadany, E. & Mansour, R. 2008. A wideband vibration-based energy harvester. *Journal of micromechanics and microengineering,* 18**,** 115021.

[148] Mankame, N. D. & Ananthasuresh, G. 2004. Topology optimization for synthesis of contact-aided compliant mechanisms using regularized contact modeling. *Computers & structures,* 82**,** 1267-1290.

[149] Hao, G. 2018. A framework of designing compliant mechanisms with nonlinear stiffness characteristics. *Microsystem Technologies,* 24**,** 1795-1802.

[150] Huang, D., Zhou, S. & Litak, G. 2019. Theoretical analysis of multi-stable energy harvesters with high-order stiffness terms. *Communications in Nonlinear Science and Numerical Simulation,* 69**,** 270-286.

[151] Zhou, S., Cao, J., Erturk, A. & Lin, J. 2013. Enhanced broadband piezoelectric energy harvesting using rotatable magnets. *Applied Physics Letters,* 102**,** 173901.

[152] Lan, C. & Qin, W. 2017. Enhancing ability of harvesting energy from random vibration by decreasing the potential barrier of bistable harvester. *Mechanical Systems and Signal Processing,* 85**,** 71-81.

[153] Ferrari, M., Ferrari, V., Guizzetti, M., Andò, B., Baglio, S. & Trigona, C. 2010. Improved energy harvesting from wideband vibrations by nonlinear piezoelectric converters. *Sensors and Actuators A: Physical,* 162**,** 425-431.

[154] Yang, W. & Towfighian, S. 2017. A hybrid nonlinear vibration energy harvester. *Mechanical Systems and Signal Processing,* 90**,** 317-333.

[155] Ando, B., Baglio, S., Trigona, C., Dumas, N., Latorre, L. & Nouet, P. 2010. Nonlinear mechanism in MEMS devices for energy harvesting applications. *Journal of Micromechanics and Microengineering,* 20**,** 125020.

[156] Stanton, S. C., Mcgehee, C. C. & Mann, B. P. 2010. Nonlinear dynamics for broadband energy harvesting: Investigation of a bistable piezoelectric inertial generator. *Physica D: Nonlinear Phenomena,* 239**,** 640-653.

[157] Cottone, F., Gammaitoni, L., Vocca, H., Ferrari, M. & Ferrari, V. 2012. Piezoelectric buckled beams for random vibration energy harvesting. *Smart materials and structures,* 21**,** 035021.

[158] Sneller, A., Cette, P. & Mann, B. 2011. Experimental investigation of a post-buckled piezoelectric beam with an attached central mass used to harvest energy. *Proceedings of the Institution of Mechanical Engineers, Part I: Journal of Systems and Control Engineering,* 225**,** 497-509.

[159] Zhu, Y. & Zu, J. W. 2013. Enhanced buckled-beam piezoelectric energy harvesting using midpoint magnetic force. *Applied Physics Letters,* 103**,** 041905.

[160] Ando, B., Baglio, S., L'episcopo, G. & Trigona, C. 2012. Investigation on mechanically bistable MEMS devices for energy harvesting from vibrations. *Journal of Microelectromechanical Systems,* 21**,** 779-790.

[161] Xu, R. & Kim, S. Low-frequency, low-G MEMS piezoelectric energy harvester. Journal of Physics: Conference Series, 2015. IOP Publishing, 012013.

[162] Hao, G. & Mullins, J. 2016. On the comprehensive static characteristic analysis of a translational bistable mechanism. *Proceedings of the Institution of Mechanical Engineers, Part C: Journal of Mechanical Engineering Science,* 230**,** 3803-3817.

[163] Chen, G. & Ma, F. 2015. Kinetostatic modeling of fully compliant bistable mechanisms using Timoshenko beam constraint model. *Journal of Mechanical Design,* 137.

[164] Qiu, J., Lang, J. H. & Slocum, A. H. 2004. A curved-beam bistable mechanism. *Journal of microelectromechanical systems,* 13**,** 137-146.

[165] Betts, D. N., Kim, H. A., Bowen, C. R. & Inman, D. 2012. Optimal configurations of bistable piezo-composites for energy harvesting. *Applied Physics Letters,* 100**,** 114104.

[166] Arrieta, A., Hagedorn, P., Erturk, A. & Inman, D. 2010. A piezoelectric bistable plate for nonlinear broadband energy harvesting. *Applied Physics Letters,* 97**,** 104102.

[167] Arrieta, A., Delpero, T., Bergamini, A. & Ermanni, P. 2013. Broadband vibration energy harvesting based on cantilevered piezoelectric bi-stable composites. *Applied Physics Letters,* 102**,** 173904.

[168] Cao, J., Zhou, S., Wang, W. & Lin, J. 2015. Influence of potential well depth on nonlinear tristable energy harvesting. *Applied Physics Letters,* 106**,** 173903.

[169] Haitao, L., Weiyang, Q., Chunbo, L., Wangzheng, D. & Zhiyong, Z. 2015. Dynamics and coherence resonance of tri-stable energy harvesting system. *Smart Materials and Structures,* 25**,** 015001.

[170] Zhou, S., Cao, J., Inman, D. J., Lin, J. & Li, D. 2016. Harmonic balance analysis of nonlinear tristable energy harvesters for performance enhancement. *Journal of Sound and Vibration,* 373**,** 223-235.

[171] Kim, P. & Seok, J. 2015. Dynamic and energetic characteristics of a tri-stable magnetopiezoelastic energy harvester. *Mechanism and Machine Theory,* 94**,** 41-63.

[172] Zhou, S. & Zuo, L. 2018. Nonlinear dynamic analysis of asymmetric tristable energy harvesters for enhanced energy harvesting. *Communications in Nonlinear Science and Numerical Simulation,* 61**,** 271-284.

[173] Zhou, S., Cao, J., Inman, D. J., Lin, J., Liu, S. & Wang, Z. 2014. Broadband tristable energy harvester: modeling and experiment verification. *Applied Energy,* 133**,** 33-39.

[174] Mei, X., Zhou, S., Yang, Z., Kaizuka, T. & Nakano, K. 2019. A tri-stable energy harvester in rotational motion: Modeling, theoretical analyses and experiments. *Journal of Sound and Vibration***,** 115142.

[175] Zhou, S., Cao, J., Lin, J. & Wang, Z. 2014. Exploitation of a tristable nonlinear oscillator for improving broadband vibration energy harvesting. *The European Physical Journal-Applied Physics,* 67.

[176] Zhou, Z., Qin, W. & Zhu, P. 2018. Harvesting performance of quad-stable piezoelectric energy harvester: Modeling and experiment. *Mechanical Systems and Signal Processing,* 110**,** 260-272.

[177] Zhou, Z., Qin, W. & Zhu, P. 2016. Improve efficiency of harvesting random energy by snap-through in a quad-stable harvester. *Sensors and Actuators A: Physical,* 243**,** 151-158.

[178] Wang, C., Zhang, Q., Wang, W. & Feng, J. 2018. A low-frequency, wideband quad-stable energy harvester using combined nonlinearity and frequency up-conversion by cantilever-surface contact. *Mechanical Systems and Signal Processing,* 112**,** 305-318.

[179] Zhou, Z., Qin, W., Yang, Y. & Zhu, P. 2017. Improving efficiency of energy harvesting by a novel penta-stable configuration. *Sensors and Actuators A: Physical,* 265**,** 297-305.

[180] Kim, P. & Seok, J. 2014. A multi-stable energy harvester: Dynamic modeling and bifurcation analysis. *Journal of Sound and Vibration,* 333**,** 5525-5547.

[181] Howell, L. L., Magleby, S. P., Olsen, B. M. & Wiley, J. 2013. *Handbook of compliant mechanisms*, Wiley Online Library.

[182] Chen, G., Han, Q. & Jin, K. 2020. A Fully Compliant Tristable Mechanism Employing Both Tensural and Compresural Segments. *Journal of Mechanisms and Robotics,* 12.

[183] Han, H., Sorokin, V., Tang, L. & Cao, D. 2021. A nonlinear vibration isolator with quasi-zero-stiffness inspired by Miura-origami tube. *Nonlinear Dynamics*, 1-13.

[184] Liu, C., Yu, K. & Tang, J. 2020. New insights into the damping characteristics of a typical quasi-zero-stiffness vibration isolator. *International Journal of Non-Linear Mechanics,* 124**,** 103511.

[185] Han, H., Sorokin, V., Tang, L. & Cao, D. 2021. A nonlinear vibration isolator with quasi-zero-stiffness inspired by Miura-origami tube. *Nonlinear Dynamics,* 105**,** 1313-1325.

[186] Liu, C., Zhao, R., Yu, K., Lee, H. P. & Liao, B. 2021. A quasi-zero-stiffness device capable of vibration isolation and energy harvesting using piezoelectric buckled beams. *Energy***,** 121146.

[187] Xue, H., Hu, Y. & Wang, Q.-M. 2008. Broadband piezoelectric energy harvesting devices using multiple bimorphs with different operating frequencies. *IEEE transactions on ultrasonics, ferroelectrics, and frequency control,* 55**,** 2104-2108.

[188] Farokhi, H., Gholipour, A. & Ghayesh, M. H. 2020. Efficient Broadband Vibration Energy Harvesting Using Multiple Piezoelectric Bimorphs. *Journal of Applied Mechanics,* 87.

[189] Shahruz, S. 2006. Design of mechanical band-pass filters for energy scavenging. *Journal of sound and vibration,* 292**,** 987-998.

[190] Al-Ashtari, W., Hunstig, M., Hemsel, T. & Sextro, W. 2013. Enhanced energy harvesting using multiple piezoelectric elements: theory and experiments. *Sensors and Actuators A: Physical,* 200**,** 138-146.

[191] Zhang, H. & Afzalul, K. 2014. Design and analysis of a connected broadband multi-piezoelectric-bimorph-beam energy harvester. *IEEE transactions on ultrasonics, ferroelectrics, and frequency control,* 61**,** 1016-1023.

[192] Li, S., Crovetto, A., Peng, Z., Zhang, A., Hansen, O., Wang, M., Li, X. & Wang, F. 2016. Bi-resonant structure with piezoelectric PVDF films for energy harvesting from random vibration sources at low frequency. *Sensors and Actuators A: Physical,* 247**,** 547-554.

[193] Deng, H., Du, Y., Wang, Z., Ye, J., Zhang, J., Ma, M. & Zhong, X. 2019. Poly-stable energy harvesting based on synergetic multistable vibration. *Communications Physics,* 2**,** 21.

[194] Hu, Y. & Xu, Y. 2014. A wideband vibration energy harvester based on a folded asymmetric gapped cantilever. *Applied physics letters,* 104**,** 053902.

[195] Tang, X. & Zuo, L. 2011. Enhanced vibration energy harvesting using dual-mass systems. *Journal of sound and vibration,* 330**,** 5199-5209.

[196] Tadesse, Y., Zhang, S. & Priya, S. 2009. Multimodal energy harvesting system: piezoelectric and electromagnetic. *Journal of Intelligent Material Systems and Structures,* 20**,** 625-632.

[197] Gong, L. J., Pan, Q. S., Li, W., Yan, G. Y., Liu, Y. B. & Feng, Z. H. 2015. Harvesting vibration energy using two modal vibrations of a folded piezoelectric device. *Applied Physics Letters,* 107**,** 033904.

[198] Roundy, S., Leland, E. S., Baker, J., Carleton, E., Reilly, E., Lai, E., Otis, B., Rabaey, J. M., Wright, P. K. & Sundararajan, V. 2005. Improving power output for vibration-based energy scavengers. *IEEE Pervasive computing,* 4**,** 28-36.

[199] Zhou, S., Hobeck, J. D., Cao, J. & Inman, D. J. 2017. Analytical and experimental investigation of flexible longitudinal zigzag structures for enhanced multi-directional energy harvesting. *Smart Materials and Structures,* 26**,** 035008.

[200] Hu, G., Liang, J., Lan, C. & Tang, L. 2020. A twist piezoelectric beam for multi-directional energy harvesting. *Smart Materials and Structures,* 29**,** 11LT01.

[201] Yang, Z. & Zu, J. 2015. Toward harvesting vibration energy from multiple directions by a nonlinear compressive-mode piezoelectric transducer. *Ieee/AsMe Transactions on Mechatronics,* 21**,** 1787-1791.

[202] Chen, R., Ren, L., Xia, H., Yuan, X. & Liu, X. 2015. Energy harvesting performance of a dandelion-like multi-directional piezoelectric vibration energy harvester. *Sensors and Actuators A: Physical,* 230**,** 1-8.

[203] Hao, G. & Li, H. 2015. Conceptual designs of multi-degree of freedom compliant parallel manipulators composed of wire-beam based compliant mechanisms. *Proceedings of the Institution of Mechanical Engineers, Part C: Journal of Mechanical Engineering Science,* 229**,** 538-555.

[204] Gu, L. 2011. Low-frequency piezoelectric energy harvesting prototype suitable for the MEMS implementation. *Microelectronics Journal,* 42**,** 277-282.

[205] Ferrari, M., Baù, M., Cerini, F. & Ferrari, V. 2012. Impact-enhanced multi-beam piezoelectric converter for energy harvesting in autonomous sensors. *Procedia Engineering,* 47**,** 418-421.

[206] Liu, H., Tay, C. J., Quan, C., Kobayashi, T. & Lee, C. 2011. A scrape-through piezoelectric MEMS energy harvester with frequency broadband and up-conversion behaviors. *Microsystem technologies,* 17**,** 1747-1754.

[207] Tang, Q. & Li, X. A wide-band piezoelectric energy-harvester for high-efficiency power generation at low frequencies. 2013 Transducers & Eurosensors XXVII: The 17th International Conference on Solid-State Sensors, Actuators and Microsystems (TRANSDUCERS & EUROSENSORS XXVII), 2013. IEEE, 697-700.

[208] Tang, Q. & Li, X. 2014. Two-stage wideband energy harvester driven by multimode coupled vibration. *IEEE/ASME Transactions On Mechatronics,* 20**,** 115-121.

[209] Wickenheiser, A. & Garcia, E. 2010. Broadband vibration-based energy harvesting improvement through frequency up-conversion by magnetic excitation. *Smart materials and Structures,* 19**,** 065020.

[210] Chen, S., Ma, L., Chen, T., Liu, H. & Sun, L. A magnetic force induced frequency-up-conversion energy harvesting system. 2016 12th IEEE/ASME International Conference on Mechatronic and Embedded Systems and Applications (MESA), 2016. IEEE, 1-5.

[211] Andò, B., Baglio, S., Marletta, V., La Rosa, R. & Bulsara, A. R. A Nonlinear Harvester to Scavenge Energy from Rotational Motion. 2019 IEEE International Instrumentation and Measurement Technology Conference (I2MTC), 2019. IEEE, 1-6.

[212] Andò, B., Baglio, S., Marletta, V., Pistorio, A. & Bulsara, A. R. 2018. A low-threshold bistable device for energy scavenging from wideband mechanical vibrations. *IEEE Transactions on Instrumentation and Measurement***,** 1-11.

[213] Jung, S.-M. & Yun, K.-S. 2010. Energy-harvesting device with mechanical frequency-up conversion mechanism for increased power efficiency and wideband operation. *Applied Physics Letters,* 96**,** 111906.

[214] Kim, G.-W. & Kim, J. 2012. Compliant bistable mechanism for low frequency vibration energy harvester inspired by auditory hair bundle structures. *Smart Materials and Structures,* 22**,** 014005.

[215] Yeo, H. G., Xue, T., Roundy, S., Ma, X., Rahn, C. & Trolier-Mckinstry, S. 2018. Strongly (001) oriented bimorph PZT film on metal foils grown by rf-sputtering for wrist-worn piezoelectric energy harvesters. *Advanced Functional Materials,* 28**,** 1801327.

[216] Pillatsch, P., Yeatman, E. M. & Holmes, A. S. 2014. A piezoelectric frequency up-converting energy harvester with rotating proof mass for human body applications. *Sensors and Actuators A: Physical,* 206**,** 178-185.

[217] Fan, K., Chang, J., Chao, F. & Pedrycz, W. 2015. Design and development of a multipurpose piezoelectric energy harvester. *Energy Conversion and Management,* 96**,** 430-439.

[218] Fan, K., Chang, J., Pedrycz, W., Liu, Z. & Zhu, Y. 2015. A nonlinear piezoelectric energy harvester for various mechanical motions. *Applied Physics Letters,* 106**,** 223902.

[219] Hara, M. & Kuwano, H. 2015. Lead-Free (K, Na) NbO 3 Impact-Induced-Oscillation Microenergy Harvester. *Journal of Microelectromechanical systems,* 24**,** 1887-1895.

[220] Farhadi Machekposhti, D., Herder, J. L. & Tolou, N. 2019. Frequency doubling in elastic mechanisms using buckling of microflexures. *Applied Physics Letters,* 115**,** 143503.

[221] Farhadi Machekposhti, D., Herder, J., Semon, G. & Tolou, N. 2018. Swiss watch featuring Dutch precision. *Mikroniek: vakblad voor precisie-technologie,* 58.

[222] Machekposhti, D. F., Herder, J. L., Sémon, G. & Tolou, N. 2018. A compliant micro frequency quadrupler transmission utilizing singularity. *Journal of Microelectromechanical Systems,* 27**,** 506-512.

[223] Goldschmidtboeing, F. & Woias, P. 2008. Characterization of different beam shapes for piezoelectric energy harvesting. *Journal of micromechanics and microengineering,* 18**,** 104013.

[224] Jackson, N., O'keeffe, R., Waldron, F., O'neill, M. & Mathewson, A. 2014. Evaluation of low-acceleration MEMS piezoelectric energy harvesting devices. *Microsystem technologies,* 20**,** 671-680.

[225] Ma, X., Wilson, A., Rahn, C. D. & Trolier-Mckinstry, S. 2016. Efficient energy harvesting using piezoelectric compliant mechanisms: theory and experiment. *Journal of Vibration and Acoustics,* 138**,** 021005.

[226] Baker, J., Roundy, S. & Wright, P. Alternative geometries for increasing power density in vibration energy scavenging for wireless sensor networks. 3rd international energy conversion engineering conference, 2005. 5617.

[227] Zhang, Y. & Lee, C.-H. 2019. Piezoelectric energy harvesting pedal integrated with a compliant load amplifier. *Advances in Mechanical Engineering,* 11**,** 1687814018820142.

[228] Wen, S. & Xu, Q. Design of a Novel Piezoelectric Energy Harvester for Scavenging Energy from Human Walking. 2018 IEEE/ASME International Conference on Advanced Intelligent Mechatronics (AIM), 2018. IEEE, 792-797.

[229] Feenstra, J., Granstrom, J. & Sodano, H. 2008. Energy harvesting through a backpack employing a mechanically amplified piezoelectric stack. *Mechanical Systems and Signal Processing,* 22**,** 721-734.

[230] Cao, D.-X., Duan, X.-J., Guo, X.-Y. & Lai, S.-K. 2020. Design and performance enhancement of a force-amplified piezoelectric stack energy harvester under pressure fluctuations in hydraulic pipeline systems. *Sensors and Actuators A: Physical***,** 112031.

[231] Priya, S., Song, H.-C., Zhou, Y., Varghese, R., Chopra, A., Kim, S.-G., Kanno, I., Wu, L., Ha, D. S. & Ryu, J. 2019. A review on piezoelectric energy harvesting: materials, methods, and circuits. *Energy Harvesting and Systems,* 4**,** 3-39.

[232] Cho, K.-H., Park, H.-Y., Heo, J. S. & Priya, S. 2014. Structure–performance relationships for cantilever-type piezoelectric energy harvesters. *Journal of Applied Physics,* 115**,** 204108.

[233] Shrout, T. R. & Zhang, S. J. 2007. Lead-free piezoelectric ceramics: Alternatives for PZT? *Journal of Electroceramics,* 19**,** 113-126.

[234] Panda, P. & Sahoo, B. 2015. PZT to lead free piezo ceramics: a review. *Ferroelectrics,* 474**,** 128-143.

[235] Kamel, T. M. & De With, G. 2008. Poling of hard ferroelectric PZT ceramics. *Journal of the European Ceramic Society,* 28**,** 1827-1838.

[236] Kamel, T. M., Kools, F. & De With, G. 2007. Poling of soft piezoceramic PZT. *Journal of the European Ceramic Society,* 27**,** 2471-2479.

[237] Safari, A. & Abazari, M. 2010. Lead-free piezoelectric ceramics and thin films. *IEEE transactions on ultrasonics, ferroelectrics, and frequency control,* 57**,** 2165-2176.

[238] Saito, Y., Takao, H., Tani, T., Nonoyama, T., Takatori, K., Homma, T., Nagaya, T. & Nakamura, M. 2004. Lead-free piezoceramics. *Nature,* 432**,** 84-87.

[239] Kanno, I., Ichida, T., Adachi, K., Kotera, H., Shibata, K. & Mishima, T. 2012. Power-generation performance of lead-free (K, Na) NbO3 piezoelectric thin-film energy harvesters. *Sensors and Actuators A: Physical,* 179**,** 132-136.

[240] Kanno, I., Ichida, T., Kotera, H., Shibata, K., Horikiri, F. & Mishima, T. 2011. Vibration energy harvesters of lead-free (K, Na) NbO3 piezoelectric thin films. *Proc. PowerMEMS***,** 110-113.

[241] Wang, Z. L. 2004. Zinc oxide nanostructures: growth, properties and applications. *Journal of physics: condensed matter,* 16**,** R829.

[242] Bardaweel, H., Al Hattamleh, O., Richards, R., Bahr, D. & Richards, C. A Comparison of piezoelectric materials for MEMS power generation. The sixth International

Workshop on Micro and Nanotechnology for power generation and energy conversion applications, 2006. 207-210.

[243] Tran, A. 2014. AlN piezoelectric films for sensing and actuation.

[244] Tonisch, K., Cimalla, V., Foerster, C., Romanus, H., Ambacher, O. & Dontsov, D. 2006. Piezoelectric properties of polycrystalline AlN thin films for MEMS application. *Sensors and Actuators A: Physical,* 132**,** 658-663.

[245] Jackson, N., Keeney, L. & Mathewson, A. 2013. Flexible-CMOS and biocompatible piezoelectric AlN material for MEMS applications. *Smart Materials and Structures,* 22**,** 115033.

[246] Berg, N. G., Paskova, T. & Ivanisevic, A. 2017. Tuning the biocompatibility of aluminum nitride. *Materials Letters,* 189**,** 1-4.

[247] Karakaya, K., Renaud, M., Goedbloed, M. & Van Schaijk, R. 2008. The effect of the built-in stress level of AlN layers on the properties of piezoelectric vibration energy harvesters. *Journal of Micromechanics and Microengineering,* 18**,** 104012.

[248] Jain, A., Kj, P., Sharma, A. K., Jain, A. & Pn, R. 2015. Dielectric and piezoelectric properties of PVDF/PZT composites: a review. *Polymer Engineering & Science,* 55**,** 1589-1616.

[249] He, X., Yao, K. & Gan, B. K. 2005. Phase transition and properties of a ferroelectric poly (vinylidene fluoride-hexafluoropropylene) copolymer. *Journal of applied physics,* 97**,** 084101.

[250] Akdogan, E. K., Allahverdi, M. & Safari, A. 2005. Piezoelectric composites for sensor and actuator applications. *IEEE transactions on ultrasonics, ferroelectrics, and frequency control,* 52**,** 746-775.

[251] Ruan, L., Yao, X., Chang, Y., Zhou, L., Qin, G. & Zhang, X. 2018. Properties and Applications of the β Phase Poly (vinylidene fluoride). *Polymers,* 10**,** 228.

[252] Shen, D. 2009. *Piezoelectric energy harvesting devices for low frequency vibration applications.*

[253] Challa, V. R., Prasad, M., Shi, Y. & Fisher, F. T. 2008. A vibration energy harvesting device with bidirectional resonance frequency tunability. *Smart Materials and Structures,* 17**,** 015035.

[254] Zhu, D., Beeby, S. P., Tudor, M. J. & Harris, N. R. 2011. A credit card sized self powered smart sensor node. *Sensors and Actuators A: Physical,* 169**,** 317-325.

[255] Lei, A., Xu, R., Thyssen, A., Stoot, A. C., Christiansen, T. L., Hansen, K., Lou-Moeller, R., Thomsen, E. V. & Birkelund, K. MEMS-based thick film PZT vibrational energy

harvester. 2011 IEEE 24th international conference on micro electro mechanical systems, 2011. IEEE, 125-128.

[256] Park, J. C., Park, J. Y. & Lee, Y.-P. 2010. Modeling and characterization of piezoelectric $ d_ {33} $-mode MEMS energy harvester. *Journal of Microelectromechanical Systems,* 19**,** 1215-1222.

[257] Fang, H.-B., Liu, J.-Q., Xu, Z.-Y., Dong, L., Wang, L., Chen, D., Cai, B.-C. & Liu, Y. 2006. Fabrication and performance of MEMS-based piezoelectric power generator for vibration energy harvesting. *Microelectronics Journal,* 37**,** 1280-1284.

[258] Lee, B., Lin, S., Wu, W., Wang, X., Chang, P. & Lee, C. 2009. Piezoelectric MEMS generators fabricated with an aerosol deposition PZT thin film. *Journal of Micromechanics and Microengineering,* 19**,** 065014.

[259] Isarakorn, D., Briand, D., Janphuang, P., Sambri, A., Gariglio, S., Triscone, J.-M., Guy, F., Reiner, J., Ahn, C. & De Rooij, N. 2011. The realization and performance of vibration energy harvesting MEMS devices based on an epitaxial piezoelectric thin film. *Smart Materials and Structures,* 20**,** 025015.

[260] Muralt, P., Marzencki, M., Belgacem, B., Calame, F. & Basrour, S. 2009. Vibration energy harvesting with PZT micro device. *Procedia Chemistry,* 1**,** 1191-1194.

[261] Morimoto, K., Kanno, I., Wasa, K. & Kotera, H. 2010. High-efficiency piezoelectric energy harvesters of c-axis-oriented epitaxial PZT films transferred onto stainless steel cantilevers. *Sensors and Actuators A: Physical,* 163**,** 428-432.

[262] Durou, H., Ardila-Rodriguez, G., Ramond, A., Dollat, X., Rossi, C. & Esteve, D. 2010. Micromachined bulk PZT piezoelectric vibration harvester to improve effectiveness over low amplitude and low frequency vibrations. *Proc. Power MEMS'10***,** 27-30.

[263] Hara, M., Horikiri, F., Shibata, K., Mishima, T. & Kuwano, H. 2013. Bulk micromachined energy harvesters employing (K, Na) NbO3 thin film. *Journal of Micromechanics and Microengineering,* 23**,** 035029.

[264] Won, S. S., Lee, J., Venugopal, V., Kim, D.-J., Lee, J., Kim, I. W., Kingon, A. I. & Kim, S.-H. 2016. Lead-free Mn-doped (K0. 5, Na0. 5) NbO3 piezoelectric thin films for MEMS-based vibrational energy harvester applications. *Applied Physics Letters,* 108**,** 232908.

[265] Wang, P. & Du, H. 2015. ZnO thin film piezoelectric MEMS vibration energy harvesters with two piezoelectric elements for higher output performance. *Review of Scientific Instruments,* 86**,** 075002.

[266] Tao, K., Yi, H., Tang, L., Wu, J., Wang, P., Wang, N., Hu, L., Fu, Y., Miao, J. & Chang, H. 2019. Piezoelectric ZnO thin films for 2DOF MEMS vibrational energy harvesting. *Surface and Coatings Technology,* 359**,** 289-295.

[267] Elfrink, R., Kamel, T., Goedbloed, M., Matova, S., Hohlfeld, D., Van Andel, Y. & Van Schaijk, R. 2009. Vibration energy harvesting with aluminum nitride-based piezoelectric devices. *Journal of Micromechanics and Microengineering,* 19**,** 094005.

[268] Defosseux, M., Allain, M., Defay, E. & Basrour, S. 2012. Highly efficient piezoelectric micro harvester for low level of acceleration fabricated with a CMOS compatible process. *Sensors and Actuators A: Physical,* 188**,** 489-494.

[269] Hirasawa, T., Yen, Y., Wright, P. K., Pisano, A. P. & Lin, L. 2010. Design and fabrication of piezoelectric aluminum nitride corrugated beam energy harvester. *Proc. Power MEMS***,** 211-214.

[270] Elfrink, R., Renaud, M., Kamel, T., De Nooijer, C., Jambunathan, M., Goedbloed, M., Hohlfeld, D., Matova, S., Pop, V. & Caballero, L. 2010. Vacuum-packaged piezoelectric vibration energy harvesters: damping contributions and autonomy for a wireless sensor system. *Journal of Micromechanics and Microengineering,* 20**,** 104001.

[271] Marzencki, M., Ammar, Y. & Basrour, S. 2008. Integrated power harvesting system including a MEMS generator and a power management circuit. *Sensors and Actuators A: Physical,* 145**,** 363-370.

[272] Andosca, R., Mcdonald, T. G., Genova, V., Rosenberg, S., Keating, J., Benedixen, C. & Wu, J. 2012. Experimental and theoretical studies on MEMS piezoelectric vibrational energy harvesters with mass loading. *Sensors and Actuators A: Physical,* 178**,** 76-87.

[273] Dow, A. B. A., Bittner, A., Schmid, U. & Kherani, N. P. 2014. Design, fabrication and testing of a piezoelectric energy microgenerator. *Microsystem technologies,* 20**,** 1035-1040.

[274] Jackson, N., O'keeffe, R., Waldron, F., O'neill, M. & Mathewson, A. 2013. Influence of aluminum nitride crystal orientation on MEMS energy harvesting device performance. *Journal of Micromechanics and Microengineering,* 23**,** 075014.

[275] Kim, S., Towfeeq, I., Dong, Y., Gorman, S., Rao, A. M. & Koley, G. 2018. P (VDF-TrFE) film on PDMS substrate for energy harvesting applications. *Applied Sciences,* 8**,** 213.

[276] Montazer, B. & Sarma, U. 2018. Design and optimization of quadrilateral shaped PVDF cantilever for efficient conversion of energy from ambient vibration. *IEEE Sensors Journal,* 18**,** 3977-3988.

[277] Cao, Z., Zhang, J. & Kuwano, H. 2011. Vibration energy harvesting characterization of 1 cm2 Poly (vinylidene fluoride) generators in vacuum. *Japanese Journal of Applied Physics,* 50**,** 09ND15.

[278] Song, J., Zhao, G., Li, B. & Wang, J. 2017. Design optimization of PVDF-based piezoelectric energy harvesters. *Heliyon,* 3.

[279] Gallego, J. A. & Herder, J. L. Criteria for the static balancing of compliant mechanisms. International Design Engineering Technical Conferences and Computers and Information in Engineering Conference, 2010. 465-473.

[280] Merriam, E. G., Colton, M., Magleby, S. & Howell, L. L. The design of a fully compliant statically balanced mechanism. ASME 2013 International Design Engineering Technical Conferences and Computers and Information in Engineering Conference, 2014. American Society of Mechanical Engineers Digital Collection.

[281] Zhou, Z., Gao, Y., Sun, L., Dong, W. & Du, Z. 2020. A bistable mechanism with linear negative stiffness and large in-plane lateral stiffness: design, modeling and case studies. *Mechanical Sciences,* 11**,** 75-89.

[282] Kim, C. & Ebenstein, D. 2012. Curve decomposition for large deflection analysis of fixed-guided beams with application to statically balanced compliant mechanisms. *Journal of Mechanisms and Robotics,* 4.

[283] Hoetmer, K., Woo, G., Kim, C. & Herder, J. 2010. Negative stiffness building blocks for statically balanced compliant mechanisms: design and testing. *Journal of Mechanisms and Robotics,* 2.

[284] Hao, G., Mullins, J. & Cronin, K. 2017. Simplified modelling and development of a bi-directionally adjustable constant-force compliant gripper. *Proceedings of the Institution of Mechanical Engineers, Part C: Journal of Mechanical Engineering Science,* 231**,** 2110-2123.

[285] Xu, Q. 2017. Design of a large-stroke bistable mechanism for the application in constant-force micropositioning stage. *Journal of Mechanisms and Robotics,* 9.

[286] Hao, G. & Mullins, J. 2015. On the infinitely-stable rotational mechanism using the off-axis rotation of a bistable translational mechanism. *Mechanical Sciences,* 6**,** 75-80.

[287] Awtar, S. & Slocum, A. H. 2007. Constraint-based design of parallel kinematic XY flexure mechanisms.

[288] Dijksman, J. F. 1979. A study of some aspects of the mechanical behaviour of cross-spring pivots and plate spring mechanisms with negative stiffness.

[289] Van Eijk, J. 1985. On the design of plate-spring mechanisms.

[290] Zhang, C. 2010. An introduction to averaging method. *Dynamics at the Horsetooth, online,* 2.

[291] Fečkan, M. & Pačuta, J. 2020. Averaging Methods for Second-Order Differential Equations and Their Application for Impact Systems. *Mathematics,* 8**,** 916.

[292] Liu, C. & Yu, K. 2020. Design and experimental study of a quasi-zero-stiffness vibration isolator incorporating transverse groove springs. *Archives of Civil and Mechanical Engineering,* 20**,** 67.

[293] Liu, C. & Yu, K. 2020. Superharmonic resonance of the quasi-zero-stiffness vibration isolator and its effect on the isolation performance. *Nonlinear Dynamics***,** 1-23.

[294] Oppenheim, A. V. 1999. *Discrete-time signal processing*, Pearson Education India.

[295] Cammarano, A., Neild, S., Burrow, S. & Inman, D. 2014. The bandwidth of optimized nonlinear vibration-based energy harvesters. *Smart Materials and Structures,* 23**,** 055019.

[296] Hoetmer, K., Woo, G., Kim, C. & Herder, J. 2010. Negative stiffness building blocks for statically balanced compliant mechanisms: design and testing.

[297] Liu, H., Zhong, J., Lee, C., Lee, S.-W. & Lin, L. 2018. A comprehensive review on piezoelectric energy harvesting technology: Materials, mechanisms, and applications. *Applied Physics Reviews,* 5**,** 041306.

[298] Teoh, H.-C., Yaacob, K. A., Saad, A. & Mariatti, M. 2018. Enhancement of thermal and electrical conductivities of cyanoacrylate by addition of carbon based nanofillers. *Journal of Materials Science: Materials in Electronics,* 29**,** 9861-9870.

[299] Ma, F., Chen, G. & Wang, H. 2020. Large-Stroke Constant-Force Mechanisms Utilizing Second Buckling Mode of Flexible Beams: Evaluation Metrics and Design Approach. *Journal of Mechanical Design,* 142**,** 103303.

[300] Gandhi, P., Sonawale, K., Soni, V., Patanwala, N. & Bansode, A. 2012. Design for assembly guidelines for high-performance compliant mechanisms. *Journal of Mechanical Design,* 134**,** 121006.

[301] Okosun, F., Celikin, M. & Pakrashi, V. 2020. A numerical model for experimental designs of vibration-based leak detection and monitoring of water pipes using piezoelectric patches. *Sensors,* 20**,** 6708.

[302] Tipalin, S. A., Belousov, V. B. & Shpunkin, N. F. Investigation of Uneven Properties of Stainless Steel 12Kh18N10T Depending on the Thickness of the Sheet. Defect and Diffusion Forum, 2021. Trans Tech Publ, 28-36.

[303] Yongrae, R., Varadan, V. V. & Varadan, V. K. 2002. Characterization of all the elastic, dielectric, and piezoelectric constants of uniaxially oriented poled PVDF films. *IEEE Transactions on Ultrasonics, Ferroelectrics, and Frequency Control,* 49**,** 836-847.

[304] Jackson, N., O'keeffe, R., Waldron, F., O'neill, M. & Mathewson, A. 2014. Evaluation of low-acceleration MEMS piezoelectric energy harvesting devices. *Microsystem technologies,* 20**,** 671-680.

[305] Zhang, Z., Xiang, H. & Tang, L. 2021. Modeling, analysis and comparison of four charging interface circuits for piezoelectric energy harvesting. *Mechanical Systems and Signal Processing,* 152**,** 107476.

[306] Priya, S., Song, H.-C., Zhou, Y., Varghese, R., Chopra, A., Kim, S.-G., Kanno, I., Wu, L., Ha, D. S. & Ryu, J. 2017. A review on piezoelectric energy harvesting: materials, methods, and circuits. *Energy Harvesting and Systems,* 4**,** 3-39.

[307] Lohn, S. K., Pereira, E. L. L., Camara, H. F. & Deschamps, C. J. 2016. Experimental investigation of damping coefficient for compressor reed valves.

[308] Rao, S. S. & Yap, F. F. 2011. *Mechanical vibrations*, Prentice hall Upper Saddle River.

[309] Kronauer, R. E. & Musa, S. A. 1966. Necessary conditions for subharmonic and superharmonic synchronization in weakly nonlinear systems. *Quarterly of Applied Mathematics,* 24**,** 153-160.

[310] Tang, L., Yang, Y. & Soh, C. K. 2013. Broadband vibration energy harvesting techniques. *Advances in energy harvesting methods.* Springer.

[311] Žnidarič, A., Pakrashi, V., O'brien, E. & O'connor, A. 2011. A review of road structure data in six European countries. *Proceedings of the Institution of Civil Engineers-Urban design and planning,* 164**,** 225-232.

[312] Joseph, G. V., Hao, G. & Pakrashi, V. 2019. Fragility analysis using vibration energy harvesters. *The European Physical Journal Special Topics,* 228**,** 1625-1633.

[313] Joseph, G. V., Hao, G. & Pakrashi, V. 2018. Extreme value estimates using vibration energy harvesting. *Journal of Sound and Vibration,* 437**,** 29-39.

[314] Yang, W. & Towfighian, S. 2019. A parametric resonator with low threshold excitation for vibration energy harvesting. *Journal of Sound and Vibration,* 446**,** 129-143.

[315] Yang, W. & Towfighian, S. 2017. Internal resonance and low frequency vibration energy harvesting. *Smart Materials and Structures,* 26**,** 095008.

[316] Nie, X., Tan, T., Yan, Z., Yan, Z. & Hajj, M. R. 2019. Broadband and high-efficient L-shaped piezoelectric energy harvester based on internal resonance. *International Journal of Mechanical Sciences,* 159**,** 287-305.

[317] Levin, L. A. & Le Bris, N. 2015. The deep ocean under climate change. *Science,* 350**,** 766-768.

[318] Rodrigues, C., Nunes, D., Clemente, D., Mathias, N., Correia, J., Rosa-Santos, P., Taveira-Pinto, F., Morais, T., Pereira, A. & Ventura, J. 2020. Emerging triboelectric nanogenerators for ocean wave energy harvesting: state of the art and future perspectives. *Energy & Environmental Science,* 13**,** 2657-2683.

[319] Poulain, P. M., Warn-Varnas, A. & Niiler, P. 1996. Near-surface circulation of the Nordic seas as measured by Lagrangian drifters. *Journal of Geophysical Research: Oceans,* 101**,** 18237-18258.

[320] Kabir, E., Kumar, P., Kumar, S., Adelodun, A. A. & Kim, K.-H. 2018. Solar energy: Potential and future prospects. *Renewable and Sustainable Energy Reviews,* 82**,** 894-900.

[321] Løken, T. K., Neshaug, V. & Sætran, L. R. 2016. Energy systems on an autonomous offshore measurement station. *Energy Procedia,* 94**,** 218-226.

[322] Falnes, J. 2007. A review of wave-energy extraction. *Marine structures,* 20**,** 185-201.

[323] Carandell, M., Toma, D. M., Carbonell, M., Del Río, J. & Gasulla, M. 2020. Design and testing of a kinetic energy harvester embedded into an oceanic drifter. *IEEE Sensors Journal,* 20**,** 13930-13939.

[324] Zhang, D., Shi, J., Si, Y. & Li, T. 2019. Multi-grating triboelectric nanogenerator for harvesting low-frequency ocean wave energy. *Nano Energy,* 61**,** 132-140.

[325] Carandell, M., Toma, D. M., Gasulla, M. & Del Río, J. Experimental validation of a kinetic energy harvester device for oceanic drifter applications. OCEANS 2019-Marseille, 2019. IEEE, 1-7.

[326] Munk, W. H. 1950. Proceedings 1st Internaltional Conference on Coastal Engineering, Long Beach, California: ASCE: 1-4.

[327] Carandell, M., Toma, D. M., Del Río, J. & Gasulla, M. Optimum MPPT Strategy for Low-Power Pendulum-Type Wave Energy Converters. 2020 IEEE Sensors, 2020. IEEE, 1-4.

[328] Dotti, F. E., Reguera, F. & Machado, S. P. 2015. A review on the nonlinear dynamics of pendulum systems for energy harvesting from ocean waves. *PANACM***,** 1516-1529.

[329]   Liang, H., Carandell, M., Olszewski, O. & Hao, G. 2022. A New Nonlinear Compliant Mechanism for Harvesting Energy from Ocean Waves. *Oceans 2022: Chennia*, 1-7.

[330]   Qian, F., Liao, Y., Zuo, L. & Jones, P. 2021. System-level finite element analysis of piezoelectric energy harvesters with rectified interface circuits and experimental validation. *Mechanical Systems and Signal Processing,* 151**,** 107440.

[331]   Todaro, M. T., Guido, F., Mastronardi, V., Desmaele, D., Epifani, G., Algieri, L. & De Vittorio, M. 2017. Piezoelectric MEMS vibrational energy harvesters: Advances and outlook. *Microelectronic Engineering,* 183-184**,** 23-36.

[332]   Jackson, N., Olszewski, O. Z., O'murchu, C. & Mathewson, A. 2017. Shock-induced aluminum nitride based MEMS energy harvester to power a leadless pacemaker. *Sensors and Actuators A: Physical,* 264**,** 212-218.

[333]   Kuppens, P. R., Herder, J. L. & Tolou, N. 2019. Permanent stiffness reduction by thermal oxidation of silicon. *Journal of Microelectromechanical Systems,* 28**,** 900-909.

[334]   Middlemiss, R., Samarelli, A., Paul, D., Hough, J., Rowan, S. & Hammond, G. 2016. Measurement of the Earth tides with a MEMS gravimeter. *Nature,* 531**,** 614-617.

[335]   Rezaei, M., Talebitooti, R. & Liao, W.-H. 2021. Exploiting bi-stable magneto-piezoelastic absorber for simultaneous energy harvesting and vibration mitigation. *International Journal of Mechanical Sciences,* 207**,** 106618.

[336]   Dhote, S., Yang, Z., Behdinan, K. & Zu, J. 2018. Enhanced broadband multi-mode compliant orthoplanar spring piezoelectric vibration energy harvester using magnetic force. *International Journal of Mechanical Sciences,* 135**,** 63-71.

[337]   Yang, T. & Cao, Q. 2019. Dynamics and performance evaluation of a novel tristable hybrid energy harvester for ultra-low level vibration resources. *International Journal of Mechanical Sciences,* 156**,** 123-136.

[338]   Hu, G., Tang, L., Das, R. & Marzocca, P. 2018. A two-degree-of-freedom piezoelectric energy harvester with stoppers for achieving enhanced performance. *International Journal of Mechanical Sciences,* 149**,** 500-507.

Appendix A: Settings of the static FEA simulation on the force-displacement relationship of the SBCM structure in COMSOL

There are two stationary study steps in the FEA simulation on the force-displacement characters of the SBCM structure. Therefore, the key settings for this static FEA simulation are introduced in two parts corresponding to the two study steps.

Step 1: Preloading on the negative-stiffness beams

1) The global parameter is defined in the "**Settings**" window of "**Parameters 1**" under "**Global Definitions**" in the "**Model Builder**" window. The parameter is presented in Table A.1.

Table A.1. Global parameter of "*Amp*" in the stationary simulation.

Name	Expression	Value	Description
Amp	7.04 [mm]	0.00704 m	Amplitude of the harmonic base excitation

2) Select "**Fixed Constraint**" under "**Boundaries**" in the "**Physics**" tag. "**Fixed Constraint 1**" appears under the "**Solid Mechanics**" in the "**Model Builder**" window.

3) In the "**Settings**" window of "**Fixed Constraint 1**", select Boundaries 5, 6, 7 and 8 in the Boundary Selection box. During the stationary simulation, the outer frame is fixed.

4) Repeat the operation in 1) and add "**Fixed Constraint 2**" in the model. In the "**Settings**" window of "**Fixed Constraint 2**", select Boundaries 9 and 10 in the Boundary Selection box. During the stationary simulation, the motion of the mass block is also restricted.

5) Click "**Contact Pairs**" from "**Pairs**" in the "**Definitions**" tag, "**Contact Pair 1**" then appears under "**Definitions**" of "**Component 1**" in the "**Model Builder**" window.

6) In the "**Settings**" window of "**Contact Pair 1**", select Boundary 1 in "**Source Boundaries**" and select Boundary 2 in "**Destination Boundaries**". Then the contact pair is defined.

7) Select "**Contact**" in "**Pairs**" of "**Physics**" Tag. Then "**Contact 1**" appears under "**Solid Mechanics**" in the Model Builder window.

8) In the "**Settings**" window of "**Contact 1**", choose Contact Pair 1 just defined in the "**Pairs**" block.

9) Right click "**Contact 1**" just created and select "**Adhesion**". In the "**Settings**" window, select "**Gap**" as the Activation criterion under "**Adhesion Activation**". And put 0.002 into the blank as the value for δ_0. This means boundaries whose distance is smaller than this gap value will be bonded together.

10) In the "**Settings**" window of the "Step 1: Stationary", enables "**Modify model configuration for study step**" and disable the "**Prescribed displacement**" boundary condition which is used for the second study step.

Step 2: Travel of the mass block in the targeted displacement range

1) Select "**Prescribed Displacement**" under "**Boundaries**" in the "**Physics**" tag. "**Prescribed Displacement 1**" appears under the "**Solid Mechanics**" in the "**Model Builder**" window.

2) In the "**Settings**" window of "**Prescribed Displacement 1**", select Boundaries 9 and 10 in the Boundary Selection box. Put "0" in the u_{0x} blank as the prescribed displacement value in horizontal direction is zero. Put "$- Dis$" in the u_{0y} blank as the prescribed displacement value in the vertical direction. Here, Dis is a parameter pre-defined as the displacement value of the movable mass block. The minus sign means moving down direction of the mass block is defined as the positive direction of the displacement x.

3) In the "**Settings**" window of "**Step 2: Stationary 2**", enable "**Auxiliary sweep**" in the "**Study Extensions**". Select "Dis" in the Parameter name blank. Put "$range(-11.4,0.05,11.4)$" in the blank of Parameter value list. This means, the displacement positions of the mass block with an interval of 0.05 mm in the displacement range of -11.4 mm and 11.4 mm (457 positions in total) will be simulated in step 2. The Parameter unit is mm.

4) In the "**Settings**" window of the "Step 2: Stationary", enables "**Modify model configuration for study step**" and disable the "**Fixed Constraint 2**" boundary condition. The mass block then can be driven to move by the "**Prescribed Displacement 1**" operation in the second step.

After the computation on the study (including Step 1 and Step 2) is finished, the force-displacement relationship curve can be obtained and plotted for further analysis. The corresponding setting procedure is given below:

1) Right click "**Derived Values**" under "**Results**" in the "**Model builder**" window and select "**Line Integration**" under "**Integration**". "**Line integration 1**" then appears under "**Derived Values**".

2) In the "**Settings**" window of the "**Line integration 1**", select Boundaries 5, 6, 7 and 8 in the Selection blank. In the same window, select "**solid.RFy**" from the list of "**Replace expression**". This means the reaction force generated on the Boundaries of 5, 6, 7, and 8 will be captured.

3) Click "**Evaluate**" button in the same window, the reaction force data are automatically generated corresponding the displacement positions based on the stationary study.

4) The force-displacement graph will be obtained with clicking "**Table Graph**" button. The force-displacement data can also be exported from COMSOL in various forms for data processing with other more professional software.

Appendix B: Settings of the dynamic FEA simulation on the displacement response of the SBCM structure in COMSOL

Settings of the dynamic FEA simulation on the SBCM structure under harmonic base excitations are described as follows:

1) Some global parameters are defined in the "**Settings**" window of "**Parameters 1**" under "**Global Definitions**" in the "**Model Builder**" window. The parameters are presented in Table B.1. Simulations with different frequencies and accelerations can be achieved by changing values of the corresponding global parameters in this table.

Table B.1. Global parameters in the dynamic simulation.

Name	Expression	Value	Description
Amp	7.04 [mm]	0.00704 m	Amplitude of the harmonic base excitation
f	3 [Hz]	3 Hz	Frequency of the harmonic base excitation
period	1/f	0.33333 s	Time of one vibration period
time_solve	20*period	6.6667 s	Time of one simulation
time_step	period/40	0.0083333 s	Time interval in simulation

2) The sinusoidal base displacement pattern is defined in COMSOL. Right click "**Definitions**" under "**Component 1**" in the "**Model Builder**" window. Select "**Waveform**" from "**Functions**" in the list. In the "**Settings**" window of "**Waveform 1**", select "**Sine**" in the "**Parameters**" section. Put set "*2*pi*f*" as the value of the "**Angular frequency**". Change the content of both "**Label**" and "**Function name**" to "Sine".

3) Right click "**Definitions**" under "**Component 1**" in the "**Model Builder**" window and select "**Variables**". The harmonic base displacement pattern is defined as a variable, "actuation", in the "**Settings**" window as shown in Table B.2.

4) The defined sinusoidal base displacement pattern is applied on the frame by "**Prescribed Displacement**" boundary condition. Select "**Prescribed Displacement**" under "**Boundaries**"

in the "**Physics**" toolbar. "**Prescribed Displacement 1**" appears under the "**Solid Mechanics**" in the "**Model Builder**" window.

Table B.2. Definition of the harmonic base displacement pattern.

Name	Expression	Unit	Description
actuation	Amp*Sine(t[1/s])	m	Harmonic base displacement pattern

5) In the "**Settings**" window of "**Prescribed Displacement 1**", select Boundaries 5, 6, 7 and 8 in the Boundary Selection box. Put "0" in the "u_{0x}" blank as the prescribed displacement value in horizontal direction is zero. Put "actuation*"* in the "u_{0y}" blank as the prescribed displacement value in the vertical direction. In this way, the fame of the SBCM structure will move following the sinusoidal displacement pattern in the vertical direction in time domain.

6) A proper setting on damping is necessary for a stable time-domain simulation. Right click "**Linear Elastic Material 1**" in the "**Solid Mechanics**" under "**Component 1**" in the "**Model Builder**" window. Select "**Damping**" in the list. In the "**Settings**" window of "**Damping 1**", select "**All Domain**" in the selection section. Select "**Rayleigh damping**" in the "**Damping Settings**". Put "0" in the blank of "α_{dM}", and put "0.02" in the blank of "β_{dK}". The damping ratio here is given based on the dynamic experiments in Chapter 5.

7) Right click "**Study 1**" in the "**Model Builder**" window and select "**Time Dependent**" in the list of "**Study Steps**". "**Step 2: Time dependent**" then appears under "**Study 1**".

8) In the "**Settings**" window of "**Step 2: Time dependent**", put "*range(0,time_step,time_solve)*" in the blank of "**Times**" in "**Study Settings**" section, which defines the how long the harmonic vibration lasts and the interval time in the simulation.

9) In the "**Settings**" window of the "**Step 2: Time Dependent**", enables "**Modify model configuration for study step**" and disable the "**Fixed Constraint 1**" and "**Fixed Constraint 1**", which fix both the frame and the mass block in the previous stationary step for preloading. The mass block is free to vibrate under the base excitation defined by the "**Prescribed Displacement 1**" in the time-dependent step.

Following settings are corresponding to the generation of displacement curves of the SBCM based on the dynamic FEA results:

10) In the "**Model Builder**" window, right click "**Results**" and select "**1D Plot group**" in the list. Right click "**1D Plot group 1**", which appears in under "**Results**", and select "**Point Graph**" in the list. In the "**Settings**" window of the "**Point Graph 1**", select Point 1 in Fig. 4.9 in the "**Selection**" blank. In the "**y-Axis Data**" section, put "*v*" in the blank of "**Expression**" and put "*mm*" in the "**Unit**" blank. Enable "**Description**" and put "*Base displacement*" in the blank. In the "**Legends**" section, select "**Description**". Click "**Plot**" button in the left-up corner of the "**Settings**" window, the displacement-time curve of the base/frame is then plotted in the "**Graph**" window.

11) Following the same procedure in 1) and create a new "**1D Plot group**". Select Point 2 in Fig. 4.9 in the "**Selection**" blank in the "**Settings**" window of "**Point graph 2**". Enable "**Description**" and put "**Mass displacement**" in the blank. Other settings are the same with those in 1). The displacement-time curve of the mass block is then plotted in the same "**Graph**" window together with the base displacement-time curve.

12) For plotting the displacement-time curve of the relative displacement between the base and the mass, the majority procedures are the same. In the "**settings**" window of "**Point graph 3**", select point 2 in the "**Selection**" blank. In the "**y-Axis Data**" section, put "*v-Amp*Sine(t[1/s])*" in the blank of "**Expression**". Enable "**Description**" and put "**Relative displacement**" in the blank. Click **Plot**" button in the left-up corner of the "**Settings**" window, the displacement-curves of the base, mass and their relative displacement are plotted in the same graph in different colors with legends.

Appendix C: Data of oceanic drifter motion patterns induced by the synthesized airy wave and the Jonswap wave from Orcaflex

Table C.1. Data of drifter displacement pattern in the vertical direction induced by the Jonswap wave.

Time [s]	Disp. [mm]	Time [s]	Disp. [mm]	Time [s]	Disp. [mm]	Time [s]	Disp. [mm]	Time [s]	Disp. [mm]
0	0.000	3.3	28.036	6.6	-41.406	9.9	-286.975	13.2	-218.504
0.1	0.000	3.4	22.497	6.7	-38.269	10	-212.129	13.3	-198.415
0.2	0.000	3.5	15.401	6.8	-26.409	10.1	-130.494	13.4	-201.271
0.3	-0.003	3.6	6.873	6.9	-5.708	10.2	-45.376	13.5	-225.707
0.4	-0.016	3.7	-2.668	7	15.081	10.3	29.721	13.6	-247.208
0.5	-0.053	3.8	-13.379	7.1	27.260	10.4	73.134	13.7	-251.933
0.6	-0.131	3.9	-25.306	7.2	25.936	10.5	71.493	13.8	-237.427
0.7	-0.263	4	-38.654	7.3	12.370	10.6	29.744	13.9	-213.389
0.8	-0.453	4.1	-53.288	7.4	-5.757	10.7	-25.825	14	-178.205
0.9	-0.691	4.2	-68.333	7.5	-19.259	10.8	-66.774	14.1	-127.030
1	-0.953	4.3	-79.459	7.6	-24.181	10.9	-93.417	14.2	-63.960
1.1	-1.214	4.4	-80.986	7.7	-17.363	11	-111.178	14.3	13.971
1.2	-1.472	4.5	-70.655	7.8	-1.298	11.1	-115.989	14.4	97.404
1.3	-1.735	4.6	-50.414	7.9	21.465	11.2	-109.103	14.5	159.229
1.4	-1.987	4.7	-24.976	8	63.855	11.3	-92.572	14.6	187.787
1.5	-2.173	4.8	3.782	8.1	111.967	11.4	-62.021	14.7	191.067
1.6	-2.250	4.9	36.977	8.2	137.800	11.5	-17.821	14.8	185.863
1.7	-2.224	5	64.427	8.3	157.550	11.6	40.101	14.9	183.040
1.8	-2.113	5.1	73.359	8.4	151.238	11.7	109.779	15	185.848
1.9	-1.887	5.2	64.672	8.5	106.811	11.8	164.698	15.1	197.176
2	-1.446	5.3	38.458	8.6	45.783	11.9	181.359	15.2	217.614
2.1	-0.630	5.4	1.921	8.7	-22.537	12	159.679	15.3	243.793
2.2	0.699	5.5	-30.077	8.8	-98.029	12.1	109.755	15.4	272.998
2.3	2.631	5.6	-51.917	8.9	-177.17	12.2	50.147	15.5	298.449
2.4	5.292	5.7	-62.645	9	-249.66	12.3	-4.191	15.6	301.442
2.5	8.801	5.8	-58.840	9.1	-316.52	12.4	-52.213	15.7	265.269
2.6	13.194	5.9	-44.544	9.2	-374.82	12.5	-98.382	15.8	191.418
2.7	18.380	6	-27.617	9.3	-413.88	12.6	-138.678	15.9	99.629
2.8	23.984	6.1	-14.493	9.4	-437.63	12.7	-173.237	16	16.623
2.9	29.256	6.2	-11.116	9.5	-446.23	12.8	-204.828	16.1	-52.785
3	33.067	6.3	-15.423	9.6	-433.08	12.9	-227.091	16.2	-114.935
3.1	34.204	6.4	-25.668	9.7	-401.98	13	-236.722	16.3	-166.063
3.2	32.241	6.5	-37.413	9.8	-353.08	13.1	-235.198	16.4	-203.308

Appendix C: Data of oceanic drifter motion patterns induced by the synthesized airy wave and the Jonswap wave from Orcaflex

Table C.1. Data of drifter displacement pattern in the vertical direction induced by the Jonswap wave.

Time [s]	Disp. [mm]	Time [s]	Disp. [mm]	Time [s]	Disp. [mm]	Time [s]	Disp. [mm]	Time [s]	Disp. [mm]
16.5	-230.44	20.3	-401.13	24.1	-97.431	27.9	-542.96	31.7	-247.50
16.6	-260.76	20.4	-326.17	24.2	-118.45	28	-466.01	31.8	-194.48
16.7	-320.91	20.5	-243.34	24.3	-138.14	28.1	-373.60	31.9	-141.67
16.8	-393.54	20.6	-155.69	24.4	-153.30	28.2	-266.40	32	-109.90
16.9	-442.42	20.7	-65.793	24.5	-155.31	28.3	-147.44	32.1	-84.281
17	-469.76	20.8	9.557	24.6	-143.27	28.4	-22.822	32.2	-67.370
17.1	-473.46	20.9	31.211	24.7	-119.39	28.5	95.055	32.3	-40.658
17.2	-461.06	21	-12.154	24.8	-82.557	28.6	173.688	32.4	-2.733
17.3	-436.78	21.1	-81.651	24.9	-39.809	28.7	193.383	32.5	27.844
17.4	-397.58	21.2	-142.45	25	-1.477	28.8	170.594	32.6	58.302
17.5	-346.30	21.3	-184.80	25.1	24.640	28.9	128.093	32.7	102.653
17.6	-282.54	21.4	-206.11	25.2	27.993	29	73.449	32.8	137.292
17.7	-202.84	21.5	-206.66	25.3	13.810	29.1	13.196	32.9	152.377
17.8	-108.33	21.6	-187.02	25.4	2.434	29.2	-44.832	33	153.105
17.9	1.247	21.7	-152.41	25.5	5.796	29.3	-100.72	33.1	115.922
18	114.246	21.8	-109.15	25.6	32.479	29.4	-151.76	33.2	46.667
18.1	198.235	21.9	-61.899	25.7	78.847	29.5	-191.19	33.3	-20.156
18.2	237.192	22	-20.118	25.8	144.622	29.6	-216.27	33.4	-70.394
18.3	234.424	22.1	5.572	25.9	228.033	29.7	-221.53	33.5	-107.06
18.4	200.943	22.2	11.089	26	307.343	29.8	-204.53	33.6	-118.53
18.5	149.644	22.3	0.909	26.1	352.397	29.9	-169.52	33.7	-105.84
18.6	84.624	22.4	-13.709	26.2	347.868	30	-116.05	33.8	-76.322
18.7	5.384	22.5	-24.044	26.3	301.035	30.1	-47.156	33.9	-25.469
18.8	-83.090	22.6	-26.178	26.4	228.253	30.2	30.204	34	34.418
18.9	-171.69	22.7	-13.288	26.5	135.770	30.3	113.406	34.1	87.352
19	-254.77	22.8	14.838	26.6	25.045	30.4	183.423	34.2	132.066
19.1	-330.50	22.9	38.474	26.7	-94.599	30.5	212.875	34.3	152.139
19.2	-398.22	23	39.010	26.8	-210.08	30.6	193.381	34.4	151.377
19.3	-456.55	23.1	14.475	26.9	-316.74	30.7	131.159	34.5	145.779
19.4	-505.39	23.2	-16.710	27	-413.14	30.8	44.934	34.6	120.905
19.5	-544.60	23.3	-44.665	27.1	-495.73	30.9	-33.917	34.7	90.751
19.6	-572.67	23.4	-66.913	27.2	-53.50	31	-99.894	34.8	60.114
19.7	-588.83	23.5	-79.994	27.3	-615.51	31.1	-165.64	34.9	11.863
19.8	-592.16	23.6	-86.075	27.4	-649.23	31.2	-221.42	35	-49.986
19.9	-581.32	23.7	-85.337	27.5	-665.30	31.3	-262.63	35.1	-104.48
20	-556.60	23.8	-77.568	27.6	-663.35	31.4	-291.58	35.2	-149.74
20.1	-518.16	23.9	-74.483	27.7	-641.78	31.5	-295.04	35.3	-188.88
20.2	-465.80	24	-81.252	27.8	-601.70	31.6	-277.96	35.4	-209.75

Appendix C: Data of oceanic drifter motion patterns induced by the synthesized airy wave and the Jonswap wave from Orcaflex

Table C.1. Data of drifter displacement pattern in the vertical direction induced by the Jonswap wave.

Time [s]	Disp. [mm]	Time [s]	Disp. [mm]	Time [s]	Disp. [mm]	Time [s]	Disp. [mm]	Time [s]	Disp. [mm]
35.5	-209.39	38.5	300.278	41.5	292.498	44.5	-162.29	47.5	-56.398
35.6	-187.67	38.6	302.698	41.6	364.179	44.6	-151.80	47.6	-55.466
35.7	-148.56	38.7	285.761	41.7	436.357	44.7	-172.43	47.7	-49.878
35.8	-110.31	38.8	254.509	41.8	506.458	44.8	-188.64	47.8	-29.895
35.9	-74.795	38.9	215.270	41.9	545.718	44.9	-182.15	47.9	-12.263
36	-45.608	39	173.835	42	524.688	45	-157.19	48	-17.224
36.1	-50.813	39.1	114.562	42.1	468.365	45.1	-121.23	48.1	-48.473
36.2	-94.664	39.2	32.249	42.2	405.270	45.2	-76.995	48.2	-108.01
36.3	-135.43	39.3	-64.379	42.3	342.107	45.3	-29.473	48.3	-166.68
36.4	-172.32	39.4	-168.66	42.4	285.248	45.4	14.275	48.4	-204.61
36.5	-201.95	39.5	-278.77	42.5	229.681	45.5	52.294	48.5	-228.34
36.6	-201.82	39.6	-386.91	42.6	171.028	45.6	83.913	48.6	-234.99
36.7	-189.27	39.7	-485.52	42.7	116.106	45.7	105.996	48.7	-223.83
36.8	-168.69	39.8	-570.50	42.8	64.044	45.8	117.996	48.8	-204.42
36.9	-133.39	39.9	-633.17	42.9	12.243	45.9	122.334	48.9	-177.14
37	-96.818	40	-671.58	43	-33.294	46	121.783	49	-142.29
37.1	-58.809	40.1	-687.26	43.1	-70.627	46.1	120.500	49.1	-103.56
37.2	-12.692	40.2	-675.57	43.2	-106.5	46.2	121.700	49.2	-62.767
37.3	28.678	40.3	-638.08	43.3	-157.82	46.3	123.551	49.3	-43.357
37.4	52.652	40.4	-576.67	43.4	-236.04	46.4	112.079	49.4	-57.331
37.5	58.588	40.5	-491.38	43.5	-316.82	46.5	67.982	49.5	-81.962
37.6	39.300	40.6	-387.35	43.6	-374.26	46.6	-0.991	49.6	-103.05
37.7	11.834	40.7	-267.27	43.7	-412.70	46.7	-60.502	49.7	-111.14
37.8	12.195	40.8	-145.34	43.8	-431.74	46.8	-97.101	49.8	-106.02
37.9	39.317	40.9	-45.96	43.9	-430.03	46.9	-111.59	49.9	-87.658
38	82.215	41	30.966	44	-414.30	47	-109.53	50	-50.061
38.1	134.573	41.1	89.179	44.1	-382.55	47.1	-98.300		
38.2	189.538	41.2	136.147	44.2	-335.19	47.2	-83.295		
38.3	239.628	41.3	183.464	44.3	-278.67	47.3	-70.183		
38.4	278.167	41.4	232.995	44.4	-214.41	47.4	-61.258		

Note: The data in Table C.1 and Table C.2 are from the EnABLES TA project (No. 106) collaborated with Polytechnic University of Catalonia in Spain.

Appendix C: Data of oceanic drifter motion patterns induced by the synthesized airy wave and the Jonswap wave from Orcaflex

Table C.2. Data of drifter displacement pattern in the vertical direction induced by the synthesized airy wave.

Time [s]	Disp. [mm]	Time [s]	Disp. [mm]	Time [s]	Disp. [mm]	Time [s]	Disp. [mm]	Time [s]	Disp. [mm]
0	0.000	3.8	51.052	7.6	-396.100	11.4	324.939	15.2	-835.62
0.1	0.000	3.9	16.821	7.7	-395.227	11.5	212.647	15.3	-809.93
0.2	0.001	4	-21.904	7.8	-383.658	11.6	105.655	15.4	-762.28
0.3	0.008	4.1	-64.475	7.9	-359.747	11.7	5.297	15.5	-692.67
0.4	0.033	4.2	-109.99	8	-322.302	11.8	-88.975	15.6	-602.46
0.5	0.091	4.3	-157.33	8.1	-270.629	11.9	-178.49	15.7	-494.71
0.6	0.201	4.4	-205.11	8.2	-204.726	12	-263.27	15.8	-374.74
0.7	0.383	4.5	-251.84	8.3	-125.477	12.1	-340.60	15.9	-250.04
0.8	0.650	4.6	-295.98	8.4	-34.788	12.2	-406.04	16	-127.78
0.9	1.021	4.7	-336.08	8.5	64.408	12.3	-455.59	16.1	-11.751
1	1.525	4.8	-370.92	8.6	168.575	12.4	-487.09	16.2	98.522
1.1	2.208	4.9	-399.48	8.7	274.019	12.5	-500.11	16.3	205.611
1.2	3.151	5	-420.97	8.8	377.763	12.6	-495.98	16.4	311.382
1.3	4.470	5.1	-434.87	8.9	477.963	12.7	-477.77	16.5	415.753
1.4	6.312	5.2	-440.98	9	573.729	12.8	-450.54	16.6	516.905
1.5	8.847	5.3	-439.48	9.1	664.559	12.9	-420.90	16.7	611.861
1.6	12.253	5.4	-430.96	9.2	749.723	13	-394.93	16.8	696.997
1.7	16.689	5.5	-416.44	9.3	828.106	13.1	-375.68	16.9	769.233
1.8	22.286	5.6	-397.27	9.4	898.327	13.2	-362.48	17	827.164
1.9	29.125	5.7	-375.02	9.5	959.018	13.3	-352.79	17.1	871.543
2	37.232	5.8	-351.30	9.6	1009.158	13.4	-344.42	17.2	904.567
2.1	46.571	5.9	-327.63	9.7	1048.299	13.5	-336.68	17.3	928.562
2.2	57.039	6	-305.28	9.8	1076.520	13.6	-330.66	17.4	945.217
2.3	68.465	6.1	-285.27	9.9	1094.293	13.7	-329.09	17.5	955.586
2.4	80.603	6.2	-268.33	10	1102.307	13.8	-335.84	17.6	960.404
2.5	93.124	6.3	-255.03	10.1	1101.229	13.9	-354.65	17.7	960.228
2.6	105.619	6.4	-245.80	10.2	1091.671	14	-387.15	17.8	955.386
2.7	117.601	6.5	-241.02	10.3	1074.159	14.1	-431.48	17.9	945.588
2.8	128.510	6.6	-240.98	10.4	1049.232	14.2	-483.08	18	929.281
2.9	137.737	6.7	-245.86	10.5	1017.338	14.3	-536.93	18.1	903.093
3	144.644	6.8	-255.68	10.6	978.753	14.4	-589.16	18.2	862.901
3.1	148.595	6.9	-270.16	10.7	933.360	14.5	-637.75	18.3	806.584
3.2	148.975	7	-288.61	10.8	880.199	14.6	-682.49	18.4	736.400
3.3	145.188	7.1	-309.88	10.9	817.203	14.7	-724.36	18.5	658.447
3.4	136.725	7.2	-332.41	11	741.758	14.8	-763.96	18.6	579.670
3.5	123.214	7.3	-354.31	11.1	652.336	14.9	-799.61	18.7	505.302
3.6	104.438	7.4	-373.59	11.2	550.086	15	-826.93	18.8	438.001
3.7	80.348	7.5	-388.21	11.3	439.106	15.1	-840.42	18.9	377.795

Appendix C: Data of oceanic drifter motion patterns induced by the synthesized airy wave and the Jonswap wave from Orcaflex

Table C.2. Data of drifter displacement pattern in the vertical direction induced by the synthesized airy wave.

Time [s]	Disp. [mm]	Time [s]	Disp. [mm]	Time [s]	Disp. [mm]	Time [s]	Disp. [mm]	Time [s]	Disp. [mm]
19	321.996	22.8	-1008.2	26.6	441.390	30.4	-946.29	34.2	753.496
19.1	266.694	22.9	-943.65	26.7	454.644	30.5	-874.03	34.3	812.184
19.2	209.886	23	-860.41	26.8	474.859	30.6	-790.03	34.4	864.929
19.3	154.110	23.1	-762.79	26.9	499.608	30.7	-698.79	34.5	909.529
19.4	105.079	23.2	-656.41	27	525.103	30.8	-605.53	34.6	944.070
19.5	68.051	23.3	-546.82	27.1	547.194	30.9	-514.99	34.7	967.436
19.6	45.560	23.4	-437.74	27.2	562.920	31	-430.31	34.8	979.513
19.7	37.449	23.5	-330.49	27.3	571.422	31.1	-352.50	34.9	981.032
19.8	41.284	23.6	-224.99	27.4	573.634	31.2	-281.09	35	972.968
19.9	52.117	23.7	-121.04	27.5	571.065	31.3	-215.17	35.1	956.200
20	63.161	23.8	-19.328	27.6	564.738	31.4	-154.35	35.2	931.301
20.1	68.281	23.9	78.447	27.7	554.738	31.5	-98.901	35.3	898.700
20.2	64.916	24	169.899	27.8	540.425	31.6	-49.747	35.4	858.710
20.3	54.820	24.1	252.638	27.9	520.596	31.7	-8.104	35.5	811.407
20.4	41.585	24.2	324.913	28	493.721	31.8	24.958	35.6	756.573
20.5	27.914	24.3	386.185	28.1	458.269	31.9	49.003	35.7	693.588
20.6	14.652	24.4	437.191	28.2	413.043	32	64.564	35.8	621.304
20.7	1.146	24.5	479.486	28.3	357.653	32.1	73.117	35.9	538.285
20.8	-14.427	24.6	514.676	28.4	292.633	32.2	76.709	36	443.515
20.9	-35.178	24.7	544.104	28.5	219.236	32.3	77.458	36.1	337.225
21	-65.136	24.8	568.674	28.6	139.001	32.4	77.105	36.2	221.368
21.1	-107.84	24.9	588.908	28.7	53.268	32.5	76.752	36.3	99.359
21.2	-164.51	25	604.726	28.8	-37.123	32.6	76.890	36.4	-24.772
21.3	-233.10	25.1	615.207	28.9	-132.07	32.7	77.717	36.5	-147.46
21.4	-309.29	25.2	618.715	29	-232.27	32.8	79.642	36.6	-266.24
21.5	-388.48	25.3	613.577	29.1	-338.54	32.9	83.983	36.7	-379.73
21.6	-467.32	25.4	599.258	29.2	-450.43	33	93.132	36.8	-486.86
21.7	-544.45	25.5	577.210	29.3	-565.00	33.1	109.927	36.9	-585.98
21.8	-620.57	25.6	550.660	29.4	-677.25	33.2	136.869	37	-674.23
21.9	-697.80	25.7	523.536	29.5	-781.58	33.3	175.336	37.1	-748.01
22	-777.62	25.8	499.233	29.6	-873.22	33.4	225.159	37.2	-804.03
22.1	-858.25	25.9	479.811	29.7	-948.91	33.5	284.578	37.3	-840.05
22.2	-934.04	26	465.613	29.8	-1006.6	33.6	350.665	37.4	-855.0
22.3	-997.88	26.1	455.502	29.9	-1045.2	33.7	420.037	37.5	-849.16
22.4	-1044.0	26.2	447.653	30	-1064.2	33.8	489.877	37.6	-823.82
22.5	-1069.2	26.3	441.027	30.1	-1063.6	33.9	558.595	37.7	-781.69
22.6	-1071.8	26.4	436.307	30.2	-1042.8	34	625.658	37.8	-727.10
22.7	-1051.4	26.5	435.664	30.3	-1003.4	34.1	690.851	37.9	-666.32

Appendix C: Data of oceanic drifter motion patterns induced by the synthesized airy wave and the Jonswap wave from Orcaflex

Table C.2. Data of drifter displacement pattern in the vertical direction induced by the synthesized airy wave.

Time [s]	Disp. [mm]	Time [s]	Disp. [mm]	Time [s]	Disp. [mm]	Time [s]	Disp. [mm]	Time [s]	Disp. [mm]
38	-606.43	40.5	-256.342	43	899.472	45.5	-295.75	48	-393.58
38.1	-552.88	40.6	-157.822	43.1	842.197	45.6	-299.00	48.1	-257.76
38.2	-507.34	40.7	-47.054	43.2	769.656	45.7	-301.25	48.2	-127.68
38.3	-468.17	40.8	69.230	43.3	679.299	45.8	-303.35	48.3	-10.591
38.4	-432.78	40.9	183.881	43.4	573.556	45.9	-308.24	48.4	94.013
38.5	-399.57	41	292.250	43.5	459.437	46	-320.99	48.5	191.889
38.6	-368.64	41.1	393.970	43.6	345.013	46.1	-347.49	48.6	288.149
38.7	-341.81	41.2	491.402	43.7	236.317	46.2	-391.07	48.7	384.527
38.8	-322.21	41.3	586.703	43.8	136.528	46.3	-449.54	48.8	480.211
38.9	-313.33	41.4	680.257	43.9	46.099	46.4	-516.02	48.9	573.010
39	-317.36	41.5	770.571	44	-37.339	46.5	-582.99	49	659.509
39.1	-333.53	41.6	854.823	44.1	-117.58	46.6	-645.16	49.1	735.188
39.2	-358.05	41.7	929.294	44.2	-196.24	46.7	-700.01	49.2	795.791
39.3	-385.99	41.8	990.512	44.3	-270.17	46.8	-747.38	49.3	839.397
39.4	-412.99	41.9	1036.550	44.4	-333.10	46.9	-789.21	49.4	867.448
39.5	-436.22	42	1067.752	44.5	-379.66	47	-827.80	49.5	883.590
39.6	-454.51	42.1	1086.143	44.6	-407.47	47.1	-862.84	49.6	891.453
39.7	-468.12	42.2	1094.090	44.7	-416.41	47.2	-889.96	49.7	893.500
39.8	-477.78	42.3	1093.330	44.8	-408.02	47.3	-902.57	49.8	891.260
39.9	-483.35	42.4	1084.886	44.9	-385.67	47.4	-895.42	49.9	885.767
40	-482.52	42.5	1069.381	45	-355.18	47.5	-865.87	50	877.777
40.1	-471.18	42.6	1047.314	45.1	-325.21	47.6	-813.16		
40.2	-445.05	42.7	1019.208	45.2	-303.67	47.7	-737.65		
40.3	-401.16	42.8	985.507	45.3	-293.71	47.8	-640.50		
40.4	-338.17	42.9	946.076	45.4	-292.74	47.9	-524.14		

Appendix D: Settings of multi-physics FEA simulations on the SBCM structure excited by drifter motion patterns in COMSOL

The vertical displacement patterns of the oceanic drifter induced by ocean waves are generated from Orcaflex® as introduced in Section 6.1.1. The displacement data with respect to time are saved in two columns in the format of .CSV. This CSV file is then imported in the FEA model in COMSOL using the Interpolation function. Detailed settings are introduced as follows:

1) An Interpolation function should be defined first in the COMSOL model. Click "**Interpolation**" in the "**Definition**" toolbar, "**Interpolation 1**" is then added under "**Definition**" of "**Component 1**" in the "**Model Builder**" window. In the "Settings" window of "**Interpolation 1**", it is found the interpolation function is named as "**int1**" by default. Select "**Local table**" for "**Data source**" in the same settings window. Find and select the displacement data file (.CSV) through the "**Load from file**" button, the displacement data is then imported in the COMSOL model and they are defined as a function named as "**Int1**".

2) In the same "**Settings**" window of "**Interpolation 1**", put "s" in the blank of "**Arguments**" and put "mm" in the blank of "**Function**".

3) Click "**Local variables**" in the "**Definition**" toolbar and add "**Variable 1**" under "**Definition**" of "**Component 1**" in the "**Model Builder**" window. The imported displacement data of the oceanic drifter is defined as a variable which is named as "Actuation". In the "**Settings**" window of the "**Variable 1**", finish the definition of "Actuation" by filling the blank table in "**Variables**" with the content in Table D.1.

Table D.1. Definition of the harmonic base displacement pattern.

Name	Expression	Unit	Description
Actuation	int1(t)	m	Oceanic drifter displacement pattern

4) The imported displacement pattern of the oceanic drifter is applied on the frame by "**Prescribed Displacement**" boundary condition. The detailed settings for "**Prescribed**

Displacement" in the dynamic time-domain simulations have been introduced as setting steps 4) and 5) in Section 4.3.1 and they are not repeated here.

Settings of the FEA simulation with multiple coupling physics (i.e. Solid Mechanics, Electrostatics and Electrical Circuit) on the SBCM-based PVEH in time domain are presented as follows. The imported oceanic drifter displacement patterns are utilized as base excitation signals.

1) In the "**Physics**" toolbar, click "**Add Physics**" button. In this "**Add physics**" window appeared, double click **"Piezoelectricity"** under "**Structural Mechanics**", then the physics of "**Solid mechanics**" and "**Electrostatics**" are added at the same time in the FEA mode under "**Component 1**". In the same "**Add physics**" window, double click **"Electrical Circuits"** under "**AC/DC**", the physic of "**Electric circuit**" is then added in the FEA mode under "**Component 1**".

2) Click "**Parameters 1**" under "**Global Definitions**" in the "**Model Builder**" window, define the parameter of "R_load" with the settings in Table D.2.

Table D.2. Global parameter of "R_load" in the stationary simulation.

Name	Expression	Value	Description
R_load	1000[kohm]	1E6 Ω	External load resistance

3) Damping is important for the time-domain simulation because it determines the simulation stability. Assume that that geometries for the SBCM and PVDF films are created and the materials are selected (the corresponding setting procedure is not described here) in the FEA model, this step defines the damping parameters in the mechanical structure. In the "**Model Builder**" window, right click "**Linear Elastic Material 1**" under "**Component 1**" → "**Solid Mechanics**". Choose "**Damping**" in the drop-down list. In the "**Settings**" window of "**Damping 1**", choose "**Rayleigh damping**" from the "**Damping type**" list in the "**Damping settings**" section. It should be noted that either "**Viscous damping**" or "**Rayleigh damping**" is suitable for time-domain simulation. Put "0" and "0.001" in the blanks for "α_{dM}" and "α_{dK}", respectively.

4) In the "**Model Builder**" window, right click "**Piezoelectric Material 1**" under "**Component 1**" → "**Solid Mechanics**". Choose "**Mechanical Damping**" in the drop-down list. In the "**Settings**" window of "**Mechanical Damping 1**", repeat the procedure shown in Step 3) and complete the settings on the damping of the piezoelectric materials.

5) Boundaries of the PVDF films in the 2D FEA model are illustrated in Fig. D.1. Right click "**Electrostatics (es)**" under "**Component 1**" in the "**Model builder**" window. Choose "**Ground**" in the drop-down list. In the "**Settings**" window of "**Ground 1**", select boundaries of 1 and 2 only in he "**Boundary selection**" blank. Right click "**Electrostatics (es)**" under "**Component 1**" in the "**Model builder**" window. Choose "**terminal**" in the drop-down list. In the "**Settings**" window of "**Terminal 1**", select boundaries of 3 and 4 only in he "**Boundary selection**" blank. In the same "**Settings**" window, choose "**Circuit**" from "**Terminal type**" drop-down list.
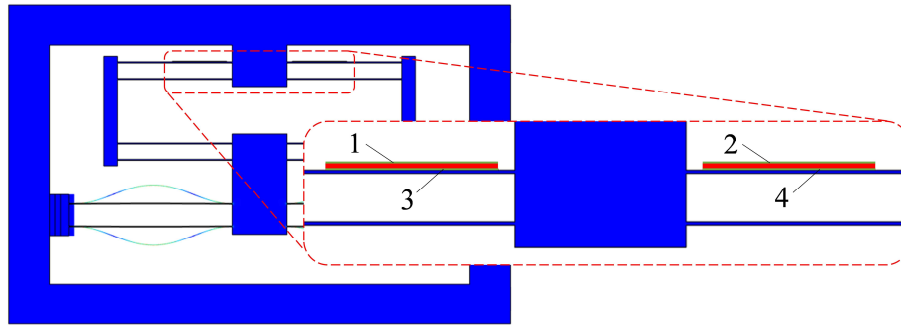

Fig. D.1. Boundaries of the PVDF films defined in the 2D FEA model of the SBCM-based PEVH in COMSOL Multiphysics®.

6) Right click "**Electrical Circuit (cir)**" under "**Component 1**" in the "**Model Builder**" window, select "**Resistor**" in the drop-down list. In the "**Settings**" window of "**Resistor**", put the parameters given in Table D.3 in the "**Node Connections**" section. In the "**Device Parameters**" section, put "R_load" in the blank of "**Resistance**". Right click "**Electrical Circuit (cir)**" again and choose "**External I-Terminal**" in the drop-down list. In the "**Settings**" window of the "**External I-Terminal**", put "1" in the "**Node name**" blank in the "**Node Connections**". Choose "**Terminal voltage (es/term I)**" from the drop-down list for V in the "**External Terminal**" section.

Table D.3. Settings in the "Node connections" section of "Resistor" for "Electrical Circuit (cir)".

Label	Node names
p	1
n	0

8) Adding multiple physics coupling with each other makes the FEA simulation more complex and nonlinear. Therefore, settings in the Solver Configurations are adjusted in particular. In the "**Model Builder**" window, locate "**Electric Potential (comp1.V)**" following the path of "**Study 1**" → "**Solver Configurations**" → "**Solution 1**" → "**Dependent Variables 2**". In the "**Settings**" window of the "**Electric Potential (comp1.V)**", select "**Manual**" in the "**Scaling**" section and put "1e-5" in the corresponding blank. Locate "**Time-dependent Solver 1**" following the same path. In the "**Settings**" window of "**Time-Dependent Solver**", select "**General alpha**" for "**Method**" and put "0.0001" in the "**Time step**" blank for a constant solving step in the computing process of the study. This setting makes the simulation more efficient and stable.

9) The voltage across the external load resistor with respect to time should be plotted and exported for further analysis after the study is computed. In the "**Model Builder**" window, right click "**Results**" and choose "**1D plot groups**". Right click the "**1D plot group 1**" which appears under "**Results**" and select "**Global**". In the "**Settings**" window of "**Global 1**", enter the settings shown in Table D.4 in the "**y-axis Data**" section. Click "**Plot**" button in the "**Settings**" window of the "**1D plot group 1**", the voltage-time curve is then plotted. In addition, the displacement curves of the SBCM model with respect to time can also be plotted based on the same results of the study.

Table D.4. Settings for voltage output across the external load resistor.

Expression	Unit	Description
cir.R1_v	mV	Voltage across the external load resistor R1